UNIVERSITY OF TRENTO

DOCTORAL SCHOOL IN PHYSICS

XXV cycle

Evolution of Arsenic nanometric distributions in Silicon under advanced ion implantation and annealing processes

PhD candidate: Evgeny Demenev

Supervisor: Damiano Giubertoni

Submitted in partial fulfilment of the requirements
of the degree of Doctor of Philosophy, April 2013.

Table of Contents

Acknowledgments

The most of all I would like to acknowledge my supervisor Damiano Giubertoni for his guidance and support throughout the entire time of our co-operative work. His deep and detailed knowledge in the field and broad perspective made learning and research interesting and rewarding.

I want to thank Fondazione Bruno Kessler (FBK) for financial supporting my Phd research activity and in particular Dr. Massimo Bersani head of Minalab unit where I carried out my research activity.

Special thanks to Salvatore Gennaro and Giancarlo Pepponi for their help and joyful time. I would like to thank the rest members of MiNaLab group who were always willing to assist and nurture me as a young researcher. I am very grateful to Dr Florian Meirer who worked at the Dart project ("Dopant profile and activation research for advanced CMOS technology", supported by the Provincia Autonoma di Trento and the European Union within the Marie Curie cofund program). Without his samples the experimental work would not have been such puzzling and interesting.

I would like to thank Majeed Foad and Vinayak Vishwanath Hassan of Applied Material for providing the material for the most of the experiments conducted within these three years of my PhD.

Most of the work was done in collaboration with different institutes and laboratory. I would like to acknowledge staff of STFC Daresbury Laboratory (UK) and especially Dr Paul Bailey, Dr Tim Noakes for providing MEIS measurements and Professor Jaap van den Berg for interesting and useful discussion concerning these results. I want to thank Ruben Bartali for helping me with electrical measurements and once again Salvatore Genaro for providing SEM images when they were essential; Georg Steinhauser from Atominstitut, Vienna University of Technology for providing INAA measurements; Manolis Hourdakis and Androula Nassiopoulou of IMEL Athens for electrical measurements.

Finally, I want to express my love and gratitude to my family: my parents for understanding, my wife for moral support, and all for their enormous patience.

The initial part of my work was carried out within the framework of the project ANNA, Integrated Infrastructure Initiative financed under Framework Program 6 by the European Commission (project n. 026134).

Abbreviations and Symbols

a/c	Amorphous / Crystalline
CMOS	Complementary Metal–Oxide–Semiconductor
Cz Si	Czochalski Grown Si
EOR	End Of Range
EXAFS	Extended X-Ray Absorption Fine Structure
FPP	Four Point Probe
I, V	Point Defects: Interstitial Or Vacancy
IC	Integrated Circuit
INAA	Instrumental Activation Analysis
ITRS	International Technology Roadmap For Semiconductors
LA	Laser Annealing
MEIS	Medium Energy Ion Scattering
ML	Monolayer
MOSFET	Metal-Oxide-Semiconductor Field Effect Transistors
nMOS	N-Type Metal-Oxide-Semiconductor
P/FDL	Perfect/Faulted Dislocation Loops
P3i	Plasma Ion Immersion Implantation
PAI	Pre-Amorphising Implant
pMOS	P-Type Metal-Oxide-Semiconductor
Ppb	Parts Per Billion (10^{-9})
Ppm	Parts Per Million (10^{-6})
RNG	Random Nucleation And Growth
R_p	Mean Projected Range
R_s	Sheet Resistance
RSF	Relative Sensitivity Factor
RTP(A)	Rapid Thermal Process(Annealing)
SIMS	Secondary Ion Mass Spectroscopy
SPE(R)	Solid Phase Epitaxy / Epitaxial Regrowth
SR	Sputtering Rate
SRIM	Stopping And Range Of Ions In Matter
TED	Transient Enhanced Diffusion
TEM	Transmission Electron Microscopy
TRIM	Transport And Range Of Ions In Matter
ULE	Ultra-Low Energy
ULSI	Ultra Large Scale Integration
USJ	Ultra-Shallow Junction
X_j	Junction Depth

INTRODUCTION

The miniaturization of silicon MOSFET devices on integrated circuits has been the driving force for microelectronics to improve performances and power consumption of electronic devices. However, several features of conventional CMOS structures became critical in this scaling down of dimensions. In particular, ultra shallow junctions (USJ) in Si for source and drain extensions demand challenging specifications for technological nodes ≤45 nm: junction depth (x_j) shallower than 15 nm, ~2 nm/ decade abruptness and high concentration of active dopants in order to maintain low values of sheet resistance. Those features mean the introduction of innovative doping schemes like ultra-low energy beam-line (ULE-BL) ion implantation or plasma immersion ion implantation (P3i) to introduce dopant atoms in Si, or like millisecond annealing to electrically activate dopant and remove lattice damage.

This thesis work is focused on the investigation of Arsenic ultra shallow distributions in Si for applications as n-type USJ. Arsenic is an attractive n-type dopant in Si since its high mass, high solid solubility and limited diffusion, including transient enhanced diffusion (TED) that is lower than Phosphorus one. However, it is known that maximum achievable active As concentration in Si is limited by clustering to values one order of magnitude lower than solid solubility. Furthermore, TED becomes not negligible considering the target of <15 nm confinement for junction depth. Those two aspects suggest that not-equilibrium annealings with limited thermal budget have to be considered to prevent dopant diffusion and reach levels of activation possibly higher than equilibrium ones. Therefore, a detailed investigation of advanced implantation/ annealing schemes for introducing As in Si is needed, with particular attention to identify the physical mechanisms involved to help the integration of those processes.

In Chapter 1 a review of the state-of-art of doping in Si is reported with particular reference to the case of As in Si. A literature overview helped to identify the main open issues about As USJ and which are the main mechanisms expected in advanced annealing schemes. In particular, the interaction of As atoms with point defects and consequent clustering or enhanced diffusion is reviewed.

In Chapter 2, the experimental techniques used in the thesis work are described in detail. In particular. Since particular attention was dedicated to obtain chemical depth distributions of As in Si, secondary ion mass spectrometry (SIMS) has been widely adopted. Complimentary information arose from other techniques like medium energy ion scattering (MEIS), instrumental neutron activation analysis (INAA), extended x-ray absorption fine structure spectroscopy (EXAFS) and sheet resistance measurements by four point probe. Main advantages and limits of each technique are reported and discussed.

In Chapter 3, an advanced SIMS protocol developed in this thesis to obtain ultra shallow depth profiles of As in Si is described. The high As concentration, the shallow and abrupt features of the

distributions, their closeness to the surface are all challenges for an accurate SIMS quantification. In fact, even if depth resolution can be optimized decreasing impact energy of primary ions, the closeness of the surface implies a relevant impact of the native surface Si oxide and of the SIMS initial transient width. Therefore, using *ad hoc* samples a quantification approach was developed to correct for the associated variations of sputtering rate and ion yield. The protocol was tested and validated through the comparison with other techniques and then applied in the rest of the thesis work.

In the last 3 chapters, experimental results are reported and discussed, investigating three main processes to produce As USJ in Si: solid phase epitaxial re-growth (SPER), sub-melt laser annealing (LA) and plasma immersion ion implantation (P3i).

Chapter 4 reports the first results obtained investigating SPER of As doped thin amorphous layers (a-layers). SPER was carried out at low temperature (550°C) since re-crystallization can exploit the substrate as crystalline seed. In principle, this allows to bring As atoms in substitutional position without any relevant in-depth diffusion. However, it is known that the moving amorphous/crystalline (a/c) interface displace As atoms resulting in a peak 'snowploughed' to the surface. To investigate this mechanism and its impact on electrical activation, samples were prepared by applying a Si^+ pre-amorphization implant (PAI) aimed to creating a 16 nm thick a-layer and then three different As fluencies (from $1x10^{14}$ to$1x10^{15}$ at/cm^2) were implanted at 2 keV. This set of samples allowed seeing the impact of As concentration on SPER rate, the segregation of As at a/c interface and a refinement of literature data was obtained. High levels of electrical activation were obtained but quickly decreasing if the 550°C thermal treatment is prolonged, especially when comparing PAI samples with samples with the only As implant, revealing a strong instability of junctions prepared by SPER.

In Chapter 5, the stability of As USJ is addressed. Arsenic 2 keV beam-line implants were prepared on a specific substrate where some B doped delta layers were buried to detect possible injection of interstitials (I) coming from USJ de-activation. Both SPER and msec sub-melt laser annealing (LA) prepared junctions were investigated, with more attention to LA samples being them more innovative. Similar samples were also prepared implanting Ge instead of As to discriminate the I contribution from the lattice damage annealing and the one related to As clustering. Results showed a strong I injection already at 550°C during SPER. Furthermore, LA temperature was found fundamental in term of stability of the As depth distribution when successively treated at 700°C. In fact, 1300°C LA As junctions showed limited TED for both As and B after 700°C treatments, whereas the LA 1100 °C samples presented a more relevant diffusion, especially for B deltas. Furthermore, Ge implanted samples showed more B TED than As implanted ones, suggesting that As high concentration reduces the flux of interstitials. This is a new result since in literature the expected behavior is the opposite, as also observed for high temperature LA samples of this work. Data interpretation was carried out suggesting a relevant impact of interstitials left after sub-

melt LA. In particular, the formation of As_nI_m clusters is proposed as an important mechanism of de-activation beside the historically accepted As_nV_m one.

Chapter 6 is dedicated to the investigation of As junctions created by AsH_3^+ P3i and LA. At first, some anomalous evidences are reported: an unexpected thick oxide layer observed on 'as implanted' samples and an increase of retained As dose after annealing. Two new samples were prepared with a high fluence P3i process and surface composition was monitored in an 'ageing' experiment. On one of the two samples a thin SiN_x based protective film was deposited *in situ* right after AsH_3 implantation and before exposing the surface to the atmosphere. Sample without this protective film evolved forming a SiO_2 layer, rich in As and much thicker than native oxides. On the other side, the SiN_x capped sample was stable, no oxide growth was observed and measured As dose was higher than in no-cap samples. Furthermore, a spontaneous formation of As_2O_3 (arsenolite phase) micro-crystals was observed on the surface of uncapped samples. Those crystals easily sublimated after thermal treatments at temperatures as low as 200°C without contributing to increase the retained As dose in Si. Results were interpreted assuming that high fluence AsH_3 plasma irradiation resulted in the deposition of an ultra-thin (few monolayers) arsenic layer. The latter would be readily oxidized when exposed to atmosphere forming micro-crystals with consequent As dose loss, unless an adequate annealing is carried out. Finally, the high As concentration in Si would trigger an 'arsenic-enhanced oxidation'.

In the conclusion section, the main results are summarized. In particular, this research showed that integration of advanced doping schemes for As USJ in Si are possible once the main mechanisms behind As TED, clustering and in general dose loss are solved. In particular, among the investigated annealing approaches, sub-melt LA resulted very promising in terms of x_j shallowness and stability as long as the LA temperature is relatively high. Otherwise, the interstitials left by a low temperature LA can interact with As atoms forming clusters and triggering TED. Plasma immersion ion implantation can be preferred to BL since it ensures very high dopant concentration and x_j ~10 nm, but the high reactivity of the irradiated surface is an issue. In fact, atmosphere exposure produces an enhanced oxidation of Si substrate and a spontaneous formation of As_2O_3 micro-crystals. The latter easily sublimates at temperature as low as 200°C with consequent As dose loss and risk of contamination of production tools. This can be avoided as long as an ultra-thin (~1 nm) cap layer is deposited in situ after P3i. Alternatively, annealing has to be carried right after implantation and possibly without atmosphere exposure in order to drive-in dopant without any loss in As_2O_3 micro-crystals and SiO_2 growth.

Chapter 1. Doping and damage annealing in Si

1.1 Introduction

Starting from mid 70s the ion implantation became the prime step in fabrication of silicon-base integrated circuits (IC) in ultra large scale integrated technology (ULSI). The main advantages, such as ability to control the depth and dose of the Implanted ion, made of this technique the dominant method for introducing dopant atoms into silicon in order to produce electrically active semiconductive (both n- and p- type) regions in complementary metal oxide semiconductor (CMOS) transistors. Currently there is no alternative doping technology which can guarantee the comparable level of accuracy and reproducibility for volume production.

The ion implantation process has, however, the effect of damaging the regular crystalline structure of the silicon lattice through collisions between the dopants and Si atoms. This damage has to be recovered to allow the substrate to have the desired electrical properties. The usual way of doing this is via thermal processes. These, in turns, can result in dopant atom motions and re-arrangement in the silicon substrate micro-structure that can affect junctions' position and electrical dopant activation. The work described in this thesis is focused on the behavior of post-implantation damage recovery, behavior and thermal stability of the created doped region. The studied implantation condition are relevant to current and future device production. An additional, using of plasma ion immersion implantation, as a possible alternative to the conventional ion implantation, is investigated.

1.2 Metal oxide semiconductor devices and future trends of microelectronics

Silicon-based microelectronics for digital logic and memory applications is based on the integration of large numbers of switches realized by Metal-Oxide-Semiconductor Field Effect Transistors (MOSFET) produced on a single silicon chip. In fact, up to billions of MOSFETs can be built on a single integrated circuit (IC) chip with an optimized cost-to-performance ratio [1]. Over the last 40 years the driving force for performance improvements has been the miniaturization of MOSEFT devices, also indicated as scaling. The latter allows an integration of larger number of devices improving the number of operations, performances and cost per operation parameters. Basic logic gates are produced on IC using combinations of n-channel MOS (NMOS) and p-channel MOS (PMOS) field effect transistors. For this reason, the adopted technology is usually referred to as complementary metal-oxide-semiconductor (CMOS) technology. The building block of this technology is schematized in figure 1.1, where a vertical section of an NMOS transistor is shown. –It is a planar structure based on three main terminals, i.e. source, drain and gate. In particular, source and drain are two highly doped regions separated by a space of silicon

of opposite doping type called MOSFET channel. The point where the doping concentration of source/drain equals the channel one is defined as junction depth (x_j). Source and drain can be considered as an emitter and collector of charge carriers (electrons for NMOS or holes for PMOS), respectively. A metallic or polysilicon gate terminal is located over the channel, separated by an insulated layer (SiO_2 or materials with higher dielectric constant). When an adequate voltage is applied to the gate, a conductive region is created between source and drain, i.e. the MOSFET channel. Free carriers are injected applying a potential difference between source and drain and can travel through the Si channel. Therefore, simply acting on the gate voltage can allow or inhibit the passage of current and thus the MOSEFT can be operated as a switching device to realize logic circuits. A crucial point defining the electrical performances of a MOSFET device are the source and drain extension (SDE) junctions, i.e. the ultra-shallow junctions (USJ) extending below the gate and that actually inject carriers in the devices. Those are the shallowest p/n junctions in MOSFET and are one of the most critical points of IC scaling. In fact, the lateral miniaturization of devices implies also a proportional vertical scaling of SDE so that today industries requirements are to confine, in depth, the electrically active doped region within a thickness of ~10^1 nm, (according to ITRS at the technological node of 22 nm X_j values are in the range of 9.5 nm [2]). Furthermore, also an abrupt junction is required to avoid the so called 'short-channel-effects' (SCE). Abruptness is usually measured in nm/decade, i.e. the lateral or vertical length necessary to observe a decade of dopant concentration decrease. Finally, reducing the volume of active carrier confined in shallow junctions increases the SDE sheet resistance, one of the main contributes to the parasitic resistance. The latter impacts on transistor drive current and on the resistance/capacitance time delay of the transistor, i.e. on power consumption and switching speed. Therefore, the ideal SDE must have ultra-shallow x_j, ultimate abruptness and very high level of active dopant to keep sheet resistance to low values. This poses substantial challenges for both controlling diffusion at such small scales and achieving high level of activation at or even above dopant atoms solubility limit in silicon.

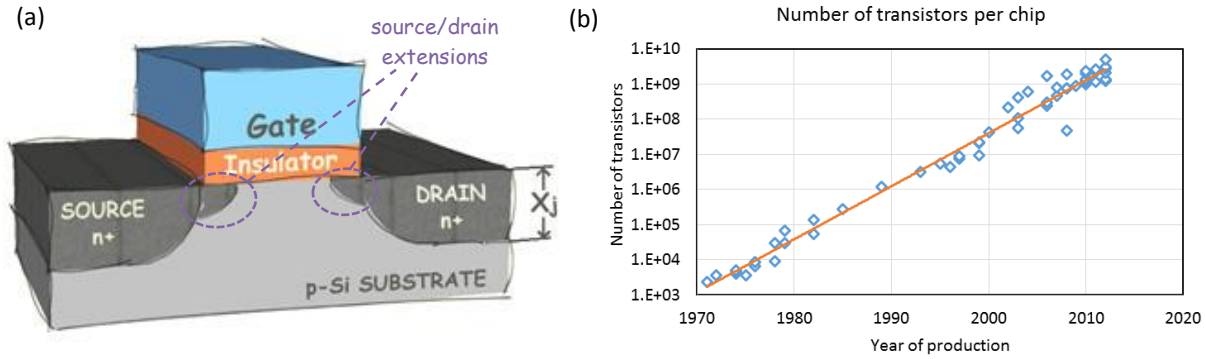

Figure 1.1. (a) Schematic cross-section of an n-MOS device. x_j – junction depth of source\drain region.
(b) Exponential grown of number of transistor in one microprocessor in the last 40 years. [3]

The concentration of free carriers in the source/drain region defines the efficiency of transistors. Their concentration can be significantly altered by adding dopant atoms in silicon lattice. Recent studies of CMOS transistor trends have targeted to keep size of SDE x_j at one half of gate length for high

performance devices [2]. For a gate length of 22 nm (which is currently the most advanced technology process available) the junction depth is 9.5 nm.

In the top part of figure 1.2 the scaling of CMOS devices at Intel, one of the leading IC manufacturers, is reported [4]. The technology node is usually described by the first level half-pitch dimension (i.e. half the distance between identical features in an array), as defined by the International Technology Roadmap for Semiconductors (ITRS). This document is periodically issued by means of a large cooperation between global chip manufactures, research community and equipment suppliers, the Semiconductor Industry Association. Its aim is defining targets for the production of future devices. The future trends of IC devices scaling for high–performance logic, as reported in the last ITRS 2012, are given in the table in the bottom part of the figure 1.2. As seen, starting from 2012, SDE x_j is expected to be as low as 10 nm and in the next years it will be significantly decreased. Creating such shallow dopant distributions is highly challenging for a conventional doping technology like beam-line ion implantation and annealing process. Those aspects will be discussed in the chapters 4-6 of the present work.

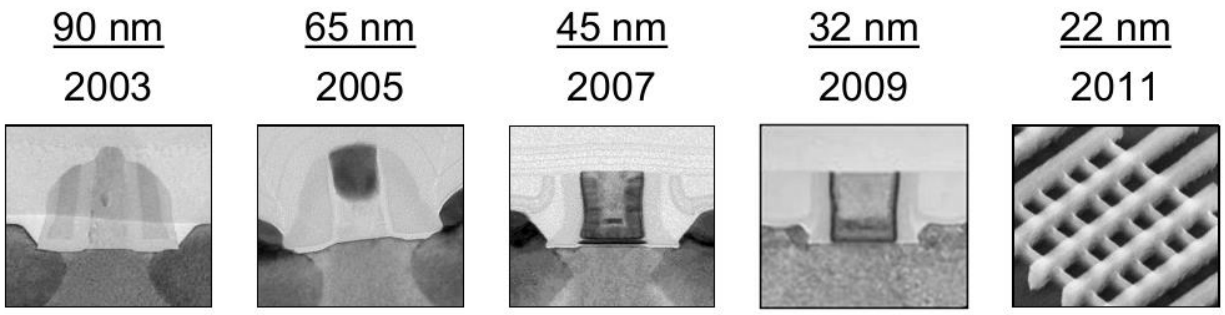

	2011	2012	2013	2014	2015	2016	2017
Physical gate length, L_{gate} (nm)	24	22	20	18	17	15	14
Source/drain extention junction depth x_j (nm)	10.5	9.5	8.7	8	7.3	-	-
Maximum resistivity (Ω/□)	660	680	750	810	900	-	-
Junction abruptness (nm/decade)	2.8	2.4	2.3	2.0	1.8	-	-

Figure 1.2. Top: TEM cross sections of integrated MOSFET structures at Intel for each indicated technology node. Bottom– future trends of IC devices scaling for high–performance logic for parameters defining USJ (from ITRS 2012 roadmap[2]).

1.3 Electrical properties and doping of silicon

Silicon is a covalent semiconductor where the atoms are arranged in a diamond structure forming covalent bonds with their four neighbors. From the electrical point of view, silicon can be defined as

'intrinsic' when the crystal is perfect and neither impurities/foreign atoms nor lattice defects are present. In this situation, Si has two separated electron energy bands, i.e. valence and conduction bands (VB and CB, respectively). Their separation or bandgap is equal to 1.1 eV (at 300 K temperature). Therefore, at absolute zero temperature, Si behaves as insulator and electrons are all in the valence bands, i.e. involved in the covalent bonds. However, at T different from zero, the relatively low value of bandgap makes possible the passage of electrons from VB to the CB by the only thermal energy. In fact, increasing temperature will provide a value of energy ~$3k_BT$ to some electrons and break their covalent bonds. This results in couples of free electrons and relative holes. Both electron and hole can be seen as free charge carriers able to move under applied electric field. However, the intrinsic carrier concentration is relatively low unless high temperatures are reached.

Silicon electrical properties can be drastically modified by introducing external atoms able to introduce energy levels in the prohibited bandgap. Elements able to introduce discrete levels close to the silicon conduction band are denominated n-type dopants, whereas the elements able to introduce levels close to the valence band are identified as p-type dopants.

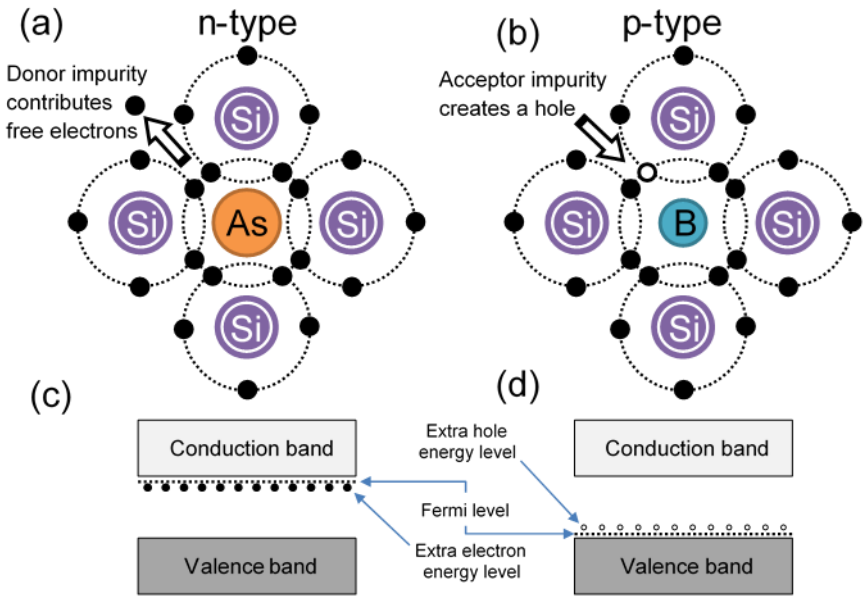

Figure 1.3. Bonding diagram (a,b) and conductive band diagram (c,d) of extrinsic semiconductors.

In n-type doped silicon, foreign atoms containing five valence electrons are placed in the silicon lattice in a substitutional position where 4 valence electrons are involved in the covalent bonds with surrounding Si atoms (figure 1.3, a). However, the fifth electron is weakly bonded to the dopant atom since it is not involved in Si-bonds. This means that the thermal energy available at room temperature can break this weak bond and the electron becomes free to move in the Si lattice, creating an additional charge carrier. The n-type dopant atoms are also called donors.

Similarly, if the silicon is doped with atoms containing only three valence electrons, the latter are involved in the covalent bonds with Si atoms whereas a hole is created in place of the forth missing

electron (figure 1.3, b). This hole can be easily filled by other electrons made mobile by the only thermal energy, and thus again a charge movement can be observed. However, this phenomenon can be represented as a movement of a positive carrier defined as 'hole' instead of the whole electron re-arrangement. Therefore, holes can also move through the lattice as positively charged carriers in p-doped silicon. P-type atoms are also called acceptors. Typical p-type dopants are group III elements such as boron, gallium or indium, whereas n-type dopants are group V elements like phosphorus, arsenic or antimony.

Hence, it is clear that varying dopant atom concentrations modifies and controls the electrical conductivity of silicon, i.e. the higher the dopant concentration the higher the conductivity. Furthermore, both positive and negative carriers can be involved in silicon conductivity. This makes possible the realization of p/n junctions that represent the fundamental building blocks of semiconductor technology. In fact, when a n-type Si region is in perfect contact with a p-type, electrons and holes diffuse through the interface leaving ionized donor and acceptor atoms, respectively. A charge-depleted region is created when this diffusion is counter-balanced by the electric field arisen from the ionized acceptor and donor atoms. The application of an external electric field can alter this equilibrium and depending on voltage polarity, current can either travel through the junction (direct polarization), e.g. when a positive voltage is applied to p-type side, or be inhibited (indirect polarization), e.g. when a negative voltage is applied to p-type side.

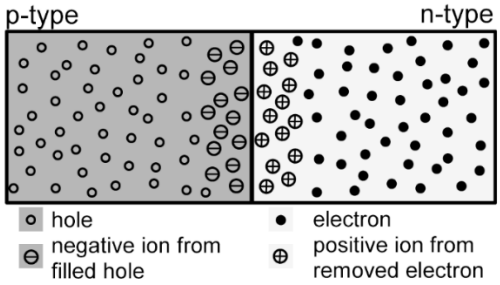

Figure 1.4. A p–n junction in thermal equilibrium with zero-bias voltage applied

In the next sections, the principal methods to produce doped regions in silicon will be reviewed.

1.4 Ion Implantation

For the past 35 years, ion implantation has been a dominant method of semiconductor doping offering unsurpassed advantages such as reproducibility, extremely accurate depth distribution and dose (<1%) control. The term dose or fluence indicates the total number of ions incident per unit of surface (ion/cm^2 or atoms/cm^2 usually) and gives a measurement of the total integral of impurities introduced in the irradiated material. In ion implantation process, ions extracted from a source (plasma, evaporation, etc…) are accelerated with an electric field and focused by a series of deflectors and electrostatic lenses to the wafer surface. Impinging ions loose energy through nuclear and electronic interactions with silicon atoms, and they eventually come to rest in the host lattice. Since practical implantation energies exceed the threshold of lattice atom displacement, the ion implantation process produces damage to Si lattice structure through collision between the dopants and Si atoms.

Since implanted ions come to rest through series of random collisions, their final position will follow a statistical depth and lateral distribution centered at a characteristic position. This center corresponds to the maximum probability of finding implanted ions and thus it represents the position of maximum implanted atom concentration. Since practically an ion beam is rastered over the whole wafer surface, the main parameters becomes the ones defining the depth distribution of the implanted ions. The latter can be approximated with a Gaussian distribution, or more precisely, with a Pearson distribution. The projection of the maximum concentration position on the direction normal to the surface is defined as projected range (R_p). In general, for a given ion, the lower the implant energy, the lower the R_p and the closer to the surface the implant distribution and thus the resulting dopant position. Furthermore, the total dopant dose introduced by ion implantation can be controlled by integrating the ion beam current, being the latter proportional to the number of ions per time unit irradiating the wafer surface.

Starting from basic ion-matter interactions, simulations using Monte-Carlo algorithm have been developed and they are a useful tool to predict in-depth distributions of large fluencies (or doses) of implanted species [5]. SRIM (stopping and range of ions in matter) is a software using these algorithms and it allows not only the calculation of the distribution of the dopant atoms but also the damage cascade produced in the irradiated material [5].

As implied in the previous paragraph, one of the drawbacks of ion implantation is the induced lattice damage. In fact, the induced atomic collisions result in a degree of lattice damage determined by the ion species, target composition, ion energy, and incidence angle and target temperature. If the dose is higher than a characteristic threshold, the overlapping of the damage cascades can also result in a full amorphization of the lattice. Since dopant atoms can contribute to the electrical conductivity when they are in substitutional positions and lattice defects are minimal, an annealing process is required to remove the crystal damage and activate dopant atoms. This will be described in detail in section 1.6.

During ion implantation in crystalline silicon (especially with low mass ions, like B) it is possible that a fraction of incident ions can penetrate deeper than expected following particular crystal planes or axial directions in the lattice. This phenomenon is called *channeling* [5–7] and it results in dopant distribution characterized by long tails. Since this can imply junction depths larger than desired, channeling effect can be partially avoided tilting the substrate away from crystallographic directions (typically by an angle of 7° in (100) Si irradiation) to minimize the exposition of lattice channels to the incident beam. However, the efficiency of this solution decreases with the implantation energy, as shown by Collart et al. in [8] for boron implants at energies lower than 5 Kev. An alternative solution consists in pre-amorphizing the Si lattice before implanting dopant atoms, eliminating every possibility of lattice

channeling. This is typically carried out implanting relatively high fluencies (≥ $5x10^{14}$ ion/cm^2) of Si^+ or other not-doping species like Ge^+ or inert gas ions like Ar^+ or Xe^+.

The most advanced transistors currently produced by industry is based on sub-32 nm technological processes. As was mentioned in previous sections, these devices require SDE $x_j \leq 10$ nm [2]. If those x_j have to be realized by conventional beam-line ion implantation as described before, implant energy has to be as low as 1 keV for arsenic or even 0.2 keV for boron. This can be a limiting factor for conventional implanters, due to the limited ion extraction from the source, space charge effects and energy contamination. The result is a low wafer throughput making alternative approaches, like Plasma Ion Immersion Implantation (P3i), more attractive.

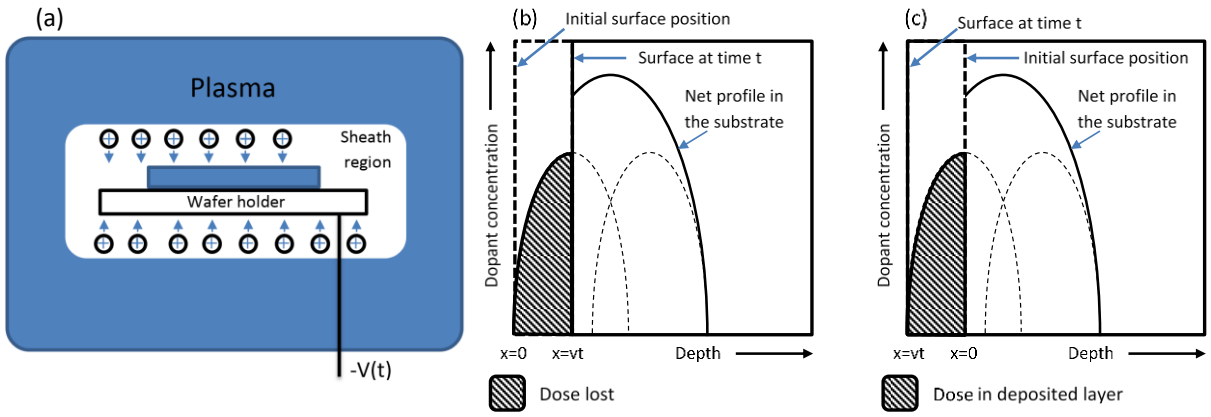

Figure 1.5. (a) Schematic of negatively bias target immersed in plasma. (b) and (c) - illustrations of simultaneous implantation/etching and implantation/deposition.

The physical principles of P3i is illustrated in figure 1.5 (a). By placing a negatively biased target inside a plasma gas whose main species contain dopant atoms (like $B_2H_6^+$ or AsH_3^+), electrons will be repelled near the surface region, establishing a 'sheath' of positive ions. The positive ions around the target will be attracted by the negative potential of target and will impinge into the wafer surface. While traveling through the sheath region, the ions gather momentum and penetrate into the target. The maximum implantation energy is equal to the potential sustained by the sheath thickness although it can be reduced by collision between the ions. This is a relevant difference with beam-line implantation, where essentially all the impinging ions possess the same energy. In P3i, incident ions have a continuous distribution of energies. Therefore, the resulting depth distribution depends on two factors: the sheath thickness, controlled by the voltage applied, and the plasma density in the chamber. Decreasing the wafer bias will result in shallower dopant profile since the x_j dependence on implant bias is linear.

In P3i doping, the plasma gas frequently contains highly reactive species, like fluorine. Depending on the conditions, presence of these species can result in simultaneous etching of the material or deposition on the substrate beside the expected dopant implantation (figure 1.5, b and c). These effects can lead to dramatic consequences in semiconductor processing and therefore they must be carefully

evaluated. Investigating this phenomena during implantation with BF_3 and SiF_4 plasmas, Jones et al. developed a mathematical model able to predict the final implanted dose (Q) in presence of etching/deposition process as a function of implantation time (t) [9]:

$$Q = \frac{\Phi L}{v}\left(1 - e^{-\frac{vt}{L}}\right) \tag{1.1}$$

where Φ is the implanted dose rate, L is the characteristic depth determined by the implanted species, and v is the velocity of surface movement. According to those results, when implantation time becomes larger than L/v ratio, the implanted dose will saturate and further processing will not increase it.

A number of technical challenges has to be solved in order to provide a well-controlled P3i process and to make it suitable to a semiconductor production flow. In 1998 Felch and Ha demonstrated that plasma implantation can be utilized in PMOS device production [10]. Reported implantation conditions showed very good results including gate oxide reliability and compatibility with different step in IC manufacturing process. Ten years later, in 2008 Qin demonstrated in first time that plasma doping can be used in formation of source/drain regions in 68 nm CMOS device [11]; overall, the electrical performance of produced device appeared to be equal or better than of produced with conventional beam line ion implantation: including lower contact resistance, similar threshold and sub-threshold characteristics, higher drive current and transconductance.

1.5 Ion implantation induced defects, damage build-up and amorphization

During ion implantation, dopant ions penetrates the Si target material with high momentum/ energy. Ion energy is transferred to target atoms through a series of collisions; when the transferred energy is greater than the energy of silicon bonding, a Si atom is knocked off its lattice site creating a vacancy and self-interstitial atom pair, also called Frenkel pair. Displaced/recoil silicon atoms, can also collide with other silicon atoms producing further vacancies and interstitials All these crystalline lattice defects are called as *point defects*. A single implanted ion may result in the formation of a high amount of point defects (10^1-10^4). The main types of point defects are illustrated in figure 1.6.

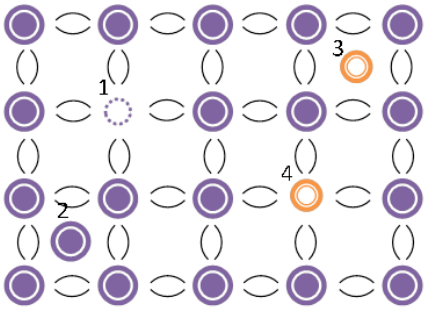

Figure 1.6. Point defects created in silicon lattice by ion implantation: 1 – vacancy, 2 and 3 – interstitials, 4 - substitutional.

A simulation of both damage and dopant distribution is shown in figure 1.7. Vacancy and interstitial distributions are both calculated for an ion implantation of As^+ 2 keV ions normally incident to the surface. The simulation is carried out using SRIM-2013 software [12] calculating 10^5 implanting trajectories. Arsenic ions form the expected Gaussian distribution with an R_p of 5.7 nm. Since ion collision

creates interstitials with velocity different from zero, a separation between vacancy and interstitial distributions is created. Thus, V-rich region is formed near the surface while a region enriched with I is located deeper in the substrate. Heavier ions as well as high implant energies result in a stronger separation between these two distributions.

If the density of damage is high enough then the lattice can be considered as amorphous. In several models the amorphization is considered to take place when the number of displaced atoms in unit volume reaches the atomic concentration (i.e. all the target atoms are displaced) [13]. In case of 2 keV implant, for a total implanted fluence of $1x10^{15}$ cm^{-2} the amorphous layer extends up to 8.6 nm (figure 1.7, dotted line) below the surface as measured by medium energy ion scattering (MEIS, see section 2.3). The abruptness of the interface between amorphous and crystalline layers is determined by the implanted species, being sharper the interfaces obtained with heavier ions.

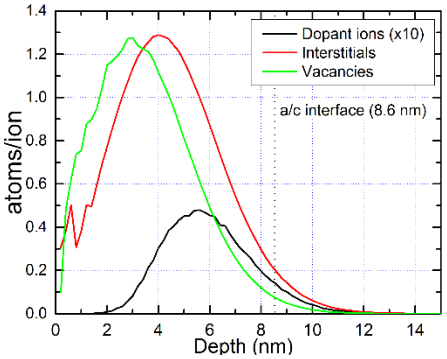

Figure 1.7. Simulated depth distribution of damage and dopant ions after 2keV arsenic implantation in Si. .

1.6 Lattice damage annealing

The damage induced by the ion implantation process represents a limiting factor in producing active dopant distributions. In fact, dopant atoms have to be in substitutional position, and in a crystalline environment, to fully contribute to electrical conductivity. Lattice damage and residual defects can reduce conductivity or introduce mechanisms of leakage in p/n junctions. It is therefore necessary to anneal the lattice damage and this is usually carried out providing thermal energy to the Si wafer. In fact, thermal energy induces a re-adjustment of the Si atoms and the consequent re-location of dopant and Si atoms in the desired substitutional position. However, annealing usually induces also solid state diffusion of dopant atoms beside their activation. This can be a fundamental parameter of evaluation of an annealing process, since the diffusion can result in junctions too deep for the required technological needs.

Older annealing processes were based on furnace systems. However, the slow ramp rates resulted in strong diffusion phenomena, especially since the latter can be enhanced in some temperature windows. For this reason, rapid thermal processing (RTP) was introduced in the 80's. RTP typically exploits high power lamps able to provide heating ramp of ~100-200°C/s for temperatures up to 1200°C. By this way it is possible to limit the thermal budget and very short annealings at very high temperatures can be carried out. The advantage is that temperature windows of strong diffusion can be by-passed and highly active layers with shallow xj are achievable. In the next sections we will review some of the most promising new annealing schemes that are under study for USJ fabrication.

1.7 Solid phase epitaxial regrowth and extended defects

Thin films of amorphous phase can be created in Si by ion implantation as described in previous section. However, amorphous phase in silicon is a metastable phase since it has a higher free energy compared to crystalline phase and thus there is a thermodynamic force inducing amorphous-crystalline phase transformation. In general, this transformation may occur in two different ways depending on initial conditions. In a continuous amorphous layer small grains of crystalline material may randomly nucleate and grow (so called random nucleation and grow process or RNG) resulting in a polycrystalline structure.

However, when the amorphous layer is in perfect contact with a crystalline substrate, the layer reorders at the interface to a single epitaxial crystal exploiting the substrate as a crystal seed via solid phase epitaxial regrowth (SPER), as shown on figure 1.8. In case of amorphous silicon, the SPER velocity for undoped material follows an Arrhenius-type equation with activation energy E_A = 2.76 eV:

$$v_{SPER} = v_o e^{-\frac{E_A}{kT}} \tag{1.2}$$

where the pre-exponential factor v_o = 3.68x10^8 cm/s [14]. The SPER starts at temperatures above 500°C and the growth velocity follows equation (1.2) over nearly 10 orders of magnitude before reaching material melting point. Since the value of the activation barrier for RNG is much higher (4.6eV) than the SPER one, RNG is essentially avoided for amorphous layers in contact with crystalline substrates.

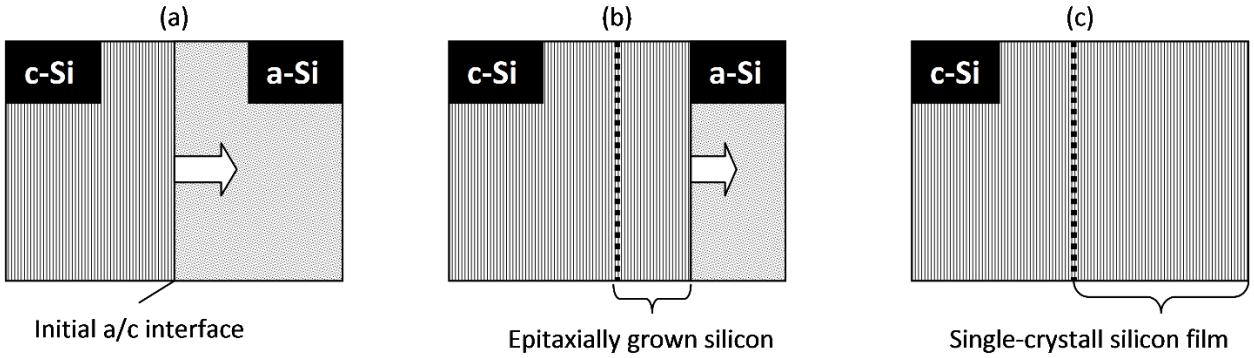

Figure 1.8. Schematic representation of solid phase epitaxial regrowth process.

The recrystallization kinetic and quality of the regrown crystal after SPER depends on the initial substrate orientation. Csepregi at al. [15] demonstrated that crystallographic orientation of the crystalline substrate has very high impact on growth velocity. They found that [001]-oriented substrates growth 25 times faster than [111] (slowest direction). Moreover, they demonstrated that this behavior is independent of temperature. The early work by Muller et al.[16] revealed that regrowth of [111] direction has not only lower crystallization rate but also results in highest residual damage, while the regrowth on [001] and [110] oriented crystal leave much less disorder. Also for both these orientations the SPER growth velocity is linear with time, indicating a layer-by-layer mechanism, unlike [111]-oriented crystals, where non-planar interfaces were observed.

Another very important factor influencing the behavior of a regrowth kinetic is the presence of dopants or impurities within the amorphous layer. The introduction of various atoms may accelerate or decelerate SPER velocity, depending on their concentration and electrical properties. Williams and Elliman [17–19] reported that adding light levels of electrically-active species (less than 2-3 atomic percent's) such as phosphorus, arsenic, and boron increases growth rate linearly with dopant concentration. When the concentration of these dopants becomes sufficiently high (more than 5 atomic percent's), exceeding the dopant-dependent solubility limit, regrowth rate drops sharply. The authors speculated that the decrease of velocity might be attributed to the stress created by the dopant in crystalline phase. On the other side, the introduction of electrically-inactive species such as oxygen, carbon, and nitrogen decreases SPER rate as reported by Kennedy at al. [20]. Generally SPER rate variations are justified by the presence of different type of defective sites at amorphous-crystalline interface, like Si dangling bonds, kinks, or fivefold-coordinated Si atoms in amorphous silicon.

Since the value of SPER activation energy is much lower than typical dopant diffusion one, the regrowth of amorphous Si layer can be carried out at temperatures and times low enough to avoid any significant dopant diffusion, especially when [001]-oriented substrates are used. This makes SPER as a process in principle able to realize USJ, since it can provide high concentration of substitutional dopants without relevant diffusion.

However, even if the quality of crystallinity of SPER layers is very high, several types of defects still may be present. During recrystallization most of the dopant atoms (A) are placed into substitutional sites in silicon lattice, forming substitutional point defects (A_s). Nevertheless, these atoms may also form different types of inactive atoms with other point defects (I or V), especially when the concentration of dopant is very high. For instance, in case of arsenic implanted material, which is of interest in present work, the most stable clusters contain vacancy surrounded by one or few atoms of arsenic (As_nV) [22], although in presence of excess of interstitials, clusters where As incorporates interstitial Si (SiI) can be formed [23]. A formation of these clusters is discussed in detail in chapter 5. Unlike arsenic, boron mainly forms clusters involving only interstitials (boron-interstitial clusters, or BIC's) [24].

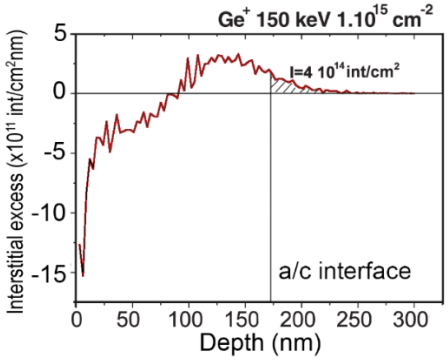

Figure 1.9. Depth profile of interstitial excess after 150keV $1x10^{15}cm^{-2}$ Ge implantation, adapted from [21]

Another technologically relevant type of crystal disorder is the End-Of-Range (EOR) damage, which is produced upon SPER conditions below the original amorphous/crystalline interface position. This

region is highly supersaturated with interstitials defects as shown in figure 1.9. During recrystallization these I's are immobile due to high SPER rate and low diffusivity and consequently they tend to 'precipitate' forming EOR defects [25]. During the thermal treatment these defect evolve through a ripening process due to reduced energy of larger defects. Smaller clusters release interstitials while dissociate and meanwhile the larger ones grow attracting the released interstitials. At initial stage of annealing the vast majority of interstitial are stored as di-interstitial [26]. During the subsequent annealing at moderate

temperature (below 800°C) they grow forming larger clusters with the most stable containing 4 or 8 atoms ("magic" clusters) [27]. For larger annealing time, interstitials aggregate into extended defects, which can be "rod-like" defects ({113} defects), perfect and faulted dislocation loops (PDL's and FDL's) [28]. Figure 1.10 show the TEM image of each defect (from [29]). These defects can contribute to the leakage current in the junction when they are placed into the space charge region of the device. If the annealing continues, these defects undergo Ostwald ripening and then they dissolve and may disappear [30] producing a flow of interstitial atoms which can cause a significant diffusion of dopant. The effect is known as transient enhanced diffusion, or TED [31], [32].

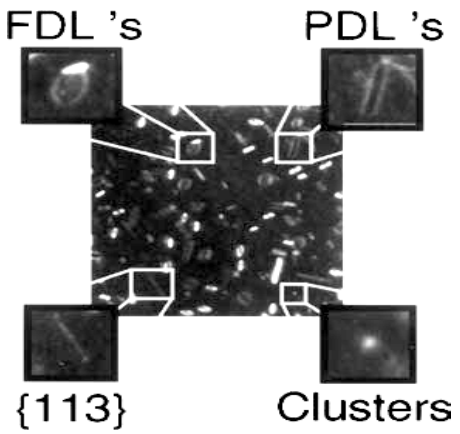

Figure 1.10. TEM images of defects present in the EOR damage area of ion implanted Si. Adapted from [21]

1.8 Millisecond annealing: Laser annealing and damage evolution

In the last years, new annealing processes have been investigated due to the need of high electrical dopant activation together with minimal diffusion. In particular, thermal treatments able to limit thermal budget providing very short annealing times at high temperatures have been proven effective in terms of both limited dopant diffusion and high activation. Millisecond thermal treatments like Flash or laser sub-melt annealings (LA) are two promising solutions in this respect. In these annealing techniques, a pulse of energy (either submitted by a laser or by a lamp flash) is absorbed in a narrow region underneath the surface (few μm's). The irradiated thickness is, hence, extremely thin compared to the whole wafer thickness. Under these conditions a large temperature gradient is produced, and the substrate can act like a heat sink for an extremely quick conductive cooling of the surface after the pulse. However, the full integration of this kind of annealing processes is possible only if the evolution of ion induced damage and dopant diffusion and activation is clarified. In case of msec annealings applied to Ge^+ PAI created amorphous layers (a-layer), recent results showed that as long as the a-layer is thicker than ~10 nm, the damage evolution is quite similar to what observed for 'slower' RTA processes: I's first

coalesce in {113} defects just below the original a/c interface, then evolving to dislocation loops that eventually are dissolved. However, the msec annealing time shifts the dissolution of the defects to higher temperatures and thus remaining defects can be detected at temperatures as high as 1300°C. Cristiano *et al.* [33] reported this behavior for a $1x10^{15}$ at/cm^2 at 30 keV Ge PAI following Flash annealing: the DL density was lower for a 1325°C Flash compared to 1275°C whereas the average size increased in accord to the Ostwald ripening mechanism. However, when Ge PAI was carried out with a 2 keV energy ($1x10^{15}$ at/cm^2 fluence), a ~5 nm thick a-layer was created and the damage evolution was different. In fact, after a 1300°C Flash annealing extended defects still existed but they were only {113} defects of less than 10 nm length. Estimation of I's trapped in those defects showed that their total amount is the lowest if compared with higher energy PAI cases, i.e. only ~$4.5x10^{12}$ cm^{-2} for 2 keV PAI against ~$2.5x10^{13}$ cm^{-2} for 15 and 30 keV PAI, respectively. The reason for this different behavior was indicated in the surface proximity: the interstitial distribution gradient toward the surface becomes so high, that interstitials are fast driven to the surface where they can be dissolved, leaving less of them to form larger defects. Furthermore, the effect of annealing temperature for the 2 keV PAI case was also investigated in [33]. TEM plan views show that the density of {113}'s drastically decreases when temperature increases from 1100 to 1300°C.

Another interesting evidence about msec annealing on PAI samples was reported by Sharp et al. in [34]. The authors investigated Ge-PAI thin layers (Ge energy from 2 to 10 keV, fluencies from 5 to $10x10^{14}$ at/cm^2) heavily doped by boron introduced by ion implantation ($1x10^{15}$ at/cm^2 at 0.5 keV). Annealing was carried out with msec laser sub-melt process at 1150 °C with number of pulses varying from 1 to 10. When a post-LA thermal treatment was carried out for 60 s at 600-900°C, the B doped samples with either 5 or 10 keV PAI energy underwent a typical electrical activation/de-activation path. In fact, B atoms are supposed to form B-interstitial clusters (BIC) with I's coming from EOR defects in this range of temperature during the Ostwald ripening phase and the following dissolution [30]. On the other hand, the 2 keV PAI samples turned out to be the most stable although they initially were the less electrically active after the only LA. At the same time, B diffusion was minimal for the 2 keV PAI samples whereas relevant TED phenomena were reported for 5 and 10 keV PAI. TEM plan views reported large I clusters and defects for 1 scan at 1100°C on 5 and 10 keV PAI samples, then evolving to DL's for a 10 scan annealing. Those clusters and defects can be the responsible for the TED and de-activation of B distributions upon following thermal treatments at 700-800 °C. However, the 2 keV PAI samples, where B diffusion and deactivation was minimal, showed that very few 'TEM-visible' defects had formed. Two mechanisms were proposed by the authors: the surface proximity as describe above; the formation of BIC's since high B concentration and I distributions are basically overlapped. In fact, BIC's are more stable than self-interstitial clusters of comparable size and thus they can act as temporary sink for I blocking the expected Ostwald ripening.

A similar effect was reported for arsenic implants into silicon by Brindos et al. [35]. In their work the As implanted silicon with peak concentration ranging from $2x10^{17}$ to $3x10^{19}$ cm^{-3} were subjected to the thermal treatment at 750°C in order to nucleate and dissolve {113} defects. The analysis with a plan view electron microscope revealed that with increasing of As concentration, the number and size of {113} defects reduce. Furthermore, comparison of number of I atoms in {113} defects with a number of arsenic shown that for every two atoms of arsenic, remove approximately one interstitial atom from EOR defects. Authors suggested that the main mechanism responsible for this is the trapping of I's by arsenic atoms subsequently forming As_2I clusters.

To summarize, msec annealings like Flash or sub-melt LA generally induce the same Si lattice defect evolution observed for more conventional thermal treatments like RTA or furnace annealing when applied to thin a-layers obtained by Ge PAI. However, extended defects like DL at EOR can be observed at temperature as high as 1300°C for single scan processes. This is due to the extremely reduced thermal budget achievable with msec annealing time. The picture is different when the original a-layer thickness is below ~10 nm. In this case, the surface proximity induces a strong I gradient to the surface giving a preferential path for their dissolution preventing the usual Ostwald ripening and the formation of extended defects. As expected, the higher the msec T and the lower the defect density and average size. Finally, the overlapping of I distributions with high concentrations of dopant species able to form stable clusters with self-interstitials can represent a further path to reduce the formation of extended defects like {113} and DL.

1.9 Solid state diffusion in Silicon

As previously mentioned, a thermal treatment after ion implantation is a necessary step to recover the crystalline structure and activate the dopant atoms using classical thermal processes (e.g. furnace annealing or rapid thermal process). This annealing has typically to be performed at high temperature to achieve a high level of activation. As the result, the annealing can promote dopant atoms diffusion into silicon substrate which can have a dramatic effect on the depth of the junction. In this section, the diffusion of the element A in the silicon lattice is discussed using following notations: A_i and A_s - interstitially and substitutionally dissolved foreign atoms, I and V denote the vacancies and self-interstitial Si atoms.

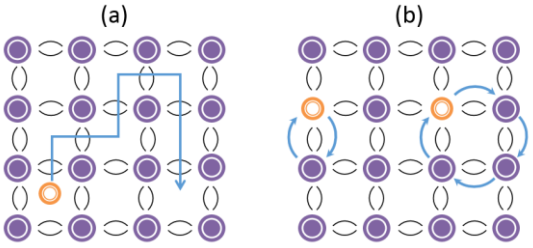

Figure 1.11. Schematic two-dimensional representations of direct diffusion mechanisms via a) interstitial lattice sites and b) substitutional lattice sites. Adapted from [36]

The diffusion of impurities in a solid, such as Si, can occur following either direct or indirect mechanism. The direct diffusion of interstitially dissolved small

atoms (A_i) like hydrogen or the 3d transition elements proceeds via interstitial lattice sites (figure 1.11, a). For a substitutional atom, the direct diffusion proceeds by exchange of lattice sites with one of lattice atom or by a ring mechanism, with more than one lattice atom involved in the exchange (figure 1.11, b).

However, the most common diffusion mechanisms are indirect. This diffusion involves intrinsic point defects, such as I's or V's, and it is usually energetically favored. These mechanism can be expressed by the following point defect reactions:

$$A_s + V \Leftrightarrow AV \quad (1.3)$$

$$A_s + I \Leftrightarrow AI \quad (1.4)$$

$$A_s + I \Leftrightarrow A_i \quad (1.5)$$

$$A_s \Leftrightarrow A_i + V \quad (1.6)$$

These reactions are presented schematically in figure 1.12 for a two-dimensional case. The reactions (1.3) and (1.4) represent the vacancy and substitutional mechanisms (figure 1.12, a and b). Isolated point defects approach substitutional impurity atoms and form next-nearest defect pairs due to Coulomb attraction and/or minimization of local strain. For long range migration of A_s the AV pair partially dissociates and the vacancy diffuses to at least a third nearest – neighbor site in the lattice before turning along a different path thereby completing the diffusion step.

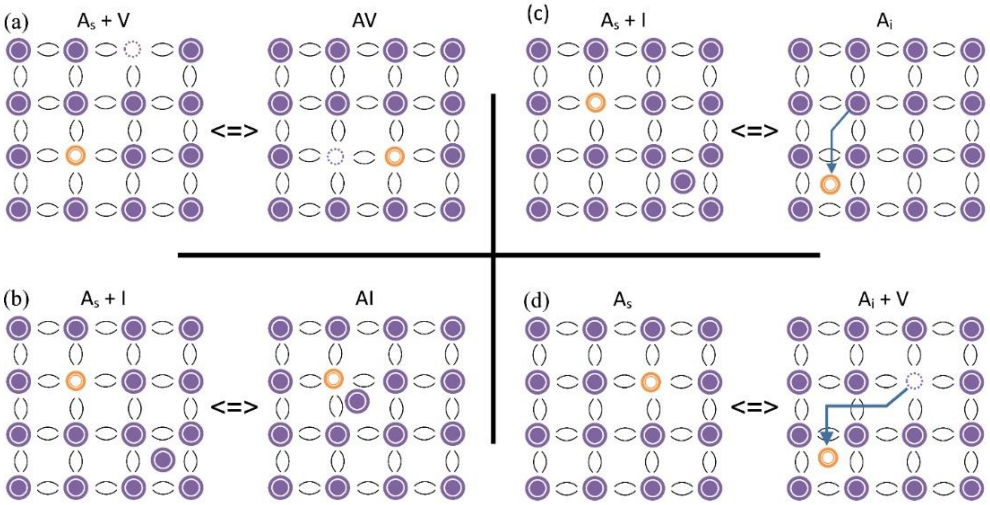

Figure 1.12. Schematic two-dimensional representation of indirect diffusion mechanisms of an element A in a solid. A_i and A_s denote interstitially and substitutionally dissolved foreign atoms, V and I denote vacancies and silicon self-interstitials. AV and AI are defect pairs of the corresponding defects. Adapted from [36]

In contrast, the diffusion via interstitialcy mechanism occurs when the AI pair does not dissociate. The reaction (1.5) is the "kick – out" mechanism, and the (1.6) is the dissociative or Frank – Turnbull mechanism (figure 1.12, c and d). These mechanisms usually describe the diffusion behavior of elements that are mainly dissolved on substitutional sites but move as interstitial defects (like gold, zinc, or sulfur).

1.9.1 Standard Fickian diffusion

For a low concentration (i.e. when the concentration of dopant is less than intrinsic carrier concentration), the redistribution of impurity can be described by Fickian diffusion. The flux of dopant atoms (J_x) traversing through a unit area in a unit time is proportional to the concentration (C) gradient of dopant according to the first Fick's law:

$$J_x = -D\frac{\partial C(x,t)}{\partial x} \tag{1.7}$$

where D is the diffusion coefficient which is equal to:

$$D = D_0 e^{\frac{-E_{act}}{kT}} \tag{1.8}$$

where D_0 is a frequency factor, that is dependent upon the atomic jump frequency and distance, E_{act} is the activation energy for diffusion, and k is the Boltzmann constant.

From the law of mass conservation, the change in dopant concentration is equal to the decrease of diffusion flux. In general form, the mass transfer can be expressed as:

$$\frac{\partial C(x,t)}{\partial t} = \frac{\partial}{\partial x}\left(D\frac{\partial C(x,t)}{\partial x}\right) + G_A \tag{1.9}$$

The G_A term describes possible reactions between the impurity and other defects. In the system when no reaction takes place the $G_A = 0$. This equation is called the second Fick's law and it can be successfully used to describe the equilibrium diffusion of impurities with a good agreement to experimental results [37].

However, technologically relevant concentrations of dopant in semiconductor often exceed the intrinsic carrier concentration level and in this regime the diffusion is different from Fickian. At high concentration the dopant diffuses as impurity/point defect complexes. At the temperatures where diffusion occurs, reasonable part of implanted dopants will be expected to have taken up substitutional sites. The diffusivity of dopant atoms in Si is governed by the local concentration of point defects according to:

$$D = D_I\left(\frac{\langle C_I\rangle}{C_I^*}\right) + D_V\left(\frac{\langle C_V\rangle}{C_V^*}\right) \tag{1.10}$$

The diffusion coefficients D_I and D_V are the intrinsic diffusivities due to interactions with self-interstitials (I) and vacancies (V) and $\langle C_x\rangle/C_x^*$ are the local/equilibrium concentration of corresponding point defects [38]. The main diffusion mechanism, interstitial or vacancy mediated, depends on implantation species. The boron is known to diffuse entirely by interstitial mechanisms, like Ga or P, whereas Sb mainly diffuse by vacancy mechanisms. In case of Arsenic both interstitial and vacancy mechanism are relevant almost equally.

1.9.2 Transient enhanced diffusion

The main challenge related to the dopant diffusion is the so-called transient enhanced diffusion (TED). Anomalous diffusion of dopants is observed where the diffusivity can be increased by several orders of magnitude from that calculated for equilibrium diffusion. The first study of TED was reported by Michel et al. in [39] where they observed that the most significant diffusion of boron implanted profile occurs at the initial stage of thermal treatments and then it decays with time. This enhancement of the diffusion was first attributed to the release of Si interstitials during the dissolution of {113} defects during annealing at temperatures from 670°C to 815°C [40]. However is has been shown that not only {113} defects are responsible for TED. It was reported by Zhang et al in [41] that in low energy B^+-implanted silicon the TED occurred even if no {113} has been observed by TEM. In addition, Bonafos et al. reported boron TED in presence of other type of defects such as dislocation loops [42]. Therefore, the TED was related to the dissolution of several types of defects, including atomic clusters where few atoms are involved possibly together with some point defects.

1.9.3 Uphill diffusion

During SPER of heavily doped amorphous silicon one can observe an abnormal diffusion of dopant in direction opposite to the concentration gradient. This anomalous diffusion has been first described in experimental studies of carbon in Fe-Si-C ternary system [43]. Since then, and especially since the introduction of ion implantation, several experimental works reported the effect in silicon [44–47] and many studies were done in order to explain this phenomenon using coupled point defect diffusion model and by introducing I-trap model [48]. Uphill diffusion is extremely significant for the technology of ultra-shallow junctions because at low temperature treatment it causes a much stronger dopant redistribution than conventional thermal diffusion, often ending up with electrically inactive dopant segregations in native oxide or at its interface with Si.

There are few main approaches for explaining the uphill diffusion. In 1975 Sato [49] observed alkali-enrichment in diffusion coronas around quartz xenocrysts in andesite and basalt and experimentally confirmed then this enrichment is caused by uphill diffusion of alkali's in diffusion zones during dissolution of quartz. The proposed explanation is that the component diffuses along its chemical potential gradient (not concentration gradient) and uphill diffusion is only possible in systems where activity coefficient is inversely proportional to component concentration. Based on this concept Zhang [50] presented a modified effective binary diffusion model which allows quantitative fit to experimental results and predict occurrence (or absence) of uphill diffusion using only two parameters: the intrinsic effective binary diffusivity and a parameter related to two liquid partition coefficient. This method can be successfully applied to systems where the composition variation is small across the diffusion profile.

Arsenic in Si shows similar behaviors and segregation peaks are often observed at the SiO_2/Si interface after most annealing processes and also when dopant concentration is below solid solubility. The responsible mechanisms were widely discussed in literature and a definitive picture is not yet clear. However, most works converge on two main points. First, at SiO_2/Si interface there is a presence of energetically favorite places that can trap As atoms and segregate them, preventing further release and diffusion [51–53]. Second, especially at low temperature during SPER on high As concentrations, dopant atoms are segregated at the moving amorphous/crystalline interface and swept or 'snow-ploughed' towards the surface following SPER front [54].

A simple model for the arsenic uphill diffusion due to SPER was proposed by Suzuki at al. in [55]. Using high resolution RBS measurements, they analyzed arsenic redistribution during SPER at 600 °C, when arsenic redistribution occurs only at the regrowing interface. In this system, it was shown that arsenic redistribution can be expressed by using only two parameters: the reaction length, i.e. the distance around the amorphous/crystalline interface where redistribution occurs, and a segregation coefficient, describing the ration of As concentration on amorphous and crystalline sides of the interface. This model was applied to different arsenic implanted samples (results are reported in the section 4.5).

1.9.4 Arsenic and boron equilibrium diffusion in silicon

Since most work of this thesis deals with As behavior in Si, we summarize here the diffusion coefficients. Arsenic atoms can diffuse in Si by both self-interstitials and vacancies. The diffusion coefficient can thus be described for general case [56]:

$$D_{As}(T) = D^{x} + \frac{n}{n_i} D^{-} = 8.0\, e^{-\frac{4.05}{kT}} + \frac{n}{n_i} 12.8\, e^{-\frac{4.05}{kT}} \qquad (1.11)$$

where D_{As} is the intrinsic diffusion coefficient, D^x identify the intrinsic diffusion coefficient and D^- the extrinsic one; n and n_i are the actual electron concentration and the intrinsic electron one, respectively, k is the Boltzmann's constant (1.3806×10^{23} J/K) and T is absolute temperature (K).

Boron atoms mainly diffuse via a interstitial mediated mechanism [57]. The intrinsic diffusion coefficients in the form of Arrhenius expression can be written as [58]:

$$\mathrm{D}_B(\mathrm{T}) = (0.080 \pm 0.004)\mathrm{e}^{\frac{(-3.08\pm0.09)}{kT}} cm^2/s \qquad (1.12)$$

The diffusion coefficient can be enhanced in the presence of point defects. The As TED will be discussed in next section and enhancement diffusion of boron in silicon is a matter of a study reported in chapter 5.

1.10 Arsenic – Silicon system: solid solubility, electrical activation and diffusion mechanisms

Arsenic in Silicon system under investigation in this thesis can be described at the equilibrium by the phase diagram reported in figure 1.13. From that, it is evident that a SiAs phase is in equilibrium with the arsenic in silicon phase (As doped) for temperature below the eutectic point at 1097 °C. When arsenic concentration goes beyond the solid solubility line, SiAs precipitates can form unless kinetics constraints prevent it or retard it. As solid solubility in Si has been widely studied and can be analytically described as from [59] for temperatures 800-1050 °C:

$$C_{sat} = 1.3\text{x}10^{23}\ \text{e}^{\frac{(-0.42)}{kT}} cm^{-3} \tag{1.13}$$

It is evident that solid solubility is rather high, being > 1x10^{21} at/cm^3 for temperatures higher than 750°C. This represents a very appealing aspects for choosing As as n-type in Si for USJ applications. However, the actual measured maximum active carrier concentration was reported to be typically one order of magnitude lower than solid solubility, even if extended defects are not observed. Solmi et al. in [60] experimentally determined the maximum active dopant concentration in function of temperature, that can be described by this expression valid between 700 and 1200 °C:

$$n_{e(As)} = 2.2\text{x}10^{22}\ \text{e}^{\frac{(-0.47)}{kT}} cm^{-3} \tag{1.14}$$

This means that for temperatures higher 750°C, the maximum active dopant concentration is on the order of 10^{20} cm^{-3}. Furthermore, since activation energies are similar for both solid solubility and maximum active dopant concentration, the offset between the two values is maintained in all the IC fabrication steps.

Therefore, even if dopant electrical activation not-equilibrium processes like SPER or sub melt LA are capable of producing very high activation levels of dopants [61], [62], the latter can 'de-activate' to equilibrium values, lower than solid solubility, if successive thermal treatments are carried out.

The lower than solid solubility maximum active dopant concentration is attributed to the formation of electrically inactive clusters involving As atoms and point defects [63–66], where As atoms are only slightly displaced from the Si lattice sites. For this reasons, the electrically inactive As atoms cannot be detected by neither conventional channeling RBS experiments [62], [67], [68] nor MEIS [69]. However, high resolution RBS measurements proved that As atoms are actually 0.022 nm displaced from lattice sites in electrically de-activated As distributions [70–72]. Further experimental evidences from EXAFS [63], [73], [74], X-ray standing wave analysis (XSW) [75], positron annihilation spectroscopy (PAS) [76–78] and theoretical calculations [63–65] suggested that the main mechanism behind the electrical de-

activation is As atom clustering around one or more vacancies (V), i.e. the so called As_nV or As_nV_m defects ($n \leq 4$; $m \leq 2$ typically).

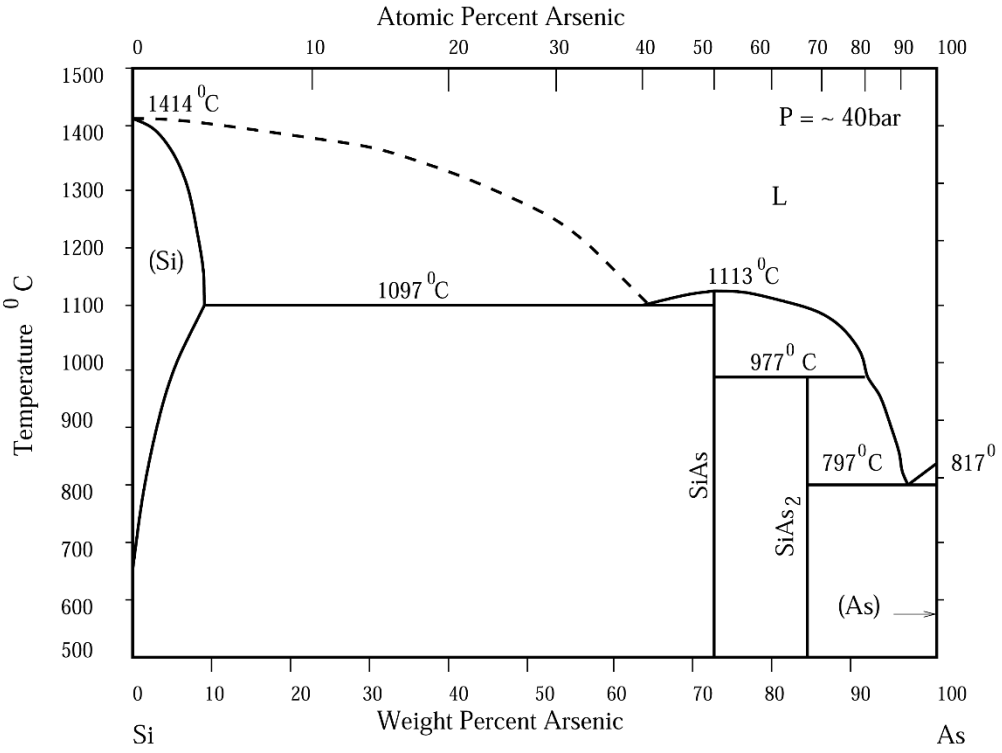

Figure 1.13. Arsenic-silicon phase diagram [79]. At high concentration arsenic in silicon forms a monoclinic SiAs phase.

A definitive evidence for an As_nV mechanism came from the experiment performed by Rousseau *et al.* [66], [80]. The authors used a particular substrate with buried boron doped delta layers (thickness 200 nm, B peak concentration ~$1x10^{18}$ at/cm^3) with the aim of using them as a self-interstitial detector since B diffuses mainly through a mechanism involving interstitial Si [31], [81]. Highly active As distributions were then created on this substrate by ion implanting As^+ at doses ranging from $4x10^{15}$ to $3.2x10^{16}$ at 35 keV energy followed by a laser melt annealing. The latter completely removed the lattice damage and uniformly re-distributed the As atoms over a depth of 200 nm, reaching a level of activation well beyond the expected equilibrium value. Samples were successively treated at temperatures ranging from 500 to 750°C to induce electrical de-activation. Results showed that up to a value of $4.6x10^{20}$ at/cm^3 of As concentration, the B deltas showed a relevant transient enhanced diffusion (TED) after 4 minutes at 750°C with an enhancement factor (ratio between the observed diffusion coefficient and the equilibrium one) as high as 7500 compared to equilibrium diffusion. For As concentrations higher than $5x10^{20}$ at/cm^3, B TED was progressively reduced. This result was interpreted supposing that the As distributions are de-activated by forming As_nV clusters and emitting (Si) self-interstitials through the reaction:

$$As_nSi \Rightarrow As_nV + I$$

where I identifies the emitted interstitial. At high As concentration, the emission of self-interstitials would be so high that they precipitate with the consequent formation of larger defects, as revealed by TEM

analysis ([82] and references therein). In fact, TEM cross sections show that beside the expected end-of-range (EOR) defect band below the original amorphous/crystal interface, a further dislocation loop band can be observed in correspondence with the projected range of As, i.e. where the de-activation is expected to be stronger. Furthermore, the same delta doped substrate was also implanted with Ge^+ ions at $8x10^{15}$ at/cm^2 fluence and 35 keV in order to generate the same lattice damage (Ge and As atoms have very similar atomic mass) and discriminate between interstitials coming from EOR defect dissolution and the ones coming from As clustering. In this case, B TED was observed as well but only with an enhancement factor of 43 for a thermal treatment of 2 hrs at 750°C, compared to a factor of 350 observed for the analogous As implants. This clearly indicated that in As implants there is an additional source of interstitials beside the EOR dissolution. Several complementary results [75], [76] confirmed the interpretation of the results based on As_nV mechanism and theoretical calculations [64], [65] confirmed a high stability of As_nV clusters, with a binding energy increasing with the number of As atoms around the vacancy.

However, more recent theoretical calculations predicted that also clusters involving self-interstitials and As atoms (As_nI_m) can be stable, despite the fact that their binding energy is lower than the one for As_nV clusters [83], [84]. Furthermore, it was expected that As-interstitials pairs have a relatively low migration barrier and can thus represent a mechanism for an As TED [85] beside the mechanism involving As-V pairs in a percolation network already proposed by other authors [64], [86], [87], i.e. the mechanism traditionally identified as the As TED cause. The As_nI_m relative stability, an 'easy' V-I annihilation for As_nV clusters [88] and the As-I low migration barrier suggest a different behavior in case of an excess of interstitials, e.g. after an ion implantation process. In fact, As atoms can diffuse relatively fast in the form of As-I or As_i pairs and form clusters like As_nI as preliminary or metastable complexes before the formation of the more stable As_nV ones [52], [83], [84]. Harrison compiled a detailed energy formation map (figure 1.14) for different arsenic-defect complexes. The map shows that the clustering can occur via both vacancy- and interstitial-mediated pathways, but the latter can be expected to dominate in ion implant annealing, considering the excess of interstitials present at the onset of thermal treatments. Experimental evidences were reported in the last decade showing the relevant contribution of the As-I mechanism to As TED [52], [56], [89]. In particular, Solmi *et al.* [56] concluded that a thermal treatment at 800°C of a $5x10^{15}$ at/cm2 at 35 keV implant induced a relevant TED due to interstitials coming partially from ion implant damage and EOR defect dissolution (2/3 fraction) and from interstitials coming from As_nV clustering [56] (the remaining third). They arrived to this result observing further As diffusion in a sample already previously treated at 1030°C for 5 seconds to remove all the ion implantation damage.

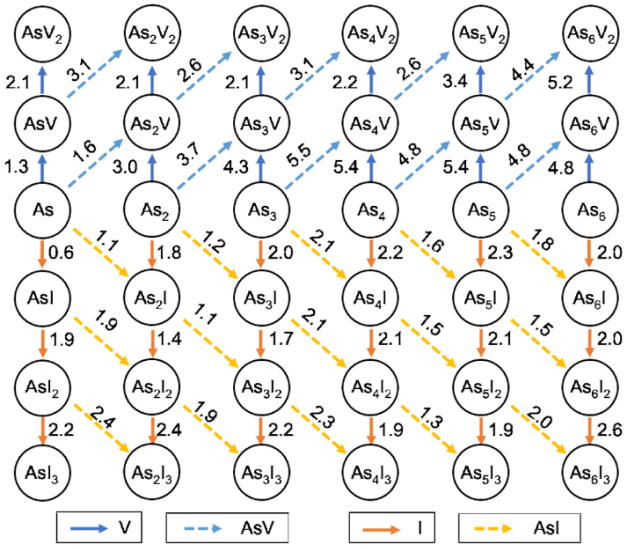

Figure 1.14. A potential energy map of arsenic-defect complexes (adapted from [83]). Energy gains (eV) for the binding of each mobile complexes (V, I, AsV, AsI) noted above corresponding arrows.

Ning Kong *et al.* studied As TED in samples where not-amorphizing (5-7x10^{13} at/cm^2) Si$^+$ ion implants were used to induce super-saturation of either vacancies or interstitials [89]. In particular, a 160 keV, 7x10^{13} at/cm^2 Si$^+$ implant on a silicon-on-insulator substrate (SOI, Si thickness 100 nm) created a layer rich in vacancy concentration, without the risk of their annihilation/recombination with the interstitials blocked in the buried oxide layer (BOX). In this specific sample after a 750°C 10 min. annealing, As profiles were basically frozen for the low fluence sample (6x10^{13} at/cm^2) and only a slight diffusion was observed for the 1x10^{15} at/cm^2 sample as proved by SIMS [89]. On the other hand, the interstitial rich samples presented a relevant As TED especially for 750°C treatments. Furthermore, they used two samples initially annealed t 1025°C 10 s and then Si$^+$ implanted at two different implant conditions in order to create in correspondence to the pre-existing annealed As distribution two different structural conditions: i) I-rich region ii) V-rich region. The samples were then thermally treated at 750°C for 10 minutes and again the authors observed the strongest TED for I-rich samples whereas the V-rich profiles did not change. This clearly proved that the main contribution to As TED is coming from interstitial-related mechanisms. Actually, the 1x10^{15} at/cm^2 implant showed a slight TED at low concentration also in the V-rich case. This TED was attributed by the authors to a small contribution of As-V mechanism for the high concentration case. In a successive paper the same authors developed a kinetic Monte-Carlo method (kMC) based on fundamental parameters like binding energies and migration barriers obtained by Density Functional Theory (DFT) calculations [52]. The model allowed fitting SIMS profiles for the several cases of point defect population. Following their results, it is clear that a high density of free interstitials is expected in the first stages of a 750°C thermal treatment for either 'I-rich' or 'only As' samples. The time of this stage of high I-density corresponds to the highest TED regime. However, as the annealing time is increased, interstitials are progressively annihilated by re-combination with vacancies. It is interesting to note that the density of As-I pairs is always lower than the As-V density, also for the I-rich case, probably because of the stronger

binding energy of AsV clusters and the easy recombination of AsI in presence of vacancies [52], [85], [88]. However, the lower migration barrier for AsI complexes (0.87 eV) compared to AsV complexes (1.75 eV) makes a strong TED possible as long as the density of interstitials is not too low. In fact, in V-rich samples the I population is very low and no relevant TED is observed, despite the high density of AsV complexes. Furthermore, the kMC model described also the evolution of As atoms blocked in immobile As_nI or As_nV electrically inactive clusters. In the first 15 s of the thermal treatment at 750°C, all inactive-As is essentially in As_nI clusters even for the V-rich samples, whereas for longer annealing times the population of such clusters drops along with a consequent raise of the As_nV population [52]. The creation of As_nI clusters would also explain previously reported results from Brindos et al. [35] for low ($2x10^{17}$ – $3x10^{19}$ at/cm^3) As concentration doped Si. After having activated As distributions with a 45 min. annealing at 1050°C, they implanted Si^+ at medium dose ($1x10^{14}$ at/cm^3 at 40 keV) to create an excess of I and thermally treated the samples at 750°C. Their TEM plan views revealed that {113} defects, normally expected from I precipitations, were reduced in density and size for the higher As concentrations. This seems to confirm that in presence of As atoms, self-interstitials are energetically favored in complexes different from {113} defects.

1.11 Conclusion

From what reported in literature and summarized in the previous sections, it is clear that Arsenic represents a valuable solution for realizing USJ in Si-CMOS technology of future nodes. High solid solubility, high mass, low diffusivity and reduced TED compared to P are all attractive aspects. At the same time, given the extremely shallow distributions to be realized, TED phenomena are not negligible and need to be avoided/contained. Furthermore, the required high dopant concentration poses problems of maximum electrical activation achievable and technological solutions must deal not only with solid solubility but also with atomic clustering. Therefore, the production of high active concentration doped layers, and their stability is a fundamental integration issue. The evaluations of those phenomena and the experimental identification of the physical mechanisms behind them is the matter of this thesis work.

Chapter 2. Methods and experimental techniques

2.1 Methods and experimental techniques

Throughout this study, different techniques were applied in order to investigate evolution of the structural and electric properties of the samples.

Ultra-low energy *Secondary Ion Mass Spectrometry (SIMS)* analysis has been used to obtain arsenic depth profiles in silicon. The combination of a 300 eV cesium beam with an advanced quantification approach has allowed the analysis of ultra-shallow dopant distributions. Typical SIMS artefacts, which are significant at such small scale, were compensated with a quantification method based on the variation of ion yield and sputtering rate versus depth. The method calibration was performed by comparison with depth profiles obtained with Medium Energy Ion Scattering (MEIS) for a set of purposely-selected samples. MEIS analysis is not affected by matrix effects; it is generally less sensitive than SIMS but it is well suited for the analysis of As implants in the concentration and depth range treated here.

Instrumental Neutron Activation Analysis (INAA) is not sensitive to the profile shape but it provides the total dopant fluence or dose, and it does not suffer from matrix effects. The dose derived from integrated SIMS profiles was hence counterchecked against the INAA values.

Information about dopant activation was obtained from electrical measurements performed using *Four-Point Probe measurements*. In addition, an investigation of the local order around arsenic atoms in Si was carried out by means of Extended X-ray Absorption Fine Structure (EXAFS). EXAFS was performed to evaluate the deactivation by atomic clustering caused by post-annealing thermal treatments.

2.2 Secondary Ion Mass Spectrometry (SIMS)

Secondary ion mass spectrometry is a widely used technique for the analysis of impurities in solids. The technique can detect almost all chemical elements with their relative isotopes in a specimen with very low concentration (typically parts per million (ppm) and in some materials below 1ppb). It offers a high dynamic range, typically over 6 orders of magnitude. The ability to provide elemental (isotopic) depth profiles over a depth range from a few angstroms (Å) to tens of microns (µm) made this analytical technique one of the most powerful and used tool for solid materials analyses.

All main steps of a SIMS analysis such as data acquisition, interpretation, and quantification are discussed in the following sections.

2.2.1 Fundamental Principles

SIMS is based on two main physical phenomena: *material sputtering* and *particle ionization*. In a SIMS analysis, the surface of the specimen is bombarded with a beam of charged particles, typically atomic or molecular ions. The primary ion beam typically has energies from 0.5 to 25 keV, but in special configurations it can be reduced to 250 or even 150 eV (see paragraph 0). A fraction of the incident ions penetrates the solid and deposits energy into the surface layer breaking bonds around the impact region. Elastic collisions are the main mechanism of energy loss in this range of energies. Every single collision of an incident ion will transfer part of its energy to the atoms of the material; while the incident ions are implanted to a depth, penetration depth (R), of the order of 1 - 100 Å reaching their final rest position they randomly displace the atoms of the sample. The energy transferred to the material atoms involved in the collision with a primary ion is often sufficient to set them into motion and cause them to collide with other atoms of the material giving rise to a so-called collision cascade. In the collision cascade some atoms will acquire a momentum directed towards the sample surface and if their kinetic energy is bigger than the surface binding energy they will be ejected into the vacuum. The emission of particles from direct impact with the primary ion is a rare event. The sputtering is one of the key phenomena of SIMS analysis. Its schematic representation is shown in figure 2.1. The energy of the emitted particles is very low (5-10 ev) and the vast majority of them are coming from the top 2 monolayers of the sample (more than 95%). The efficiency of sputtering (sputtering yield) is given by the number of particle per incident ion.

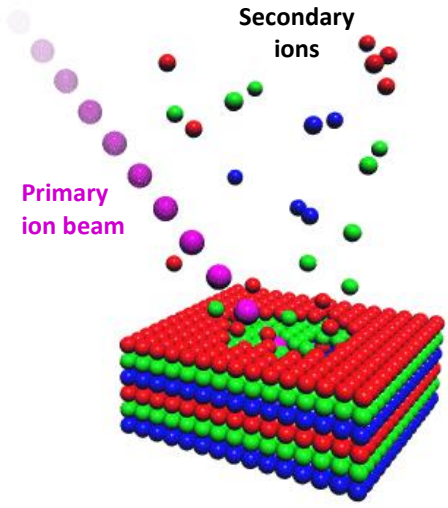

Figure 2.1. Schematic of surface sputtering during SISM analysis. Illustration from [90]

The sputtering process is very sensitive to analytical conditions and the dependence of sputtering yield on experimental conditions was a matter of plenty of researches over the last 40 years [91], [92].

For what concerns the sample the main characteristics influencing the efficiency of sputtering are:

- Mass of the atoms
- Crystal structure
- Binding energy of the surface.
- Orientation of the crystals
- Temperature of the sample

Considering the primary incident beam the parameters to be considered are:

- Atomic number
- Energy
- Incident angle

The sputtered particles (atoms and molecules) are mostly neutral and only less than 1% are ejected as single charged ions [93], [94]. Multi-charged species are rarer but still cannot be neglected due to their possible 'mass interference': as will be shown below, in SIMS analysis element isotopes are separated by their mass/charge ratio, thus a double-charged particle will provide the same signal as a twice-lighter particle with a single charge.

The ionization process is the second key phenomenon of SIMS analyses. This can be described analytically by a parameter (ion yield) that can be defined as the number of ions produced per sputtered atom. Given an element its ion yield is a function of the specific ion coming from a specific sputtered material. There is still no universally accepted theory for the formation of secondary ions. However, many models were proposed for the process (overview of the main models can be found in [95]) and they are all based on an exponential dependence of the ion yield on the ionization potential (for positive ions) or electron affinity (for negative ions). Anyway the ionization processes may be classified in two categories:

1) Ions production induced by processes of exchange of kinetic energy between the primary ion and the particle emitted by sputtering. In the ionization takes place with the emission of an Auger electron by the particles that leave the surface of the sample in an excited state. This type of ionization is typically observed when using inert gases as primary beam
2) Chemical emission where charge exchange is induced by reactive species present in the sample or introduced by primary ion bombardment. Among the species commonly used as a primary ion, cesium (as the other electropositive species) facilitates the process of emission of negative ions, while oxygen (as the other electronegative species) enhances the emission of positive ions

As previously mentioned, the ionization yield can vary by several orders of magnitude for the same element in different materials or for different ions in the same material. This phenomenon is commonly referred to as "*matrix effect*" and in general it is hardly possible to predict it [96]. The most obvious influences on the ion yield are due to the ionization potential for positive ions and electronic affinity for negative ions.

Independently of primary ion both negative and positive secondary ions are emitted and they exists not only as single atom particle but also as large clusters (molecular ions or fragments). In the first years of SIMS technique, noble gas ions such as Ar^+ and Xe^+ were used as primary ion species in order to limit the chemical perturbation of the analyzed surface. However, at the end of the '70s it was proven that using highly reactive primary ions O_2^+ and Cs^+ allowed an increase of orders of magnitude of ion yield and thus of sensitivity.

Although this 'reactive' sputtering is drastically altering composition and chemistry of sample surface, the original information is preserved as long as the sputtering conditions are stable and the material is the same, since the recorded signals are basically functions of the original composition. For this reasons SIMS instruments often have different sources installed to allow using different ions.

The ionization efficiency variation leads to different conditions of analysis for various elements, as indicated in the periodic table (figure 2.2).

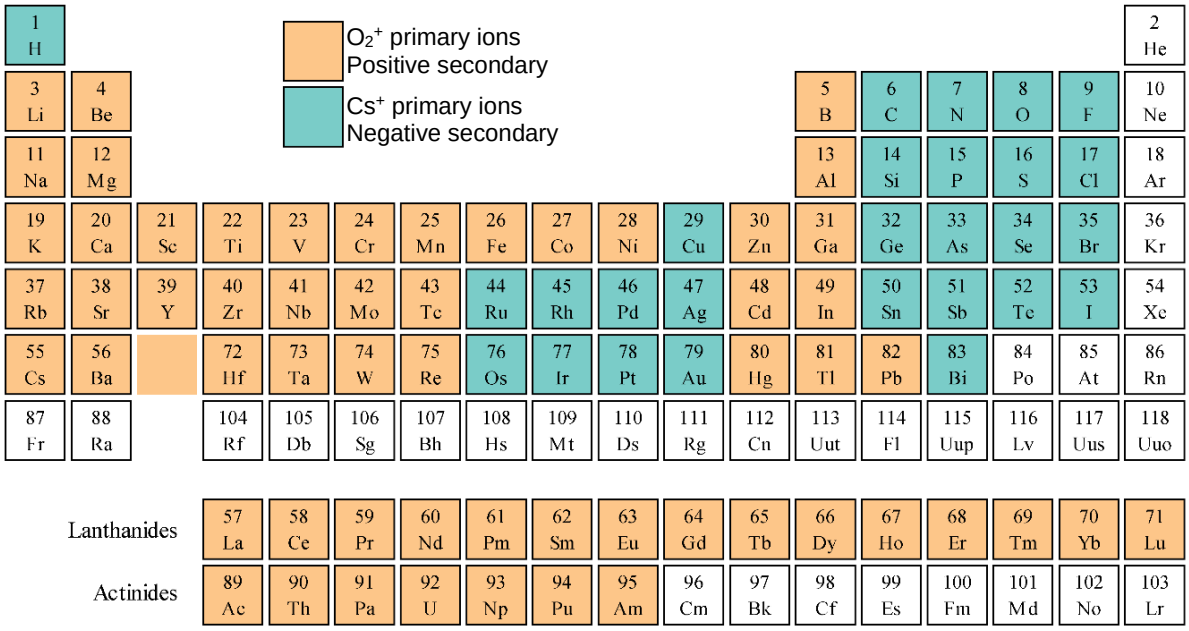

Figure 2.2. Analytical conditions with best ionization efficiency for different chemical species. Adapted from [97]

2.2.2 SIMS operative modes

SIMS analysis have three major applications depending on analytical conditions and detector configuration: surface analysis (static SIMS); highly sensitive bulk analysis and elemental profiling (dynamic SIMS); and analysis of lateral heterogeneity (chemical mapping).

In a static SIMS, a specimen surface is sputtered by a beam with a very low primary ion current density (< 10 nA/ cm^2) and a complete mass spectrum is acquired. By limiting the amount of primary ions to a fluence that does not sputter away the majority of the uppermost monolayer, it is possible to collect signal from only the top surface of the material. The information can thus be complementary to other proper surface techniques like X-ray photoelectron spectroscopy (XPS) or Auger electron spectroscopy (AES), but with the advantage of collecting signals for all the elements of the periodic table.

In dynamic SIMS regime, the sputtering beam density is much higher than in previous case (from 3µmA/ cm^2 to 1mA/ cm^2) and the material erosion rate is intentionally higher. After a time length depending on primary beam parameters (impact energy, incidence angle, ion current density), the sputtering process reaches a dynamic equilibrium state in which the amount of deposited primary ions are equal to the amount of these ions leaving the surface due to the sputtering, keeping the primary ion elemental concentration constant on the surface. Therefore, the recorded spectrum will be at any time correspondent to the average composition over the eroded volume. In this regime, much higher sensitivity to trace elements is achievable. Depth profiling is a sub kind of dynamic SIMS in which intensity of ions are recorded as a function of analysis time. Element depth profile is obtained by tuning mass analyzer to a corresponding mass/charge ratio and measuring the peak intensity. Detailed discussion on SIMS depth profiling analysis mode will be discuss in a dedicate paragraph. Furthermore, if the equilibrium sputtering is achieved and the sputtering rate does not undergo significant changing during the analysis, the time of the analysis can be converted into a depth scale (usually by physical measurements of the final crater depth at the end of analysis).

Finally, it is also possible to obtain chemical surface maps using either dynamic or static SIMS. In fact, secondary ions are emitted from areas adjacent to the impact site of primary ions. Therefore, a spatial recording of secondary ions can result in an element-isotope two-dimensional (2D) image carrying the information of the 2D distribution of the elements on the sample surface. Secondary ions can be recorded like general picture of the irradiated area using a position sensitive detector like a fluorescent channel plate. In this case, lateral resolution would be given by the secondary ion optics, and typically is of the order of 5-10 µm. Alternatively, secondary ions can recorded in a synchronized way with the primary beam *rastering* resulting in a scanning ion image in a similar way to a scanning electron microscope (SEM). In this second case, the lateral resolution is given by the size of the primary ion beam

diameter. The sensitivity of the imaging analysis is typically poorer, especially if the primary ion beam intensity is kept low to reduce erosion during the acquisition of the several masses, but it is very useful as a complementary technique to the previous two configurations.

For the characterization of ultra-shallow dopant profiles as required in this thesis work, low impact energy dynamic SIMS is best suited and was thus widely used in this work. Furthermore, the different applications of SIMS require different classes of mass spectrometer (quadrupole, magnetic sector, or time of flight). In the frame of this work the instrument equipped with a magnetic sector was used and in the next sections only this class of mass spectrometer is considered.

2.2.3 SIMS instrumentation

2.2.3.1 General

To perform Depth profiling analyses a Dynamic SIMS mass spectrometer is required. A schematic representation of this kind of instrument is shown in figure 2.3.

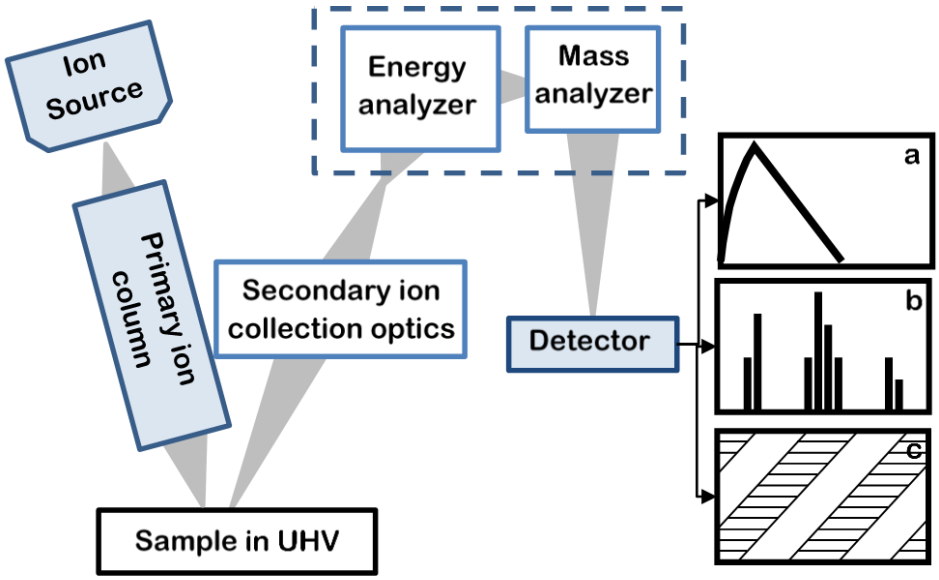

Figure 2.3. A schematic representation of a SIMS instrument

A dynamic SIMS instrument is equipped with one or more independent ion sources, to produce primary ions. Primary ions are extracted from the source then focused in a beam through a set of electro-static lenses located in the primary column. Ultra high vacuum (UHV) ~10^{-9} mbar is required to avoid any scattering of the charged particles with ambient molecules. A final set of electrostatic deflector and lens define the beam focusing and positioning on the sample surface. The latter is positioned in another UHV chamber called analysis chamber. UHV is here required not only to prevent both primary and secondary

ion scattering with gas atoms/molecules, but also to prevent modifications/perturbations of the freshly sputtered/eroded sample surface.

The focused beam sputters the surface of the specimen and creates a cloud of secondary particles including atoms, molecules, electrons, photons and ions. The latter can be extracted and accelerated towards the secondary ion collection optics using an electric field given by some extraction electrodes placed right above the sample surface. The collimated secondary ion beam is guided to the mass spectrometer. In modern magnetic mass spectrometers, it actually consists of a combination of an electrostatic and a magnetic sector analyzer. In the electrostatic analyzer, the ions travel between two parallel plates separated by a distance *d* with a radius of curvature r_E. A potential *V* between the two plates permits only those ions with the specific energy *E* to be transmitted without striking the plates:

$$E = \frac{qVr_E}{2d} \tag{2.1}$$

Therefore, the electrostatic analyzer essentially 'monochromatizes' the secondary ion beam eliminating the problem of the small differences in kinetic energy arising from the emission mechanism. In fact, even if the main component of secondary ion kinetic energy is given by the extraction field (typically ~2-5 keV), a secondary component is given by the sputtering phenomenon itself, since ions are emitted with their own energy (~10^1 eV) as a consequence of the collision cascade. This small divergence in KE would turn out in a poorer mass resolution through the magnetic sector.

The mass analyzer in dynamic state of art instrument is done by a magnetic sector spectrometer, a static magnetic field B orthogonal to secondary ion trajectories forces the mono-energetic beam into a curved path according to the force of Lorentz. The radius r_B depends on the mass/charge ratio of the particle:

$$\frac{m}{q} = \frac{qB^2r_B^2}{2E} = \frac{B^2r_B^2d}{Vr_E} \tag{2.2}$$

Therefore, given a fixed geometry with a well-defined curvature radius, the variation of B allows recording a mass spectrum registering ion intensities for each B or m/q value. In figure 2.4 a schematic representation of magnetic sector analyzer is reported.

The magnetic sector is capable of separating ions with masses different by only 0.005% which corresponds to the mass resolution of 20,000 expressed in the conventional terms of M/ΔM, where M represents the mass barycentrum between 2 isotopes and ΔM their mass difference, respectively . Such high mass resolution is required for detecting isotopic molecules with similar mass (e.g. $^{29}Si^1H_2$ and $^{30}Si^1H$ are separated by only 0.01 a.m.u.).

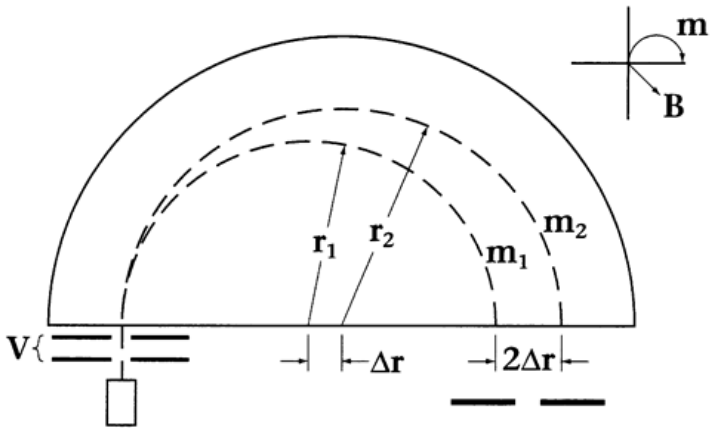

Figure 2.4. Magnetic sector analyzer. By fixing Accelerating Voltage and varying B intensity, the detection of different Ions during the sputtering of the sample is achieved

Secondary ion signals can then be detected and recorded Most of the SIMS instruments are equipped with three different detectors. The first one is a multi micro-channel plate (MCP) where secondary ions hit a matrix of fluorescent micro-channels providing a direct image of the ion irradiated surface. This detector is used to acquire ion maps of sample surfaces. The second detector is an *electron multiplier* (EM). In this detector secondary ions hit some electrodes biased to high voltage. This collision creates a flow of secondary electrons that are then accelerated to a sequential series of electrodes (dynodes) aiming to multiply their intensity, since each time electrons hit one of the plates, their number increases. In general, the electron current registered at the end of the dynode sequence is proportional to the intensity of the hitting ion beam. However, when the ion beam intensity is high, the detector is saturated, i.e. the produced electron intensity reaches a maximum and does not follow further increases of ion intensities. This saturation typically occurs for intensities above 10^6 count/second. To avoid this non-linearity and to preserve the detector dynodes from any possible damage, the secondary ion beam is automatically switched from EM to a *Faraday Cup* (FC) detector when the intensity reaches this saturation maximum. In the FC detector the charge of the secondary ions is measured directly without any multiplication.

2.2.3.2 SC-Wf Ultra Cameca

In the present work SIMS analyses were carried out by using a Cameca SC Ultra/Wf instrument. This equipment reported in the figure 2.5 is optimized to perform analyses on microelectronics samples and semiconductor materials. Particularly, the characteristics of the instrument allow to do Ultra Shallow depth profiles with an optimized depth resolution.

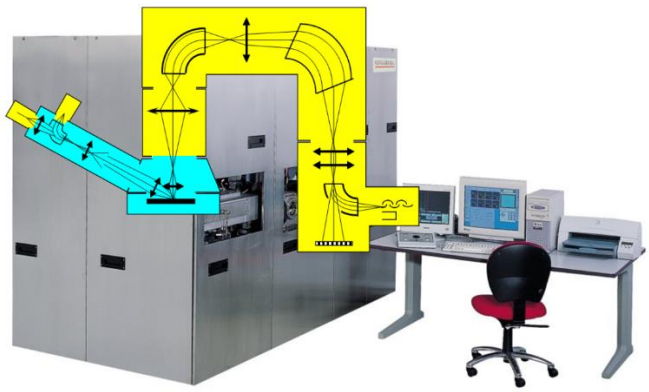

Figure 2.5. Cameca SC Ultra/Wf instrument and a schematic diagram of the ion optic

Sc-ultra instrument is equipped by two ion sources in order to produce O_2^+ and Cs^+ primary beam. The primary column is fixed with an incident angle of 60° with respect to the sample normal. Moreover sub-keV implantation energies can be achieved in positive and negative polarity due to the possibility to work in "floating" mode (see paragraph 2.2.5). 1x1 cm^2 size samples are placed in a special holder which is capable to contain up to 25 specimens at once. The holder is placed into an analytical chamber with a dimension of 500mm. This sample holder allows to improve analysis reproducibility, fixing the precision better than 1%.

2.2.4 Quantitative analysis

Depth profiling is one of the main applications of dynamic SIMS. A profile is given by the combination of a depth information related to the sputtering rate, and hence the crater depth at the instant of counting particles with the desired mass, and the number of particles that reach the detector. The result of a measurement consists of secondary ion intensities (counts per time) in function of sputtering time. Secondary ion intensity and sputtering time have to be translated in concentration and depth, respectively.

Let I_x be the intensity (counts/second) of atomic ion of a certain isotope ***x*** detected per unit time, I_{pr} be the intensity of the primary ion beam expressed in nA and q the elementary charge. The number of impinging particles is then I_{pr}/q. I_x can then be written as:

$$I_x = \frac{I_{pr}}{q} \cdot C \cdot Y_{tot} \cdot \alpha_x \cdot \gamma_x \cdot \eta_x \cdot \frac{A_{an}}{A_{sp}} \qquad (2.3)$$

where ***C*** is the relative concentration of the element *x*, i.e. the ratio between the atomic concentration of x-element referred to the atomic concentration of the sampled matrix (C_x/C_{matrix}); $\mathbf{Y_{tot}}$ is the sputtering yield, i.e. the number of emitted atoms per incident ion; $\boldsymbol{\alpha_x}$ is the ion yield that is the ratio defined as the ration between ionized and neutral species of the x-atom, γ is the isotopic abundance. $\boldsymbol{\eta_x}$ indicates the instrumental transmission factor corresponding to the signal losses in the system including the detector

efficiency which in general can be different for the different species.. $\mathbf{Y_{tot}}$ depends on analytical conditions such as primary ion species, impact energy and incidence angle, and on the material composition and in general can be simulated numerically. Usually the value of total yield is ranging from 1 to 20. Finally the A_{an}/A_{sp} is a geometrical factor representing the ratio of sputtered and analyzed areas.

Despite equation (2.3) may look relative simple, it is worth to point out that a direct SIMS measurement quantification from first principles is hardly achievable. In fact, both sputtering and ion yields strongly depends on surface composition. The latter is heavily affected by the retention of the primary ions, i.e. the fraction of them remaining on the SIMS crater bottom once an equilibrium is established between impinging and re-sputtered primary ions. Therefore, the concentration reported in (1.3) is not the original one, i.e. the one to be measured, but a function of it. The link between the actual concentration and the original one is hard to determine since the defining parameters (original composition, sputtering yield, and primary ion retention) are not independent. Therefore direct quantitative results from the only measurement on an unknown sample are in most cases not possible. Hence quantification is typically carried out by comparison with materials of known composition where an empirical sensitivity factor can be determined. Let us consider two ion species detected in the same analysis and their signal intensities: I_x related to the element whose profile has to be determined; I_r related to a species due to an element contained in the matrix, i.e. one of the main constituent of the sample in exam. If we consider the ratio of the of the two signals the geometric factor A_{an}/A_{sp} the primary ion beam flux I_{pr}/q and the sputtering yield Y_{tot} cancel out because they are not species dependent. All the species dependent parameters can be grouped into one constant in a way that:

$$\frac{C_x}{C_r} = \alpha \frac{I_x}{I_r} \tag{2.4}$$

If the element *r* is chosen in such a way that its concentration is a constant within the sample (matrix species) we can also include it into the constant α. The obtained constant is called *relative sensitivity factor* (RSF) of the element *x* in the matrix *r*. The concentration of the element can be expressed in simple form:

$$C_x = \frac{I_x}{I_r} RSF_x \tag{2.5}$$

With a measurement of a sample where C_x is known (from a standard measurements), the RSF_x may be obtained and the equation (2.5) can then be used to quantify the unknown sample. It is important to notice, that value of RSF is specific for a given element/matrix combination and given analytical settings.

For the conversion of the analysis time (t) to a depth scale (z), the sputtering rate must be known:

$$z(t) = \frac{dz}{dt} t \tag{2.6}$$

In a first approximation, if the sample analyzed is compositionally homogenous along the probed depth, the sputtering rate can be assumed to be constant throughout the profile. Hence by measuring the crater depth (d_{tot}) at the end of the analysis time (T), the sputtering rate can be determined as follows:

$$SR = \frac{d_{tot}}{T} \tag{2.7}$$

The validity of the assumption of constant sputtering rate and the effects influencing the sputtering rate will be discussed in section 2.2.6.

In dynamic SIMS the depth resolution (e.g. the ability to discriminate between atoms in adjacent thin layers) depends on primary beam parameters. Generally it can be evaluated as a decay length (nm\decade) measured on ultimately steep distribution like delta-doping or sharp interfaces. Typically the lower the impact energy the better the depth resolution. Using energies below 1 kev, resolutions as good as 2 nm can be achieved. In fact, a low impact energy reduces primary ion penetration and the associated mixing events. However these conditions make it harder to focus the beam without reducing its intensity. A poorly focused beam can in turn cause a degradation of depth resolution due to lateral inhomogeneity of sputtering conditions within the analyzed area, large craters with less sharp edges (described latter in section 2.2.6). To operate with ion beam with energy lower than 1 kev the used instrument is equipped with a primary column capable to operate in so called *primary floating column regime*.

2.2.5 The Primary Floating Column Concept

In a 'conventional' SIMS instrument the primary ions are transported from the ion source through the primary ion-optical column at an energy defined by the potential of the source electrode. In fact, the energy of primary ions is essentially given by the difference between the acceleration voltage of the source and the potential of the column set at ground level. The impact energy is the actual energy that primary ions have when they hit the sample surface. It is given by the difference between the energy of the ions and the sample bias, i.e. the voltage applied of the sample to extract secondary ions. Therefore, if a low impact energy is necessary to improve depth resolution, the only way is to lower the acceleration voltage of the source. This reduces the primary beam intensity/density. This is a serious limitation since it is known that especially for impact energies lower than 1 keV the sputtering yield drops to very low levels [98]. A low intensity/low impact energy beam results in a very low sputtering rate and the analysis time becomes too long to ensure good stability and good throughput. Furthermore, acceleration voltage cannot be arbitrarily lowered since ion sources work properly for voltages ≥ 2kV. In case of negative secondary ion mode, the sample bias is set to negative values and thus to reduce impact energy not only the acceleration voltage, but also the sample bias have to be decreased, with the consequences of a reduced extraction of secondary ions and thus a worse sensitivity. Furthermore, the source has to be set to a positive voltage otherwise primary ions cannot travel through the ground set primary column:

therefore, in a conventional magnetic sector instrument, the minimum impact energy can hardly be lowered below 2-3 keV for negative secondary ion mode.

In the Cameca WF/Sc-Ultra, an electrostatic potential can be applied to the primary column (floating voltage/floating column) differently from conventional instruments where the column is at ground voltage. Therefore ions can be accelerated and focused with respect to this floating voltage, i.e. keeping the acceleration voltage at an adequately high values to have a good beam intensity. At the end of the columns, the ions face an electrode with the same voltage of the sample and are thus decelerated to the required impact energy just before the impact with the sample. A schematic representation of this configuration is shown in figure 2.6.

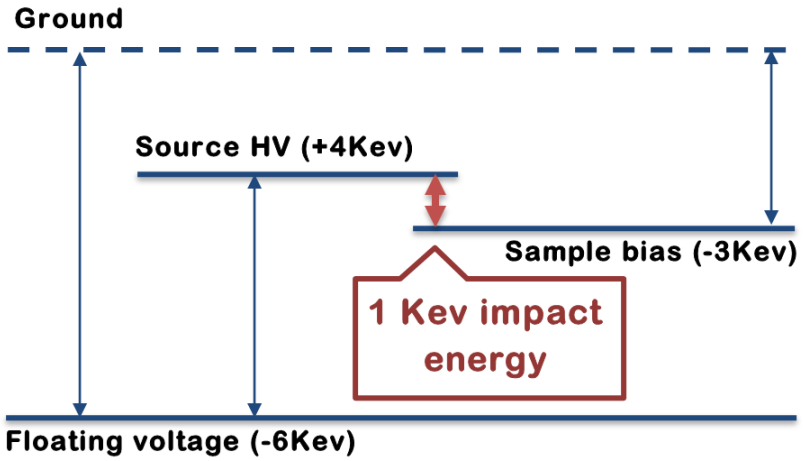

Figure 2.6. Floating column bias sketch. The floating column is biased at -6Kev. 4Kev ion beam is slowed down to 1Kev at the end of the primary column.

In the example, the source is set at 4 kV and the floating voltage at - 6Kev whereas sample bias is -3 keV (negative secondary ions). The floating column processes the 4 keV ion beam, and the primary ions are then slowed down to 1 keV at the end of the primary column. The advantages are: high source acceleration allows high beam densities; the possibility of keeping high bias allows a good extraction of secondary ions and thus a good sensitivity; finally, simply acting on floating voltage allows tuning the impact energy to the desired value. However, there are limitations on focusing and it is not possible to focus ion beams with impact energy < 1 keV on bias voltages higher than 3 keV.

Together with floating column, extraction optics, figure 2.7, is optimized for ULE analyses. A new geometry allows to maintain a suitable instrument transmission also at low energy. This is achieved by setting last primary column lens and first secondary column extraction lens at the same voltage of sample bias. This creates an essentially no-electric field region for the primary ions, helping to keep the desired incidence and focusing of the beam.

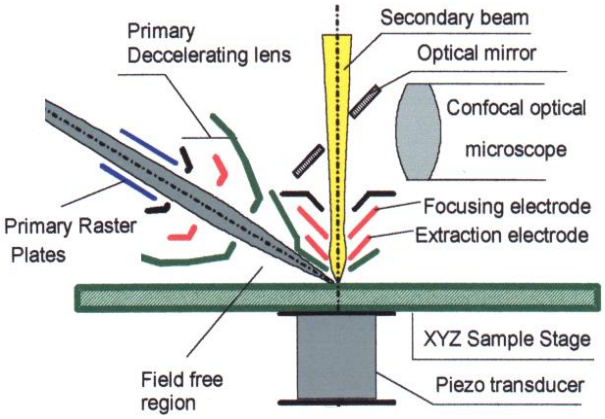

Figure 2.7. Extraction optic geometry, optimized for ultra-shallow profiles

2.2.6 Limitation and common artefacts of SIMS

The complexity and variety of phenomena related to the SIMS analysis give rise to deviations of the measured profiles from the 'real' ones and must be accounted for. These effects are usually referred as SIMS artefacts.

2.2.6.1 Ion beam mixing

Depth resolution of dynamic SIMS is mainly limited by the different processes related to the mixing of the material analyzed due to the impact of the primary ion beam and it includes recoil mixing, cascade mixing and radiation enhanced diffusion. Recoil mixing is the effect of direct collision the primary ion with atoms of the sample; the received momentum drives these atoms into the sample. In the collision cascade (described in 2.2.1) the atoms movement causes so called cascade mixing. Direction of the initial momentum of impinged ions changes its direction resulting in an isotropic movement of atoms. The radiation enhanced diffusion describes the significant increase of the thermal diffusion due to high concentration of vacancies and interstitial atoms produced by ion bombardment.

Material mixing cannot be totally avoided, but it is possible to reduce it by lowering the primary ion energy. Alternatively, there has been attempts to take into account the influence of material mixing by a theoretical modeling of the phenomena and the introduction of a *SIMS response function* [99]: an empirical function describing the depth distribution of analyzed ions at every moment. The proposed response function can be modeled over several orders of magnitude by the convolution of two exponentials and a Gaussian [100]. However, the proposed models work only in specific cases and cannot be applied to arbitrary experimental configurations.

For an idealized box-shape distribution the impact of ion beam mixing on the detected profiles is shown in the figure 2.8. When the analyzed profile is thicker than the altered layer created by impinging primary ions like in peak 3 of figure 2.8, the SIMS detected profile is similar to real distribution but with

smoothed edges. When peak width and altered layer are comparable like in peak 2, then measured profile looks like a smooth peak instead of the expected box-like distribution .Measured peak integral is the same as the original one and the shape of this peak would be dictated by 'SIMS response function' [100]. The latter defines the depth resolution: any distribution thinner than this function width (like peak 1) will be measured like this, producing a similar distribution but with lower magnitude.

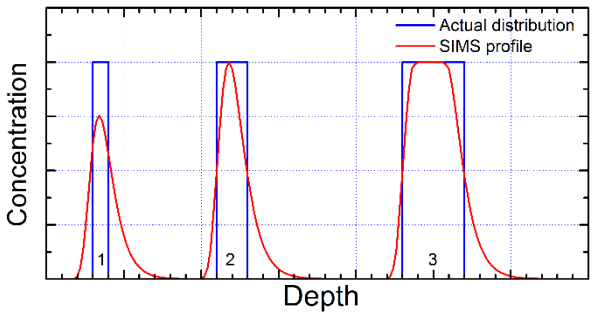

Figure 2.8. Box-like profile convolution due to low depth resolution.

2.2.6.2 *Edge effect*

As the erosion of the sputtered area proceeds, a crater is formed. The abruptness of the crater edges depends on the focus and homogeneity of the primary beam. Secondary ions coming from the edge regions influence the collected depth profile, particularly depth resolution and signal background.

In the figure 2.9 a linear scan obtained on a SIMS crater (Cs+ at 500 eV bombardment) by a mechanical stylus profilometer of a crater sputtered with a Cs^+ beam at 500 eV in Si is shown. If the concentration of the element of interest is not uniform (i.e. changes with depth), the measured value will be different from the real one, because the detected concentration is not the one at the crater bottom but it is partially convoluted with the gradient on the edges. In practice this effect is avoided by restricting the sampling area to the center of the crater (as indicated with the green color), typically collecting ions from an area whose lateral dimensions are 1/3 of the sputtered area. This can be done either in 'mechanically way' using an adequate aperture for secondary ion beam, or in 'electronic way' using an electronic gate selecting secondary ions coming only from the center of the crater.

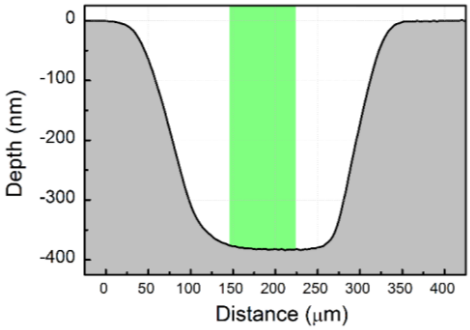

Figure 2.9. SIMS crater sputtered with 500ev Cs^+ beam.

2.2.6.3 *Sputtering induced roughness*

During ion sputtering, solid surfaces often develop micro- and nano- topography, generically indicated as surface roughness, typically resulting in parallel long ripples oriented in direction either parallel or normal to the beam projection on sample surface [101]. The formation of roughness derives from a balance between the local angle dependent sputtering yield which unevenly removes material

from the surface and different kinds of surface diffusion phenomena smoothing the surface back, resulting in regular and periodic oscillations of the surface [102]. The roughness may drastically decrease depth resolution because the secondary ions will no longer be extracted from the same depth (figure 2.10) [103]. Furthermore, during roughness development both sputtering and ion yield are not stable and secondary ion depth profiles result distorted.

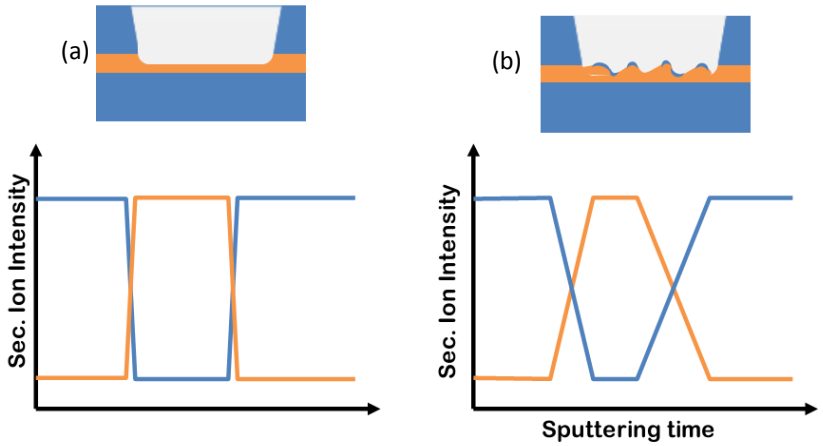

Figure 2.10. Influence of roughness formation on registered secondary ion intensity: vertical section of SIMS crater (top row); obtained SIMS profiles (bottom row)

An effective method to suppress roughness formation is the sample rotation around an axis normal to the sample surface and passing through the center of the sputtered area [104]. If the sample is rotating during sputtering, the beam will hit different sides of the developing topography losing the isotropy of the structures and smoothing the crater surface. The typical result is a reduced topography if not a complete smoothing of the crater bottom with the consequence of improving depth resolution and depth calibration [105], [106].

2.2.6.4 Initial transient

During the sputtering of the first few nm's of material, a composition on the sample surface is strongly changing due to iteration of the sample with sputtered beam. Detected SIMS depth profiles suffer in the initial part of *an initial transient*, corresponding to the thickness of material to be sputtered essentially before an equilibrium has been established between implanted and re-sputtered primary species, i.e. before a constant composition of the SIMS crater bottom has been established. Before this 'steady' equilibrium, both sputtering and ion yields are not stabilized and consequently their variation influence the recorded secondary ion signal even if the composition is constant. In fact, when analysis starts, a secondary ion signal appears gradually starting from zero and after some time depending on ion beam density it stabilizes at some equilibrium value related to the actual concentration of the elements. The depth over which the signal increases is directly related to the primary ion impact energy and incidence angle since those two parameters together with ion species and sample composition define the

interaction ion/ matter. Therefore, this initial transient typically decreases increasing incidence angle and decreasing energy and for instance, at 1 keV Cs^+ sputtering amounts to 2-3 nm. For deep profiles the accurate knowledge of the concentration in the initial transient can be neglected since its relative weight on the whole profiles is limited. However, in case of ultra shallow junctions (USJ) in Si or other surface confined distributions, i.e. where most dopant is confined within the first 10 nm, an accurate characterization of this region is essential.

As pointed out earlier, in the initial transient region not only the ionization yield is affected but also the sputtering rate. The actual sputtering rate can be a few times higher in the very beginning of the analysis (an example is given in Chapter 3). In the approximation where the average sputtering rate is calculated according to the measurement of the crater depth at the end of the analysis, this initial variation can affect the calibration especially when initial transient width is comparable to the length of the depth profile.

The effect of the profile distortion due to the initial sputtering rate variation at the beginning of the analysis is schematically demonstrated in figure 2.11. The sputtering rate during initial transient is usually faster than the equilibrium one; this case is considered in the figure. For instance, the actual distribution (red dash line) is recorded between time t_1 and t_2 as expected following the real sputtered depth/ time behavior (red continuous line). However, if sputtering time is converted to depth using the final crater depth, the erosion is assumed to have been linear with time, i.e. it followed the continuous green line. Therefore instant t_1 and t_2 would correspond to 'lower-than-real' depths. The measured distribution is not only shifted towards the surface but also narrower than the actual one (green dash line). This effect was always evident when comparing the SIMS results with other techniques (like RBS or MEIS or GI-XRF, e.g. [107]). It is worth to mention that roughness formation can increase the initial transient width, affecting in the same way profile accuracy [108], [109].

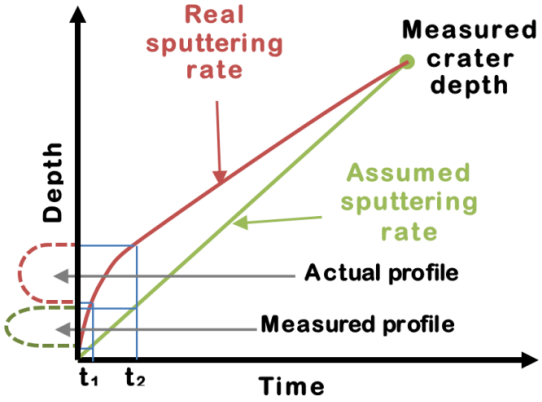

Figure 2.11. Distortion of SIMS profile due to sputtering rate variation.

As mentioned above the effect becomes less important and can be neglected if the transient width is a minimal part of the whole profile. In chapter 3 the more accurate determination of the depth scale is described

2.2.6.5 *Matrix effect*

SIMS can show strong variations in the secondary ion yield for the same element concentration in different matrices. In fact, composition variations result in relevant differences of ion and sputtering yield, and thus the same ion species can have variations of intensity not necessarily dependent on variations of concentration of the element relative to the ion species. It is obvious that this matrix effect is face whenever there is a change of composition, either in multi-layer systems or also when an element is higher than the dilute regime of < 1%.

The most frequently encountered matrix effect in Si depth profiling is related to the presence of an oxidized layer on top of the measured sample. In fact, when a silicon wafer is exposed to the atmosphere a SiO_2 layer is readily formed also at room temperature and it is called native oxide. If the dopant is placed into the near surface region, the recorded ion yield will be affected by the presence of the oxide resulting a deviation of measured profile from the real one.

The effect of this phenomena in multi-layer systems can be partially compensated during the data quantification using proper values of relative sensitivity factors (RSF) in different layers. The value of RSF in additional layers for given element in a given matrix can be measured using standards and then obtained values can be applied to every layer using equation (2.6).

The chapter 3 of this work is dedicated to accurate quantification of matrix effect in silicon using ultra-low energy SIMS with Cs^+ primary ion beam.

2.3 Medium Energy Ion Spectrometry (MEIS)

Medium Energy Ion Scattering (MEIS) is a refinement of Rutherford Backscattering Spectrometry where energy and angle resolved detection of backscattered ions provides surface structural and compositional information. The main advantage of MEIS over SIMS is that it can provide absolute quantitative analysis with sub-nanometer depth resolution in the near-surface region [110]. One of the constrictions of the technique is that it has poor sensitivity for 'light' elements in 'heavy' matrix. On the contrary, the combination of 'heavy' arsenic atoms with the relatively light silicon substrate allows the acquisition of MEIS depth profiles with a good resolution.

2.3.1 Basic principles.

In a typical MEIS analysis a sample of interest is bombarded with a collimated beam of mono energetic (50 - 400 keV) light ions (H^+ or He^+) along a known direction and the scattered particles are detected over a wide angular range (typically 30 degrees). The energy of the back scattered particles depends on the elastic and inelastic energy loss processes inside the sample.

Elastic energy loss is governed by collisions between the nuclei of projectile ion and the target atom. The kinematics can be obtained using energy and momentum conservation principles. Figure 2.12 shows the scattering configuration of the process. The incident particle will transfer part of its energy to the target atom depending on its mass and scattering angle [111]:

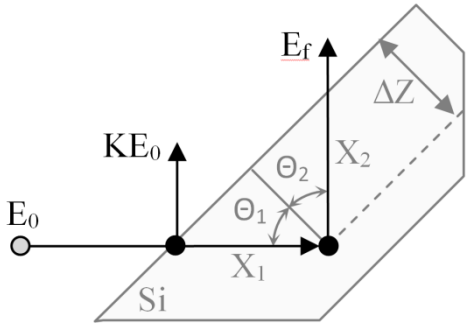

Figure 2.12. MEIS scattering configuration

$$K = \left[\frac{\sqrt{M_2^2 + M_1^2 \sin^2\theta} + M_1 \cos\theta}{M_1 + M_2}\right]^2 \quad (2.8)$$

where M_1 is the mass of the incident ion, M_2 is the mass of the target atom and θ is the scattering angle. Since the mass of the ion M_1 is known from the choice of ion species and the scattering angle θ is actually detector angle in experiment target mass M_2 can be calculated using measured energies of the ion before and after collision. This allows MEIS distinguish between scatterings off different elements.

The depth information of the target atoms can be obtained from contribution of inelastic energy loss on the energy of the outgoing ion. If scattering takes place at some unknown depth then energy of ion will be less than energy of ion scattered from the surface, for the same scattering angle. This is because the incident ion losses its energy while travelling inside the sample due to inelastic energy loss in interaction with target electrons, and hence detected energy is less than expected.

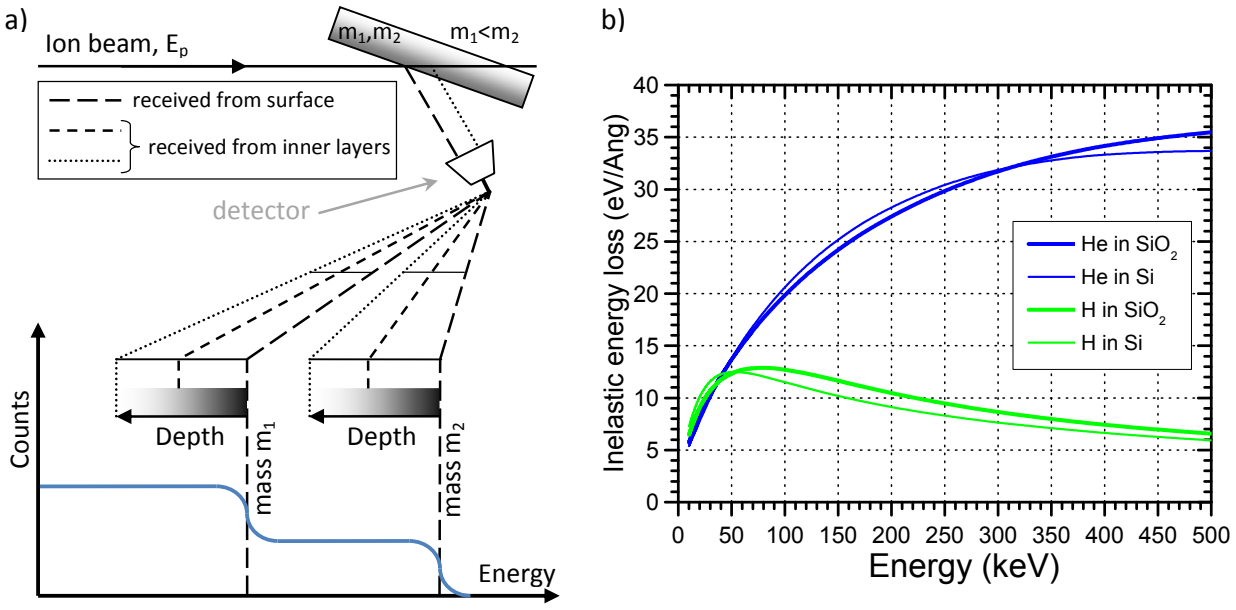

Figure 2.13. a) principle of a depth profiling generation; b) inelastic energy loss as a function of beam energy for H and He ions in Si and SiO_2

The inelastic energy loss (dE/dx, commonly expressed in eV/Angstrom and usually refers as stopping power) of a particle depends on ion and target material and on the ion energy; knowing the stopping power one can generate the depth scale [112]. An example of energy loss values as a function of incident ion energy for H and He ions is Si and SiO_2 obtained from the SRIM-2012 [113] software is presented on figure 2.13, b. In MEIS the depth calibration accuracy is limited by the accuracy of stopping power values used in the calculation.

Figure 2.13, a, shows typical experimental geometry of a MEIS experiment used for depth profiling and the method to generate depth scale for different target masses.

The number of target atoms is determined in principle by the probability of a collision between the incident particles and target atoms using the simple formula for the backscattering yield Y [112]:

$$Y = Q_d = \frac{d\sigma}{d\Omega}\Omega Q N t \qquad (2.9)$$

$d\sigma/d\Omega$ is differential scattering cross section, Q_d and Q are the number of detected and incident particles respectively, Ω is a detector solid angle and Nt is the areal density to be determined.

Actual concentration of any particular element can be obtained if we can calculate the exact cross-section values or by comparing the result with a standard sample with known composition. However relative composition of different element can easily be obtained and hence the stoichiometry of a sample can be determined using these methods.

2.3.2 Ion channeling and blocking

Besides the information related to the mass, concentration and in-depth distribution of the different atomic species inside the sample, MEIS allows the extraction of information about the specimen crystallinity. If the sample has a crystalline structure the incident beam can be aligned along some crystallographic direction and thereby the number of atoms visible to the beam can be altered (Figure 2.14, a). Although some of incident ions are reflected by the atoms of a surface layer (particle 2), most of them can be "steered" by a series of small angle deflections in the Coulomb field of the target atoms (particle 2). Energy losses in such collisions are small and incident ions pass much deeper inside the solid before the total relaxation. In this case backscattering yield from the sample surface remains the same whereas yield from the atoms located under the surface layers reduces drastically (the shadowing effect). Similarly, the scattered ions experience the same direction-dependent effect as incident ones when some of the scattering direction are blocked by other atoms (the blocking effect, figure 2.14, b)

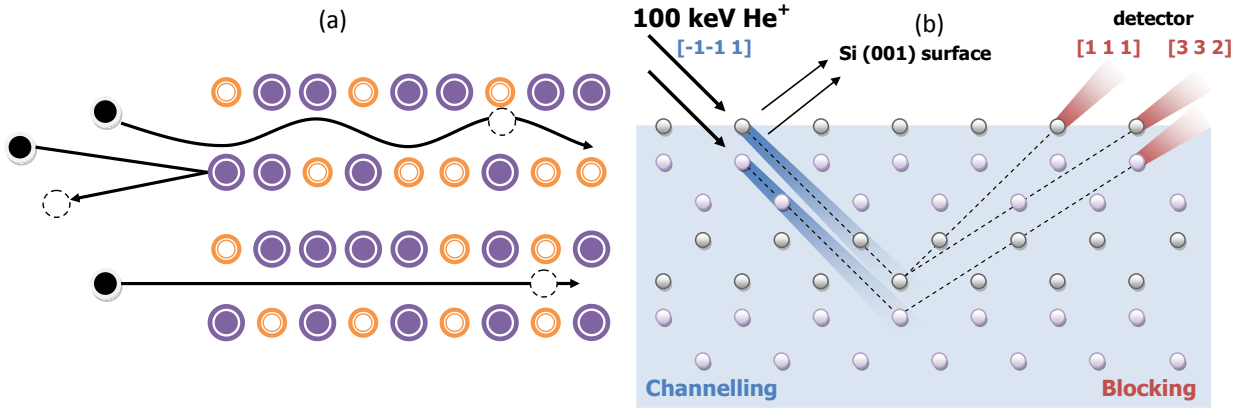

Figure 2.14. Illustration of the channeling (a) and a double alignment configuration used in MEIS experiments, showing the shadowing and blocking (b, illustration adapted from [114])

In amorphous material due to the random position of target atoms the scattering always occurs from any depth; the crystalline material might be considered as "amorphous" using random orientated incident direction. In practice, this direction is achieved tilting the sample by a 5-7° angle away from channeled direction. This orientation does not correspond to any high-symmetry crystallographic direction and hence it is expected to give strong sub-surface scattering. On figure 2.15 MEIS spectra obtained using both random (tilted) and channeled directions are shown. If the surface peak remains the same for both directions, this indicates amorphization of the surface of the target. On the other hand, the channeled surface peak is lower than the random one (like in the shown case). In this case the scattering yield is much lower than in pure amorphous material meaning that the degree of lattice damage on the surface is lower. The shadowing effects drastically reduces the backscattering yield coming from the buried layers and this is very evident in the shown example (by factor of 30).

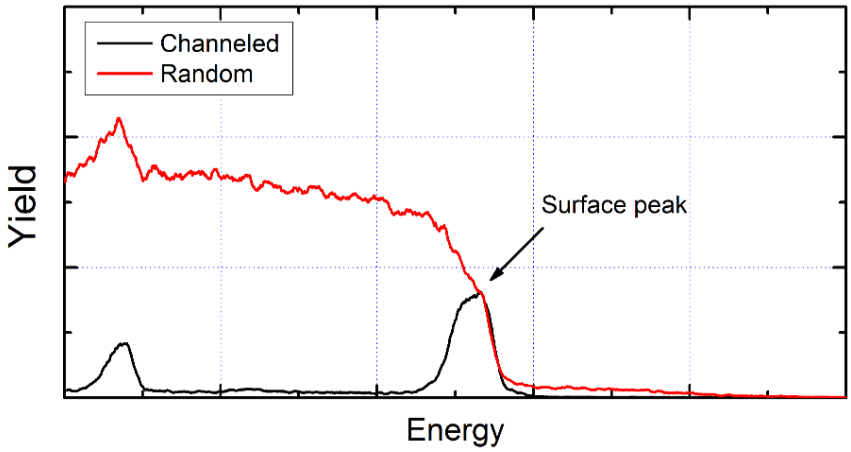

Figure 2.15. Comparison between energy spectra obtained in two different direction: random and channeled. In the channeled case the reduction of the yield coming from buried layers is due to shadowing effect of the surface atoms.

The shadowing effect is only applicable to the atom of the target placed in substitutional sites. In the channeling configuration the atoms placed in interstitial sites are producing the same backscattering signal as if they were amorphous material. Moreover, all lattice defects affect the channeled incident ions and contribute to de-channel the beam. The analysis for many different primary beam angle and detection over a wide angular range, combined with simulation of the measurements can give accurate structural information able to detect atomic displacements as small as 0.05 angstroms

2.3.3 MEIS: Analytical conditions

MEIS measurements were carried out at the STFC Daresbury Laboratory (UK) by Dr Paul Bailey, Dr Tim Noakes in collaboration with prof. Jaap van den Berg of University of Salford. The analysis was carried out under UHV using a highly collimated 100 keV He^+ ion beam. All samples were analyzed under double alignment conditions, exploiting the channeling and blocking properties of the underlying crystalline Si lattice to minimize background scattering [111], [115], [116]. For these samples an incidence angle of 54.7° was chosen, to align the [-1-1 1] channel to the incident ion beam. The electrostatic analyzer was set to an approximate angle of 65° thus allowing both the [111] and [332] blocking directions to be captured in the 2-D data set. From this data set cuts were taken along the [111] and [332] blocking directions to produce energy spectra in double alignment at scattering angles of 70.5° and 60.5°, respectively. The used configuration is schematically demonstrated in figure 2.14, b. These scattering parameters and ion beam energy were chosen as they produced the best compromise between depth resolution, which improves with decreasing scattering angle, while still clearly resolving the scattering peaks of different masses, which improves with increasing scattering angle and incident ion energy. Only results taken at 70.5° are presented here since there is some overlap between the Si and As peaks in the 60.5° spectra, which renders these less useful.

For the As in Si system, the most studied in this thesis work, the conversion of scattering yield to concentration is achieved through an internal calibration by comparing the As yield with the random Si yield level obtained from an amorphized Si sample, taking into account the squared ratio of the scattering cross sections for Si and As ($\propto(Z_1/Z_2)^2$), where Z is the atomic number. Applying some corrections as reported in [33, 34], the scattering conditions used in this investigation (as detailed below) result in an accuracy better than 5% on concentration determination. At the same time, the depth accuracy is better than $\pm$ 0.2 nm.

2.4 Other techniques

2.4.1 Instrumental Neutron Activation Analysis (INAA)

Neutron activation analysis is an accurate and sensitive analytical technique used for both qualitative and quantitative trace element analysis. Since this technique was proposed and demonstrated in 1936 by Von Hevesy and Levi INAA has been developed and employed for a wide variety of applications. Because most materials are "transparent" to both the probe (neutrons) and the signal (gamma rays), there are few matrix effects associated with the analysis and standardization of the measurement is simple and straightforward [117].

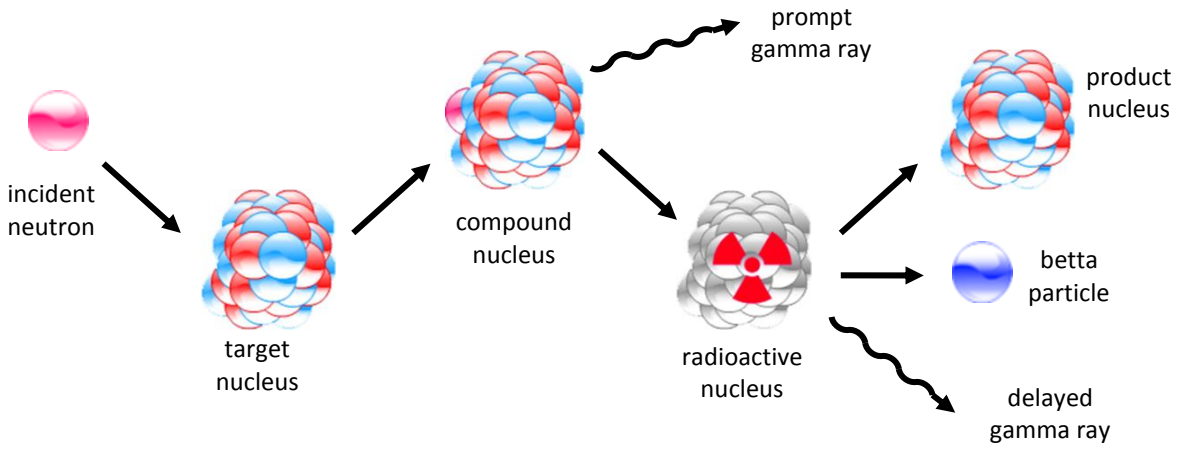

Figure 2.16. Diagram illustrating the process of neutron capture by a target nucleus followed by the emission of gamma rays

In INAA, the sample is exposed to a flux of neutrons (figure 2.16). Incident neutrons collide and interact with the nuclei. The most common reaction is the neutron capture where an unstable isotope is created with mass increased by 1 a.m.u. This typically de-excites into a more stable configuration by the emission of one or more prompt gamma rays with a half-life of 10^{-13} – 10^{-3} sec [118]. The radioactive nucleus then decays to a stable species by beta emission a further (delayed) gamma emission. Depending upon the particular radioactive species, half-lives can range from fractions of a second to several years.

Emitted gamma can be used by INAA for elemental analysis. Carried energy and the rate or the half-life of the decay are unique features of a particular isotope undergoing decay. By collecting and measuring the full spectrum of gamma rays emitted by a sample it is possible to identify and precisely quantify the range of radioisotopes present in the sample, and thus to determine the elemental composition of the sample.

In principle, it is possible to perform quantitative INAA by using the general formula for activation:

$$\omega = \frac{M \cdot R_x \cdot e^{\lambda_x \cdot t_d}}{\varepsilon_x \cdot \sigma \cdot \phi \cdot N_A \cdot I_N \cdot (1 - e^{\lambda_x \cdot t_i})} \tag{2.10}$$

where ω is the mass of unknown element in sample, M - atomic weight of unknown element, R_x - measured count rate of unknown element (activity), λ_x - decay constant of the measured radionuclide of the unknown element, t_d - decay time (time between irradiation end and midpoint of counting period), ε_x - counting efficiency of the detected gamma energy, σ - thermal neutron reaction cross section of the unknown element, ϕ - neutron flux in irradiation position, N_A - Avogadro's number, I_N - natural occurrence of the target isotope in the actual element, and t_i - irradiation time.

The parameters σ and ϕ are difficult to determine exactly but they can be canceled out from equation using a comparative analysis where the activity in the unknown sample is compared to the activity in a simultaneously irradiated standard containing a known amount of the same element. If these samples are measured on the same detector, difference in decay between them need to be corrected. One usually corrects the measured counts for both samples back to the end of irradiation using the half-life of the measured isotope. Dividing (2.10) for unknown sample (p) on the same expression for the standard (s):

$$\frac{\omega_p}{\omega_s} = \frac{\frac{M \cdot R_{xp} \cdot e^{\lambda_x \cdot t_{dx}}}{\varepsilon_{xp} \cdot \sigma \cdot \phi \cdot N_A \cdot I_N \cdot (1 - e^{\lambda_x} \cdot t_i)}}{\frac{M \cdot R_{xs} \cdot e^{\lambda_x \cdot t_{ds}}}{\varepsilon_{xs} \cdot \sigma \cdot \phi \cdot N_A \cdot I_N \cdot (1 - e^{\lambda_x} \cdot t_i)}} \tag{2.11}$$

If the samples are measured on the same detector, then $\varepsilon_{xp} = \varepsilon_{xs}$ and expression (2.11) simplifies into:

$$\frac{\omega_p}{\omega_s} = \frac{R_{xp} \cdot e^{\lambda_x \cdot t_{dx}}}{R_{xs} \cdot e^{\lambda_x \cdot t_{ds}}} \tag{2.12}$$

This expression can be simplified even more assuming that irradiation, decay and counting time are the same for all measured samples and standards. In this case, all time-dependent factors cancel out and the above equation simplifies into:

$$C_p = C_s \frac{W_s}{W_p} \frac{R_{xp}}{R_{xs}} \tag{2.13}$$

where C - concentration of the element and W is a weight of the sample and standard.

The physical principles of the analysis are so well understood that neutron activation analysis is one of the primary techniques used by the National Institute of Standards and Technology to certify the concentration of elements in standard reference materials.

For the current problem, INAA measurements have been carried out at the TRIGA Mark II reactor of the Atominstitut, Vienna University of Technology. The samples of a size around 3-4 cm^2 were irradiated for 1200s under neuron flux with a density of approximately $3 \cdot 10^{12}$ cm^{-2} s^{-1}. After neutron irradiation, a

cooling time of at least 60 minutes allowed the fast neutron activation products of silicon, ^{28}Al ($T_{1/2}$ = 2.2414 min) and ^{29}Al ($T_{1/2}$ = 6.56 min) to decay almost completely and allowed an undisturbed measurement of the thermal neutron activation product ^{76}As ($T_{1/2}$ = 1.0942 d). The measuring times were chosen independently for each sample, until the error due to counting statistics was <5% rel. for the 559.1 keV peak of ^{76}As in each spectrum. The samples were measured in a fixed position at a distance of approximately 10 cm beside the detector so that the slightest possible changes in the geometry of the sample next to the detector could be neglected. The γ-spectrometry was performed with a 222 cm^3 HPGe-detector (1.78 Kev resolution at the 1332 Kev ^{60}Co peak; 48.2% relative efficiency), connected to a PC-based multi-channel analyzer with a preloaded filter and a Loss-Free Counting system. The area of the wafer pieces was calculated by derivation from the sample mass, Si density, and thickness. The total amount of As atoms in a sample was determined from semi-quantitative analysis (equation (2.13)) measuring a standard with a well-known As fluence.

2.4.2 Extended X-ray Absorption Fine Structure (EXAFS)

X-ray Absorption Fine Structure (XAFS) spectroscopy is a technique used for analyzing the chemical and physical state of an atom based on how the atom absorbs the x-ray radiation at energies near and above the core-level binding energies. In a XAFS experiment, the sample is irradiated with x-rays and the absorption probability $\mu(E)$ as a function of the radiation energy is measured, according to the Beer's law:

$$\mathrm{I(E)} = \mathrm{I}_0 e^{-\mu(E)t} \tag{2.14}$$

where I_0 is x-ray intensity incident on a sample, t is the sample thickness, and I is the intensity of the radiation transmitted through the sample.

In general, the absorption probability progressively increases with photon energy (μ ~$1/E^3$). However, at some energies, which are characteristic for each atomic species, a sudden increase of the absorption occurs. This happens when the energy of the incoming x-ray photon is close to the binding energy of an inner core level electron of an atom: this electron absorbs the energy leaving the atom. This *X-ray photoelectric effect* is the basis of XAFS spectroscopy and the sudden increase in the absorption coefficient at the energy at which photoelectron emission occurs is called an *absorption edge*.

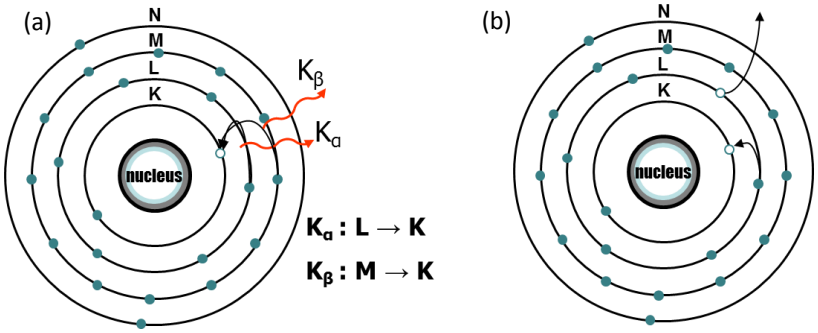

Figure 2.17. Vacant core hole in the atom is filled by the electron from a higher shell emitting x-ray fluorescence (a) or an Auger electron (b)

When an x-ray photon is absorbed, the absorbing atom is excited, emits a photoelectron (which creates a core hole) and relaxes back to its "ground state" filling the core hole with an electron from a higher shell. This de-excitation goes along with the emission of an x-ray fluorescence photon or an Auger electron (figure 2.17). X-ray fluorescence or Auger emission occurs at discrete energies corresponding to the electron configuration of the absorbing atom and can be used to identify the atom.

If the absorbing atom is surrounded by other atoms, the emitted photoelectron is scattered by them, creating interference between outgoing and scattered photoelectron wave functions. This interference varies with energy, causing oscillations of the X-ray absorption probability $\mu(E)$. An example of $\mu(E)$ for FeO near the absorption edge is shown in figure 2.18.

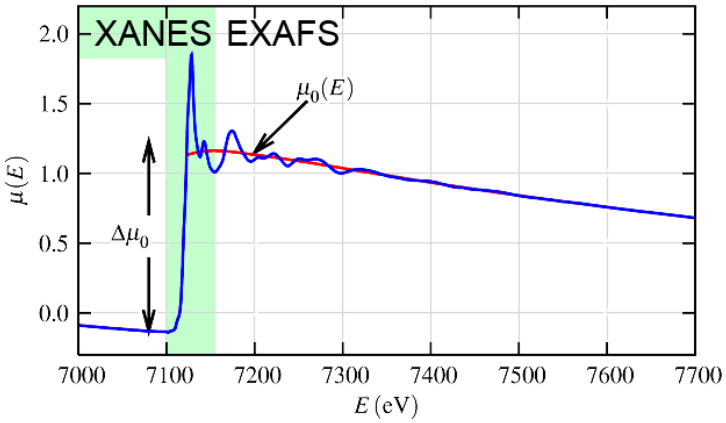

Figure 2.18. X-ray absorption probability of FeO as a function of radiation energy (adapted from [119]). The red curve $\mu_0(E)$ corresponds to a background function and $\Delta\mu_0(E_0)$ is the edge step..

As indicated in the figure, the x-ray absorption spectrum (or XAFS function) is typically divided into two regions: the x-ray absorption near-edge structure (XANES) region and extended x-ray absorption fine-structure (EXAFS) region. The XANES is strongly sensitive to the formal oxidation state and coordination chemistry of the absorbing atom whereas the EXAFS can be used to extract information about the atoms local structure: distances to neighboring atom, their number and species (their approximate atomic number). The local structure of a dopant in a semiconductor material correlates with its active state. This information can be extracted from the EXAFS region of the x-ray absorption spectrum and only EXAFS is considered within the frame of this work.

To extract information from EXAFS, the oscillations of the absorption coefficient are isolated by subtracting the background level from the XAFS. This level corresponds to the signal from an isolated atom, where photoelectron wave function does not interfere with the local environment of the atom. The EXAFS fine structure function χ(E) is defined as:

$$\chi(\mathrm{E}) = \frac{\mu(E) - \mu_0(E)}{\Delta\mu(E_0)} \tag{2.15}$$

where μ(E) is the measured absorption coefficient, μ_0(E) is the smooth background function corresponding to the absorption probability of an isolated atom, and $\Delta\mu_0(E_0)$ is the energy step at the absorption edge E_0 (as shown in figure 2.18). For further processing and interpretation, it is convenient to express the XAFS in terms of the photo-electron wave number, k, rather than the x-ray energy, which has a dimensions of 1/distance and is defined as:

$$\mathrm{k} = \frac{\sqrt{2m(E - E_0)}}{\hbar^2} \tag{2.16}$$

The function χ(k) is commonly referred to as ”the EXAFS” and it describes the oscillations as a function of the photo electron wave number. These oscillations decay very fast (as shown in figure 2.19)

with increasing k and therefore, to emphasize these oscillations, χ(k) is usually multiplied by a power of k (typically 2 or 3), as show in figure 2.19, b.

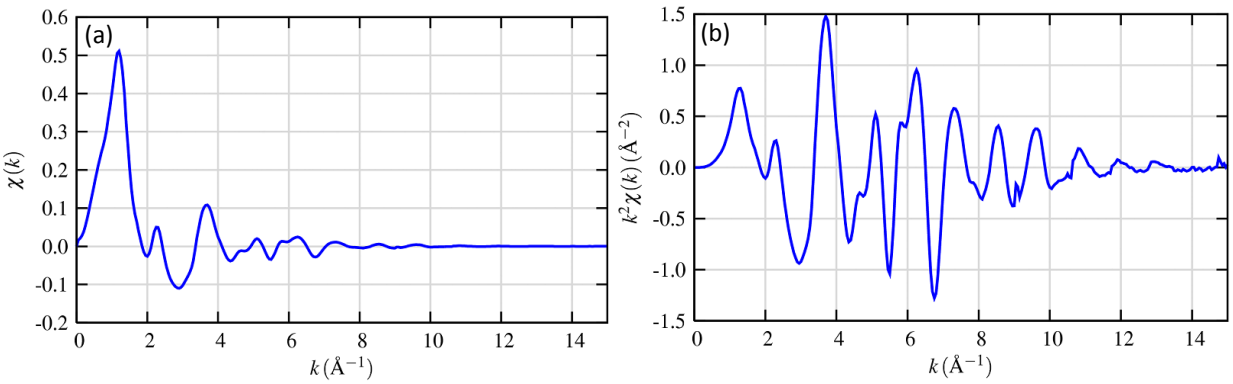

Figure 2.19. An example of the EXAFS χ(k) of FeO as a function of photoelectron wave number (a) and the k-weighted EXAFS $k^2\chi(k)$ (b). Illustration from [119].

The EXAFS is a combination of different frequencies and these frequencies corresponds to the scattering of the photoelectron wave-function from different neighbors. In general, the EXAFS can be modeled using the *EXAFS equation*:

$$\chi(\mathrm{k}) = \sum_j \frac{N_j f_j(k) e^{-2k^2\sigma_j^2} e^{-2R_j/\lambda(k)}}{kR_j^2} \sin[2kR_j + \delta_j(k)] \qquad (2.17)$$

The sum in this equation sums over all "coordination shells" of equidistant neighboring atoms. In the equation (2.17), the phase f(k) and shift δ(k) are the photo-electron scattering properties of the neighboring atom, N is the number of atoms in the shell, R is the distance from the atom of interest, and σ^2 is the disorder in the neighbor distance (also called Debye-Waller factor). Knowing the parameters f(k) and δ(k), it is possible to determine R, N and σ^2 from the EXAFS equation.

Finally, the variable k can be transposed to a distance using the Fourier transform of χ(k). Since every k corresponds to a wave scattered from neighbor atoms in a coordination shell, its Fourier transform (FT) is related to the distance to this shell. Since the Fourier function is complex it is represented by both imaginary and real parts, its magnitude is used for analysis. The FT of the EXAFS (now a function of distance) is the most common way to look at the measurement results. The Fourier transform of the EXAFS function presented in figure 2.19, a, is shown in figure 2.20.

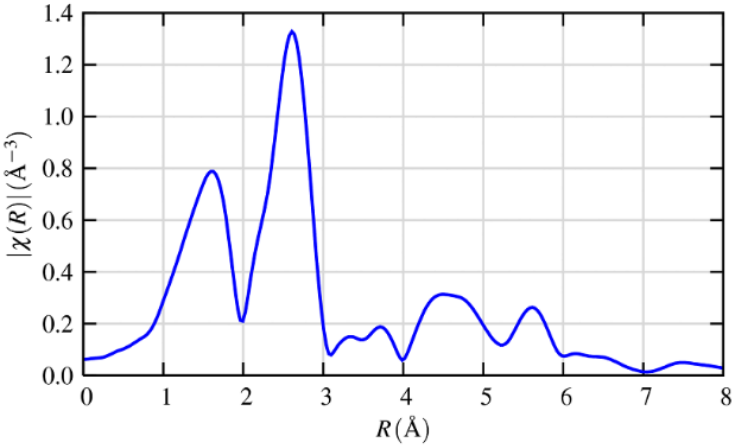

Figure 2.20. Fourier transform of the EXAFS function. Illustration from [119]

The peaks in the EXAFS function χ(R) correspond to the scattering of the photoelectron wave-function from atomic neighbors at different distances.

The measurements of X-ray absorption fine structure have been performed in fluorescence mode at beamline 11-2 of the SSRL. The samples were aligned for grazing incidence of the synchrotron beam adjusting an angle 3-4 times larger than the critical angle of total (external) reflection of X-rays to sample the whole dopant distribution while minimizing the background signal from the substrate. The energy of the synchrotron beam was monochromatized by means of Si single crystal Si(220) with nominal energy resolutions of $1\text{x}10^{-4}$ (ΔE/E), respectively. As K-edge spectra have been acquired in the energy range of 11600-12900eV (up to k = 16) with variable energy steps (10eV prior to the edge, 0.25eV across the edge and constant k=0.05 in the post edge region).

2.4.3 Four Point Probe

The electronic properties of a semiconductor material can be used directly to estimate level of dopant activation. In this work evaluation of electrical properties was carried out using the van der Pauw technique which, due to its convenience, is widely used in research and industry to analyze uniform samples. From the measurement of the resistance, all main electrical properties of samples can be obtained: the sheet resistance R_s, the sheet carrier density n_s, and the carrier mobility μ.

The electrical resistance of a sample can be determined from several measurements of voltage and current across the sample and the most adopted approach is Four Point Probe (4PP) measurement. The most general 4PP method was suggested by van der Pauw [120], where an arbitrarily shaped thin-plate sample, electrically uniform on the plane, can be measured with four relatively small contact points placed on sample edges. A common geometry for the sample with 4 electrical contacts at the four corners of a roughly square sample is depicted on figure 2.21

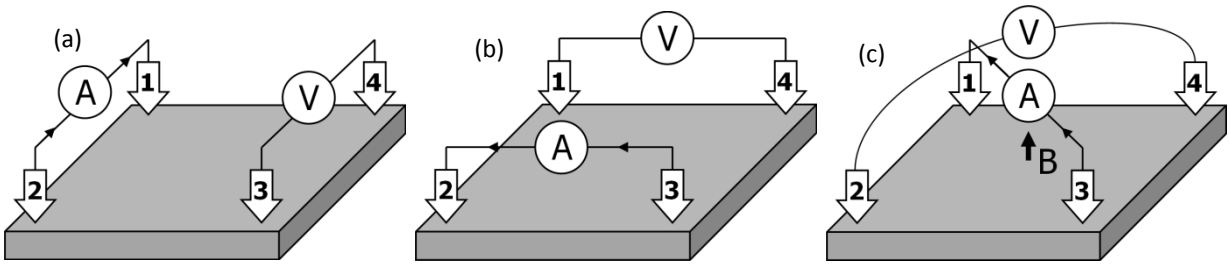

Figure 2.21. Set up for measuring characteristic resistances using Four Point Probe technique (a, b). Configuration for the Hall Effect measurement (c).

In this configuration, to make a measurement, a dc current is injected along one edge of the sample (for instance, I_{12}) and the voltage across the opposite edge (in this case, V_{34}) is measured. From these two values, a resistance R_A can be found using Ohm's law (resistance R_B is obtained with the same types of measurement carried out using terminals rotated by 90°, figure 2.21 b):

$$R_A = \frac{I_{12}}{V_{34}};\ R_B = \frac{I_{23}}{V_{41}} \tag{2.18}$$

Since in ion implanted samples like the ones used in this work the thickness of the doped region is not always known, it is common practice to refer to the sheet value of the resistance. The sheet resistance R_s (resistance ρ normalized by thickness d) can be obtained using these two characteristic resistances R_A and R_B through the van der Pauw equation [121]:

$$e^{-\pi R_A/R_s} + e^{-\pi R_B/R_s} = 1 \tag{2.19}$$

This equation can be written in a simplified form:

$$R_s = \frac{\rho}{d} = \frac{\pi}{\ln(2)} \frac{R_A + R_B}{2} f\left(\frac{R_A}{R_B}\right) \quad (2.20)$$

where *f* is a correction factor for an unsymmetrical sample. It cannot be given as a closed function and it determined by solving numerically for *f* the following expression [121]:

$$\frac{R_A - R_B}{R_A + R_B} = f \cdot arccosh\left(\frac{1}{2} e^{\ln(2)/f}\right) \quad (2.21)$$

For uniformly implanted material R_A and R_B are equal but in practice there is a difference between measured values due to geometrical factors (it is difficult to prepare the sample of symmetric shape). The difference between the characteristic resistances is small (less than 20%) and correction factor value is almost 1 and thus it can be excluded from equation (2.20) (for instance, f(2.0)≈0.96):

$$R_s = \frac{\pi}{\ln(2)} \frac{R_A + R_B}{2} \quad (2.22)$$

Originally the van der Pauw method was intended for a measuring of homogeneous samples but in practice this technique can be applied to miscellaneous material with slight modification. Almost all four point probe instruments are adopted to increase accuracy averaging resistivity measurements obtained applying both negative and positive voltage to contacts on each side of the sample (rather than measuring only R_A and R_B).

Chapter 3. Advanced SIMS

3.1 Introduction

The quantitative analysis by secondary ion mass spectrometry (SIMS) of ultra-shallow dopant distributions in semiconductors, and in particular in silicon, is still one of the widest but also most challenging applications of dynamic SIMS [122]. The main issues are the extreme abruptness of the distributions, requiring ultra-low energy (ULE) sputtering, the high dopant concentration, and the combined effect of the sputtering initial transient width and of the surface native or induced SiO_2 layer.

In this chapter, a model for the quantification of SIMS raw data is presented. The model was developed with the aim of reducing the artefacts typically faced in ultra-shallow junction (USJ) characterization. This model includes previous observations ([123], [124]) related to arsenic quantification at SiO_2/Si interface by SIMS as well as further improvements obtained from experimental results. Ad-hoc realized As implants through a thin (11nm) SiO_2 layer were used to calibrate the model in presence of an oxide/silicon interface. The correction procedure was then tested on a series of samples with ultra-shallow arsenic implants at high dose on silicon and cross-checked with medium energy ion scattering (MEIS) results. MEIS is of great value in ultra-shallow depth profiling of elements heavier than Si as it gives ultimate depth resolution (<1nm) and avoids typical SIMS problems (e.g. initial transient width and matrix effects)[125]. Given a proper calibration, quantification from first principles of the experimental results makes MEIS very useful to provide very accurate measurements. However, besides being relatively time consuming and requiring specific large-scale facilities, MEIS gives best results only for heavy elements in light matrix, and it offers much poorer detection limit than the ones typically achievable by SIMS.

The model was then applied to low temperature annealed (550°C) ULE implants. Results show that the concentration calibration can be reasonably adjusted and the usually reported 1-2 nm shift of profiles is corrected giving a good match between SIMS and MEIS to within 0.3 nm.

3.2 Experimental conditions and samples description

For this work, several different sets of ultra-shallow arsenic junctions were measured by Secondary Ion Mass Spectrometry. SIMS depth profiles were obtained with a Cameca Wf/Sc-Ultra instrument using a 300 eV impact energy Cs^+ primary ion beam at 45° incidence angle. Secondary ions signals were recorded for $^{28}Si_2^-$, $^{28}Si^{75}As^-$ and $^{18}O^-$ in high mass resolution (m/Δm =2500). This set of ion species was chosen for the As SIMS analysis in silicon because the relative sensitivity factor (RSF) change due to the high As concentration is lower compared to others [126].

All samples used to develop the model can be divided in 3 main groups. The main group consists of five samples prepared by implanting As^+ ions in (100) single crystal silicon wafers (only native SiO_2 on top). Five different implantation energies were used ranging from 0.5 to 5 keV; implantation was carried out at normal incidence with respect to the wafer surface and the nominal implanted As fluence was $1x10^{15}$ at/cm^2 for all these samples.

The second set of samples was prepared implanting As^+ ions in 3 (100) single crystal Si wafers with a nominally 11 nm thick SiO_2 film deposited on top. All the implants were carried out with a $7x10^{14}$ at/cm^2 nominal fluence. Implant energy was set to 3, 5 and 10 keV, respectively. These energies were chosen to obtain arsenic distributed differently with respect to SiO_2/Si interface for each one of the 3 wafers.

The third group included 6 arsenic implanted (100) silicon wafers with implant energy of 2 keV and 3 different doses from $1x10^{14}$, $5x10^{14}$, $1x10^{15}$ at/cm^2. The implantation was performed into crystalline (100) p-type silicon wafers and the same substrate submitted to a pre-amorphization implant (PAI). The PAI was performed with 5 keV Si^+ ions at a fluence of $1x10^{15}$ at/cm^2 which resulted in a 16 nm amorphous layer (a-layer) as measured by MEIS.

Two more samples were used for the determination of the sputtering rate. The first sample (Ref-B) was a boron delta doped Si multi-layer grown by reduced pressure chemical vapor deposition (RP-CVD) at a temperature of 725°C. The sample had been characterized by TEM and presented 5 pairs of 1 nm thick B deltas, each pair being separated by the other by 18.1 nm of Si [127]. The spacing's between B peaks were 1, 2, 3, 5 and 8 nm moving from the surface to the bulk of the sample. Being the first delta at 18.1 nm depth and thus beyond any transition effect, the distance between first and second delta pairs could be used for determination of absolute sputtering rate (SR) in silicon substrate. The second sample (Ref-A) was a 3kev arsenic ion implanted (100) silicon substrate with $1.25x10^{14}$ cm^{-2} fluence independently measured with other analytical techniques [128]. The sample was used as a reference material to obtain RSF for SIMS measurements of As in Si and it was routinely analyzed between measurements of unknown samples in order to control the stability of analytical conditions.

Most samples were also measured using Medium Energy Ion Spectroscopy. MEIS spectra were obtained using a 100 keV He^+ ion beam and the double alignment configuration, in which the channeling direction [-1,-1,1] was combined with the [1,1,1] blocking direction: these conditions make it possible to separate the of As and Si masses and provide excellent depth resolution better than a nanometer [129]. More details about MEIS analysis are reported in paragraph 2.3; the quantification procedure has been described in detail in [130].

A summary of samples characteristics is shown in the table 3.1, together with final values of SiO_2 thickness and retained fluence measured by SIMS and/or MEIS.

Table 3.1. Sample description and SIMS and MEIS measured arsenic fluencies. PAI indicates that implantation was made on pre-amorphized substrate. Ref-B Is the boron delta doped Si multi-layer grown by RP-CVD, containing 5 pairs of 1 nm thick B deltas, each pair being separated by the other by 18.1 nm of Si.

Sample name	Implantation energy, Kev	Arsenic total fluence (at/cm^2)			Oxide thickness, SIMS/MEIS, nm
		Nominal	SIMS	MEIS	
SH0	2	$1x10^{15}$	$0.99x10^{15}$	$1.00x10^{15}$	1.8/1.6
SH1	2	$1x10^{15}$	$0.98x10^{15}$	$0.97x10^{15}$	1.8/1.8
SH2	2	$1x10^{15}$	$1.04x10^{15}$	$1.05x10^{15}$	1.7/1.6
SH3	2	$1x10^{15}$	$1.03x10^{15}$	$0.97x10^{15}$	1.6/1.8
SH5	2	$1x10^{15}$	$1.02x10^{15}$	$1.02x10^{15}$	1.6/1.7
SO3	3	$7x10^{14}$	$6.65x10^{14}$	$7.04x10^{14}$	11.1/10.5
SO5	5	$7x10^{14}$	$6.97x10^{14}$	$7.04x10^{14}$	11.1/11.8
SO10	10	$7x10^{14}$	$7.41x10^{14}$	$5.88x10^{14}$	10.8/11.2
SL2	2	$1x10^{14}$	$1.04x10^{14}$	$1.04x10^{14}$	1.5/1.5
SM2	2	$5x10^{14}$	$4.91x10^{14}$	$5.16x10^{14}$	1.7/1.5
SH2	2	$1x10^{15}$	$1.05x10^{15}$	$1.04x10^{15}$	1.7/1.5
SL2-PAI	2	$1x10^{14}$	$1.02x10^{14}$	$1.35x10^{14}$	1.3/1.5
SM2-PAI	2	$5x10^{14}$	$5.04x10^{14}$	$4.90x10^{14}$	1.4/1.5
SH2-PAI	2	$1x10^{15}$	$1.02x10^{15}$	$1.03x10^{15}$	1.6/1.5
Ref-A	3	$1.25x10^{14}$	$1.25x10^{14}$	-	1.4/-
Ref-B	Boron delta doped silicon				

3.3 Normalization and analysis in oxide

SIMS analysis of ultra-shallow dopant distributions in silicon is affected by several artefacts (see section 2.2.6). Being such dopant distributions confined in the top few nm of the original Si substrate, an important fraction is contained in the initial transient width, i.e. the thickness of Si that has to be removed before a sputtering steady equilibrium is established. A further complication is due to the presence of native or induced SiO_2 layers at the surface and the related variation of sputtering and ion yield at the SiO_2/Si interface. Finally, the high dopant concentration usually required to maintain low values of sheet resistance means that the distributions are far from the dilute regime (concentration <1 %) and thus the dopant itself can affect ion and sputtering yield. Therefore, it is necessary to assess an analysis protocol able to deal with and reduce such artefacts in order to improve depth profile accuracy.

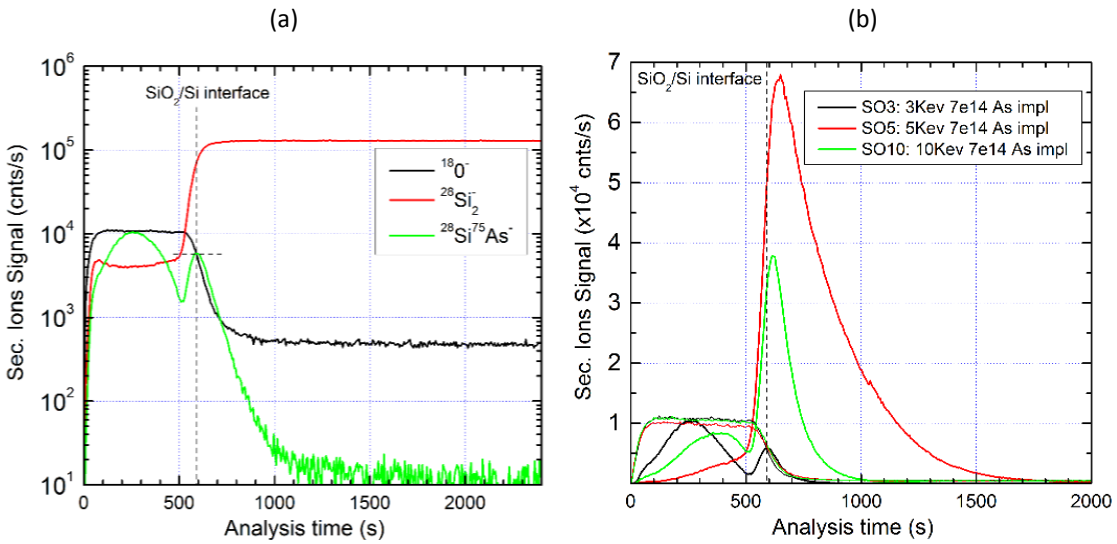

Figure 3.1. Secondary ion signals measured for SO3 sample (a). The arsenic ion signals in the samples implanted through 11 nm of oxide at different energies (b). The SiO_2/Si interface is set at half-maximum of oxygen signal.

An example of a 'raw' profile recorded by SIMS is shown in figure 3.1 (a). The sample was the SO3, As^+ 7x10^{14} at./cm^2 at 3 keV implant on the 11 nm SiO_2/Si stack. The sputtering was done using a 300 ev Cs^+ ion beam at 60° incidence angle with respect to the surface normal. At this low energy a first sputtering equilibrium was achieved within the 11 nm thick oxide layer, as can be deduced from the stability of the $^{18}O^-$ and $^{28}Si_2^-$ ion signals between 75 and 500 s analysis time. After this, at 500 s time the sputtering reached the SiO_2/Si interface and a new transient starts before a new equilibrium is reached in Si when the entire oxide layer has been sputtered away from the crater bottom. In principle both sputtering and ion yield vary in this interface region and the quantification of the profiles is not trivial due to the lack of sputtering equilibrium. The SIMS quantification protocol has to be able to deal with at least 3 regions for such system: oxide layer, interface region, silicon substrate.

The quantification of raw SIMS profiles starts with the common linear conversion from sputtering time to depth using a constant SR approach and from the $SiAs^-$ secondary ion intensity conversion to As concentration using the RSF and equation (2.6). Both SR and RSF are the ones appropriate for the quantification in silicon and they are determined from Ref-B and Ref-A, respectively. The main idea beyond the advanced quantitative approach is the use of different quantification parameters (SR and RSF) in different parts of sample, i.e. in SiO_2 region and in silicon bulk, respectively. The interface between these two regions was defined at the half-step value of the oxygen signal.

In order to build the protocol, at first two different methods of normalization for the calculation and application of the RSF were considered. In the first method, called *point-by-point normalization*, the RSF obtained from the standard is applied in every point of the recorded profile using the RSF equation:

$$C_{As} = RSF \frac{I_{As}}{I_{matrix}} \quad (3.1)$$

where C_{As} is the concentration of arsenic, I_{As} the intensity of As-based secondary ions (in this case $^{28}Si^{75}As^-$) and I_{matrix} is the intensity of matrix specie ions ($^{28}Si_2^-$) recorded at the same point/sputtering time as I_{As}. The second method is based on a *normalization to the average matrix signal*, i.e. I_{matrix} is not the value registered at each sputtering instant but an average of the same signal calculated after the sputtering equilibrium has been reached. In the first method, it is assumed that both I_{as} and I_{matrix} experience the same effects resulting from sputtering and ion yield variations. Since this is not immediately true, the second method can easily provide a different normalization to be tested where the idea is basically the opposite, i.e. that the I_{As} signal is independent by the artefacts due to the variations of sputtering and ion yield. In this second case, the counts-to-concentration conversion turns to the linear conversion of ion intensity to the element concentration. It is not possible to state which one of the two approaches is correct starting from first principles. In literature several experimental studies about As SIMS depth profiling using different normalization approaches are reported [124], [126] experimentally showing that the most accurate normalization method mainly depends on the choice of ion species for both matrix and analyte element. The choice of different normalization methods can be a first 'quick' solution to reduce near-surface artefacts such as initial transient or matrix effects due to presence of native oxide or high dopant concentration. However, the introduction of RSF and SR variation between oxide layer and silicon can improve the accuracy and makes the quantification protocol of more general application.

The two normalization methods were tested in order to define their ability to provide accurate quantitative results in the SiO_2/Si system. Samples SO3 , SO5, SO10 were considered for this purpose. The recorded raw ion signals (counts per second) are depicted in figure 3.1(b) for sample SO3. Preliminarily the sputtering rate (SR) and the RSF appropriate for silicon were obtained from the measurement of the references Ref-A and Ref-B. The SR for SiO_2 was obtained from analysis of various samples with SiO_2 thickness ranging from 2 to 12 nm. Successively, a parameter defining the ratio between the RSF value for the oxide region and the relative value in silicon was introduced. Total arsenic fluencies in the SO3, SO5, and SO10 samples were then calculated varying the RSF in SiO_2 (and consequently the RSF ratio) for both normalization methods. The results are reported in figure 3.2.

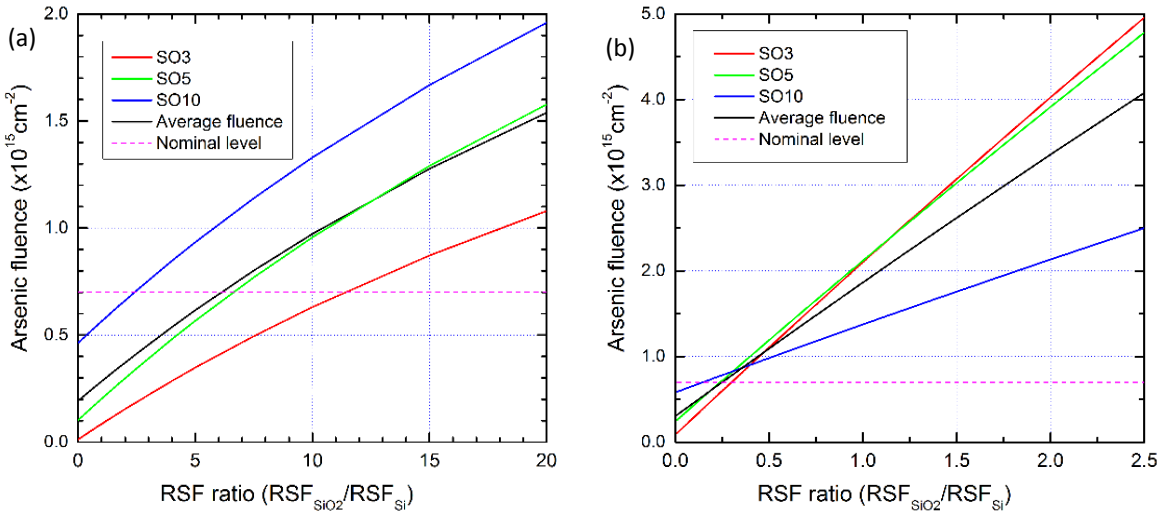

Figure 3.2. Dependence of the total arsenic fluence determined using different RSF ratios:
(a) - normalization to an average silicon signal, (b) - point-by-point normalization.

The nominal fluence of these samples is $7x10^{14}$ cm^{-2} as confirmed by INAA measurements: total measured fluence for SO3 sample was $7.08x10^{14}$. As seen in the figure 3.2 only point-by-point normalization (b) could provide a convergence to the same fluence value for all three measured samples for an RSF ratio value is close to 0.31. Furthermore, this 'convergent' fluence is very close to the nominal one, although there is some discrepancy about 25-30%. In case of normalization to an average silicon signal the intersection of these three curves occurs at negative values (without any physical meaning) making this choice of normalization not convenient. A complementary experiment was carried out using $^{75}As^-$ ion species instead of $^{28}Si^{75}As^-$ (not presented here) where the results was the opposite: it was impossible to obtain a convergent fluence value using point-by-point normalization whereas normalization to average matrix signal gives good quantitative results. Therefore, in case of $^{75}As^-$ monitoring the 'average' normalization has to be used

3.4 Behavior at the SiO_2/Si interface

Modeling a transition of SR and RSF values from oxide to silicon can be performed in a few different ways. The simplest one is to use a 'step-like' function centered at the depth of SiO_2/Si interface. It is important to remark that this approach makes sense and can provide accurate results as long as the difference between RSF values is not significant (less than a factor 10), otherwise the ionization and sputtering yield related interface effects cannot simply be managed in this way. In general, the ionization and sputtering yield behavior at the interfaces is rather complicated since the two are inter-dependent. In fact, when passing from SiO_2 to Si, for instance, sputtering yield varies since the surface composition progressively changes, being less the fraction of oxygen atoms. This sputtering modification affects also the retention of primary beam species (Cs^+ in this case) and the surface composition will further vary to a new value. This varied composition will define not only a different ion yield but also a different sputtering yield. This mutual variation will continue as long as a new sputtering equilibrium has not been reached,

i.e. when reaching bulk Si and a balance between retained and re-sputtered primary beam ions is established. Therefore, the use of empirically determined models able to describe the variation of SR and RSF at an interface can be a viable and easier approach to obtain accurate depth profiles. Their validation can be obtained through the comparison of the results with complimentary techniques able to provide accurate and independent results, without the need of the knowledge of the detailed mechanisms acting at the interface. A typical approach can be the use of some internal markers like a matrix species ion signals, e.g. oxygen or silicon-related ion species for SiO_2/Si, to describe the transition between two regions at an interface. In fact during SIMS analysis ionization efficiency is reported being proportional to the concentration of reactive atoms like oxygen of cesium in a power from 2 to 3 [131]. On the other hand, the equilibrium atomic density of oxygen or cesium is inversely proportional to sputtering yield in first approximation [132]. Therefore, in first approximation RSF (and thus SR) can be assumed proportional to an oxygen related signal like $^{16}O^-$ or $^{18}O^-$ recorded during analysis (in the power between 1 and 2). Furthermore, the assumption that RSF and SR vary proportionally to the oxygen signal showed very good experimental results for ULE SIMS in [125].

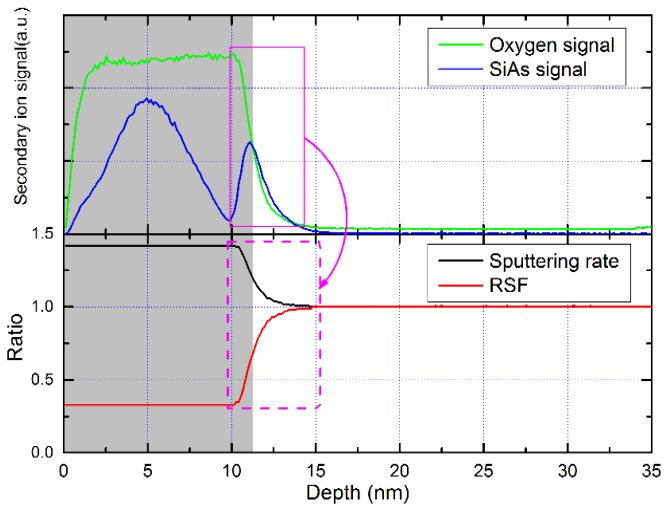

Figure 3.3. Sputtering rate (SR) and relative sensitivity factor in the sample SO3 as a ration between value in every point of profile and equilibrium ration in the silicon bulk.

Correction coefficients (for SR and RSF) are defined as the ratio between actual value of either SR or RSF and the respective equilibrium value in silicon bulk. For these analytical conditions (sputtering by 300 eV/ 45° Cs^+ beam, collecting $^{28}Si^{75}As^-$ and normalizing point-by-point) RSF in oxide is 0.31 times lower (obtained in section 3.3) and sputtering rate is 1.42 time higher (obtained from analysis of various samples with SiO_2 thickness ranging from 2 to 12 nm) than in silicon. The variation of the correction coefficients at the interface was assumed linearly proportional to the $^{18}O^-$ signal measured during analysis. The multiplicative correction coefficients of sputtering rate and RSF is shown in figure 3.3 for sample SO3 as example case. The values near the interface were calculated using the following equation:

$$\alpha = \frac{I^{18O} - I^{18O}_{min}}{I^{18O}_{max} - I^{18O}_{min}}(\alpha_{oxide} - 1) + 1 \qquad (3.2)$$

where α is either SR of RSF correction coefficient, I^{18O} the intensity of $^{18}O^-$ secondary ions, I_{max} and I_{min} correspond to the maximum or minimum $^{18}O^-$ signal values, α_{oxide} is the equilibrium value in SiO_2 layer.

Results of the application of this method for samples SO3, SO5, and SO10 are presented in figure 3.4. The SIMS profiles are compared to the As depth profiles as obtained from MEIS spectra. Unlike SIMS, MEIS can provide more accurate depth profiles since their quantification is obtained from first principles and it is not affected by matrix effects. In the first plot (a) the SIMS profiles were quantified using the common approach where single and constant SR and RSF values are applied after obtaining them of the Ref-A standard sample. As expected, this approach gives inaccurate depth profiles in both terms of arsenic distribution shape and total arsenic fluence. The total measured amount of arsenic exceeds $2x10^{15}$ at/cm^2, which is almost 3 times higher than nominal value. However, assuming the variation of SR and RSF as shown in figure 3.3, the differences between the profiles become much less evident (figure 3.3, b). The measured arsenic fluence for these profiles are 6.65, 6.97, and $7.41x10^{14}$ at/cm^2; the discrepancy of measured fluence from nominal value is less than 6%. However, even if the values obtained with the proposed corrections are closer to the nominal ones, there are still some artifacts near the oxide interface as revealed by the comparison with MEIS. For the 10 kev implanted sample where the As concentration at the interface is higher, the higher discrepancies are observed since the peak in the MEIS profile appears to be nearer to surface in comparison with SIMS (usually it is the opposite). The impact of this inaccuracy on arsenic shallow distributions is reinvestigated in the next section using arsenic shallow implants in Si.

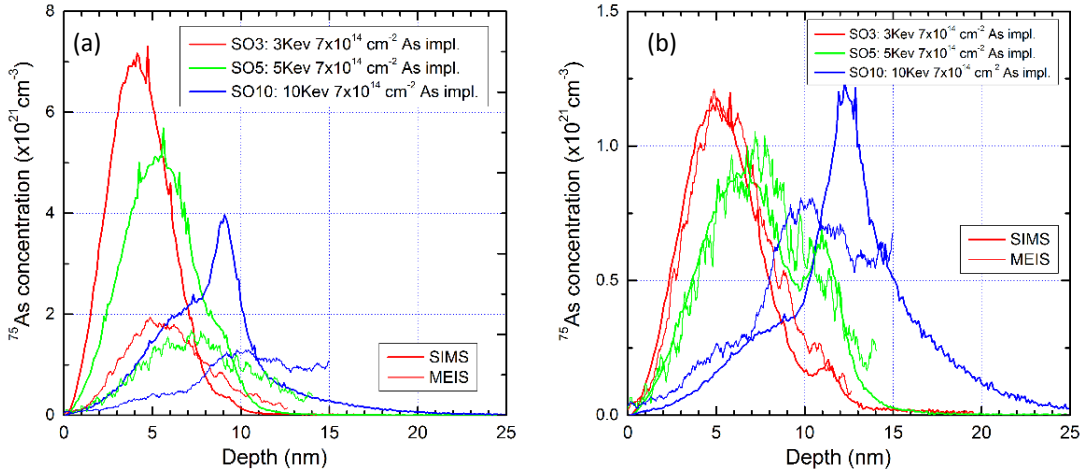

Figure 3.4. Comparison of MEIS depth profiles with SIMS result obtained using different quantitative approaches: (a) – using single SR and RSF obtained from Si standard sample; (b) – using different values in oxide and in silicon.

3.5 Initial transient and SiO_2/Si interface overlap

The difference between SIMS and MEIS results is very evident when the implanted dopant is distributed closer to the surface. Figure 3.5 (a, b, linear and logarithmic scales respectively) shows both SIMS and MEIS results of SH samples: silicon substrates implanted with $1x10^{15}$ at/cm^2 As fluence at energies ranging from 0.5 to 5 Kev. The SIMS profiles were obtained using the correction of sputtering rate and relative sensitive factor in oxide layer as described in the previous paragraph. Low energy implants show the highest discrepancy with MEIS results, whereas the 5 kev implanted sample SH5 is less affected by effects causing this difference. Moreover, most discrepancies are concentrated at ~2 nm depth where the SiO_2/Si nm interface is located according to the MEIS spectra (not shown).

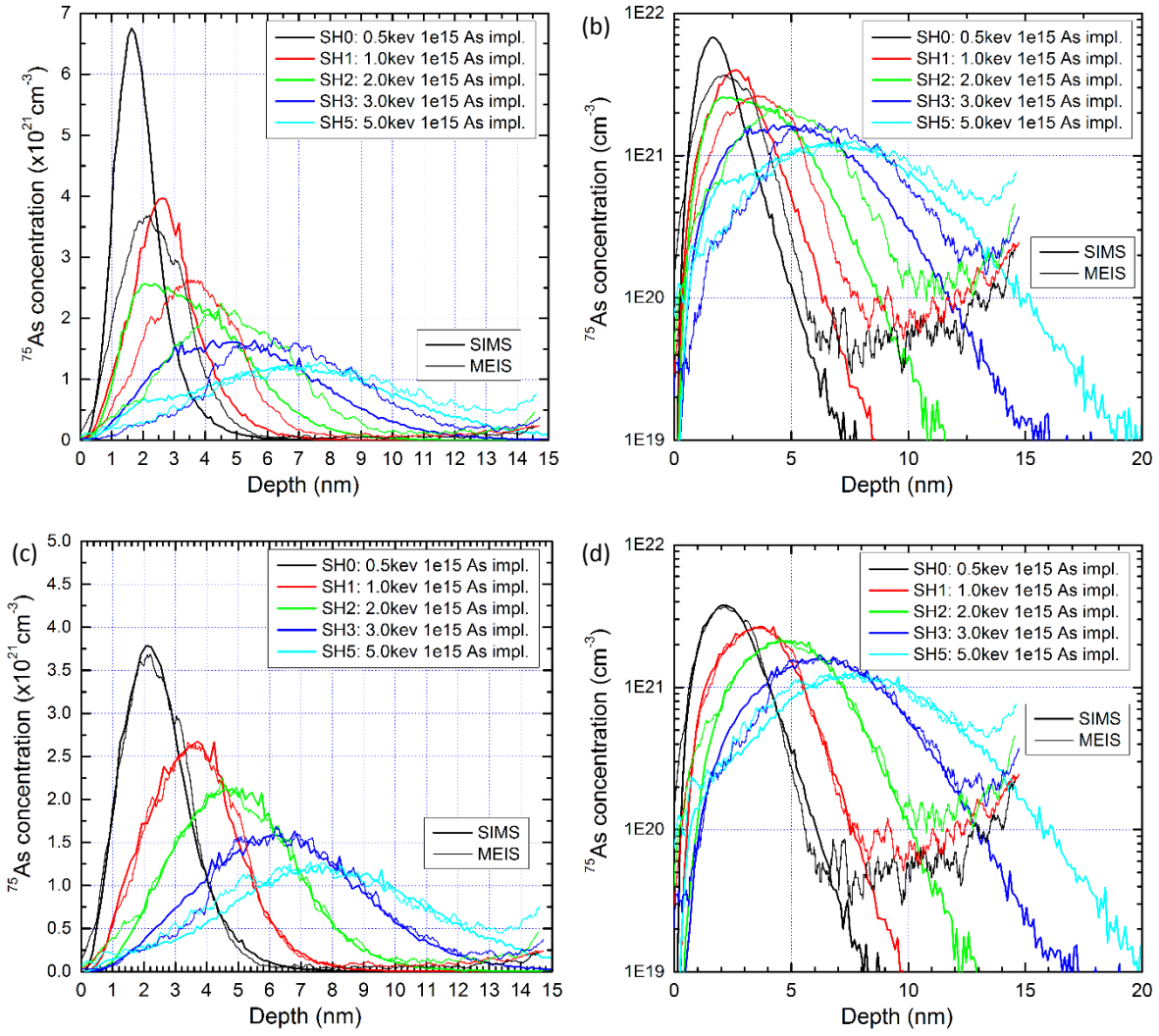

Figure 3.5. Comparison between SIMS (thick lines) and MEIS (thin lines) arsenic depth profiles of SH samples ($1x10^{15}$ at/cm^2, implantation energy from 0.5 to 5 Kev), where only SiO_2/Si correction is applied (a and b) and where SIMS was fitted to MEIS profiles changing SR and RSF in every point (c and d).

SIMS profiles obtained at ultra low energy are expected to be slightly shifted to the surface [123] when a sputtering rate is applied to convert sputtering time to depth. This is a direct consequence of a

faster erosion in the first stage of ion bombardment, i.e. before the steady sputtering equilibrium is established. Using a constant SR as the one determined by the final crater depth measured by a profilometer or from a delta doped reference as in this case, results in an underestimation of the depth scale in the first part of the profile (as described in the section 2.2.6.4). The scenario is here complicated by the fact that this initial transient sputtering yield overlaps with the thin native oxide and its interface with substrate. Therefore, the simple 2-layer model described in the previous section may reasonably need further correction to be able to cope with initial transients and thin oxide layers. An additional variation of sputtering rate was assumed and determined by fitting SIMS profiles to MEIS ones.

For the development of the model and the actual fitting, samples SH0 to SH5 were considered and an ad-hoc fitting procedure was applied. Let us consider a SIMS profile $C_j(t_j)$ where C_j are the concentration values derived using the RSF method, and t_j are the times of measurement. The depth is first calculated using the sputtering rate SR as derived from the standard sample measurement with the preliminary correction in the oxide as described above: depth $x_j = t_j \cdot SR \cdot \alpha_{oxide}$. For each point a correction factor α_j is applied to the sputtering rate with initial value of 1:

$$x_j = t_j \cdot SR \cdot \alpha_{oxide} \cdot \alpha_j \tag{3.3}$$

The fitting was performed minimizing an objective function that includes all the five profiles (i = 1..5 for samples SH0, SH1, SH2, SH3, SH5 respectively) as measured by SIMS and MEIS:

$$\delta = \sum_i \left(\int_0^{15nm} |C^i_{MEIS} - C^i_{SIMS}| dx \right); i = 1..5 \tag{3.4}$$

The C_{MEIS} values were obtained by linear interpolation of the original MEIS spectrum. The minimization was performed point by point starting from the surface by varying the initial α_j factor with decreasing step size (5%, 1%) constraining the α_j value in the range (0.1..3).

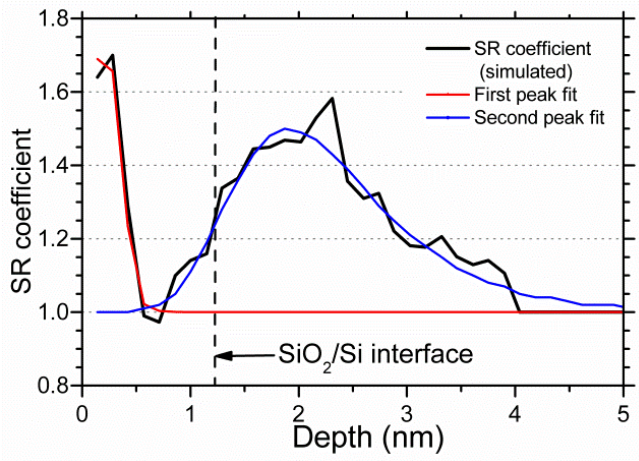

Figure 3.6. Sputtering rate (SR) correction coefficient obtained from fitting SIMS profiles of SH samples to MAIS. Two obtained peaks were fitted with nonlinear curves. SiO_2/Si interface position is defined at half maximum of oxide signal.

The correction coefficient α_j obtained by the fitting is shown in figure 3.6. The curve can be approximated well by the sum of two independent peaks: the first one is assumed to correspond to initial SR transient and the second to the transient between the SiO_2 layer and the Si substrate.

Both peaks of the SR coefficient were fitted with nonlinear analytical curves to allow their use into the quantification procedure. The fitting was done in OriginPro software (v9.0) [133] using the following nonlinear curves:

$$\alpha_1(x) = 1 + \frac{1}{a + (b \cdot (t \cdot SR))^c} \tag{3.5}$$

$$\alpha_2(x) = 1 + a \cdot e^{(-e^{-z}-z+1)}; z = \frac{(t - t_{ox}) \cdot SR - b}{c} \tag{3.6}$$

where t is the sputtering time, SR the sputtering rate in Si, t_{ox} the time correspondent to SiO_2/Si interface and x is the depth). The values of the coefficients obtained during the fitting are reported in the table 3.2 together with the standard error. The coefficient "b" in the second curve represent a shift of the peak from the position of the SiO_2\Si interface.

The result SIMS profiles after the fit to MEIS are shown in figure 3.5 (c, d). It is evident that the adopted model of SR correction can successfully eliminate difference between the two analytical techniques in terms of dopant distribution. The measured arsenic fluencies are reported earlier in the table 3.1: for all the samples measured As total fluence coincide with nominal within 4% difference.

Table 3.2. The value of coefficient determined from the fitting of the peaks using equation **(3.5**) and **(3.6**)

Coefficient	Value	Standard error
α_1 (first peak)		
a	1.424	0.028
b	2.688	0.248
c	6	0 (fixed)
α_2 (second peak)		
a	0.507	0.013
b	0.743	0.021
c	0.687	0.021

The complete model with the of SR and RSF coefficient derived for sample SO3 are shown in figure 3.7. Quantified profiles with the derived model for samples SO3, SO5 and SO10 are presented in figure 3.8 a (linear scale) and b (logarithmic scale) together with their corresponding MEIS profiles.

The SIMS profiles in the first 10 nm are fairly accurate in both depth and concentration, especially for the SO3 and SO5 with some remaining artifacts near the oxide interface causing a misalignment between the two techniques. The third sample, SO10, shows larger discrepancies due to a more pronounced shift. In this case however, a non-accurate MEIS calibration is supposed. In fact there is no physical reason for a SIMS misalignment in the bulk part of the 11 nm thick SiO_2 layer: it would make sense to have a sort of discontinuity of the concentration (or a steep gradient) in correspondence of the Si/SiO_2 interface at 11 nm and not within the SiO_2 layer. SIMS measurements carried out with different primary ion beam energies or recording different secondary ion species showed profiles similar to the reported.

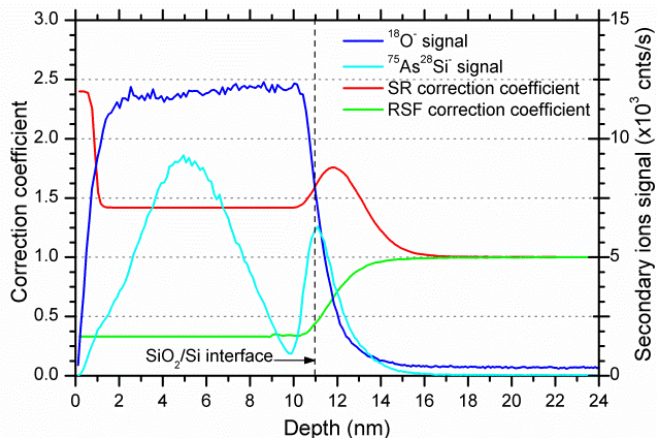

Figure 3.7. Sputtering rate and RSF behavior in the SO3 sample according to the proposed model. $^{18}O^-$ and $^{75}As^{28}Si^-$ ion signals refer to the right axis.

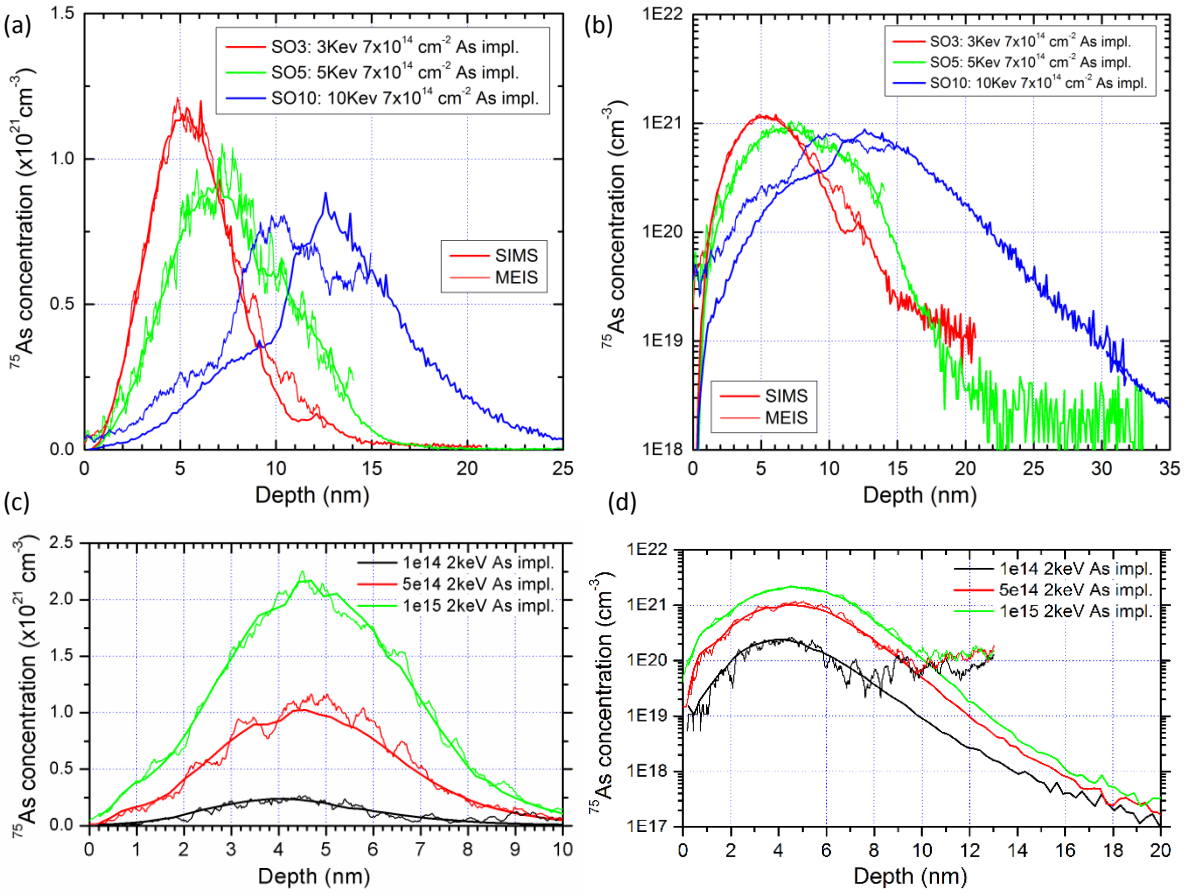

Figure 3.8. Comparison between SIMS (thick lines) and MEIS (thin lines) arsenic depth profiles of: samples with deposited 11 nm oxide layer (a, linear scale, and b, logarithmic scale); 2Kev arsenic implanted samples (c, linear scale, and d, logarithmic scale)

3.6 As fluence dependence

The proposed model was tested on two further low energy arsenic implants (2 kev) in crystalline silicon substrate with different nominal arsenic fluencies in order to evaluate its applicability to a wider range of As concentrations. Implanted fluencies were 1x10^{14}, 5x10^{14}at/cm^2 for SL2, SM2 samples, respectively. The SIMS profiles of the samples are shown in figure 3.8, c and d, reporting excellent agreement between the MEIS and SIMS techniques. The profile for sample SH2 already shown in figure 3.5

is also reported for completeness (2keV implants at different doses). The corrected SIMS profiles are able to provide the main information about the dopant distribution, projected range or a peak position with accuracy of MEIS technique and also provide excellent detection limit exceeding the MEIS on 2-3 orders of magnitude.

3.7 Conclusion

In this section a quantification model for ultra-low energy SIMS using a Cs^+ primary beam that takes into account initial transient width and Si/SiO_2 interfaces has been described. An empirically based quantification protocol allows the reduction of depth-profile distortions caused by matrix effects at the surface and related to presence of the SiO_2 layer.

Medium Energy Ion Scattering was used as reference technique due to its ability to provide depth resolution below 1nm, little or no matrix effects and quantification based on first principles. A set of arsenic implanted samples with different implantation energies (from 0.5 to 5Kev) was analyzed with both techniques. A simple correction of the analytical parameters in the oxide region assuming different sputtering rate and ion yield could not provide a satisfying agreement between these two techniques: SIMS profiles are narrower and shifted to the surface, as expected due to the initial transient sputtering yield, typically faster than the equilibrium value.

Aligning SIMS profiles to the MEIS ones revealed a pattern in the sputtering rate behavior during the SIMS analysis. Not only different values of sputtering rate and relative sensitivity factor for Si and SiO_2 had to be taken into account, but also additional peaks in the sputtering rate plot. The first peak is supposed to correspond to initial transient effect giving acceleration of sputtering in the first nm of material. The second peak is located in the interface between the silicon oxide layer and the silicon and appears due to a transition between the different matrices.

The depth profiles obtained with MEIS and SIMS corrected using proposed approach show almost identical distribution of arsenic in the samples and provide As total fluence close to the nominal in all measured cases but one.

The application of the described model is not limited to the reported combination of elements and the primary beam energy. In the model, the ion yield is subjected to minor corrections (assuming different RSF value in the oxide layer) and sputtering rate variation is due to interaction between the primary beam and the substrate; hence knowing the RSF value in SiO_2, the described model can be applied to depth profiling of any element in Si substrate without additional changes. Different Cs^+ primary beam energies have very similar behavior. For instance, the analysis with 500 eV impact energy shows the same behavior of the sputtering rate with the only difference in ratio between the values in oxide and in Si.

Chapter 4. Results I: Solid Phase Epitaxial Regrowth in Si

4.1 Overview and sample description

This chapter reports a study of the properties and the evolution of arsenic ion implants in silicon during low temperature (550°C) Solid Phase Epitaxial Regrowth (SPER). In the second part of this chapter a method of simulation of arsenic redistribution during SPER is derived.

Solid phase epitaxial regrowth corresponds to the epitaxial phenomenon occurring when an amorphous film is either deposited or created (e.g. by ion implantation) on a single crystal substrate. In this case, giving adequate energy like with a thermal treatment, the substrate can act like a seed for epitaxial re-growth and the amorphous film turns to crystalline typically at lower temperature than the one expected when no seeds are available [14], [134], [135]. In the case of silicon, SPER can occur at temperatures lower than 500°C with a re-crystallization rate thermally activated [14]. The phenomenon is particularly intriguing when impurity atoms like electrical dopant are present in the amorphous film. In fact, during the SPER process dopant atoms are incorporated in substitutional positions of the re-grown lattice, in most cases at concentrations higher than the expected equilibrium values [61], [136]. Furthermore, given the reduced thermal budget and the temperatures where Si SPER takes place, dopant diffusion is very limited [137]. This means that in principle SPER is expected to be a medium-low temperature process able to provide high level of dopant activation with reduced or absent diffusion, i.e. a process able to provide ultra-shallow junctions in Silicon.

However, several issues need to be addressed in order to integrate the SPER process in a semiconductor production flow. In particular, the metastable character of the high dopant activation can represent a problem of stability and electrical de-activation [61], [68], [138]. Furthermore, extended lattice defects (stacking faults, dislocation loops) can form at the original amorphous/ crystal interface, producing the so called end-of-range (EOR) defects [28]. The latter can affect the leakage current of p/n junctions or they can inject point defects upon successive thermal treatments inducing clustering of the dopant atoms or their transient enhanced diffusion (TED) [56], [89], [137].

Silicon wafers doped by As ion implantation and annealed by SPER were investigated in detail in the past [14], [61], [136] showing the possibility of achieving As solubility higher than equilibrium values. Lietoila *et al.* reported electrically active concentration up to $5x10^{20}$ cm^{-3} for a $6.2x10^{15}$ cm^{-2}/ 150 Kev As implant, annealed at 560°C for 4 minutes [62]. Higher values were reported from Narayan *et al.* [139] and more recently by Duffy *et al.*[136], i.e. $9x10^{21}$ cm^{-3} for $4x10^{16}$ cm^{-2}/ 30 Kev implant annealed at 700°C for 180 s, a value higher than the ones achievable on the same implant by either spike or laser millisecond annealing at 1300°C. However, the reported values refer to the substitutional As concentration as determined by Rutherford Backscattering Spectroscopy (RBS) channeling measurements. In fact, other

authors [62], [68], [138] reported a clear offset between the As substitutional fraction as determined by ion scattering techniques and the actual electrical activation fraction. Those observations are in agreement with the formation of As clusters with point defects and without strong displacements of As atoms from lattice positions. Clusters involving As atoms and vacancies (As_nV, n=1-4) or self-interstitials are thought to be responsible for this difference between metastable solid solubility and electrically active concentration [74], [77], [82]. The same clusters can also be responsible for the mechanism behind the progressive electrical de-activation of SPER As junctions observed when thermal treatment is prolonged beyond the time needed to complete the re-crystallization [61], [138] or when heating ramps are decreased increasing the thermal budget of the total SPER process [68]. Finally, clustering and precipitation mechanisms also explain the reduction of maximum active As concentrations observed when the implanted dose is higher than $1x10^{15}$ cm^{-2} for implant energies lower than 10 Kev [68], [140].

Another mechanism of active dopant loss during SPER is the observed pile-up of As atoms at the interface between native or induced surface SiO_2 and the re-grown Si lattice [141–143]. The As at the interface is segregated in disordered structures [144], [145] with As atoms not being in substitutional positions. The pile up seems to be the result of an As segregation at the moving amorphous/crystalline interface during the SPER process [137], [143], [146], when As atoms are 'snow-ploughed' by the SPER interface.

Most results reported in literature about SPER of As implanted Si refer to relatively thick amorphous layers and to relatively deep As distributions, i.e. where the effect of surface proximity is not relevant. In this study we focused our attention to the SPER process applied to ultra-shallow As implants (implant energy < 3 Kev) in Si aiming to investigate the possibility of creating junction depths lower than 20 nm with high levels of electrical activation. The experiment was also designed to understand the impact of the As concentration on the SPER mechanism. In fact, it is known that at moderate concentrations As enhances the SPER rate [147] whereas at concentrations higher than 1% the SPER process is delayed [148–150]. This As segregation at the SPER interface is another mechanism worth to be investigated.

For the SPER study two classes of samples were prepared. The first class was prepared using a p-type (100) Si substrate whereas in the second one similar substrates were subjected to a pre-amorphization implant (PAI) before As doping. PAI was carried out implanting 5 Kev Si^+ ions at a fluence of $1x10^{15}$ at/cm^2. This pre-amorphization process created a 16nm layer of amorphous silicon at the surface of the samples as measured by MEIS and Spectroscopic Ellipsometry. This amorphous layer was designed to ensure that the whole As distribution created by the successive implantation was confined within the amorphous Si. Both, PAI and non-treated, substrates were ion implanted with As^+ ions at 2 Kev with three different nominal fluencies: $1x10^{14}$ at/cm^2, $5x10^{14}$ at/cm^2 and $1x10^{15}$ at/cm^2. The chosen fluencies allowed studying the impact on electrical properties of the As concentration spanning over an order of magnitude.

It is worth noticing that even the lowest dose is expected to amorphise the non pre-amorphized Si substrate [130] allowing the mechanism of SPER. All implantations including amorphization with silicon were performed on an AMAT XR80 Quantum Leap Ion Implanter.

All the samples produced were processed with a rapid thermal annealing at 550°C for durations of 5 up to 300 seconds under a controlled laminar flow of a nitrogen-oxygen mixture (95%/5%). The use of a small amount of oxygen in the annealing atmosphere prevents out-diffusion of arsenic during annealing [142]. The relatively low annealing temperatures and times were chosen to monitor different levels of damage recovery and resulting As distributions, whilst avoiding relevant thermal diffusion of the dopant. The annealing was performed in RTP annealer "AnnealSYS" halogen lamp system by AS-Micro at FBK. The RTP process allowed reaching the 550°C with an extremely high ramp up rate (about 100°C/s), in order to ensure that the main effects responsible for the As behavior can be assigned to the dwell temperature and not to the thermal budget applied during the heating and cooling phases of the treatment The annealer chamber has a 1.5" silicon wafer as a sample holder with a thermocouple placed on the bottom of the wafer in central position. The wafer is located in the middle of a cylindrical chamber with 8 halogen lamps placed around the periphery. Although this tool allows well-controlled heating with an average ramp-up rate of 100°C/s, an additional pre-heating step to stabilize the system at 200°C was implemented to improve reproducibility before the main treatment at 550°C was carried out. Table 4.1 summarizes all samples used in the study:

Table 4.1. Samples used for SPER study characterized by SIMS and MEIS. PAI means pre-amorphization with Si ions. Annealing temperature is 550°C for all samples.

Sample name	Implantation energy	Nominal fluence (at/cm^2)	Annealing time, s
SL	2 keV	1x10^{14}	0, 5, 10, 60 or 300
SM	2 keV	5x10^{14}	0, 5, 10, 60 or 300
SH	2 keV	1x10^{15}	0, 5, 10, 60 or 300
SL-PAI	2 keV	1x10^{14}	0, 10, 30, 60 or 300
SM-PAI	2 keV	5x10^{14}	0, 10, 30, 60 or 300
SH-PAI	2 keV	1x10^{15}	0, 10, 30, 60 or 300
R-1	3 keV	1.25x10^{14}	0
R-2	3 keV	7x10^{14}	0

At this low temperature the regrowth rate is quite high in comparison to the mobility of arsenic atoms in the layer, hence arsenic atom diffusion should be inhibited (i.e. arsenic atoms are expected to be immobile during SPER), thus all the effects of dopant redistribution should be caused by the crystallization process.

4.2 SIMS analysis of samples evolution

The thermal treatment at 550°C induces a progressive regrowth of the amorphous layer (a-layer) in all the samples. The arsenic depth distribution was monitored using Secondary Ion Mass Spectroscopy (SIMS) after different annealing times.

SIMS depth profiles were obtained with a Cameca Wf/Sc-Ultra instrument using 300 eV Cs^+ primary ion beam at 45° incident angle. Secondary ions signal were recorded for $^{30}Si^-$, $^{28}Si^{75}As^-$ and $^{18}O^-$ species in high mass resolution (Δm/m=2500).

All measured arsenic profiles are depicted in figure 4.2. Every As quantified profile is reported together with raw oxygen ($^{18}O^-$) and silicon ($^{30}Si^-$) profiles (thin lines of the same color) referring to the right axis. Oxygen profiles reveal very similar thickness of the oxide layer for all the annealed and not annealed samples. Equilibrium values of silicon and oxygen may vary due to some fluctuation of experimental conditions like pressure or quality of the beam. This fact is not related to the absolute arsenic concentration because this variation was taken into account during the quantification process.

The presence of a thin silicon oxide top film and the shallow distributions of As can induce problems in the quantification of the raw SIMS profiles due to variations of sputtering and ion yield expected for As ions when passing from SiO_2 to Si. Therefore these samples were schematized as a SiO_2/ Si double–layer structure and initially an accurate quantification procedure was defined for both silicon and oxide: the sputtering rate (SR) and relative sensitivity factor (RFS) in silicon were determined from measurements of the reference silicon material implanted with $1.25x10^{14}$ at/cm^2 arsenic at 5 Kev (sample code R-1 in Table 4.1). SR and RSF for silicon oxide were determined from another reference sample (R-2) where an arsenic ion implant of $7x10^{14}$ at/cm^2 total fluence was made through 11 nm of SiO_2 deposited on top of a (100) silicon single crystal wafer. The two reference samples allow defining SR and RSF ratios for oxide and silicon for every measurement session. The obtained ratios can then be applied according to the quantification procedure described in chapter 3. The stability of every SIMS session was monitored measuring SR and RSF from the R-1 sample every four or five measurements. The obtained values were used to linearly extrapolate the SR and RSF for all samples measured in-between thus giving more accurate values for quantification. More details about the SIMS measurements are reported in chapter 2.2 and the advanced quantification protocol is described in chapter 3.

All measured SIMS profiles show that total fluence corresponds to the nominal value within the uncertainty margin and the arsenic mean projected range (R_p) is ~5nm. Actually, no PAI low fluence sample (SL, $1x10^{14}$ cm^{-2}) shows a shallower R_p as formerly reported by Werner [130] and Van den Berg [143] for 2.5 keV implants. Werner observed that for increasing As implanted fluence (from $3x10^{13}$ to $1.8x10^{15}$ cm^{-2}), the R_p progressively shifts towards deeper values and reaches a saturation position at 5.5

nm for doses ≥ $4x10^{14}$ cm^{-2}, i.e. after the amorphization of the Si lattice has been clearly achieved. The phenomenon was interpreted like an easier accommodation of the impinging As ions in an amorphous matrix instead of that of a crystalline substrate. Since amorphization starts from a thin layer at the SiO_2/Si interface and then progressively grows in thickness, arsenic atoms would be preferentially stopped in the region closer to the surface. Once the amorphous thickness has reached a relatively stable value of 10 nm for a $1x10^{15}$ cm^{-2} fluence, the development of the As distribution proceeds with a constant R_p of 5.5 nm. In our SL sample, the $1x10^{14}$ cm^{-2} is just at the threshold value for amorphization and thus is still evident in the shallower As distribution whereas at higher values the R_p's converge to the expected value.

With reference to those observations, it is interesting to look at the 'as implanted' distributions of PAI samples where As ions were implanted in an amorphous matrix (figure 4.1). As expected, the phenomenon described above is less evident and the R_p is closer to the 'equilibrium' value of 5 nm. However, the PAI As distributions are, surprisingly, wider in the high concentration region compared to the non-PAI ones, especially between surface and R_p. Furthermore, an As segregation at the SiO_2/Si interface seems to be present in SL-PAI and SM-PAI samples, not observed in non-PAI samples and less evident in the high fluence samples, where actually PAI and non-PAI distributions converge to the same shape. This behavior can be interpreted by a similar hypothesis like presented in [130], [151], i.e. the easier allocation of As atoms in the amorphous layer under ion irradiation or even a radiation enhanced diffusion of As in the amorphous matrix. If the latter is true, As atoms would move in the amorphous layer under ion implantation ending at the SiO_2/Si interface acting as a sink for dopant atoms. A similar paradox of PAI As distributions wider than the non-PAI ones was reported by Werner in Figure 3 of his paper [130]. Although no previous evidences of a radiation enhanced diffusion of As in amorphous silicon have been claimed, high diffusivity of As in a-Si has been reported for high As concentration [152].

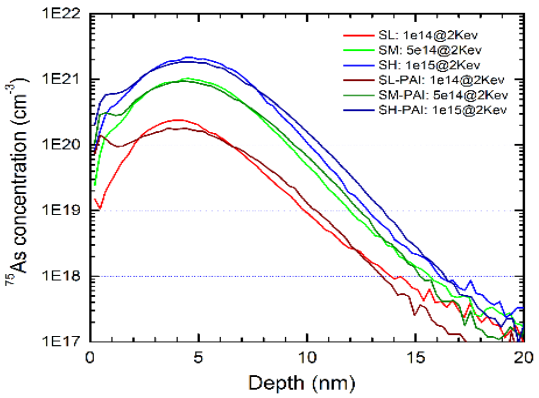

Figure 4.1. Comparison of arsenic distribution in the "as implanted" pre-amorphized and not pre-amorphized samples.

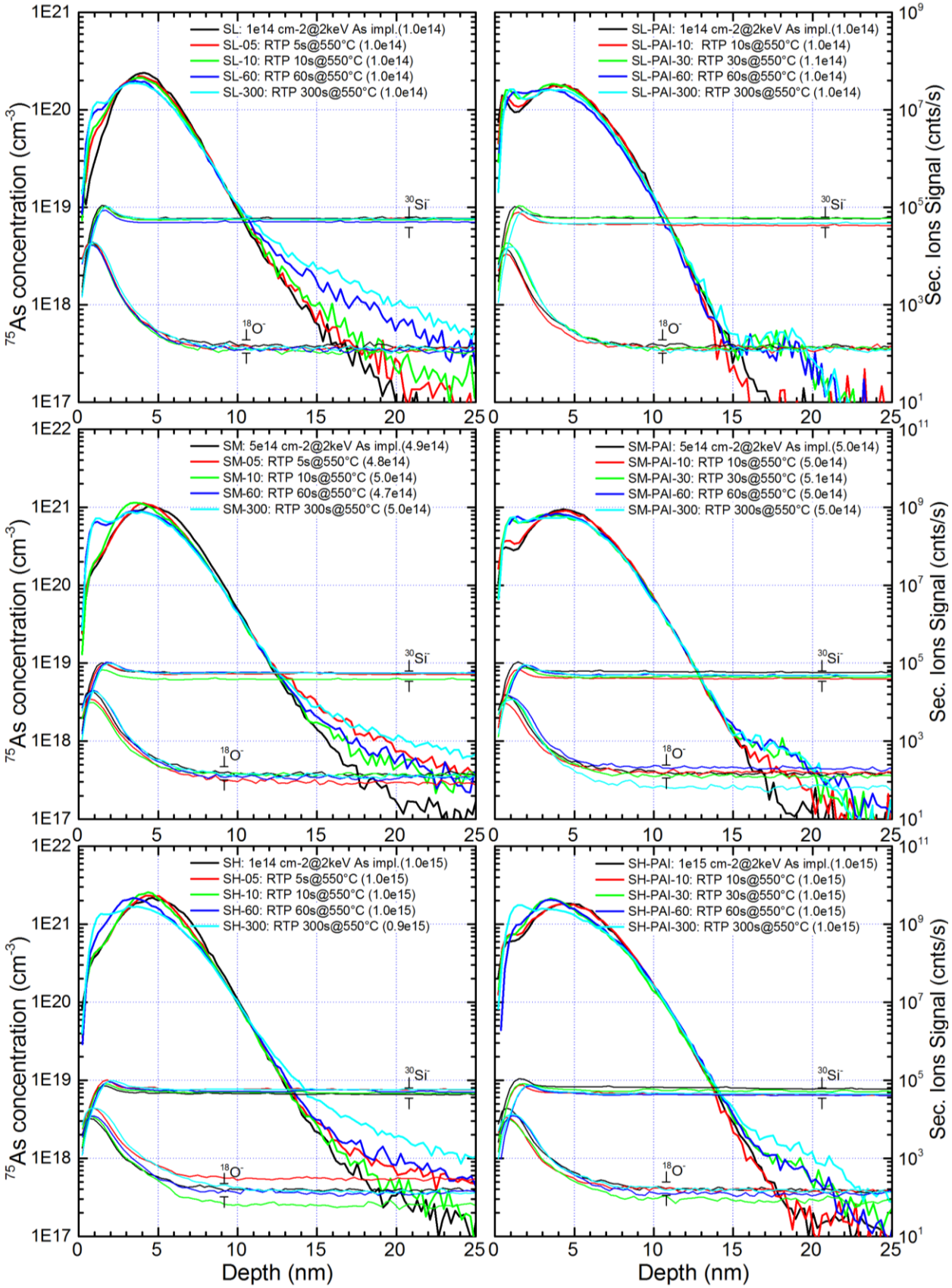

Figure 4.2. SIMS profiles of the samples after different SPER annealing times. Implantation fluence: $1x10^{14}$ at/cm^2 (top row), $5x10^{14}$ at/cm^2 (middle row), $1x10^{15}$ at/cm^2 (bottom row). Left column corresponds to samples implanted into crystalline substrate, right column to pre-amorphized (PAI) series. Silicon and oxygen raw signals (ion counts per seconds) refer to the right axis.

Although the annealing temperature was rather low, RTP annealing causes small arsenic diffusion for annealing times longer than 60s and only for As concentration lower than 10^{19} cm^{-3} for all not pre-amorphized samples (figure 4.2, left column). PAI samples (figure 4.2, right column) present accumulations of As at 18-20 nm depth, i.e. just below the original amorphous/crystalline interface as determined by MEIS (see next sections). This As accumulations indicate that in this case dopant atoms are driven to and segregated at the EOR defects expected to form below the re-crystallized layer.

Except for this small As diffusion in depth, annealing under the given conditions promote the arsenic redistribution from the peak towards the surface. This effect is more evident on a linear scale (e.g. Figure 4.3 shows the arsenic re-distribution in the sample implanted with 1x10^{15} As^+/cm^2 for different annealing times). This redistribution is due to the dopant is "swept" by the moving amorphous/crystalline interface since the observed As peaks corresponds to the a/c interface as reported in detail in section 4.5, or previously by other authors [138], [143], [146].

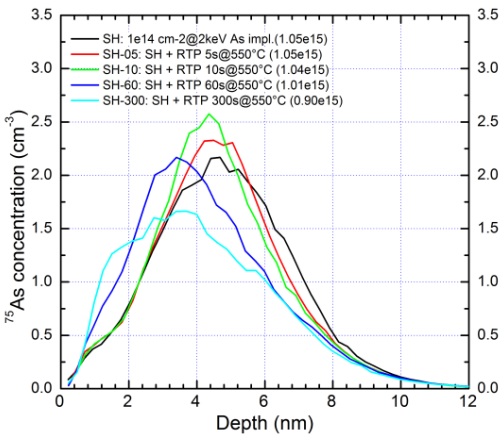

Figure 4.3. As distribution in high dose sample set (As fluence 1x10^{15} cm^{-2}) after different time SPER at 550°C.

Finally, according to SIMS measurements the total amount of arsenic in all samples is constant upon SPER annealing indicating that dopant out-diffusion is prevented by the native oxide layer. Instead of diffusing out, redistributed arsenic is segregated in a pile up at the SiO_2/Si interface. This effect is real and not an artifact of the SIMS measurements: it was previously reported in literature [129], [142] and successfully predicted by a simple simulation [153].

4.3 Electrical measurements and active arsenic model

Sheet resistance (Rs) values were obtained using four probe measurements for the samples annealed at 60 and 300 seconds, i.e. where the amorphous layer is expected to be completely re-crystallized and a higher electrical activation is expected. To prevent tip penetration typical of conventional four point probe systems, aluminum rectangular contacts (6x0.18 mm^2) were deposited and patterned through photolithography and chemical etching. The value of the electrode spacing was 600 µm. A schematic of the aluminum electrodes on the sample surface is shown in the figure 4.4, a.

By applying a current *I* between the two most external contacts and measuring a voltage V on the two internal contacts, resistivity of the sample can be calculated according to Ohm's second law using the following equation:

$$\rho = \frac{V}{I}\frac{tl}{d} \tag{4.1}$$

where *t* is thickness of the active layer in sample, *l* is the length of the contact pad (6mm), and *d* is the distance between contacts (0.6mm). The sheet resistance is defined as:

$$\rho_s = \frac{\rho}{t} = \frac{V}{I}\frac{l}{d} \tag{4.2}$$

When the Arsenic density is significantly higher than the density of the wafers acceptors we can simplify the expression for carrier mobility in a semiconductor (considering contribution of electrons only) [117]:

$$\rho_s = \frac{1}{q\int_t^0 \mu_n(n(x))n(x)dx} \tag{4.3}$$

where q is the charge of an electron μ_n is the electron mobility depending on n(x), the carrier concentration. Arsenic concentration dependence of mobility in silicon is a well-known function [154]:

$$\mu_n = \mu_0 + \frac{\mu_{max} - \mu_0}{1 + (n/C_r)^a} + \frac{\mu_1}{1 + (C_s/n)^b} \tag{4.4}$$

This expression was obtained by computer fitting of experimental data. Using different constant values of μ_{max}, μ_0, μ_1, C_r, C_s, a, and b, this expression can be applied to the μ_n versus concentration dependence for boron, phosphorus and arsenic [154]. In a more recent work [155] these constants were defined in a more accurate way using a fitting with more recent experimental results [156]. Furthermore, this model was extended introducing the effects of dopant-induced strain; however, within this thesis strain dependence was not taken into account.

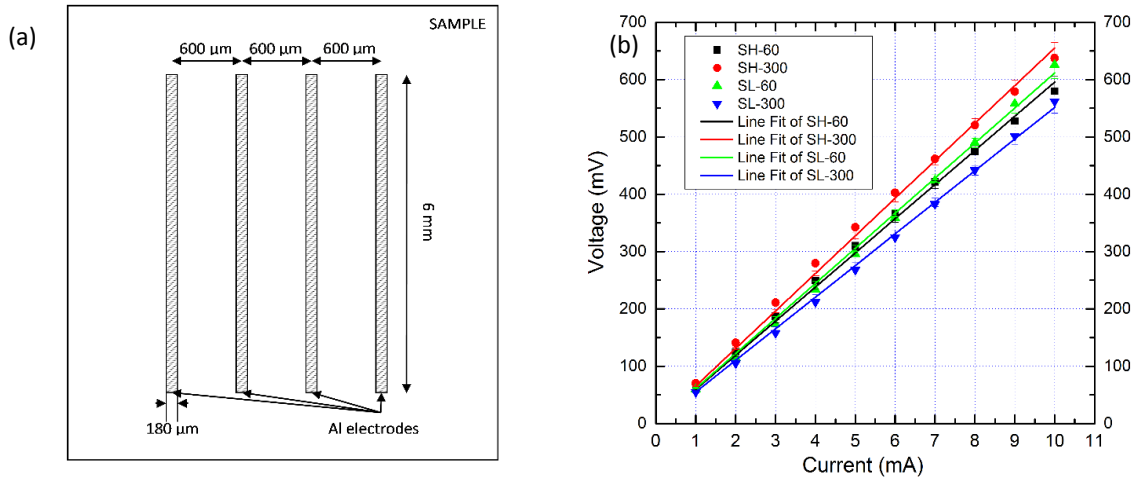

Figure 4.4. (a) Schematic representation of the sample with 4 deposited contacts
(b)V-I measurements for samples SL and SH annealed 60 and 300 seconds at 550°C.

In order to obtain the most accurate values for V/I several measurements were conducted for every sample varying the current and the obtained values were fitted using a linear equation. An example

of measured curves is shown in figure 4.4 plotting I *versus* V; resistance values (V/I) for all measured samples are reported later in table 4.2.

Values of carrier mobility μ_n and carrier concentration n_a within the ultra-shallow junction can be an indication of successful dopant activation after thermal treatment. These values can be calculated starting from the results of the four point probe measurements using equation (4.3) and assuming that μ_n and n_a are constant. However, this is a first approximation since carrier mobility depends on carrier concentration as reported before. Using equation (4.4) and the dopant concentration obtained by SIMS (figure 4.2) one can build an electron mobility curve for the doped region assuming that every As atom contributes with one free electron available for conduction, figure 4.5 black line.

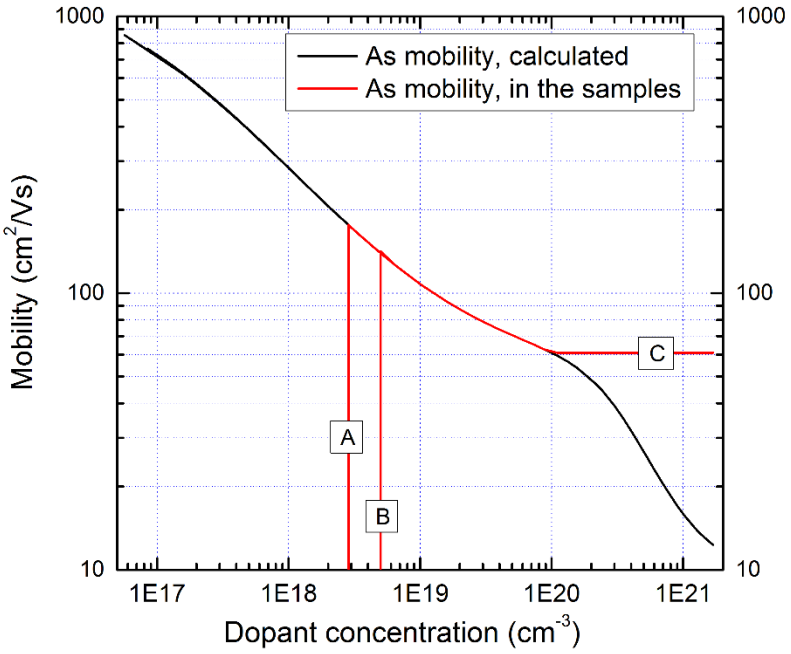

Figure 4.5. Electron mobility versus carrier concentration in As-doped silicon. Region A on the red curve indicates an absence of active dopants out of the junction depth (pre-amorphized region); B corresponds to a concentration of $5x10^{18}$ cm^{-3}. The region C corresponds to the arsenic solid solubility concentration at the SPER temperature.

The model of arsenic activation/deactivation behavior in ultra-shallow samples used in this work was proposed by Martinez-Limia et al. in [157]. According to this model arsenic atoms are present in 3 main forms after activation, as illustrated in figure 4.6. Up to the concentration value βC^{sol}_{As+} arsenic atoms are ionized as As^+, dissolved in Si and placed exactly in substitutional position surrounded by four Si atoms. This concentration value can be even higher than the active solubility concentration C^{sol}_{As+} which is the limiting value for equilibrium conditions (on the plot this concentration is shown as $\beta \cdot C^{sol}_{As+}$, where $\beta \geq 1$). We will use the designation C_{act} in the following. When the As concentration exceeds this value, dopant atoms are assumed to be forming clusters (like As_nV clusters) de-activating As atoms. This clustering occurs up to an As concentration exceeding the solid solubility concentration $C^{sol}_{As,tot}$ by factor of $\alpha \geq 1$.

Beyond this concentration value As atoms are expected to form SiAs precipitates as predicted from phase diagrams [79]. The values of the active solubility concentration C_{As+}^{sol} and the solid solubility concentration $C_{As,tot}^{sol}$ depend on the temperature at which thermal treatments are carried out and in the original work they were obtained through calibration against experimental data.

Arsenic activation after SPER is expected to be significantly higher than the equilibrium activation at the same temperature. Therefore, only As atoms placed in the re-crystallized amorphous layer can be assumed as electrically active and one can neglect the portion of the As distribution beyond the recrystallized region, i.e. the part deeper than the original amorphous/crystalline interface. The position of the interface before and after SPER using different times was measured using MEIS and are reported in the next paragraph.

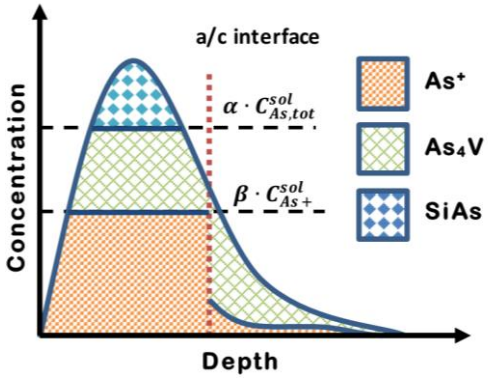

Figure 4.6. Assumed state after solid phase epitaxy according to [157]. The vertical doted indicates an initial position of amorphous/crystalline interface

To build a model to determine the active As concentration we assume that the carrier concentration n(x) in (4.3) corresponds to the concentration of substitutional As (in the above described model $\beta \cdot C_{As+}^{sol}$). Rewriting (4.3) according to the model:

$$\rho_s = \frac{1}{q \int_t^{t_{ox}} \mu_n\big(n(x)\big) n_a(x) dx} \tag{4.5}$$

where n_a is the concentration of arsenic as measured by SIMS, but limited to a maximum level given by the active solubility concentration:

$$n_a(x) = \max(n(x), C_{act}) \tag{4.6}$$

As mentioned earlier, all measured samples showed a thin native oxide already formed before annealing. Although the thickness of the SiO_2 layers is within 2 nm for all measured samples, arsenic in this layer or at the SiO_2/Si interface is expected to be not substitutional [141], [145] and thus it should be excluded from the integration range. The position of the SiO_2/Si interface (t_{ox}) for the integral calculation in (4.5) was determined using half the height of the $^{18}O^-$ secondary ion signal (more details in chapter 3).

Using the measured resistivity values, the active arsenic concentration can be calculated substituting mobility and active concentration from the equations (4.4) and (4.6) into (4.5):

$$\rho_s = \frac{1}{q \int_t^{t_{ox}} \left(\mu_0 + \frac{\mu_{max} - \mu_0}{1 + (n/C_r)^a} + \frac{\mu_1}{1 + (C_s/n)^b}\right) \cdot \max(n(x), C_{act}) dx} \tag{4.7}$$

The following values of the parameters were used: μ_0 = 52.2 cm^2/Vs, μ_{max} = 1417 cm^2/Vs, μ_1 = 43.4 cm^2/Vs, C_r = 9.68x10^{16} cm^{-3}, C_s = 3.43x10^{20} cm^{-3}, a = 0.68, b = 2.0 as reported in [155].

In the formula for the sheet resistance evaluation (4.7) the only unknown parameter is the active level of arsenic C_{act}. Values for this term for the samples were numerically determined solving equation (4.7) in the following way. First, the C_{act} was set to the maximum arsenic concentration and the right part of (4.7) was calculated using this value. After that, if the sheet resistance was different from the measured value by more than 0.01%, the active arsenic concentration was decreased by a factor of ρ_s/ρ_s^*, where ρ_s^* was the calculated value. Since this ratio is less or equal to unity, the described approach typically allows finding solutions in less than 20 steps. All these calculations were implemented in the software for advanced SIMS computation as subroutine and thus it can exploit most of the parameters used for SIMS data quantification (including the oxide interface position). An example of the applied model is depicted in figure 4.7 for sample SH-PAI annealed for 60 s. This sample shows a very high activation level resulting in a ~60% active dose fraction, the latter being the ratio between active and retained As doses.

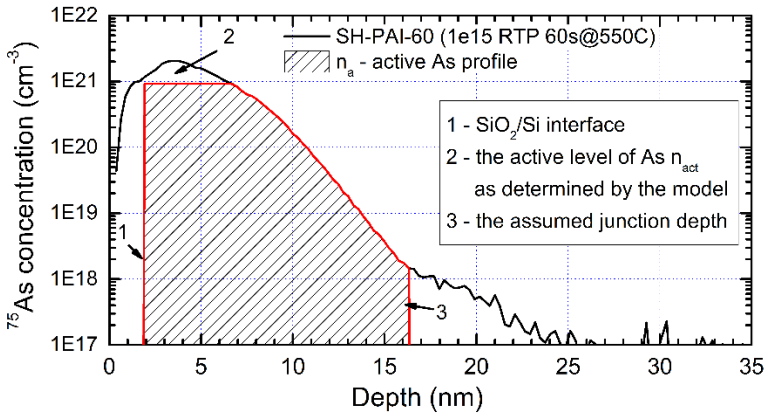

Figure 4.7. Evaluation of the active arsenic distribution from the SIMS profile and Rs value for PAI 1x10^{15} at/cm^2 sample as obtained from the model described in the text.

The results of the calculations are expressed in terms of active dose fraction (ratio between active As and retained dose) and As active level and reported in table 4.2 together with the values obtained from four point probe measurements. The mobility values are reported as obtained from equation (4.3) assuming that the mobility is a constant for all arsenic distributions. Although this approach is not entirely correct, it allows comparing the activation reported by different measurements in literature. These values of the mobility may appear rather low, but considering the very high values of carrier concentration for these junctions (>10^{21} cm^{-3}) they are in excellent agreement with the ones reported in [117], [158] (around 30 cm^2/Vs). The differences between the results of the two studies are most likely due to differences in implantation energies and annealing conditions.

The results for the lowest implanted fluencies reveal an extremely low level of active fraction. This finding is somehow surprising and could point to some limitations for the used approach's ability of

measuring such low concentrations. For all other samples, the implants performed using PAI substrates resulted in a final activation level higher than the one observed for samples implanted using non-PAI substrates, with level of electrically active dopant expected higher than the equilibrium value but lower than $1x10^{20}$ for temperatures lower than 700°C [61]. However, when annealing is carried out for 300 s, all the samples undergo a de-activation probably due to the formation of As clusters with point defects like vacancies or self-interstitials [159]. The deactivation is more evident for pre-amorphized samples. Finally, the active fractions of PAI samples are generally higher for the medium dose implants when compared to the highest dose. In the latter case, the higher As concentration can be considered as an enhancing factor for clustering and consequent de-activation.

Table 4.2. The result of calculation and electrical measurements after solid phase epitaxy.

Sample name	Junction depth, (meas.), nm	Mobility, (meas.), cm^2V/s	Sheet resistance (meas.), Ω/□	Active As conc. (est.), at/cm^3	Active dose (est.), %
SL-60	5.6	8.73	6117	$3.60x10^{19}$	14.4
SL-300	5.6	10.40	5515	$4.24x10^{19}$	16.5
SM-60	7.8	13.73	921	$2.66x10^{20}$	33.9
SM-300	7.8	16.23	953	$2.19x10^{20}$	29.7
SH-60	8.6	10.49	596	$1.01x10^{21}$	60.1
SH-300	8.6	8.98	655	$7.66x10^{20}$	50.2
SL-PAI-60	16.2	10.78	4110	$1.70x10^{19}$	15.7
SL-PAI-300	16.2	11.97	4244	$1.51x10^{19}$	14.2
SM-PAI-60	16.2	19.40	576	$6.23x10^{20}$	79.4
SM-PAI-300	16.2	18.33	646	$3.37x10^{20}$	49.3
SH-PAI-60	16.2	13.12	476	$9.15x10^{20}$	60.7
SH-PAI-300	16.2	11.07	523	$4.26x10^{20}$	41.5

4.4 Comparison with MEIS

Medium energy ion scattering (MEIS) is a complementary technique to SIMS that is able to provide important information about dopant distribution and disorder in the silicon lattice. MEIS analysis was performed at STFC Daresbury Laboratory (UK) using a 100 keV He+ ion beam and the double alignment configuration, in which the [-1,-1, 1] channeling direction was combined with the [1, 1, 1] blocking direction: these conditions make it possible to separate the masses of As and Si and provide an excellent depth resolution (less than a nanometer [129]). Analytical conditions for MEIS are reported in detail in section 2.3.3.

4.4.1 Fluence dependence

SIMS and MEIS profiles of as implanted samples are given in figure 4.8. Samples implanted into the crystalline substrate show remarkable agreement between SIMS and MEIS. Dashed lines represent profiles predicted by computer simulation of the ion implantation process made by the SRIM-2010

software [5]. In the simulation the implantation was performed through a 2 nm thick oxide layer on top of the silicon substrate. Both SIMS and MEIS show some discrepancy with the SRIM simulation, especially in the initial region. This might be a problem of the simulation since SRIM essentially calculates a 'no-dose' implant, i.e. it does not consider the progressive variation of composition with increasing fluence and thus the variation of the stopping power of the implanted matrix. At high concentrations, since arsenic atoms are much heavier than silicon atoms, the distribution projected range is expected to shift closer to the surface. SIMS corrections applied to the profiles (see Chapter 3) show reasonable results for all concentrations and are consistent with the MEIS results.

However, a difference between the SIMS and MEIS results was observed for the samples where arsenic was implanted into pre-amorphized silicon (figure 4.9). The deviation from a Gaussian distribution registered by MEIS is more evident and with arsenic segregation peak at the interface with oxide layer of higher amplitude.

On the top part of the figures the disordered silicon signal is shown. The random Si levels (at $5x10^{22}$ cm^{-3} at the Si edge) in figure 4.9 are within ~3%, showing good reproducibility of the MEIS spectra for different samples. The PAI implant causes the Si to become amorphized/highly disordered to a depth of 16.2 $\pm$1 nm. Arsenic self-amorphization causes a different thickness of the disordered Si layer depending on the implanted dose. The thickness was measured at 50% level of the Si signal and reported in table 4.2. In additional these values were confirmed using spectroscopic ellipsometry measurements.

The As total fluence as measured by both techniques is reported in table 4.3. For both SH and SH-PAI samples, the measured fluence is within 3% of the nominal value. The measured arsenic dose for the $1x10^{14}$ PAI implant is quite high (obtained by MEIS); a small inaccuracy can be due to the background counts 'comparable' to the As signal.

Table 4.3. Arsenic total fluence of as implanted samples measured by SIMS and MEIS.

Sample name	Nominal fluence (at/cm^2)	Measured by SIMS (at/cm^2)	Measured by MEIS (at/cm^2)	**Sample name**	Nominal fluence (at/cm^2)	Measured by SIMS (at/cm^2)	Measured by MEIS (at/cm^2)
SL	$1x10^{14}$	$1.04x10^{14}$	$1.04x10^{14}$	**SL-PAI**	$1x10^{14}$	$1.02x10^{14}$	$1.35x10^{14}$
SM	$5x10^{14}$	$4.91x10^{14}$	$5.16x10^{14}$	**SM-PAI**	$5x10^{14}$	$5.04x10^{14}$	$4.90x10^{14}$
SH	$1x10^{15}$	$1.05x10^{15}$	$1.04x10^{15}$	**SH-PAI**	$1x10^{15}$	$1.02x10^{15}$	$1.03x10^{15}$

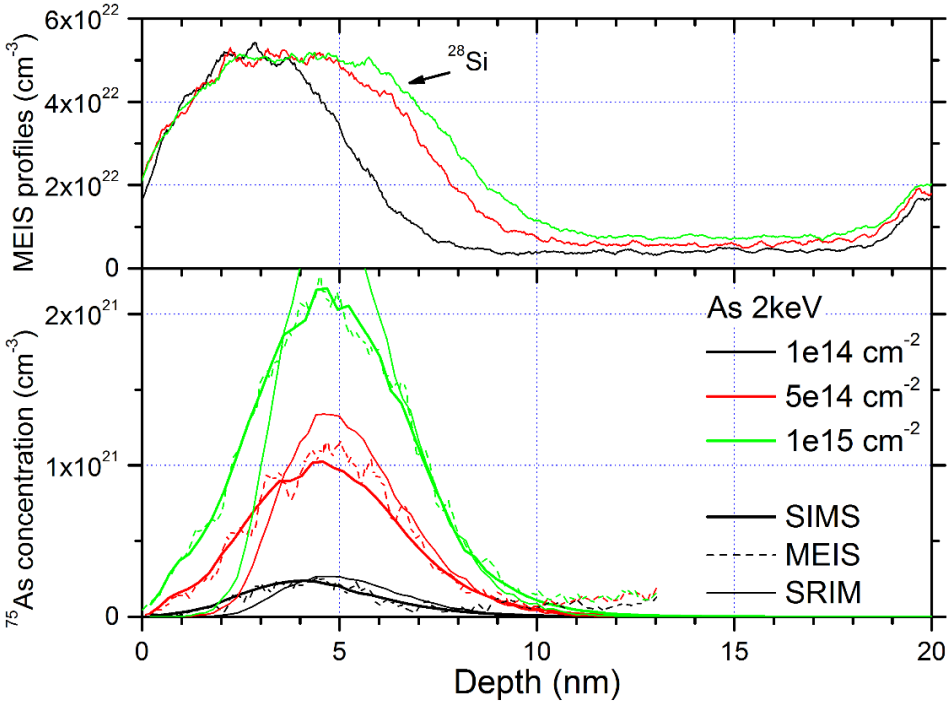

Figure 4.8. In the lower plot the comparison of the SIMS (thick lines) and MEIS (dashed lines) profiles of the 'as implanted' samples are shown (implanted at different fluencies: $1x10^{14}$ (SL), $5x10^{14}$(SM), and $1x10^{15}$ (SH) cm^{-2}, not pre-amorphized series). Thin lines correspond to the distribution calculated by SRIM. In the upper graph, MEIS measured de-placed Si atom distributions for the same samples are plotted.

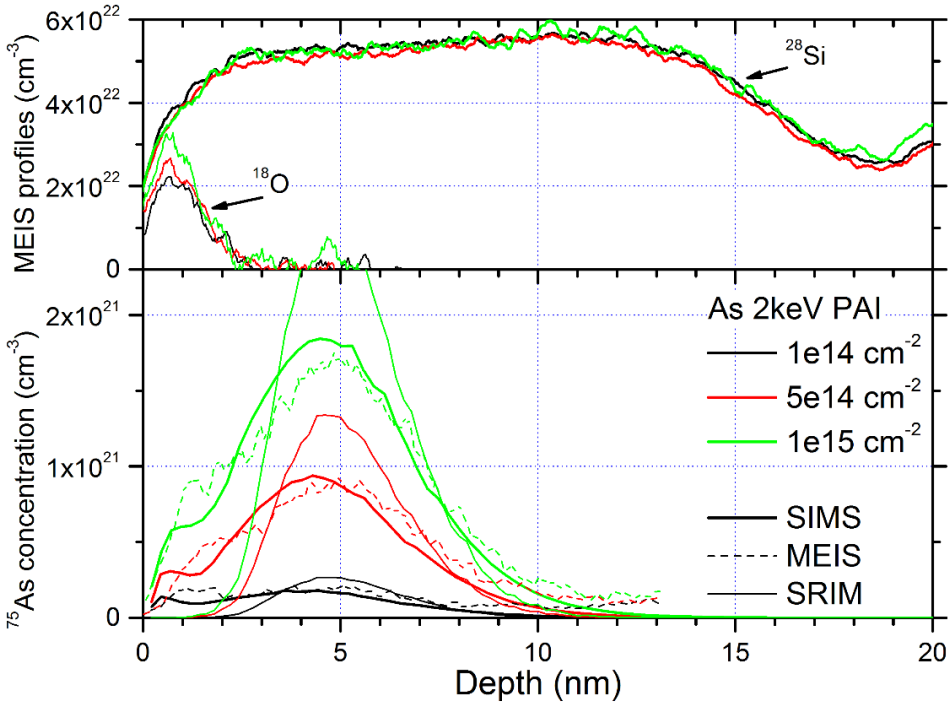

Figure 4.9. In the lower plot the comparison of the SIMS (thick lines) and MEIS (dashed lines) profiles of the 'as implanted' samples are shown (implanted at different fluencies: $1x10^{14}$ (SL-PAI), $5x10^{14}$(SM-PAI), and $1x10^{15}$ (SH-PAI) cm^{-2}, pre-amorphized series). Thin lines correspond to the distribution calculated by SRIM. In the upper graph, MEIS measured de-placed Si atom distributions for the same samples are plotted

4.4.2 Low dose implants SPER.

Arsenic implanted samples were thermally treated at 550°C for 10, 30, 60 or 300s to monitor different levels of damage recovery and resulting As distributions. The implanted As profiles are mainly contained in a depth of ~15 nm and thus, in case of pre-amorphization, they are completely contained within the 16 nm amorphized layer.

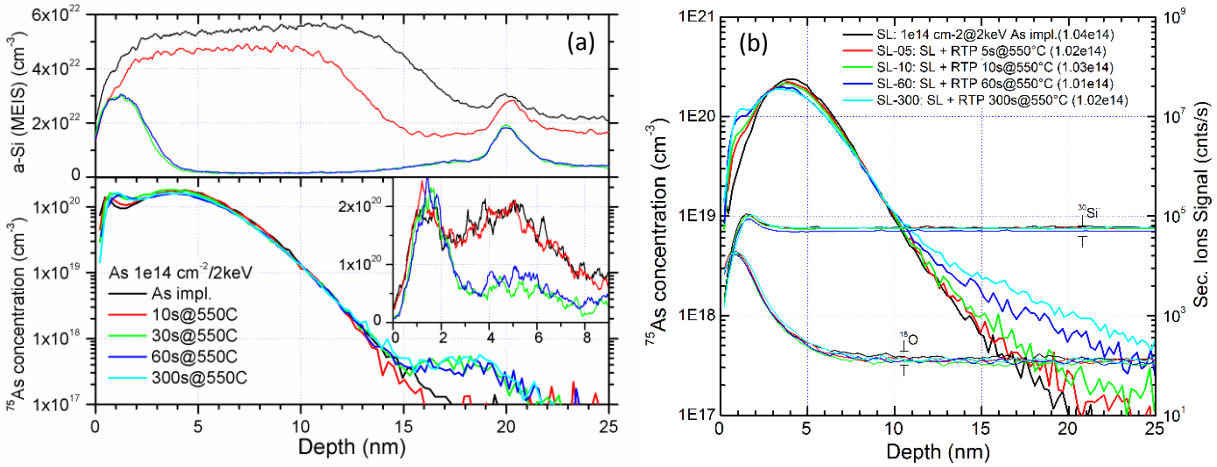

Figure 4.10. (a) Solid phase epitaxial regrowth of the 1x10^{14} implanted PAI sample after different annealing time at 550°C. Left, upper part – disordered silicon profile as measured by MEIS. Left, lower plot: SIMS determined As profiles; inset: MEIS As profiles in linear scale. (b) SIMS profiles of the not pre-amorphized set. Silicon and oxygen raw signals refer to the right axis.

The 10 s treatment re-grows only ~4 nm (figure 4.10, a) of pre-amorphized a-layer and the a/c interface does not reach the high concentration region of As distribution leaving it unchanged from the 'as implanted' one. This confirms that As diffusivity at this temperature is very low and most re-distribution is due to other mechanisms than equilibrium diffusion. Furthermore, the shift of the Si back-edge gives a SPE regrowth rate of 0.4 nm/s at 550°C. This rate is similar to the amorphous undoped silicon regrowth rate of 0.1-0.6 nm/s at 550°C reported in literature [14], [147]. The Si back edge slopes are similar for the as-implanted and 10s anneal confirming a layer-by-layer crystalline regrowth mechanism. The 30 s treatment on the other hand was enough to re-grow the whole a-layer and the amorphous/crystalline (a/c) interface has swept through the As profile changing it. MEIS shows a reduced As fluence after annealing because As atoms move into substitutional positions and are shadowed by atoms which are closer to surface. Therefore, in MEIS, only As segregated at the SiO_2/Si interface is detected. Comparing MEIS with SIMS, it is evident that most As atoms did not diffuse and only a small fraction of the dose (4x10^{13} at/cm2) is shifted towards the SiO_2/Si interface by the moving a/c interface. A small peak in the MEIS spectra at ~15-17 nm depth suggest the formation of end-of-range (EOR) defects at the original position of the a/c interface after annealing. SIMS measurements confirm an accumulation of As at the same depth, indicating that the segregation of point defects in the EOR region was also able to induce As diffusion and clustering at this depth.

In general the not-PAI samples show a behavior very similar to the PAI ones (figure 4.10, b). The main difference in the arsenic redistribution is that interstitial driven by thermal treatment diffuse in-depth creating a tail on the profile which increases with increasing time of the thermal treatment. The a/c interface is initially located at 5.6 nm depth. Unlike in the pre-amorphized case the arsenic relocation occurs much slower. It can be supposed that the As dose close to the amorphization threshold [130] does not completely amorphise the lattice. If there is some crystalline regions left in the material the SPER process can be impeded and recrystallization can follow different kinetics. Every additional annealing step moves the arsenic peak towards the surface creating the segregation peak at the SiO_2/Si interface and induces arsenic in-depth diffusion. The as-implanted sample was only measured by MEIS and there is no additional information about silicon recrystallization behavior, although, as reported it [143], even at higher temperature the SPER rate is lower than observed in the PAI case.

4.4.3 Medium dose implants SPER.

Medium dose implanted samples showed a behavior very similar to the low dose ones. The SIMS and MEIS arsenic depth profiles are reported in figure 4.11, a. The first 10 seconds of annealing induced a higher recrystallization of 7.5 nm (almost two times higher than for the low dose implants), but the high concentration region has still not been reached. In fact this acceleration of regrowth can be associated with the higher As concentration which is known to affect the regrowth [14].

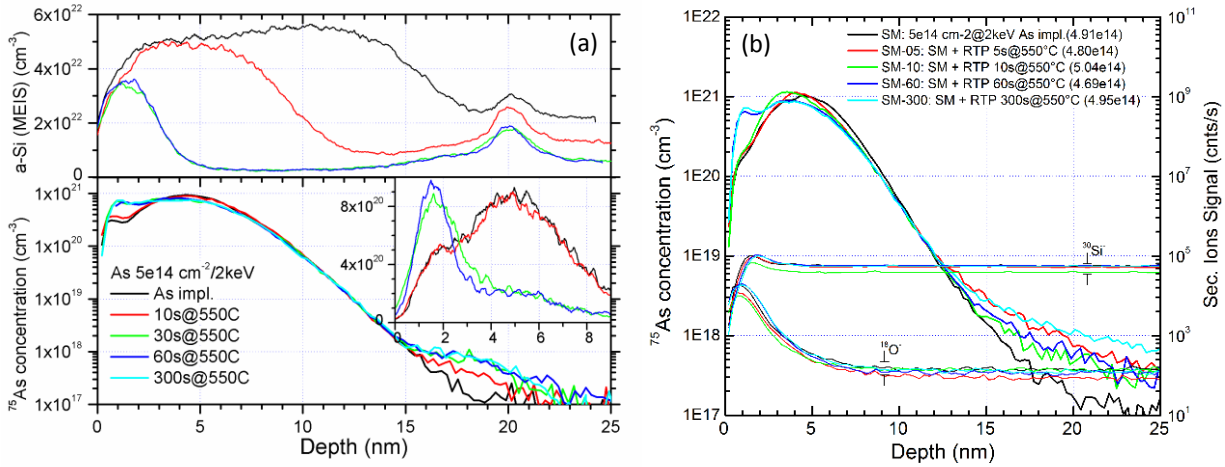

Figure 4.11. (a) Solid phase epitaxial regrowth of the 5x10^{14} implanted PAI sample after different annealing time at 550°C. Left, upper part – disordered silicon profile as measured by MEIS. Left, lower plot: SIMS determined As profiles; inset: MEIS As profiles in linear scale. (b) SIMS profiles of the not pre-amorphized set. Silicon and oxygen raw signals refer to the right axis.

Similar to the lower dose implants, after the 30 s anneal the amorphous layer has totally regrown and longer annealing times cause little change. The MEIS profile of the 60s annealed sample indicate that after annealing approximately 20-25% of the implanted As (~1x10^{14} cm^{-2}) remains still visible being non-substitutional and mostly confined at the SiO_2/Si interface. The model built merging electrical measurements and SIMS profiles shows a similar result, i.e. the expected amount of active arsenic in the

sample is 79% (details in chapter 4.3). This suggests that most As in substitutional position is also electrically active for this sample. Longer annealing reduces the substitutional fraction to 60% as obtained by electrical measurements.

The not pre-amorphized set also includes a sample annealed for 5s but not the one annealed for 30s (figure 4.11, b). According to MEIS, the recrystallization process starts at 7.8 nm depth and in fact the main relocation of dopants occurs starting from this depth. Upon annealing, an As peak appears in correspondence with the expected a/c interface and is progressively shifted towards the SiO_2/Si interface as long as the SPER proceeds. The diffusion tail is the same as in the previous case – below 10^{19} at/cm^3. The effect of dopant segregation at the oxide interface is more evident than in the previous sample set: 16% of the total arsenic is captured at the SiO_2/Si interface (10% for the low fluence implants).

4.4.4 High dose PAI implants SPER.

The SPER behavior of high fluence PAI samples was different due to the high As concentration (figure 4.12, a). The 10 s treatment induced the reduction of the original amorphous layer to a ~7 nm thickness similar to the analogous medium fluence sample. However, when the a/c interface reaches the high As concentration region, the SPER rate decreases and it takes more than 60 s to completely re-grow the a-layer, as shown by MEIS spectra (figure 4.12,a, upper part). EOR defect formation and consequent As accumulation is observed similarly to the previous cases. Segregated As peaks at the moving a/c interface are detected by both SIMS and MEIS.

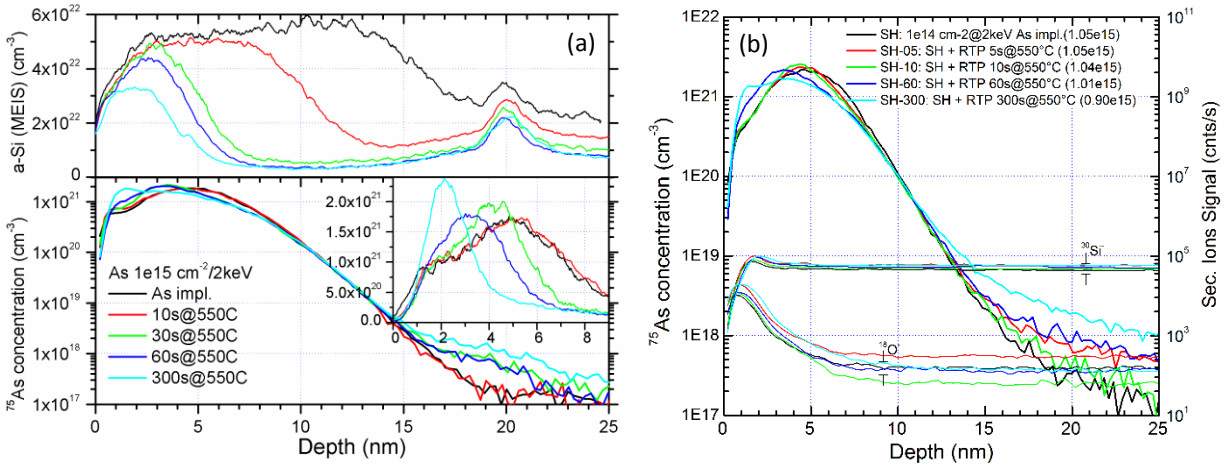

Figure 4.12. (a) Solid phase epitaxial regrowth of the 1x10^{15} implanted PAI sample after different annealing time at 550°C. Left, upper part – disordered silicon profile as measured by MEIS. Left, lower plot: SIMS determined As profiles; inset: MEIS As profiles in linear scale. (b) SIMS profiles of the not pre-amorphized set. Silicon and oxygen raw signals refer to the right axis.

The SPE regrowth rate in this case is estimated to 0.65 nm/s. As noted above, after 10 s annealing the a/c interface has not reached the high concentration and hence the As profile is unchanged. This also means that the anneal by itself does not cause any As movement into substitutional positions or As

diffusion; the As depth profiles confirm this and As relocation occurs only when the crystalline interface has moved through the high As concentration region. After the next 20s of annealing the regrowth rate has reduced to ~0.25 nm/s. After 30 s of annealing the a/c interface has reached a depth of ~ 4.5nm. In front of it an accumulation of As is observed (figure 4.12, a), which is due to the so called 'snowploughing' of As that exceeds the solid solubility of the Si matrix at 550°C. After the 300 s anneal this process finally leads to the segregated As peak positioned at ≤2 nm depth, just under the oxide. Even after the full crystallization the concentration of As still visible at the maximum of the original implant is around $3x10^{20}$ cm^{-3} or about 16% of the original as implanted concentration.

The not-PAI samples show a very similar behavior as reported in figure 4.12, b. A small reduction of the arsenic dose is detected for the longest annealing time (~10%). This indicates that the oxide layer does not totally prevent dopant out diffusion, probably due to the extremely high arsenic concentration in the near surface region.

4.4.5 Recrystallization rate simulation

SPER kinetics are heavily influenced by a dopant present within the amorphous layer. In particular, high concentrations of arsenic (up to concentrations around $2x10^{20}$ cm^{-3} [14]) can significantly accelerate the re-crystallization. Several studies reported a SPER rate enhancement after thermal annealing [15], [160]. Young-Jin Jeon et al. [161] measured this concentration dependence of arsenic on the regrowth rate of amorphous silicon by in situ, high precision, cw laser interferometry. According to the results the arsenic enhanced regrowth rate increases almost linearly up to an arsenic concentration of $2.2x10^{19}cm^{-3}$. Above that concentration non-linear saturation occurs and above $2x10^{20}$ cm^{-3} a decrease of the regrowth rate was detected [14], [162]. Using already reported data for arsenic-doped silicon from [149], [162] it is possible to estimate the regrowth rate of As doped amorphous layers.

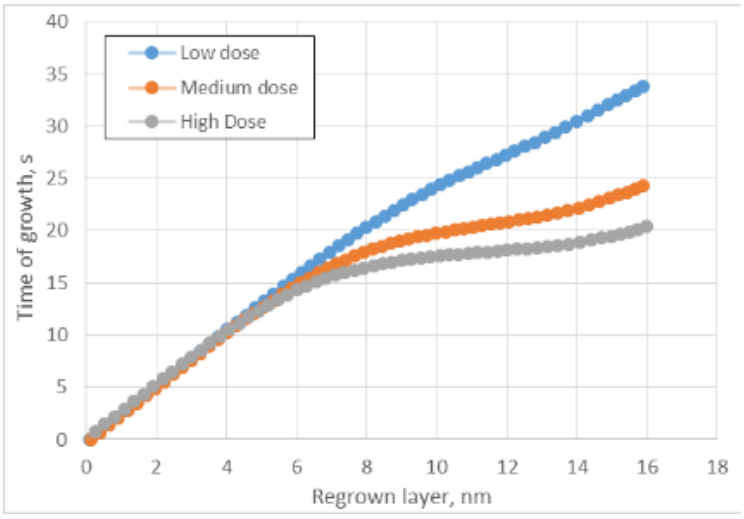

Figure 4.13. Re-crystallization time as expected from Jeon et al. [149] plotted against the distance from the original a/c interface.

Figure 4.13 shows the expected behavior of the epitaxial re-growth: the x-axis corresponds to the thickness of the regrown layer (0 is set at the initial interface position) and the y-axis is the duration of the thermal treatment at 550°C. Although this model was developed for much lower arsenic concentration (below $3x10^{20}cm^{-3}$) there is a similar behavior of experimentally measured and predicted data. The discrepancy can be explained by the fact that the regrowth rate depends on arsenic concentration and this factor changes during SPER due to dopant redistribution. The behavior of this redistribution is evaluated in the next paragraph.

4.5 Model of arsenic redistribution in high concentration region

The sweeping of arsenic by the moving a/c interface and its consequence, the apparent uphill diffusion, are well known effects [130], [137], [143]. The redistribution has been modeled in literature using different approaches: introducing a phase field equation [163] or a conventional diffusion equation with moving boundary conditions at the recrystallization front [164]. The complicated theory of these models does not allow understanding the general features of the phenomena, although they successfully describe them. Another, more empirical, model with only a few parameters for describing the dopant pile-up upon SPER was proposed by Suzuki et al. [55]. The model assumes that diffusion of the dopant in the regrown and amorphous layers is negligible and the redistribution occurs only near the a/c interface depending on a segregation coefficient, defined as the ratio between the As concentration at the a/c interface on the amorphous and crystalline side, respectively. This model was used as the basis for the fitting of the arsenic redistribution observed in this work. Few improvements were added to the Suzuki model to provide more accurate results in the near-interface region and to apply it to a wider range of impurity concentrations.

The main idea behind the arsenic redistribution model is very straightforward. Consider the SPER of the samples with a Gaussian shaped distribution of dopant and with initial a/c position inside the implanted region (figure 4.14 a, black line). In this plot the surface of the sample is on the left side and the growth starts at depth x_0. In practice the a/c interface moves continuously, but for computational reasons we used a discrete system where the x_i indicate the computational grid. x_0 corresponds to the initial a/c interface position.

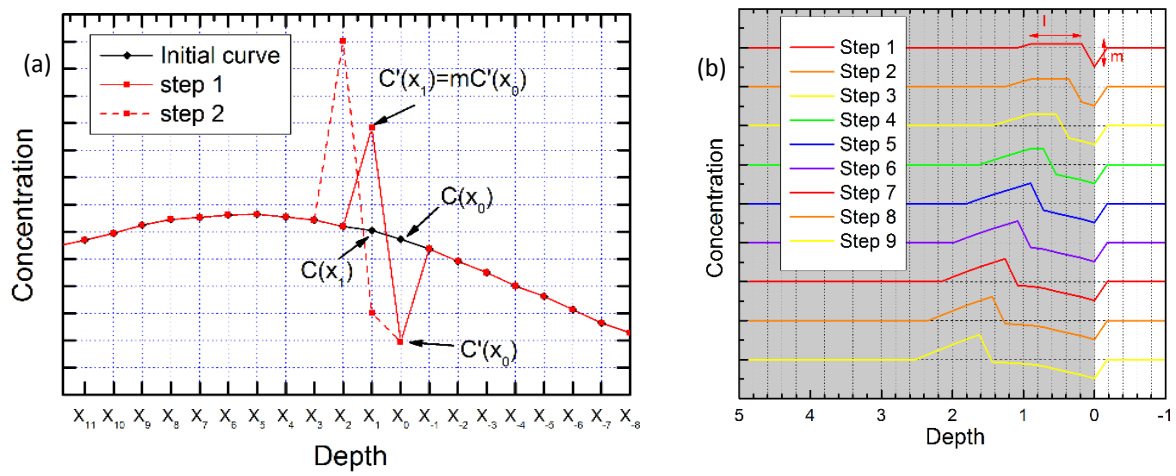

Figure 4.14. (a) Illustration of the redistribution mechanism. X_0 corresponds to the initial position of a/c interface. (b) Recrystallization of uniformly doped sample. The first 8 computational steps for the model with redistribution length 0.7 nm and m=2. 0 on the depth axis is set at initial position of a/c interface.

Consider the crystallization of the first layer at depth x_0 (figure 4.14 a, red line). The initial dopant concentration at this point is $C(x_0)$. As it was assumed by the authors of [55], the a/c interface relocates dopant toward the surface from point x_0 to point x_1 when it moves and the concentration at the new interface position (the point x_1) will be "*m*" times higher than concentration in the just crystallized layer x_0:

$$C'(x_1) = m \cdot C'(x_0) \tag{4.8}$$

where C'() is the concentration after the recrystallization step and m is the *segregation coefficient* as defined before. Taking into account the fact that total amount of the dopant should stay constant:

$$C'(x_1) - C(x_1) = C(x_0) - C'(x_0) \tag{4.9}$$

One can express the concentration in the point x_0 after crystallization like:

$$C'(x_0) = \frac{C(x_0) + C(x_1)}{1 + m} \tag{4.10}$$

The same calculation can be applied to all the next layers of the profile. According to the authors in [146] the calculated final distribution (when the a/c interface reaches the interface with the surface oxide layer) gives very good results for a very high concentration of arsenic (as implanted sample $1x10^{15}$ cm^{-2} at 3kev), figure 4.15.

However this approach cannot be used to completely simulate the final distribution due to a lack of information about the real concentration near the moving a/c interface. Moreover, the precision of the simulation is limited by the discretization of the computational grid because the distance between two adjacent points is a fitting parameter corresponding to the reaction length in which impurities exchange near the interface.

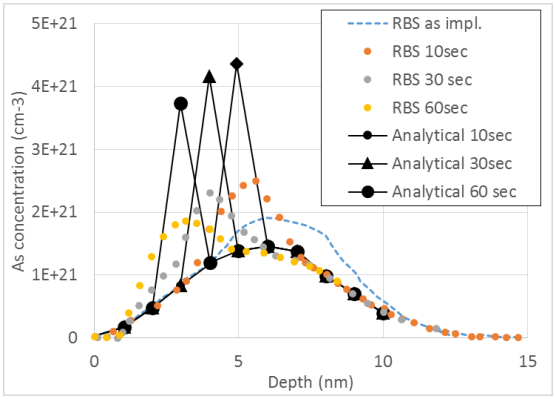

Figure 4.15. Comparison of theoretical and experimental As profiles adapted form [55].

These two limitations can easily be overcome by using a reaction length not bound to the lattice. The total dose of the dopant relocated at the first step is (from (4.10), the same is true for an arbitrary step):

$$\Phi_{step\ 1} = \mathrm{C}(x_1) - \frac{\mathrm{C}(x_0) + \mathrm{C}(x_1)}{1 + m} \tag{4.11}$$

Instead of moving this dose to the next point as proposed by authors, the dose is divided evenly among all points within the reaction length (l). A schematic of the redistribution is shown in the figure 4.14b.

Moreover, the authors only fitted one implant condition (3keV, 1x10^{15} at/cm^2) whereas our wider spectrum of concentrations allows us to improve the analytical model by suggesting a concentration dependent segregation coefficient. In fact, applying the Suzuki model to the low and medium fluence implanted sample we obtained a discrepancy with experimental results and we propose that the difference is due to concentration-dependence of the segregation coefficient.

After analysis of all experimental datasets, the dependency of m on the arsenic concentration was obtained by using the best fit of the simulated, final arsenic distribution to the one measured by SIMS. The fit was made numerically, evaluating the average concentration difference in every point of the regrown part of each profile. The resulting behavior of the segregation coefficient m is presented in figure 4.16. It can be well approximated with an exponential curve (red line) using the following equation:

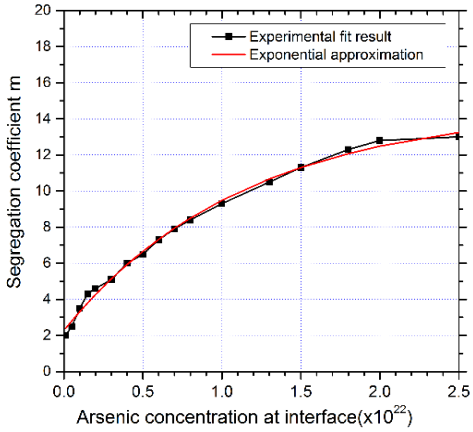

Figure 4.16. Segregation coefficient as a function of As concentration at a/c interface.

$$\mathrm{m}(C) = 14.622 - (12.433)e^{-\frac{C(x)}{1.142e22}} \quad (4.12)$$

where *C(x)* is the As concentration at the a/c interface. It is important to note that this dependence is valid for the adjusted model but not for the one proposed by Suzuki at al. in [146]. The concentration of the dopant at the interface becomes very high after a few steps and in order to compensate this, the segregation coefficient needs to be changed more radically. The estimation of the concentration dependence in this case was also made and reported in [165]:

$$\mathrm{m}'(C) = 1.5e^{-\frac{C(x)}{1.5e21}} \quad (4.13)$$

This enabled a good fit also for low fluence samples where less As is relocated upon SPER. In fact, the higher *C(x)*, the more As is segregated at the a/c interface. This empirical approach allows the removal of lattice and diffusion models and predicts not only the peak position but also the shape of the redistributed profile. An example of the obtained results is reported in figure 4.17 for the 1x10^{15} at/cm^2 PAI sample. Using an a-layer thickness as determined by MEIS, a good agreement between model and SIMS profiles is observed, considering the limits of depth resolution implied by the sputtering process.

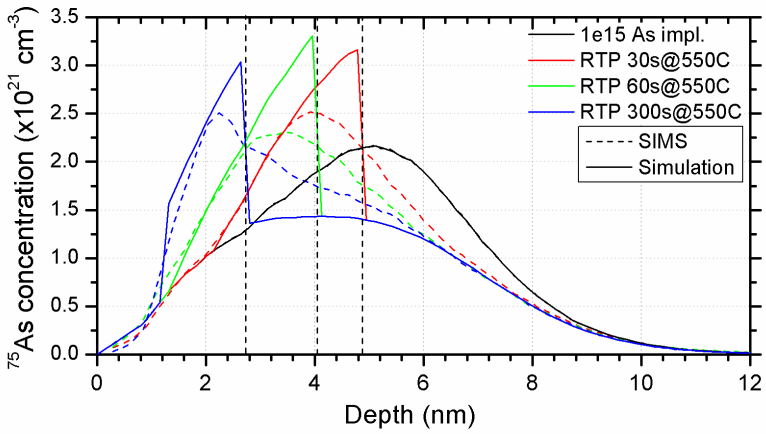

Figure 4.17. PAI sample implanted with 2 keV As at 1x10^{15} at/cm^2: comparison between SIMS profiles and results of a model describing the As segregation at a/c interface. a-layer thicknesses were taken from MEIS results

SIMS measurements of the samples after full recrystallization did not reveal any dopant loss whereas both MEIS and SIMS showed the growth of an arsenic peak segregated at the SiO_2/Si interface. It is known that oxide on the top of a silicon substrate prevents arsenic out-diffusion during SPER [142]. Previous works [166] showed that unlike phosphorus or boron, arsenic segregates in the last monolayer of silicon creating also a small amount of SiAs precipitations if the concentration is higher than solid solubility in silicon. The segregated atoms of arsenic are expected to be electrically inactive and can be detected by MEIS being off the lattice sites (e.g. figure 4.12). The total amount of arsenic detected at the SiO_2/Si interface after the 300 s anneal is about 5x10^{14} cm^{-2} which almost corresponds to a single monolayer and is theoretically considered possible [167].

The segregation of arsenic at the interface was also taken into account in the redistribution model. The thickness of the amorphous layer left after 300s thermal annealing (figure 4.17, blue curve) is less than the redistribution length. It is noticeable that a step appears on the profile at the place where the oxide layer ends, since arsenic is expected to not diffuse into SiO_2 at those temperatures and thus segregates at the interface. However, experimental results can hardly depict a very sharp SiO_2/Si interface: the observed transition between these two materials occurs on the scale of a couple of nm's according to the expected depth resolution of SIMS or MEIS. Therefore, it is proposed to assume that arsenic is trapped into the last monolayer of silicon but position and thickness of this layer is slightly spread in depth. The oxide signal detected during the SIMS analysis can be used as an indicator of this spread similarly as it was used for advanced SIMS quantification in chapter 3. For computational purposes the transient curve was fitted with a probability integral so the probability of atoms being trapped at the interface at depth *x* can be expressed with a Gauss function:

$$p(x) \sim e^{-\frac{(x-x_0)^2}{2}} \tag{4.14}$$

where x_0 corresponds to the SiO_2/Si interface position. In figure 4.18 the yellow curve represents the transient between the oxide and the silicon regions as obtained from the SIMS $^{18}O^-$ signal. The pink curve corresponds to the final segregation distribution after re-crystallization has been completed.

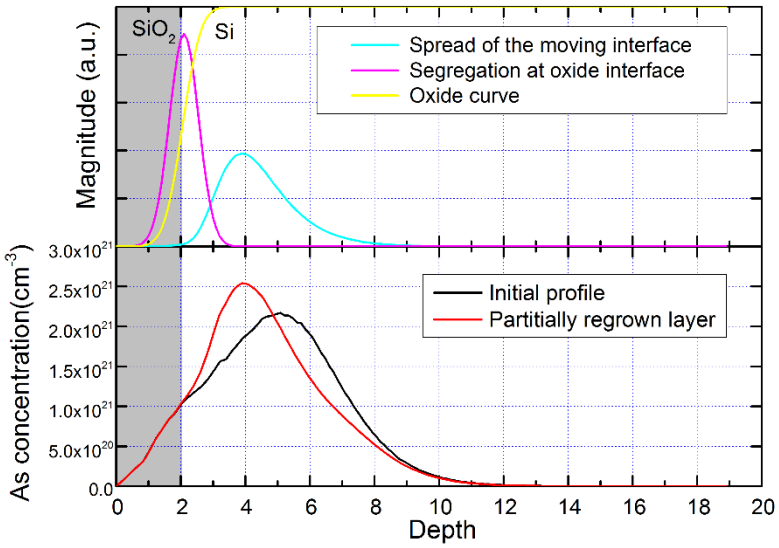

Figure 4.18. Simulation of SPER Top plot: Yellow curve corresponds to the transient between silicon and oxide part. Pink – differential curve of the interface (proportional to the possibility of atoms being trapped at the depth). Cyan curve – moving a/c interface.Bottom plot: $1x10^{15}$ as implanted PAI sample (black) and the simulation of partially (up to 4nm position) grown profile (red).

The discrepancy between predicted and experimental profiles at the moving interface shown in figure 4.17 can be significantly diminished by introducing the depth spread of the interface (figure 4.18, cyan line). Several physical processes can contribute to the form of the spread.

The first effect is connected to the lateral non-uniformity of the a/c interface. In theory the a/c interface is a plane moving from its initial position towards the surface, but practically the initial position of the interface might be slightly different at different points of the sample. On this scale the difference of even a single silicon atomic layer can have significant impact on the final distribution (every silicon atom gives presumably 0.27 nm difference in the a/c interface position). However, this spreading of the interface causes a different behavior of the dopant redistribution at the interface but not in the back-side of the interface, i.e. in the already crystallized material.

The other source of discrepancy between simulated profiles and experimental data is related to the SIMS depth resolution. Ion beam sputtering induces a mixing of the sample's surface (for a 300eV Cs beam the mixed depth is 1-2 nm) and thus secondary ions are emitted not only from the surface at the crater bottom but also from atoms coming from deeper layers. This effect is negligible as long as profiles are smooth compared to the depth resolution, i.e. for profiles with a low concentration gradient. In the case of SPER 'snow-plough' the dopant concentration profiles' derivative is very high (e.g. in figure 4.17). Therefore even an ultra-low impact energy SIMS analysis of the arsenic distribution simulated in figure 4.18, results in a wider curve with a gradient drop of at least 1 decade/nm (depending on the associated depth resolution) instead of a sharp drop at the amorphous layer back-side. Depth resolution depends on various factors such as material composition, primary beam ion species, its impact energy and incidence angle, and the uniformity of the sputtering beam [99], [100]. However, it is worth to note that the depth resolution affects every measurement in the same way (if carried out with the same analytical conditions) and thus, in general, still enables a meaningful comparison of profiles.

The resulting spread of the interface position (figure 4.18, cyan line) was extracted from experimental data and the shape is equal for all sample series. The theoretical equation for the interface position distribution is an asymmetrical peak function:

$$T(x) = e^{-e^{a}+a+1}$$
$$a = -\frac{x - x_0}{\Delta} \qquad (4.15)$$

where x is the distance from the surface whereas x_0 is the a/c interface position and Δ corresponds to the width of the peak. The shape of this curve is very similar to the shape of the SIMS response function reported in [100] and thus it can be assumed that the main contribution to this spread is stemming from ion mixing induced by primary ion beam.

The distribution of arsenic during SPER as measured and predicted using the described model is presented in figure 4.19. Only high fluence profiles are shown because the medium and low ones basically have only two states – unchanged (10 sec annealed) and fully regrown (30 sec and more).

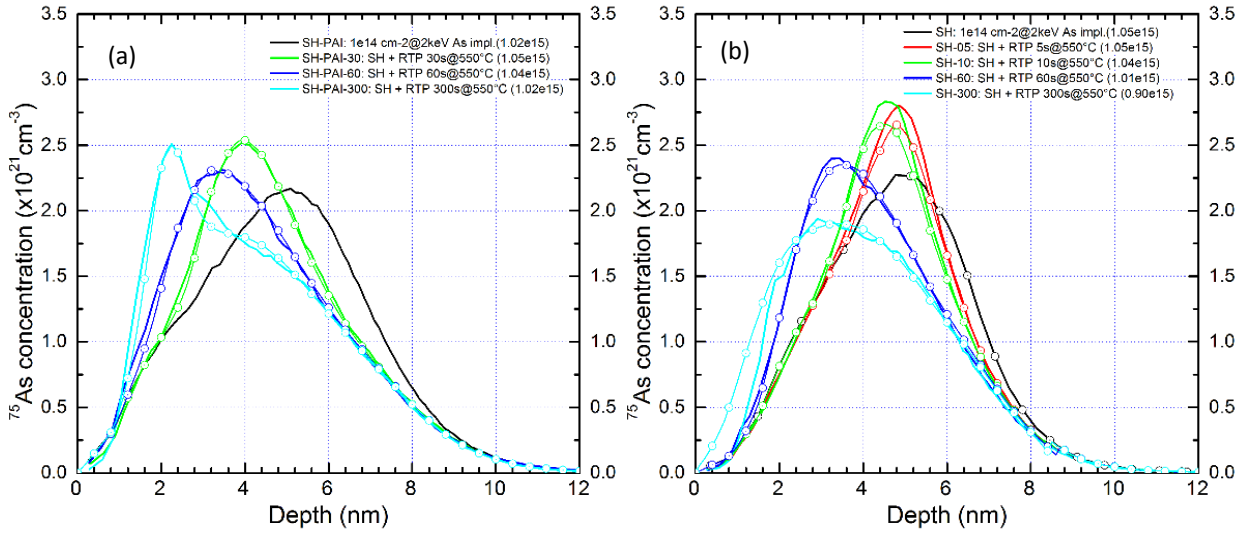

Figure 4.19. Comparison between experimentally obtained arsenic distributions (thick lines) and simulations of the SPER of as implanted samples (thin line with symbols): (a) pre-amorphized with silicon substrate (SPER starts from 16nm depth), (b) arsenic self-amorphized samples (SPER starts at 8.6 nm as measured by MEIS)

The interface position for the simulation (figure 4.19) was determined from MEIS measurements (PAI samples). For not pre-amorphized samples the a/c interface position was assumed at the arsenic peak. Both analytical technics have an accuracy of 0.2-0.3 nm and so the final a/c interface position was varied within 0.2nm region if necessary to obtain the best fit with experimental profiles. The predicted profiles of the 300s annealed samples were obtained by putting the a/c interface position at the samples surface.

4.6 Conclusion

This chapter reports the results of the investigation of the SPER process of As implanted silicon analyzed using MEIS, SIMS and R_s measurements. In the first part the results of ultra-low energy Secondary Ion Mass Spectrometry measurement of samples annealed at 550°C are presented. The SIMS results show the arsenic redistribution (uphill diffusion) at this low temperature for all samples: three different doses ($1x10^{14}$, $5x10^{14}$, and $1x10^{15}$ at/cm^2) implanted at 2 Kev and two different silicon substrates (single crystal and amorphous). Neither arsenic loss nor oxide growth was detected (thermal treatment was done in a partially oxidized atmosphere).

The electrical measurements of the annealed samples revealed that typically the PAI step produced a final activation level higher than in the non-PAI samples, with a level of electrically active dopant expected to be higher than the equilibrium value. A fairly good activation of arsenic was detected for the pre-amorphized medium fluence ($5x10^{14}$ cm^{-3}) implants annealed for 60 seconds at 550°C (up to 80% of the dopant). Subsequent thermal treatment resulted in arsenic deactivation (down to the 50% level). High fluence PAI implants have lower activation levels (only 60% for 60s annealing with a following reduction to 40% for 300s) but with the active concentration of arsenic close to the solid solubility limit ($1x10^{21}$ cm^{-3}). The results on the lowest implanted fluencies reveal an extremely low active fraction (less than 20%) - something not expected and raising concerns about the used approach's ability to measure such low concentrations.

Comparison of the SIMS and MEIS results showed that the amorphous re-growth rate depends on the As concentration, being slower the higher the As concentration. Although no relevant in-depth diffusion was observed, As is re-distributed to two regions. High concentrations are swept by the a/c interface and As is finally located at the SiO_2/Si interface. At the same time, a small fraction of the dopant is trapped in EOR defects. An analytical model was applied to describe and predict the As relocation towards the surface. A segregation coefficient dependent on the As concentration was proposed. The very good agreement between SIMS experimental results and simulations was achieved using an additional adjustment such as broadening of the a/c interface and the SiO_2/Si interface position.

The arsenic segregation at the SiO_2/Si interface was also detected by MEIS and SIMS. The fact that all segregated arsenic was detected by MEIS indicates non-substitutional (and thus non-active) state of the As atoms.

Chapter 5. Results II: Arsenic deactivation in silicon

5.1 Introduction

The previous chapter showed how a non-equilibrium annealing like solid phase epitaxial re-growth (SPER) can create a high level of electrical activation of arsenic doped silicon samples, as reported also in literature [62], [136]. However in highly doped silicon (when As concentrations exceed 10^{20} cm^{-3}) the active arsenic is mostly present in a metastable form and subsequent thermal treatments at temperatures above 500°C can lead to a decrease of the active As fraction.

The general picture of arsenic de-activation and diffusion based on combining older literature results and more recent papers is the following: at the equilibrium and as long as the As concentration is below the solid solubility, a solution of As atoms in either substitutional positions or in clusters around vacancies (As_nV_m, n≤4 and m≤2) is established, being the fractions of As atoms in the two classes depending on dopant concentration and annealing temperature [60], [168]. Older experiments [63], [66], [80], [169] started from laser *melting* annealed As distributions resulting in high levels of metastable substitutionality without any relevant lattice damage left. The path to the equilibrium and thus to de-activation was through the As_nV mechanism as brilliantly proved by Rousseau *et al.* [66]. However, peculiar kinetic constraints can favor the formation of clusters involving interstitials. This can be the case for thermal treatments carried out on ion implanted material where a super-saturation of self-interstitials is present. Furthermore, if the As implanted fluence is higher than the threshold value for amorphization, the formation and dissolution of EOR defects can provide further self-interstitials affecting both As TED and clustering through an I-based mechanism. The phenomenon is particularly evident in the 700-800 °C range, whereas at higher temperatures strong As diffusion and higher solubility enable higher levels of activation. At 700-800°C, a high concentration distribution will progressively de-activate starting from As_nI clusters since the high I density and the low migration barrier of AsI complexes will favor their formation. However, for longer annealing times the As_nI clusters will eventually evolve to the most stable As_nV clusters as expected when an excess of I is not present [83].

In this chapter the deactivation of arsenic in ultra-shallow implants, similar to the ones used in the SPER study (chapter 4) has been studied with regard to its effect on transient enhanced diffusion. The activation of dopant was performed using millisecond *sub-melt* laser annealing (LA) which is expected to provide very high level of activation as reported by Giubertoni et al. in [170]. The deactivation upon subsequent thermal treatments at 700 °C was indirectly monitored through the diffusion of Boron similarly to what proposed by Rousseau et al. [122]. An additional sample implanted with Germanium instead of Arsenic was used to try and separate the contribution of lattice defects related to the implantation process on the boron TED.

5.2 Experimental description

In order to monitor arsenic deactivation and related TED, two wafers with a specifically prepared silicon substrate were used implanting them with 2 different ion species. The substrate was designed in a similar way to the one originally proposed by Rousseau et al. in [80]. In their work, the diffusion of 200 nm thick buried boron-doped layers was used to monitor the flow of interstitials possibly emitted during arsenic deactivation and/or damage evolution. In our case, this design was adapted to shallower distributions of the dopant and it is schematically presented in figure 5.1. Five 10 nm thick epitaxial layers of boron doped silicon layer were grown, each one separated from the other by 50 nm of undoped silicon. Boron concentration in the layers was about $3x10^{18}$ at/cm^3, i.e. lower than the level at which the impact of boron concentration become relevant on its diffusivity [171].

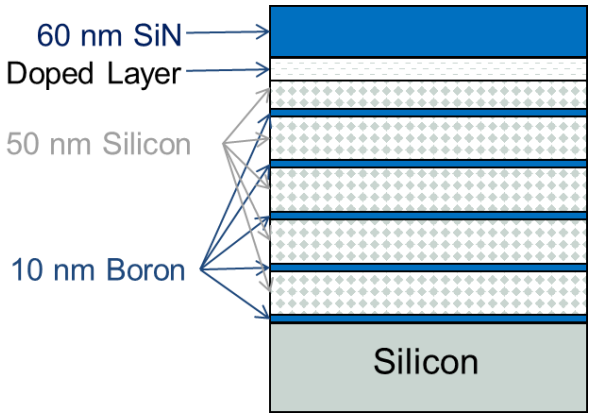

Figure 5.1. Schematic representation of the samples substrate: five delta layers of boron were buried in silicon substrate and separated by 50 nm of silicon. 60 nm SiN cap was deposited after implantation.

Two silicon wafers with this substrate were then implanted with either arsenic or germanium with fluencies of $1x10^{15}$ at/cm^3 at 2 keV (normal incidence), i.e. an implant condition of interest for realizing ultra-shallow junctions (USJ) in Si. The atomic mass of Ge is close to the one of As and hence the 'as implanted' dopant distribution, lattice damage and induced strain are expected to be very similar for the two implants. In particular, germanium was chosen because of its high solubility in silicon and thus no clustering/precipitation related effects are expected besides the normal lattice damage evolution.

After implantation, a 60 nm SiN_x cap was deposited at low temperature on the surface of the samples in order to prevent dopant out-diffusion or surface oxidation, which can cause an additional flow of interstitials. The capped samples were subjected to a sub-melt msec LA to remove the lattice damage induced by the ion implantation process and to activate the implanted dopant. 1100°C and 1300°C annealing temperatures were achieved using a scanning diode laser in a N_2 atmosphere. The temperature was controlled with a pyrometer calibrated through a NIST traceable standard. The annealing duration was 1 ms at the given temperatures with a ramp-up and ramp-down rate of the order of 10^6 °C/s.

Afterwards, the samples (not laser annealed and annealed at 1100° and 1300°C respectively) were submitted to a rapid thermal annealing (RTA) at 700°C for durations from 1 to 30 minutes in a flowing nitrogen-oxygen mixture (95%/5%) flowing ambient to prevent As out-diffusion [142]. The annealing was performed in the RTP annealer As-Micro (AnnealSYS), halogen lamp system, with a heating ramp rate of ~100°C/s. These parameters and this procedure were chosen to make sure that the main effect on the

dopant behavior can be ascribed to the dwell temperature and not to thermal budgets supplied during the sample heating and cooling stages. The details of the RTP annealing are reported in section 4.1. The chosen temperature provides the strongest electrical deactivation as previously shown in [140]. The detailed list of samples used in this work is presented in table 5.1.

Table 5.1. Samples used for arsenic deactivation study characterized by SIMS.

Implanted species	Arsenic			Germanium		
LA temperature, °C	0	1100	1300	0	1100	1300
RTP annealing time at 700°C, min.	Sample code					
0	SA00	SA11	SA13	SG00	SG11	SG13
1	SA00R1	SA11R1	SA13R1	SG00R1	SG11R1	SG13R1
5	SA00R5	SA11R5	SA13R5	SG00R5	SG11R5	SG13R5
10	SA00R10	SA11R10	SA13R10	SG00R10	SG11R10	SG13R10
30	SA00R30	SA11R30	SA13R30	SG00R30	SG11R30	SG13R30

A separate group of samples was prepared at conditions similar to the ones used for samples in the solid phase epitaxial regrowth study (Chapter 4): arsenic implanted samples with no laser annealing were thermally treated at 550°C for a duration of 10, 60, and 300 seconds. These samples were analyzed separately and the results are reported in section 5.7. The list of the samples is reported in the table 5.2.

Table 5.2. Samples used for the SPER study. Annealing temperature is 550°C.

Annealing time, s	Arsenic	Germanium
10	SAR10	SGR10
60	SAR60	SGR60
300	SAR300	SGR300

SIMS analysis was carried out to obtain As and B depth profiles for every sample. Two distinguished sessions were carried out for the two dopant species. During the first session, the arsenic SIMS profiles were obtained using 300 eV impact energy (45° incidence angle) Cs^+ primary ion beam and $^{18}O^-$, $^{30}Si^-$, and $^{75}As^-$ secondary ions were recorded in high mass resolution (M/ΔM=2500). In these samples the arsenic distribution is located near the SiN/Si interface and cannot be accurately quantified due to the absence of a standard material for such systems. However, the matrix effects related to the double-layer system can be partially compensated by choosing ion species independent of the matrix element. For this reason As^- monoatomic species were followed during the SIMS analysis, although $^{28}Si^{75}As^-$ ions have higher yield providing a better dynamic range. At this low energy, the SIMS depth resolution can significantly deteriorate if thick layers have to be sputtered, since roughness effects can develop [172]. Furthermore, as it is difficult to focus a 300 eV beam to spots with diameters below 75-50 nm, edge effects can arise when more than 50-75 nm of material has to be eroded. Finally, relatively thick insulator layers suffer of charging phenomena during SIMS sputtering due to the electrostatic charge deposition induced by the primary ions implantation and secondary ions emission. The deposited (usually positive) charge affects the incidence of primary ions, particularly for low energy impact, resulting in de-focusing and

misalignment of the ion beam and consequent edge effects and loss of depth resolution. Before the SIMS analysis the samples were thus subjected to chemical etching in HF acid solution in order to remove SiN_x cap. Although HF should selectively remove nitride cap leaving the silicon substrate undamaged, in some cases it was observed that it can also easily remove a few top nanometers of silicon, probably due to the high concentration of arsenic. In such cases when arsenic SIMS depth profiles are compared in groups, they are aligned on the falling edge of the distribution where legitimate, e.g. in the high concentration part of the distribution where the dopant is blocked for most of the thermal processes investigated.

The boron distribution was measured using 1 keV impact energy (68° incidence) $^{18}O_2^+$ primary ion beam and recording $^{28}Si^+$, $^{10}B^+$ and $^{11}B^+$ positive ions. A controlled oxygen leak was introduced in the analysis chamber directing it to the sample surface, resulting in a pressure of ~$6x10^{-6}$ mbar. This O_2 pressure ensures higher ion yields and thus better sensitivity inducing a full oxidation of the SIMS crater bottom. The combination of the selected impact energy/incidence angle and O_2 leak is expected to produce the formation of a regular topography (ripples) in the crater along with a consequent sputtering rate variation and depth resolution deterioration. Therefore, the sample was rotated during sputtering as proposed by Zalar [173] and the sputtering rate and depth resolution were constant and adequate for B delta depth profiling [106], [174]. Raw $^{10}B^+$ and $^{11}B^+$ signals were converted to concentration after normalization and using a relative sensitivity factor (RSF) obtained from the analysis of a B $1x10^{19}$ at/cm^3 uniformly doped Si sample traceable to NIST standard reference material No. 2137. The total boron concentration was obtained as the sum of ^{10}B and ^{11}B concentrations.

5.3 SIMS analysis: method of boron diffusion evaluation and LA samples

Boron depth profiles of arsenic and germanium implanted samples before the thermal treatment are shown in figure 5.2 in logarithmic (top) and linear (bottom) scales. The zero of the depth scale is set at the first peak position for convenience. 'As implanted' samples with no laser annealing (SA00 and SG00) show Gaussian-like boron distributions with peak concentration of $3.3x10^{18}$ at./cm^3. Full width at half maximum (FWHM or σ) is 7.7 nm whereas the trailing edge and the decay length are 9.3 and 10.8 nm/decade, respectively. A Boron diffusion could be detected after the LA step for all the samples, indicating that the adopted sputtering conditions are adequate to provide the needed depth resolution to appreciate those small changes.

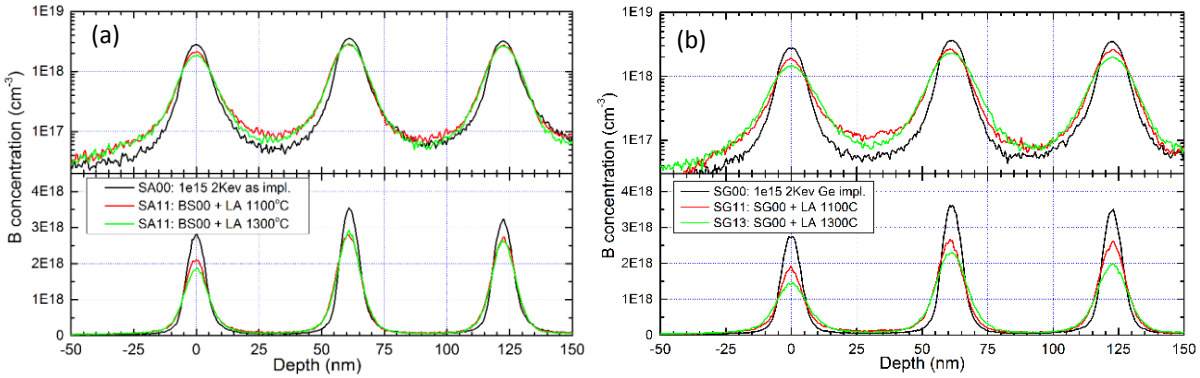

Figure 5.2. SIMS boron depth profiles of 'as implanted' (black) and laser annealed samples (green and red) in logarithmic (top) and linear (bottom) scales for samples ion implanted with arsenic (a) and germanium (b) at 2 keV energy and 1x10^{15} at./cm^2 fluence.

In general, germanium and arsenic ion implantation should produce similar lattice damage having similar atomic mass (75 a.m.u. for As and 74 a.m.u. for the implanted Ge isotope). In the arsenic implanted samples (figure 5.2, a), LA induces small boron diffusion similar for both 1100 and 1300 °C temperature. In samples with implanted germanium ions (figure 5.2, a) the diffusion appears to be more pronounced after LA. As previously mentioned, B is expected to diffuse mainly via an interstitial (I) mediated mechanism [57]. Therefore whenever a B diffusion is observed in the buried deltas, it must be assumed that Is are somehow emitted from the neighboring regions. In general, emission of Is can occur for EOR defect formation or dissolution, As clustering with point defects, and silicon oxidation. The latter can be considered negligible for the samples of this study since all the thermal treatments including LA were carried out keeping the SiN_x cap. The other two mechanisms or their combination can be assumed as the main 'I-emitters' and quantitative evaluation of B TED may help to discriminate between them and understand which one is predominant for the different ion implanted species/annealing combination.

For a quantitative comparison of the boron profiles, information about the peak width and height was extracted by a least squares fit. Every boron SIMS profile was fitted by a set of gaussian curves (the number of curves depended on the number of available boron peaks, usually from 3 to 5) defined as

$$C(x) = Ae^{-\frac{(x-x_{peak})^2}{\sigma^2}} \qquad (5.1)$$

where A is the peak height, x_{peak} the center of each Gaussian and σ the Gaussian width. The 3 to 5 values of σ and A of the Gaussians of every profile/sample were averaged and these average values were used for diffusion evaluation. An example of the fitting is shown in figure 5.3.

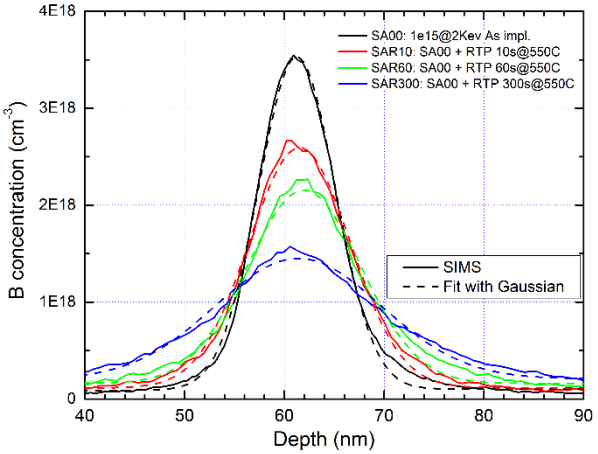

Figure 5.3. Examples of SIMS measured boron delta-layers fitted with Gaussian curves. The depth scale origin is set at the first peak position.

The diffusion coefficient of boron can be determined by the evolution of the SIMS profiles. Assuming the shape of initial profiles is Gaussian and that the diffusion coefficient does not depend on the boron concentration (given its low value), the diffusion coefficient D as a function of the temperature T and time t of thermal treatment can be determined from the variation of the delta peak width as:

$$\mathrm{D(T)} = \frac{(\sigma^2(t,T) - \sigma_{init}^2)}{4t}\ cm^2/s \tag{5.2}$$

where σ_{init} is the width of the initial profile, t is the annealing time and T is the absolute temperature [175]. An enhancement coefficient to quantify the B TED can be defined as the ratio between the measured diffusion coefficient and the one for relative intrinsic equilibrium expected at the same temperature. In spite of the huge amount of data published in the last 50 years, an estimation of a diffusion coefficient for boron in silicon using different models can give quite different results ([58] and references therein). The reason for this is that boron is very sensitive to the presence of point defects within a material. In this work the value of the boron diffusion coefficient obtained from ab initio calculation in [58] was used:

$$\mathrm{D}_i\mathrm{(T)} = (0.080 \pm 0.004)\mathrm{e}^{\frac{(-3.08\pm0.09)}{k_B T}}\ cm^2/s \tag{5.3}$$

However, it is worth to notice that even within the margins of accuracy of the parameters given in (5.3), $D_i(T)$ may vary by a factor of 3. The value of the used diffusion coefficient was 9.078×10^{-18} cm^2/s for 700°C and 1.13×10^{-20} cm^2/s for 550°C.

5.4 SIMS analysis: Arsenic depth distributions

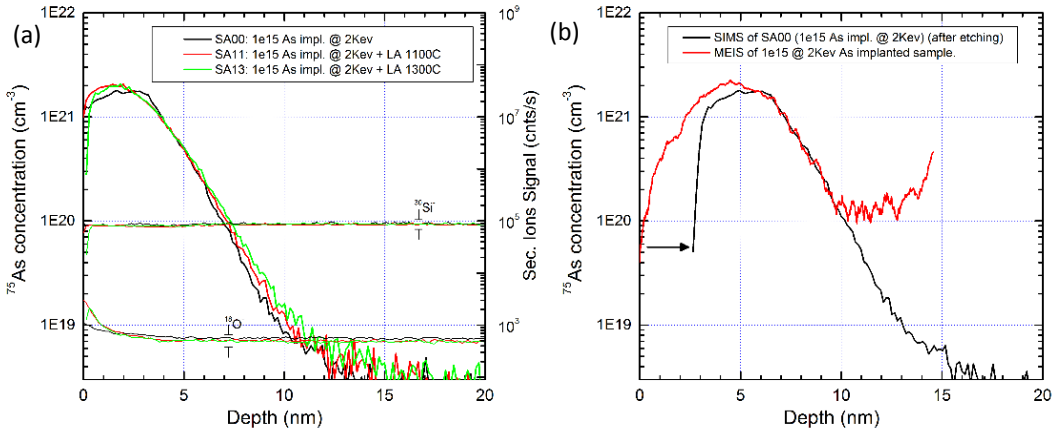

Figure 5.4. (a) Arsenic SIMS profiles of the 'as implanted' and laser annealed samples. (b) Comparison of the SIMS profile after etching with the MEIS results: the SIMS curve is shifted by 2.5 nm in depth in order to match the decay edge of the MEIS profile.

The arsenic depth profiles of 'as implanted' and LA samples are presented in figure 5.4 (a). The 'as implanted' projected range is about 3 nm, i.e. shallower than the ~5 nm measured for the analogous 2 keV As implants (the ones described in chapter 3 or 4). Since the profiles shown in figure 5.4 (a) were already corrected according to the protocol described in chapter 3, the only reason for this misalignment is that the etching process was probably not as selective as expected. Comparison with the MEIS profile of a sample implanted at the same energy (figure 5.4, b) shows that the top 2.5 nm of the silicon layer were removed after etching. The arsenic profiles (in figure 5.4, a, and further in the text) were aligned at the falling edge in a way that the 0 depth corresponds to the surface of the 'as implanted' sample after etching. It is evident that the millisecond LA did not induce any relevant As in-depth diffusion. Furthermore, no relevant As segregation peaks were observed at the surface like in the 550°C SPER samples. Since samples are affected by over-etching, this segregation peak may have been removed during the etching of the SiN_x cap. Alternatively, the SiN_x/Si interface may induce different segregation mechanisms compared to the SiO_2/Si interface. However, a similar lack of As segregation peak was already reported for samples processed in the same way and without SiN_x cap [145], [170], suggesting that msec annealing does not induce an As surface segregation. A closer look at the 0-4 nm portion of the As distributions actually shows that a slight As redistribution is visible as previously reported [145]. Therefore, it cannot be excluded that the N_2 atmosphere of the annealing allowed some As loss and a segregation peak did not form. Although the As segregation peak is considered mostly inactive, in the study reported in this chapter the attention was focused on the clustering mechanisms related to high As concentration distribution and a detailed investigation of possible segregation phenomena for msec annealing was not performed.

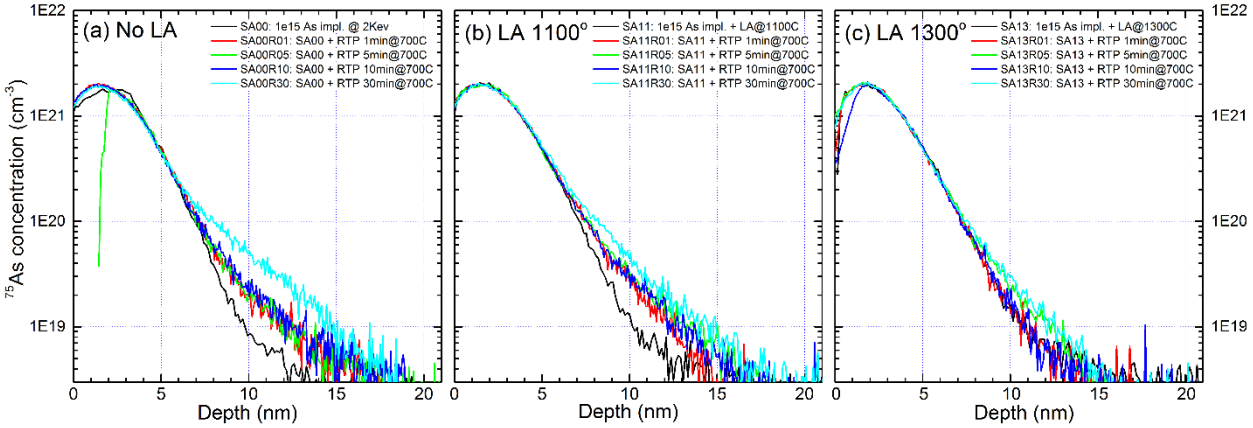

Figure 5.5. (a) Arsenic SIMS profiles after thermal treatments at 700°C: without laser annealing before 700°C treatment (a), laser annealed at 1100°C (b), laser annealed at 1300°C (c). The depth axis origin is set to the surface of the as implanted not annealed sample after etching. To overcome different over-etching effects, all profiles are aligned at the falling edge of the high concentration (> $5x10^{20}$ at./cm^3) part of the arsenic distribution, assuming it as mostly immobile.

SIMS measurements carried out on the samples treated at 700°C are reported in figure 5.5. No-LA samples (the SA00 group) present a different As distribution in the top 4 nm after the 700°C treatment in a similar way to what was observed in the LA profiles of figure 5.4. This suggest two conclusions: 1) the 700°C SPER process and msec annealing induce a similar re-distribution of As atoms in the high concentration part, despite the relevant temperature difference; 2) the SPER induced As surface segregation peak is missing also for the 700°C No-LA samples. Since for a 700°C SPER process this peak is usually observed [137], [138], [143], it can be assumed that either the SiN_x/Si interface does not allow As segregation or an over-etching removed this segregation in all the samples. Looking at the deeper part of the profiles, the As diffusion tail increases after 700°C/ 1min. annealing for samples without LA and with 1100 °C LA, respectively. The situation is then constant and annealing times longer than 30 minutes are required to appreciate further diffusion. Arsenic diffusion is observed only for concentrations lower than $8x10^{19}$ at/cm^3 for No-LA samples and lower than $1.5x10^{20}$ at/cm^3 for 1100°C, respectively. On the other hand, no relevant As diffusion is observed for 1300°C LA samples for times shorter than 10 minutes. A small diffusion can only be observed for longer annealing. This phenomenon is related to the concentration of defects within the arsenic layer before the thermal treatment. Similar RTP temperature was used in the work of Kong et al. in [176]. In their work the detailed Monte-Carlo simulation of defects evolution in arsenic implanted silicon is reported using a new model. It was demonstrated that the arsenic enhanced diffusion at this temperature is due to arsenic-interstitial mechanism and that contributions from vacancies to TED are insignificant. In the light of this we can propose that high temperature laser annealing could dissolve most of the interstitials left after the implantation whilst the 1100°C LA showed very similar behavior to the not-annealed case experiencing a clear TED phenomenon.

Another evidence in favor of the As-I presence and their influence on the As diffusion is that there is no noticeable difference on the As distributions in the samples thermally treated for 1, 5 and 10

minutes. In the simulation made by Kong et al. they show that although the arsenic is trapped in As_xI_y clusters in the beginning, the concentration of As in these clusters reduces drastically after 15 seconds at 750°C; at the same time the As_xV_y clusters become dominant. The arsenic diffusion through vacancies is relatively low but can be relevant for a long time annealing, like 30 min (figure 5.5.).

More information about the behavior of interstitials can be obtained by measuring the diffusion of the buried boron δ-layers in the samples. Boron mainly diffuses via interstitials and hence the enhancement in its diffusion should be an indicator for a flux of interstitials stemming from the implanted region.

5.5 Influence of the 700°C thermal treatment.

Although, normally, intrinsic diffusion of B is not relevant at 700°C, thermal treatment on No-LA samples induced various degree of diffusion of the boron delta layers as depicted in figure 5.6. In particular, Ge implanted samples show a relevant TED of B deltas for the 700°C thermal treatment due to the huge I flux, with B distributions already spread after only 1 minute annealing (figure 5.6, bottom plot). It is interesting to note that at the original first delta position a 'locked' peak appears after 1 minute and remains unchanged for longer times, probably due to the formation of boron-interstitial clusters (BIC)[31].

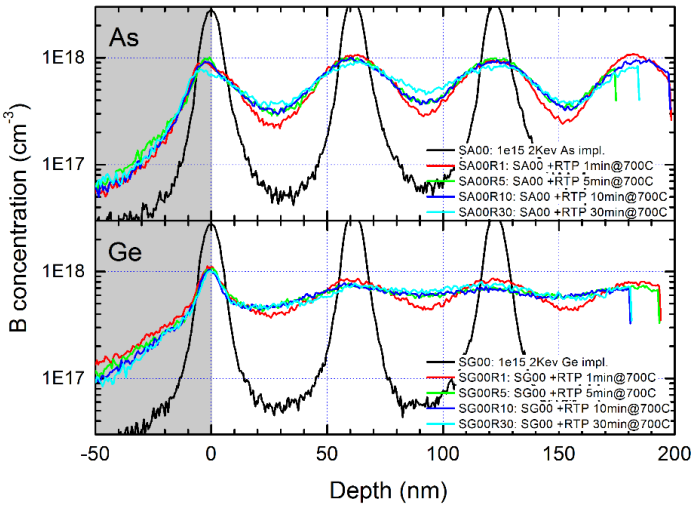

Figure 5.6. Boron depth profiles of As (top) and Ge (bottom) implanted samples after thermal treatment at 700C.

On the other hand, when As is implanted instead of Ge, the B TED behavior is appreciably different despite the expected similar a-layer and lattice damage (figure 5.6, top plot). In fact, B TED is clearly lower than in the Ge case suggesting a reduced I's flux.

The B diffusivity enhancement for Ge implanted samples is nearly twice the one for As implants for all the annealing times. This result is in contradiction to what was reported by Rousseau [66]when comparing similar phenomena for lower concentrations of both As and Ge. A detailed discussion about this will be carried out in section 5.6.

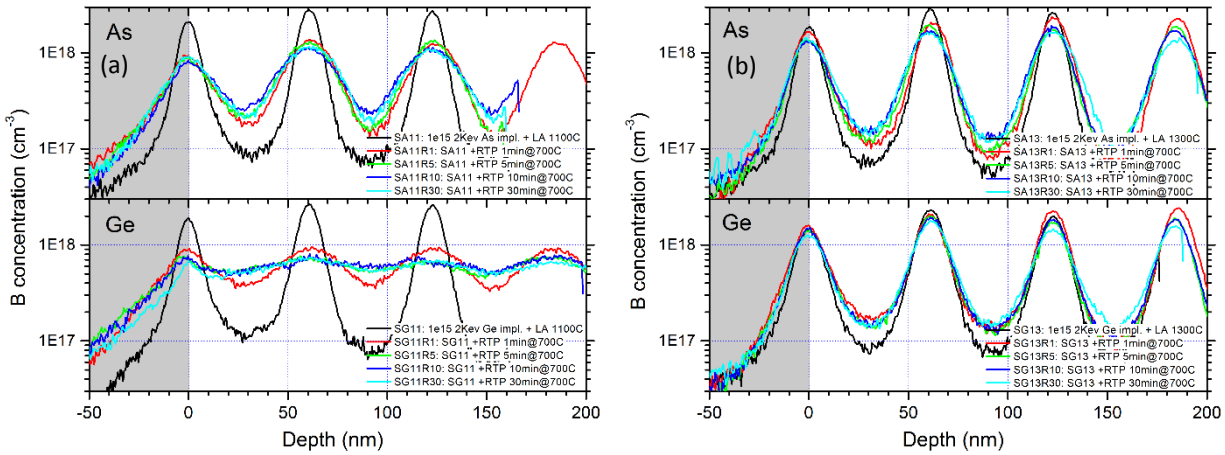

Figure 5.7. SIMS boron depth profiles of As (top) and Ge (bottom) implanted samples laser annealed at 1100°C (a) and 1300°C (b) and then thermally treated at 700C.

The laser annealing causes a reduction of the boron diffusion during post-laser annealing, although the behavior is very different for different temperatures (figure 5.7, a and b). After 1300°C annealing of the Ge implanted sample, the only relevant diffusion occurs within the first minute of the post laser annealing (figure 5.7, b, bottom plot). The following thermal treatments show barely detectable boron movement: as will be shown later, this might be related to the intrinsic diffusion of boron. The laser annealing of the As implanted samples also shows an enhancement in terms of boron TED. Although the spread of the boron deltas is more pronounced than in case of Ge, a general stability of the profile shape indicates a significant reduction in the flux of interstitials coming from the implanted region. The detected diffusion of boron after 1300°C LA suggests that at this temperature msec annealing was able to successfully remove most of the defects causing the TED.

Arsenic implanted samples laser treated at 1100°C show less diffusion than the Ge implanted ones (figure 5.7, a). The annealing could only partially remove defects and most of the dopant still exists in inactive form. The Ge implanted samples after low temperature laser annealing show a picture very similar to the not annealed case: in fact, after 1 minute at 700°C, the B deltas are still observable although a relevant diffusion has already taken place. Further annealing results in a complete spread of the delta structures. The only difference from the not LA series is the first boron peak. In the previous case, the locked peak already appeared after the 1 minute annealing and its maximum concentration of 10^{18} cm^{-3} is barely changed with annealing time. When the samples are laser annealed at 1100°C, the locked peak still appears although it can be detected only in the sample that has been submitted to the longest annealing time with a concentration below $7x10^{17}$ cm^{-3}.

5.6 B diffusion results and discussion

5.6.1 Boron diffusion and enhancement values

The values of the boron diffusion coefficient were extracted from the SIMS profiles using equation (5.2) and the results are presented in the table 5.3:

Table 5.3. Diffusion coefficient (cm^2/s) obtained from the shapes of the boron delta layers.

Implanted species	Arsenic			Germanium		
LA temperature, °C	0	1100	1300	0	1100	1300
Annealing time at 700°C, min						
1	$2.0x10^{-13}$	$1.0x10^{-13}$	$2.9x10^{-14}$	$3.7x10^{-13}$	$3.3x10^{-13}$	$5.0x10^{-15}$
5	$6.1x10^{-14}$	$2.1x10^{-14}$	$6.8x10^{-15}$	1.3E-13	$1.1x10^{-13}$	$1.3x10^{-15}$
10	$3.4x10^{-14}$	$1.6x10^{-14}$	$4.8x10^{-15}$	6.6E-14	$7.2x10^{-14}$	$1.1x10^{-15}$
30	$1.5x10^{-14}$	$5.7x10^{-15}$	$2.1x10^{-15}$	2.1E-14	$2.1x10^{-14}$	$1.1x10^{-15}$

The boron diffusion enhancement is reported in the table 5.4. The values are calculated assuming the intrinsic boron diffusion coefficient of $9.08x10^{-18}$ cm^2/s at700°C.

Table 5.4. Enhancement of the boron diffusion obtained from the shapes of the boron delta layers.

Implanted species	Arsenic			Germanium		
LA temperature, °C	0	1100	1300	0	1100	1300
Annealing time at 700°C, min						
1	$2.21x10^4$	$1.14x10^4$	3190	$4.12x10^4$	$3.66x10^4$	550
5	6700	2324	747	$1.47x10^4$	$1.18x10^4$	144
10	370	1740	534	7260	7914	123
30	1610	625	230	2290	2336	124

Figure 5.8 shows the boron diffusion coefficient obtained from experimental data (a) and the enhancement (b) of the boron diffusion coefficient in log-log scale. The pink line represents data obtained by Rousseau et al. in [66] for the sample with a similar arsenic concentration $1.9x10^{21}$. In their experiment, a slightly higher temperature of annealing (750°C) was used.

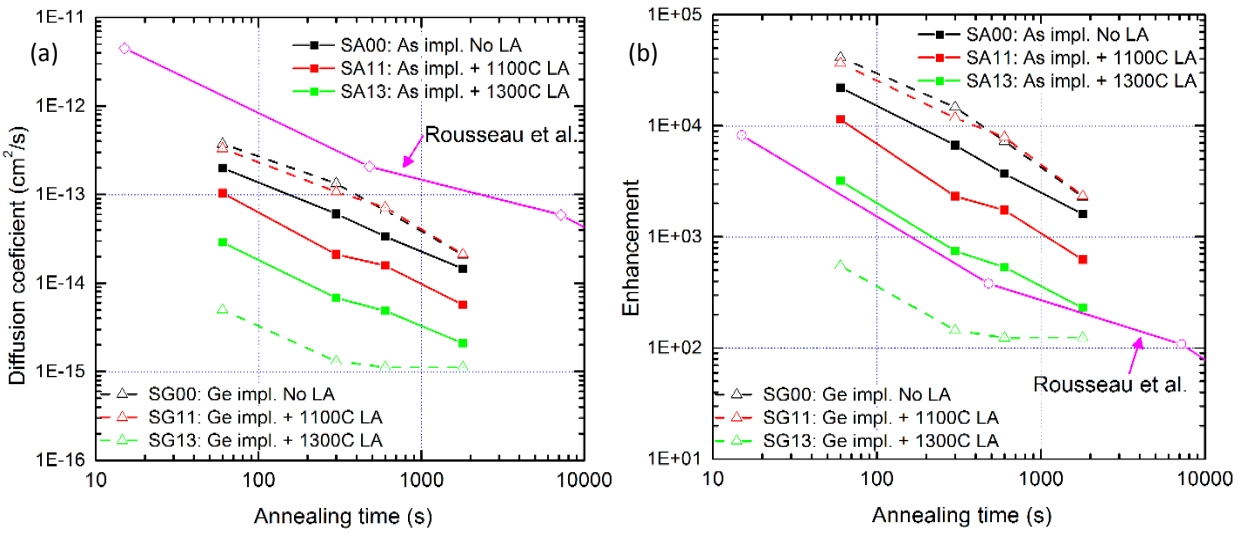

Figure 5.8. Boron diffusion coefficient at 700 °C calculated from the SIMS boron peak broadening after post-LA thermal treatment (a). Enhancement of the measured diffusion coefficient (b) (ratio between measured value and intrinsic boron diffusion at 700 °C). The pink curve represents data reported in [66] (where the annealing temperature was 750°C).

5.6.2 Samples without LA treatment

In the samples implanted with As (SA00 series) the TED of boron is nearly half the value of that observed for Ge implanted samples (SG00 series) for all annealing times (black solid and black dashed lines in figure 5.8). Since surface proximity seems not to prevent the I flux to the bulk and the effect is supposed to be similar for both As and Ge implants, the phenomenon must have another origin. In the work of Rousseau et al. [66], [177] it was reported that when As concentrations are higher than $1x10^{21}$ at/cm^3 the B TED on buried deltas is reduced, since the strong de-activation would induce an I injection so strong that defects like the ones usually observed only at EOR can be observed. Those defects would represent a further sink for interstitials preventing them from traveling towards the B deltas. However, the surface proximity should represent a preferential sink. For instance Cristiano *et al.* observed a reduction of {113} defects for a 2 keV Ge implants and the absence of their transformation to bigger dislocation loops even after a 1300 °C flash annealing [33]. An alternative hypothesis can be that As de-activation takes place through clustering with I's forming As_nI complexes. The latter may be more stable than defects involving only I's like the ones at EOR and thus their dissolution would be slower explaining the reduced B TED when compared to Ge implants. It is worth to repeat that for As implanted samples the I flux is still relevant which is also evident from the As TED observed for concentrations lower than $9x10^{19}$ at/cm^3 (Figure 5.5, a). This concentration value is very close to the value reported for the equilibrium maximum electrical activation achievable at 700°C, i.e. $8.1x10^{19}$ at/cm^3 according to Solmi et al [60], [168]. This confirms that at concentrations higher than this value As atoms are clustered and not very mobile.

5.6.3 Influence of laser annealing.

Ge implanted samples, LA at 1100°C, have a behavior more similar to the samples which were not-annealed than to the samples annealed at 1300°C (figure 5.8). The B TED is a clear indication of a great I flux, probably from the ripening and dissolution of the {113} defects observed by other authors upon re-crystallization and damage removal [33]. The enhancement factor of B diffusivity for Ge implanted samples decreases from $3.6x10^4$ to $2.3x10^3$ when the 700 °C annealing time is increased from 1 to 30 minutes, indicating a progressive reduction of the I flux. Furthermore, the $3.6x10^4$ enhancement factor after 1 minute at 700°C for the 1100°C LA samples is appreciably lower than the $4.1x10^4$ value measured for the analogous No-LA sample but nearly two orders of magnitudes higher than the value measured for the relative 1300°C LA sample ($5.5x10^2$). Finally, it is worth noticing that after 30 minutes at 700°C the Ge sample diffusivity enhancements measured for No-LA and 1100°C LA samples converge to the same value, i.e. $2.3x10^3$. The latter is still an order of magnitude higher than the respective one measured for the 1300°C LA samples.

Implanting As instead of Ge produces a drastic change in terms of B TED. The enhancement factor after 1 minute annealing at 700°C is $1.1x10^4$, decreasing to $6.2x10^2$ after 30 minutes, i.e. roughly 4 times lower than the values measured for the Ge implanted samples. The result clearly reveals that the high As concentration reduces the concentration of free interstitials at 700°C. Furthermore, the enhancement factor is less than half of the one observed for no-LA samples and no convergence at 30 minutes is observed like in the case of Ge implants. Finally, the enhancement factor is at least three times higher than the one measured for the 1300°C LA samples, e.g. $1.1x10^4$ against $3.2x10^3$ for 1 min. at 700°C.

This result is somehow surprising when compared to what was reported by Rousseau et al. [66], where actually the observation was the opposite: a stronger TED for de-activating As distributions at 750-800 °C than for Ge implants. However, two observations have to be pointed out to compare results:

1. In the experiment of Rousseau et al., a *melting* LA was used and no residual lattice damage was observed after the treatment. This means that the situation faced by the highly active As distribution was different from the one of this study, since probably no point-defects were present except for the ones created by As_nV clustering upon 700-800°C thermal treatment. In the study presented here, a *sub-melt* LA was performed and, especially at 1100°C, a distribution of {113} defects and free-Is could be expected. Therefore, an As clustering with I is reasonable given their high concentration.
2. The comparison between As and Ge implants was carried out for lower peak concentrations, i.e. $4.5x10^{20}$ at/cm^3 where the strongest B TED was observed upon As de-activation [66]. The same authors reported a reduction of the B TED for As concentrations

comparable to the values of this study (> $1x10^{21}$ at/cm^3), due to Is precipitation in extended defects ({113} and DL) at the concentration maximum. The analogous high Ge concentration was not reported, but B TED for high As concentration was still higher than for the only studied Ge concentration. Furthermore, since Ge precipitates are not expected due to the high Ge solubility in Si, the increase of the Ge fluence would have only produced a thickening of the amorphous layer, probably without affecting B TED during EOR dissolution. It is thus reasonable that also high As concentrations obtained by laser *melt* annealing would de-activate at 700°C injecting an amount of Is higher or at least comparable to the one coming from EOR dissolution in Ge implanted samples. The behavior observed in this thesis is the opposite, therefore either Is are sunk at the projected range as it may be expected for high As concentration or a different clustering mechanism involving free Is has to be invoked for sub-melt LA, e.g. As_nI formation. In the first case, some extended defects should be detected by TEM, but not in the second case. (TEM measurements could not be performed in the timeframe of this thesis).

It is also worth noticing that in the LA 1100 °C As implants, the B diffusion coefficient is less than half the one of the samples without LA for 1-30 minute annealing times, indicating that the free interstitial concentration has been lowered by the millisecond LA. On the other hand, the B diffusion coefficient is 5 times higher than the one determined for the 1300°C LA and thus the free Is number must decrease when LA temperature is increased. This picture is consistent with the reduction of density and size of {113} defects when the ms LA temperature is increased as reported in literature[33]. Being the EOR defect density lower, less free Is would be available for TED and clustering, and presumably the sub-melt LA samples would converge to a 'Rousseau-like' behavior when temperature increases. The reduction of free interstitials can be deduced also from As SIMS profiles obtained after post-LA at 700°C. In fact, an As TED was reported for samples without LA or with a 1100°C LA before 700°C treatment, but basically no relevant diffusion for As is observed for post-1300 °C LA treatments except for a small diffusion for annealing longer than 5 minutes.

5.7 Deactivation during SPER at 550C

In chapter 4 it was shown that arsenic implants can experience diffusion at temperatures as low as 550 °C together with a deactivation of the dopant. A similar set of samples as introduced there was prepared and analyzed in order to observe a possible interstitial injection connected to the deactivation. Both As and Ge implanted samples were subjected to the thermal treatment at 550°C temperature. The annealing conditions and times were the same as reported in chapter 4 and shown in the table 5.5.

The evolution of boron delta layers during the annealing is shown in figure 5.9. The diffusion coefficients and enhancement coefficient for these samples are reported in table 5.5. Apart from the relatively small difference (50%) for the 60 seconds annealing, the As and Ge implanted samples show a very similar behavior. As shown in the previous chapter, the full recrystallization of the ion implanted amorphized layer is reached only after 300 second at 550°C for the As implanted samples. Although the re-crystallization rate can be reduced due to the presence of the high concentration of Ge [178], the total rate should be higher in the Ge implanted material. This can explain the difference for the samples annealed for 60 seconds: the re-crystallized layer in the Ge implanted sample is thicker than in the one implanted with As, creating a higher flux of interstitials related to the re-crystallization and formation of lattice defects. In case of the longest annealing time full re-crystallization occurred and the total amount of I released during SPER is identical, suggesting that is the damage evolution common to both class of samples the main source of Is.

Table 5.5. Diffusion coefficient and enhancement obtained from boron δ-layers shape.

Annealing time, s	Arsenic	Germanium
Diffusion coefficient, cm^2/s		
10	$9.4x10^{-14}$	$9.9x10^{-14}$
60	$2.1x10^{-14}$	$3.3x10^{-14}$
300	$1.1x10^{-14}$	$1.2x10^{-14}$
Enhancement.		
10	$1.9x10^{8}$	$2.0x10^{8}$
60	$4.2x10^{7}$	$6.6x10^{7}$
300	$2.1x10^{7}$	2.4E+07

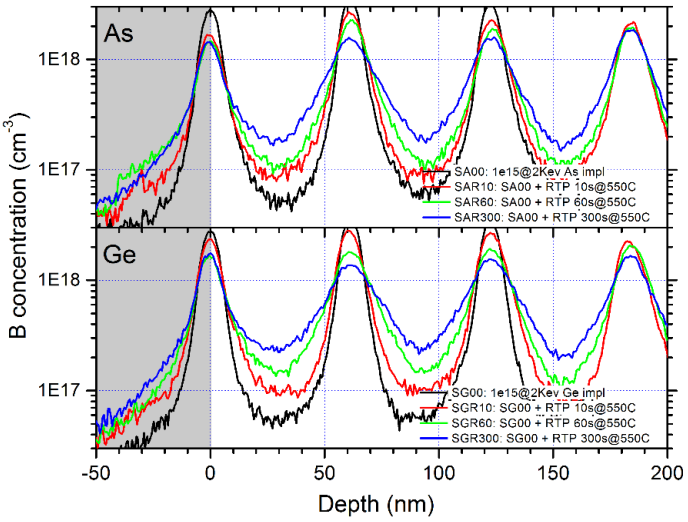

Figure 5.9. Evolution of boron profiles during SPER at 550°C.

5.8 Conclusion

In this chapter the results of the investigation of arsenic ultra-shallow junctions activated using submelt millisecond LA is reported. The design of the experiment, originally proposed by Rousseau et al. in [80], where buried boron layers are used as an interstitial detector, was adapted for low energy implants.

The results showed that the population of point defects clearly depends on the temperature of LA. The reduction of boron TED for the 1300°C annealed As implanted samples is dramatic when compared to what was observed for the not laser annealed series, suggesting that at this temperature laser annealing can successfully remove most of the defects and restore the lattice structure. The behavior of the dopant is very similar to the result described in [80] where laser melt annealing was used.

In the samples laser annealed at low temperature (1100°C), boron deltas show higher TED in Ge- than in As- implanted samples. The result clearly reveals that the high As concentration reduces the concentration of free interstitials at 700°C. Furthermore, it is opposite to the result reported by Rousseau et al. in the [66] where the authors observed much higher TED in As implanted samples. This discrepancy can be ascribed to the different activation annealing: laser *melting* in Rousseau et al. whereas non-melting conditions in our study. In the first case, all detected interstitials are related to the only As_nV cluster formation upon 700-800°C thermal treatment, whereas in the second residual point defects are expected after LA. Two different mechanisms causing this difference can be suggested: either Is are sunk at the projected range, as it may be expected for high As concentration, or a different clustering mechanism involving free Is has to be invoked for sub-melt LA, e.g. As_nI formation. The boron TED in this case is much higher than in the case of high temperature laser annealing (by a factor of 5) but lower compared to not laser annealed one.

Chapter 6. Results III: Plasma Ion immersion implantation

6.1 Introduction

The progressive downscaling of the dimensions of microelectronics silicon devices demands the implementation of new processes able to improve the overall performance in terms of speed, energy consumption and heat dissipation. Regarding the source/drain extensions x_j in CMOS technology, dopant distributions need to be ultra-shallow and with a high electrical activation. Plasma immersion ion implantation (P3i) is a well suited technique for such applications due to efficient transfer of ions from the plasma to the target surface. Resulting ultra-shallow distributions and high throughput of high fluence implants are two attractive aspects in comparison to the conventional beamline ion implantation process. Furthermore, highly conformal doping can obtained also on high aspect ratio structures like nanometric FinFET devices.

In 2008 Qin et al. demonstrated for the first time that plasma doping can be used for the formation of source/drain regions in a 68 nm CMOS device [179]. PMOS devices were realized using B_2H_6 plasma and NMOS devices using AsH_3 plasma doping. The evaluation of the electrical performance showed that none of the characteristics of the devices produced by plasma doping were inferior to the ones of the device produced by the ion implantation process. On the contrary, contact resistance, drive current and transconductance resulted in being better than in analogous devices prepared by beam-line implantation.

During the last years, P3i techniques have further developed and provide better control of the implantation process. In the first part of this chapter the results from different analytical techniques characterizing samples produced by P3i using a non-pulsed plasma source and subsequent laser annealing are reported. The results provided evidence that during implantation a silicon oxide surface layer rich in arsenic is formed similarly to the one reported in earlier publications [180], [181]. However, it was unclear if the formation of this layer is caused by the implantation process itself or if it is a post-implantation effect due to a reaction with atmosphere. Furthermore, the measured arsenic total dose after laser annealing was several times larger than both, the nominal value as well as the value for the 'as implanted' sample. In the second part of the chapter these phenomena were investigated more thoroughly using two silicon wafers produced in a similar way but capping one wafer with a SiN_x protective layer deposited on the surface right after the implantation and before exposing the wafer to the atmosphere. This cap allowed preserving the original state of the material. SIMS analysis showed that in samples with the deposited cap the As-rich oxide layer did not form, providing evidence that this layer is due to the interaction of the implanted surface with atmosphere. In addition, analysis of the implanted material (not capped) during the first weeks after the implantation revealed the spontaneous formation of arsenolite

micrometric crystals (As_2O_3) on the surface at room temperature. At the end of this chapter a hypothesis for the involved processes is presented.

6.2 Sample description and analytical conditions

Samples were fabricated on (100) Si wafers irradiated by P3i using AsH_3/H_2 plasma gas with the bias potential <2 kV in a sub 30 mTorr pressure. The studied samples can be divided into two main groups. The first group is based on a single 300 mm (100) Si wafer (S1) processed adjusting the doping parameters to implant a nominal Arsenic dose of ~$1x10^{15}$at/cm². This wafer was subsequently annealed by a pulsed laser using two laser powers. For each power, the applied thermal budget was varied increasing the number of pulses. Table 6.1 shows the matrix of S1 based samples.

Table 6.1. Summary of the analyzed samples. All the samples were produced on the same wafer S1.

Laser pulses	N pulses	3xN pulses	10xN pulses	30xN pulses
Low laser power (L)	S1L1	S1L2	S1L3	S1L4
High laser power (H)	S1H1	S1H2	S1H3	S1H4

The second group was formed by two wafers (S2 and S3) fabricated using the same implant condition as for S1, but on wafer S3 a ~1 nm thick protective film was deposited *in situ* after implantation and before exposing the irradiated surface to ambient atmosphere. This was done to prevent the highly reactive surface from interacting with oxygen in atmosphere. The uncapped wafer S2 revealed a presence of arsenolite crystals and to investigate thermal stability of latter, sample S2 was subjected to a RTP thermal treatment at different times and temperatures (200°-900°C, 10-300s) in nitrogen atmosphere. The annealing was performed in a RTP annealer As-Micro (AnnealSYS) halogen lamp system, with a heating ramp rate of ~100°C/s. The details of the RTP system are reported in section 4.1.

In addition, three samples were used as references for EXAFS measurements. The first, identified as 'MR24', is a (100) Si Cz wafer uniformly doped with arsenic with concentration of $3.55x10^{19}$ at/cm^3, traceable to NIST standard reference material 2134. This sample was used as a reference for substitutional As in Si. The second sample (SO5) is a 5 keV $7x10^{14}$at/cm^2 As^+ ion implant carried out on an 11 nm SiO_2 layer deposited on Si (100) (the same as used in chapter 3) with ~83% of arsenic located in the SiO_2 layer. The last sample (Ref-A) was a 3kev arsenic ion implanted (100) silicon substrate with $1.25x10^{14}$ cm^{-2} fluence independently measured with other analytical techniques [128].

SiMS analyses were carried out as described in section 5.2 and all the considerations regarding SIMS accuracy due to high As concentration and presence of composition gradients and interfaces in the depth of interest are relevant also for this study. $^{75}As^-$ ions were preferred to the more intense $^{28}Si^{75}As^-$

since at extremely high As concentration, less Si atoms are available to form the SiAs species introducing further deviations from linearity.

Selected samples were measured using instrumental nuclear activation analysis (INAA) in order to obtain the total arsenic dose and cross-check SIMS results. INAA analysis was carried out at the TRIGA Mark II reactor of the Atominstitut, Vienna University of Technology, with the conditions described in section 2.4.1.

The atomic local order around As atoms was investigated by extended x-ray absorption fine structure (EXAFS) analysis. Measurements were carried out in fluorescence mode at angles of incidence of 0.34 and 0.05 degrees (well above and below the critical angle of total reflection) to probe either the whole As distribution or the topmost surface. The detailed analytical conditions are described in section 2.4.2.

6.3 Formation of As-rich silicon oxide after plasma immersion ion implantation

Figure 6.1 shows SIMS As profiles of S1 samples: the left plot (a) contains profiles of samples annealed using low laser power and the right plot (b) corresponds to the high power laser ones. The SIMS profiles revealed a different thickness of the oxide layer on the surface depending on the annealing conditions. Therefore, profiles were aligned at the SiO_2/Si interface identified as the point where the $^{18}O^-$ ion signal drops to 50% of its value in oxide.

SIMS profiles of as implanted samples (figure 6.1, black line) show a shallow distribution of As in Si (as expected) but also the presence of a relatively thick (~8 nm) oxide layer. This layer has a very high As concentration, at the order of $1x10^{21}$ at/cm^3. This oxide layer is still present after low power laser annealing (S1L) and actually its thickness increases with number of laser pulses, up to 13 nm for sample S1L3. However, sample S1L4 presents an oxide thickness drastically reduced and a higher total As concentration. In general, the oxide layers of samples annealed with the high power laser radiation always show the same thickness, about 5-7 times thinner (~3 nm) than in the low power case. All the values measured for oxide thickness are reported in table 6.2.

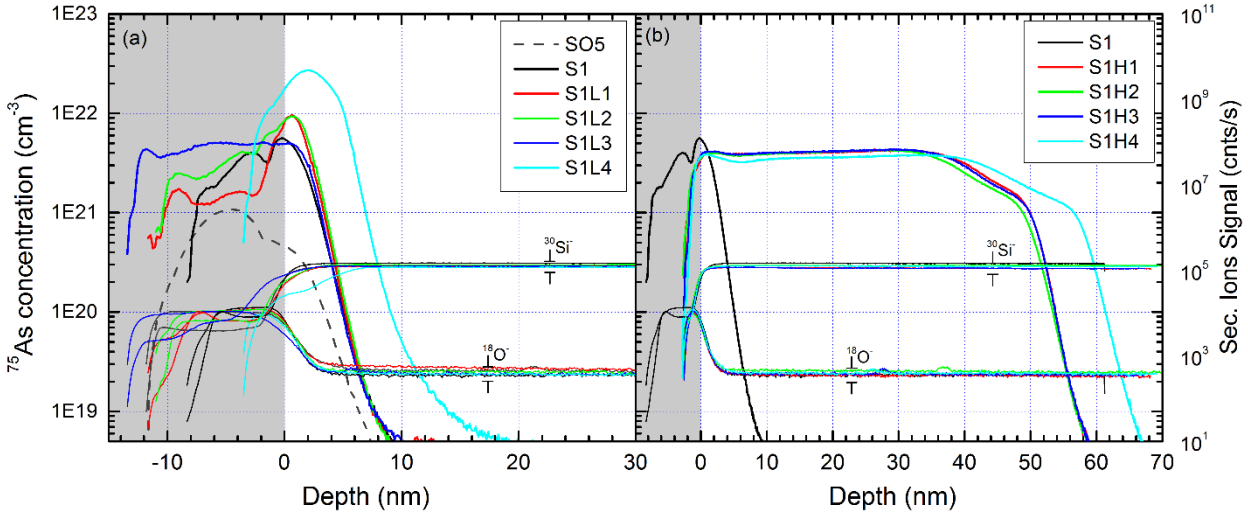

Figure 6.1. SIMS profiles of S1 samples. Arsenic profiles were aligned at SiO_2/Si interface as identified from $^{18}O^-$ signal. $^{30}Si^-$ and $^{18}O^-$ qualitative signals refer to the right axis.

The most important feature of the oxide layer in S1L samples is that it contains a significant fraction of the dopant (up to 73 % for S1L3). Assuming that the concentrations measured in oxide (10%) are accurate or at least close to the real ones, this layer cannot be considered as simple SiO_2 but more likely as Si-As-O mixture. This fact complicates SIMS quantification and can cause a deviation of the measured arsenic distribution from the real one. On the other hand, in the high power annealed samples almost all arsenic (97-98%) is inside silicon. The box-like shape of these profile together with very deep arsenic distribution suggest that the laser annealing at this energy melted the material causing a strong As diffusion in depth.

Another general result, true for all samples, is that the total amount of arsenic measured by SIMS after laser annealing is larger than the value for the 'as implanted' one, especially for high power samples. INAA analysis was performed to cross check the SIMS results. The total arsenic fluencies as obtained by both techniques are reported in the table 6.2 and figure 6.2 depicts the direct comparison of the two techniques.

The beamline implanted sample (SO5) is the only one of this set where a good agreement between SIMS and INAA was found (the difference is less than 1%). Samples S1H also show reasonable agreement; however, the fluence measured by SIMS is always higher compared to the INAA value. This discrepancy is most likely caused by the very high concentration of arsenic which leads to a non-linear dependence between detected ion signal and the real arsenic concentration. The low power laser annealed series shows much higher discrepancies: in all samples the dose obtained by SIMS is almost three times higher than the one obtained by INAA. Since these samples contain a relevant fraction of arsenic in the oxide layer, the discrepancies in the dose evaluation can be ascribed to the quantification of this region that probably cannot be treated as stoichiometric SiO_2.

Table 6.2. Results of SIMS and INAA measurements of total retained As doses. Nominal fluence in S1 sample was $1x10^{15}$ cm^{-2}. SiO_2 thicknesses and fraction of As dose in SiO_2 as determined by SIMS are reported as well.

Sample	SIMS fluence, cm^{-2}	INAA fluence, cm^{-2}	SIMS/INAA ratio	Thickness of SiO_2, nm	Part of As in SiO_2, %
SO5	$7.5x10^{14}$	$7.52x10^{14}$	0.99	11.5	83.1
S1	$3.5x10^{15}$	$1.27x10^{15}$	2.77	8.4	66.8
S1L1	$4.5x10^{15}$	$1.81x10^{15}$	2.49	11.7	49.0
S1L2	$6.0x10^{15}$	$1.93x10^{15}$	3.13	11.3	58.7
S1L3	$7.7x10^{15}$	$2.51x10^{15}$	3.05	12.6	72.9
S1L4	$1.5x10^{16}$	$4.74x10^{15}$	3.17	3.6	17.0
S1H1	$1.9x10^{16}$	$1.39x10^{16}$	1.36	2.7	2.5
S1H2	$1.7x10^{16}$	$1.45x10^{16}$	1.19	2.7	2.8
S1H3	$1.\ 9x10^{16}$	$1.32x10^{16}$	1.43	2.7	2.4
S1H4	$1.9x10^{16}$	$1.31x10^{16}$	1.42	3.0	2.1

Nevertheless, INAA measurements confirm that retained arsenic dose after annealing is higher with respect to the 'as implanted' value (figure 6.2). For the low power laser treatment, the total arsenic dose increases with the number of pulses whereas for the high power it remains almost constant suggesting that the source of arsenic which is responsible for this increase is limited. The sample S1L4 (annealed with the highest number of low power laser pulses) seems to be in an intermediate state between the extremes of the annealing conditions. Although the total dose and oxide thickness determined by SIMS would suggest the association of this sample to the high power group, the INAA results and the fact that this sample did not show a deep As distribution suggest that no melting was induced.

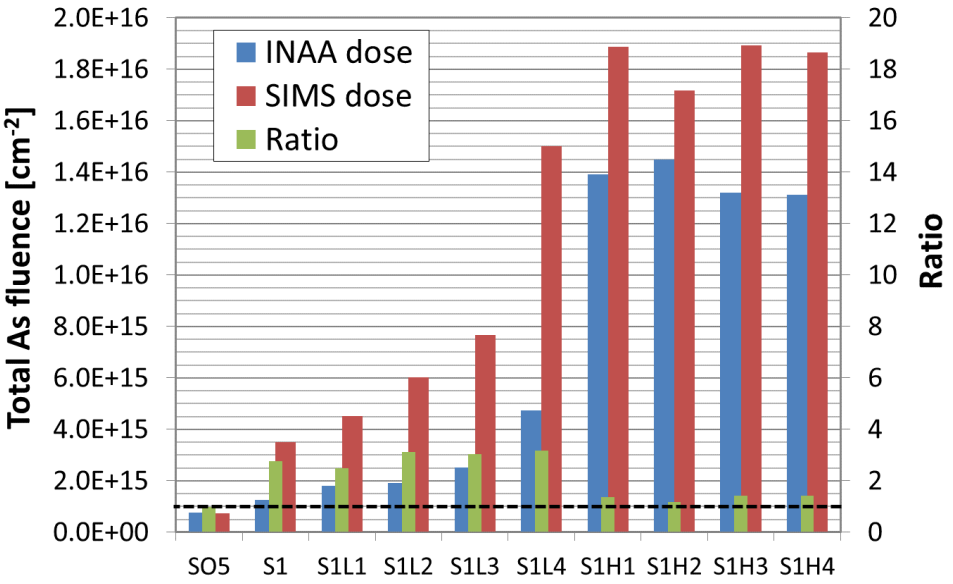

Figure 6.2. Comparison of total dose obtained by SIMS (red bars) and INAA (blue bars). Ratios between the SIMS and the INAA values are plotted in green and refer to the right axis. The nominal dose ($1x10^{15}$ cm^{-2}) on the left axis corresponds to the value of 1 on the left.

Fourier transforms (FT) of the EXAFS functions measured for the samples are displayed in figure 6.3. The results confirm most observations made from SIMS measurements. On the left plot (a) FT - EXAFS of samples annealed by the low power laser are presented in comparison with the SO5 sample, where more than 80% of arsenic is contained in the oxide layer. Peaks at 1.38 Å corresponding to the arsenic-oxygen bonding (labeled "As-O") indicate that samples contain a significant amount of arsenic within the SiO_2 layer. This is not true for the S1L4 sample (annealed with the highest number of pulses) which does not show any detectable As-O bonding, suggesting that most of the dopant is located below the SiO_2/Si interface. This agrees with the SIMS measurements that showed much thinner oxide thickness for this sample compared to the other samples of this group. Finally, none of the S1L samples showed a high local order like in MR24 standard. This indicates that the annealing at this power was not sufficient to significantly restore the crystal damage and that no detectable local order around the As atoms exists beyond the first coordination shell.

In the samples annealed with high power laser (figure 6.3, b), the As-O peak is absent similarly to the S1L4 sample. The part of arsenic in the oxide layer detected by SIMS can be considered below the detection limit. In this case the As-Si related peaks at 2 Å is higher, with the same peak position as in the reference sample for substitutional arsenic in Si (MR24), and also the peaks relative to the second and third coordination shells at about 3.4 Å and 4.1 Å are clearly visible. The weaker amplitudes indicate that the fraction of substitutional arsenic is lower than in the standard. As discussed in the previous chapter, at this high concentration arsenic can be involved in the formation of inactive clusters like As_nV and SiAs precipitates [145], [182]. Finally, the substitutional fraction in the samples is not affected by the number of laser pulses and EXAFS fitting reported in [183] estimates the substitutional fraction to be 25% for all these samples.

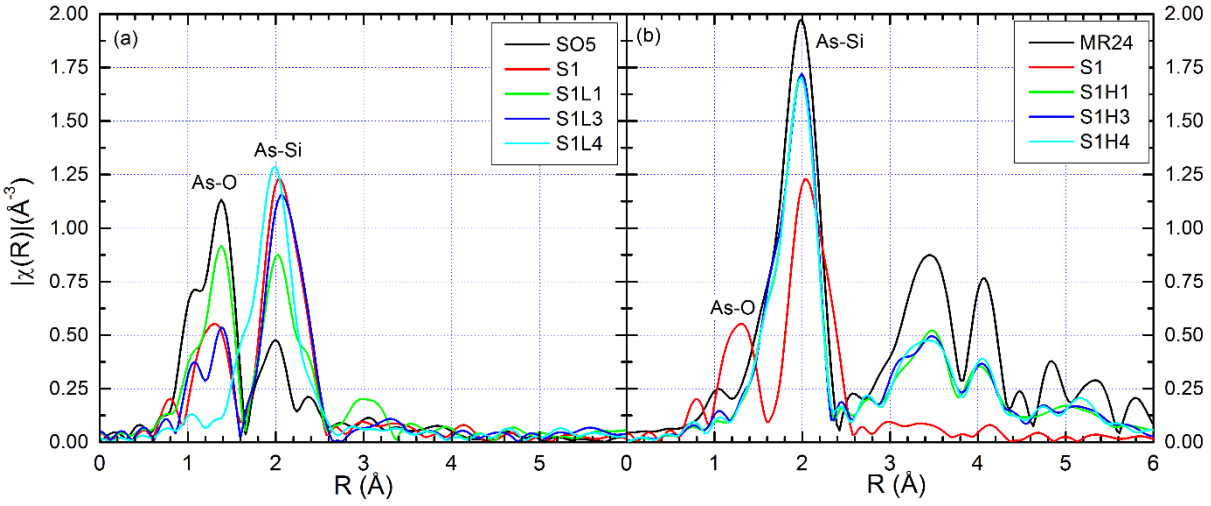

Figure 6.3. Fourier transform of EXAFS functions measured on selected P3i samples and two standards MR24 (substitutional As in SI) and SO5 (As in SiO_2). The labels indicate the peaks corresponding to the first coordination shell of As-O and As-Si structures.

6.4 Arsenic enhanced oxidation

The large degree of oxidation observed on the S1 samples can be ascribed to the high concentration of arsenic. Arsenic enhanced oxidation has already been reported e [184]. However, the temperature at which this phenomenon was observed exceeded 500°C whereas in the S1 'as implanted' sample it occurred already at room temperature. Since the first set of samples was analyzed months after implantation, a new wafer was prepared in order to investigate the behavior of the surface at the early stages of air exposure after P3i. Samples S2 and S3 were implanted similarly to the ones reported in the previous section. A protective SiN_x film ~1 nm thick was deposited at low temperature *in situ* on the surface of S3 wafer to prevent it from being exposed to the atmosphere and preserve the original surface state.

The first SIMS analysis was carried out 27 days after plasma implantation. As expected, in the capped sample S3 no formation of an oxide layer was detected. This clearly indicates that the As-rich oxide layer observed on sample S1 was not deposited during P3i but grown after exposing the wafer surface to atmosphere. Successive analysis, carried out during a six month period, revealed no change in the surface region, i.e. no oxide growth (figure 6.4, green and dark green lines).

However, in sample S2, the presence of a 2 nm thick oxide layer with a very high concentration of arsenic (figure 6.4, red line) was detected after 27 days. After ~50 days in atmosphere, this oxide layer increased from 2 to almost 5 nm (figure 6.4, dark red line). Part of the arsenic was redistributed in the growing oxide layer without any significant loss of total amount of dopant: the arsenic fluence measured was $4.3x10^{15}$ and $4.0x10^{15}$ cm^{-2}, respectively. Considering SIMS accuracy, the small difference is within the uncertainty and thus the total dose can be considered as constant. However, the total amount of arsenic measured on the capped sample (S3) is almost two times larger than the one of S2, i.e. $7.7x10^{15}$ cm^{-2}. This indicates that a relevant fraction of the dopant was lost during the first month of air exposure.

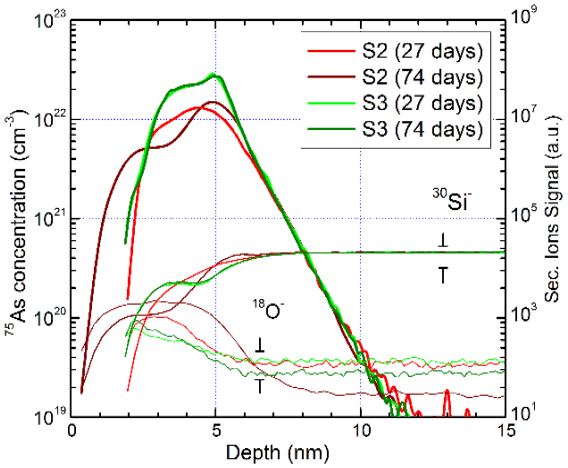

Figure 6.4. Arsenic distribution is S2 and S3 samples after 27 and 74 days after plasma implantation.

The further oxidation as monitored by SIMS is presented in Figure 6.5. Several measurements were done during a 27-360 days period. The general behavior is a progressive oxide growth within the first year of air exposure with saturation at ~7nm thickness. The dashed line represents an exponential fit of the data using the following equation:

$$\text{Oxide thickness} = 7.21 - 5.84 \cdot e^{\frac{-\text{time(days)}}{144.9}}\ nm \qquad (6.1)$$

After 1 year no further oxidation was detected. A similar oxide thickness was measured on sample S1 (previous section), i.e. 8.4 nm.

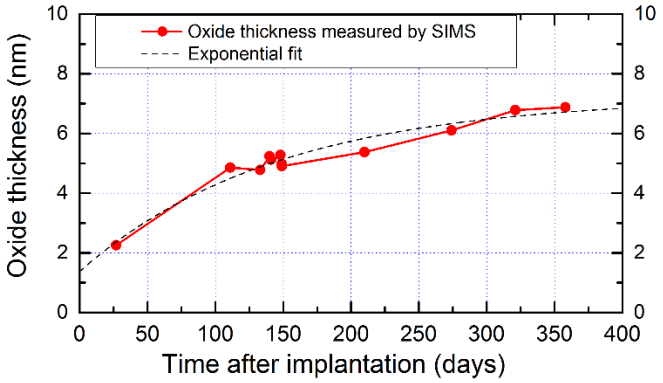

Figure 6.5. Oxide thickness of S2 sample measured by SIMS at different time after implantation. The data was fitted with exponential function (dash curve)

6.5 Formation of arsenolite microcrystals

Another phenomenon was observed on sample S2 when its surface was inspected by scanning electron microscopy (SEM). A dense distribution of regular crystals of different sizes (10 nm - 1 µm) was observed on the surface as shown in figure 6.6. This SEM plan view was obtained two months after implantation but earlier crystal formation was observed already within one week after implantation. In fact, density (~1.9×10^6 cm^{-2}) and micro-metric size of most crystals allowed their detection by optical microscopy at high magnification. Some crystals appeared not to be single particles but an agglomeration of smaller ones, e.g. the biggest complexes on the figure 6.6. Energy dispersive x-ray analysis (EDX) of the crystals indicated that these crystals are rich in arsenic and oxygen but without any relevant concentration of silicon. EDX images are shown in figure 6.6 on the right panels.

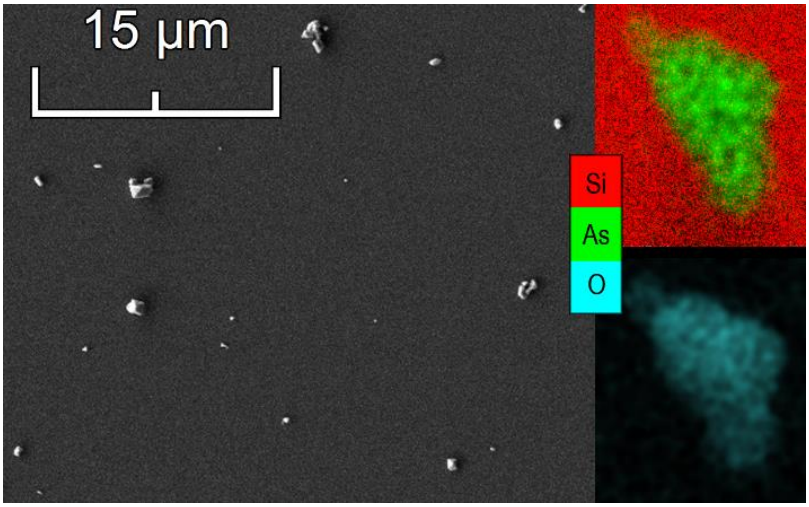

Figure 6.6. SEM plan view of S2 sample surface and EDX image of a ~1 µm crystal.

It is interesting to note, that the 20 keV electron beam used for EDX analysis caused a sublimation of the measured crystal indicating a limited thermal stability. A series of pictures taken after progressive time of electron irradiation on a crystal are shown in figure 6.7.

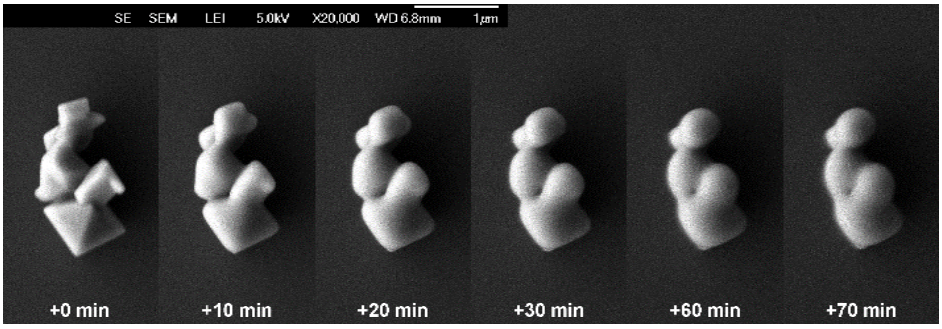

Figure 6.7. Evolution of an agglomerate of micro-crystals under electron beam irradiation during EDX analysis.

The S2 sample with crystals present on the surface was analyzed by grazing incidence EXAFS. Measurements were carried out at two different incidence angles below and above the critical angle of total reflection (0.05° and 0.34° respectively) probing either the whole arsenic distribution or the topmost surface [145], [185], [186]. The Fourier transforms of the EXAFS function recorded for sample S2 and for two standards (MR24 and SO5) are displayed in figure 6.8, a. The shallow angle FT of the EXAFS clearly shows a peak at ~1.38 Å corresponding to As seeing oxygen as nearest neighbor similar to the SO5 standard. Moreover, a strong second coordination shell appears at R≈2.9 Å. When the sample is measured at high incidence angle, these peaks become less evident and the peak related to the As-Si bonds appears at ~2 Å. This peak is slightly shifted toward larger bond lengths compared to the MR24 reference, suggesting that part of the arsenic has a different chemical state (which is reasonable assuming the very high concentration of arsenic in this sample). The comparison of the shallow angle EXAFS measurement with the expected curves calculated for arsenolite-As_2O_3 (figure 6.8, b) clearly reveals the presence of this phase/ compound on the surface. Therefore, EXAFS measurements not only confirmed the presence of arsenic oxide micro-crystals but also revealed that their phase is arsenolite.

Neither EXAFS nor SEM could confirm any presence of arsenolite crystals on the capped sample (S3). This suggest that the formation of the As_2O_3 crystals took place after P3i and when exposing the implanted surface to atmosphere.

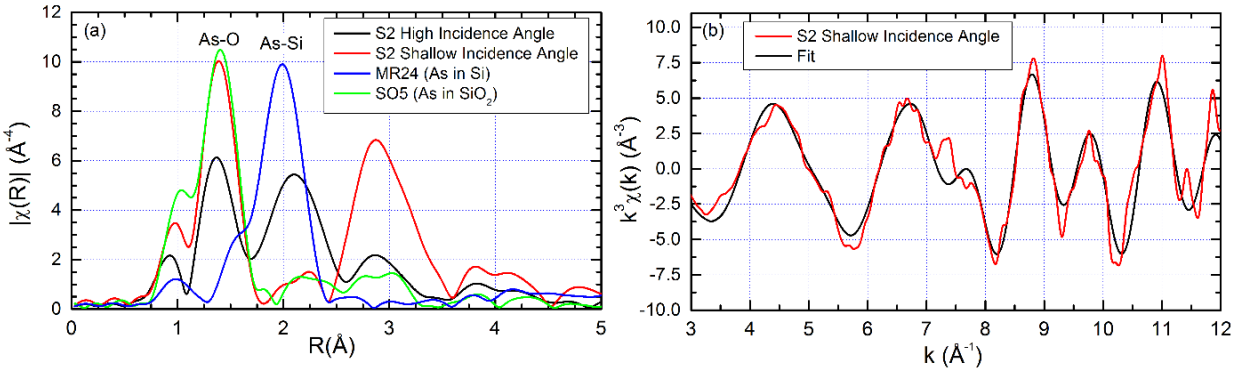

Figure 6.8. (a) Fourier transform of the EXAFS functions measured on sample S2 measured at high and shallow incidence angle, respectively. In the figure also measurements relative to standards Ref-A (substitutional As in Si) and SO5 (As in SiO_2) are reported. The labels indicate the FT peaks corresponding to the first coordination shell of As-O and As-Si structures. (b) EXAFS function measured at shallow angle on S2 together with a FEFF8 simulation using the theoretical As_2O_3 structure [187].

The amount of arsenic confined within these crystals was determined by INAA. The measurements were conducted on two specimens cut from S2 two months after P3i, one with crystals and the other with crystals mechanically removed from the surface. The doses obtained were 6.2 $x10^{15}$ and 3.5$x10^{15}$ cm^{-2} for the samples with and without crystals, respectively. This result indicates that at least 2.7$x10^{15}$ cm^{-2} of arsenic was contained inside the crystals on the samples surface. In fact, some crystals might have been lost during the transport/transfer and thus the real value can be higher. However, in sample S3 all implanted/deposited arsenic should have been preserved by the SiN_x cap. From SIMS measurements, this sample contains 7.7$x10^{15}$ cm^{-2} of arsenic which is very close to the number obtained by INAA for the uncapped sample including the crystals. This indicates that no significant arsenic loss occurred in sample S3.

6.6 Thermal treatment of the crystals

As reported in section 6.4, laser annealing of the samples resulted in a significant arsenic dose increase compared to the 'as implanted' one. The sample with crystals was processed by RTP at different temperatures (200°-900°C) in order to investigate any influence of the crystals on the retained arsenic dose, i.e. if the increase of the measured doses could be due to the dopant flowing from micro-crystals into the Si substrate. Depth profiles of sample S2 after three different thermal treatments are reported in figure 6.9, aligned at the SiO_2/Si interface. The total retained arsenic dose is reported in the legend. The SEM analysis of the sample surface after annealing did not show any presence of the arsenolite crystals. The total amount of arsenic in the silicon part is the same for all annealing conditions with only moderate - in-diffusion for the 900 °C treatment. There is instead a clear reduction of the arsenic dose in the oxide region depending on the temperature and the total retained doses were rather constant for all tested thermal treatments. These results indicate that although all crystals were removed from the surface as detected by SEM, the arsenic contained in these crystals was not driven through the oxide into silicon; presumably the crystals just sublimated.

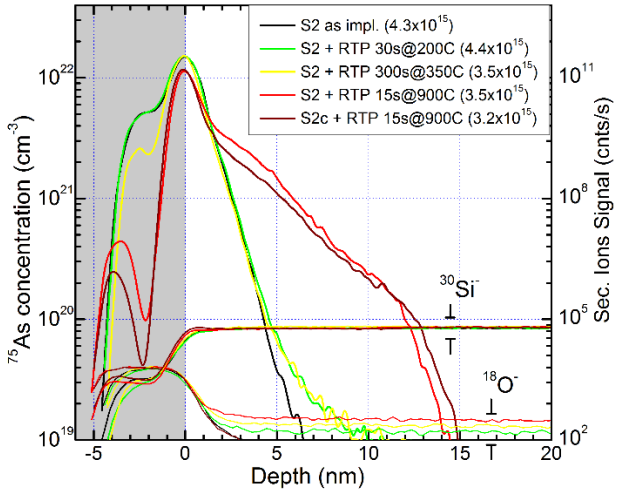

Figure 6.9. Arsenic depth profiles in S2 sample annealed with crystals after different thermal treatments. In S2c sample the crystal were removed before the annealing.

6.7 Discussion

SIMS measurement of sample S3 (capped) did not reveal any relevant changes of the arsenic distribution under the deposited cap after the first measurements, suggesting that the SiN_x layer preserved the original surface composition after implantation. Furthermore, the S3 SIMS profile (reported on the figure 6.4, green line reveals the presence of a very high As concentration (~10^{22} at/ cm^3) under the deposited cap which is not observed in sample S2. In the latter, the concentration of As in the near-surface layer as well as the total amount of As is almost two times lower than in the capped sample. Furthermore, sample S2 showed a growth of the oxide layer where As is redistributed without any relevant loss. The oxide growth saturated at 7.2 nm thickness only after several months of air exposure. In addition, during the first weeks after implantation arsenolite microcrystals grew on the sample surface absorbing at least 2.7x10^{15} cm^{-2} of arsenic according to INAA results. Assuming the atomic density of metallic arsenic as 4.6x10^{22} cm^{-3} (or 1.3x10^{15} cm^{-2} in a monolayer [188]) the amount of arsenic confined in the crystal corresponds to 2.1 monolayer of pure metallic arsenic. It is known that the P3i process can result also in the deposition of the implanted species as reported in Chapter 1. Therefore, it can be speculated that a ultra-thin layer of mainly metallic As was deposited on all 'as implanted' samples, being preserved in S3 by the SiN_x cap whereas in the others reactions with atmosphere can take place, resulting in the formation of arsenolite micro-crystals and an enhanced oxidation of the Si substrate. Similar behavior was already observed for GaAs samples [189–191]. Takagaki et al. [189] reported that similar arsenolite crystals were formed after few days of air exposure from an amorphous arsenic layer on a GaAs substrate. Those crystals easily sublimated at 200°C thermal treatment or under electron beam

irradiation. The presence of the deposited arsenic layer would also support the enhanced oxidation of the samples observed at room temperature.

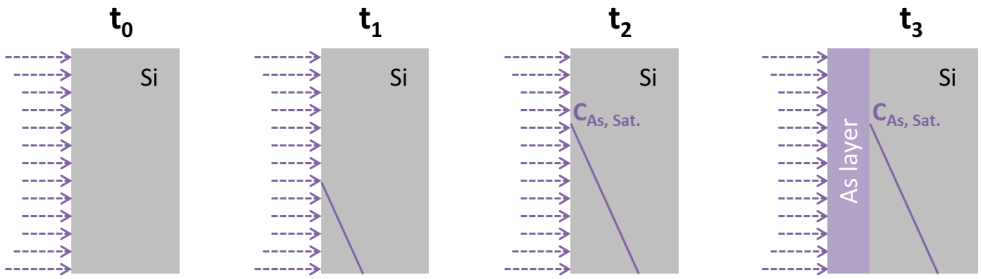

Figure 6.10. Illustration of the hypothesis of deposition of an ultra-thin As layer under high fluence P3i. (see text)

Based on those experimental evidences, the following physical mechanisms can be proposed to explain the processes going on in the sample surface during plasma implantation and on exposure to atmosphere (figure 6.10). The implantation starts at time t_0 when the wafer is exposed to the AsH_3 plasma. Arsenic atoms are implanted into the wafer creating an exponential distribution in the near-surface region (t_1). Increasing implantation time from t_1 to t_2 results in a progressively higher As concentration, especially at the surface, creating the exponential depth profile due to the continuous energy distribution. Since the matrix composition is changing to an As-rich one, the stopping power for impinging ions is modified resulting in shallower implantation. Eventually, a saturation level ($C_{As,sat}$) is reached (t_2). Afterwards, some arsenic atoms do not reach the silicon part anymore and start accumulating at the surface creating an As or As-rich layer (t_3).[9].

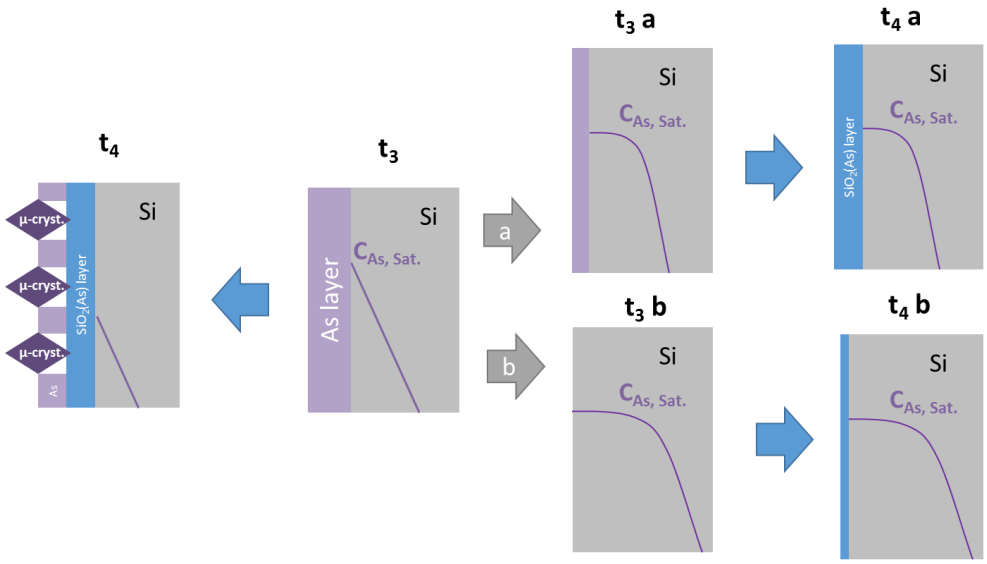

Figure 6.11. Model for high fluence P3i sample evolution when exposing to the atmosphere (see text).

Successively, when the sample is exposed to the atmosphere (figure 6.11), the thin As layer reacts with the oxygen contained in the ambient and arsenolite micro-crystals are formed. In addition, an enhanced oxidation process starts (t_4), being driven by the high concentration of arsenic at the surface. In

fact, the wafer surface after P3i is expected to be very reactive due to exposed dangling bonds. After this phase, almost half of the deposited arsenic is lost due to the formation of the microcrystals. The latter, once formed, sublimate upon annealing. The results is a retained As dose much lower than the one originally implanted which can be preserved only if a protective cap is deposited before atmosphere exposure.

However, this surface reaction can be avoided by a laser annealing treatment before prolonged air exposure. In fact, depending on the laser power, two effects can be observed: i) If the laser annealing is carried out at low power (t_3, a), an arsenic fraction will diffuse into the substrate but the remaining As fraction on surface will enhance oxidation and possibly trigger arsenolite formation. ii) When the laser power is high enough to melt the near-surface region, the layer of high arsenic concentration is distributed in depth (t_3, b). It is worth to remember that at high As concentration, an eutectic point is expected at 1097°C at equilibrium [79] and thus melting can be enhanced also at lower temperatures compared to pure Si. Consequently, all the originally implanted/deposited As can be incorporated in the Si matrix and the measurable retained As dose is very high. Finally, after high power LA, the arsenic concentration at the surface becomes too low to trigger an enhanced oxidation and only a few nm (2-3 nm) thick oxide will form (t_4, b), i.e. with a thickness similar to typical native oxide.

6.8 Conclusion

The combination of P3I and pulsed laser annealing is a very promising approach for arsenic high dose USJ formation. However it requires accurate optimization of the laser parameters in order to obtain the stability needed for the transfer to production.

An As-rich layer is deposited during implantation inducing an enhanced oxidation and formation of arsenolite (As_2O_3) crystals within a week after deposition. However, once the crystals form they can be sublimated with a low temperature thermal treatment without any relevant diffusion of dopant into the substrate. This is important for the integration of the process in semiconductor fabrication because the implanted wafer experience a similar thermal treatment during a photoresists strip process in hot acid. The subsequent cleaning of the resist can be used to remove the deposited arsenic layer and\or formed microcrystal together with As-rich oxide. Without the reactive surface layer the wafers can be treated like any other high-dose low energy arsenic implants during the following activation annealing step.

CONCLUSION

The study presented in this thesis is focused on the investigation of Arsenic ultra-shallow distributions in Si for applications as SDE dopant in CMOS technology. Three different approaches to form As USJ were investigated to understand their physical mechanisms to verify their possible application in next generation microelectronics devices.

The main analytical technique used in present work is SIMS and work has been done to improve its ability to depth profiling shallow dopant distribution in Si. Particular attention was given to the accurate quantification of near-surface region where SIMS experiences artefacts due to presence of native oxide layer and non-equilibrium sputtering. These effects result in measured shallower distributions, i.e. depth profiles are shifted to the surface. The proposed correction model was able to eliminate these issues when applied to beam-line ion implant distributions confined within the first 10 nm from surface. In the study MEIS technique was used as a reference. The corrected SIMS profiles are able to provide the main information about dopant distribution shape with accuracy comparable to MEIS technique but they provide excellent detection limit, exceeding the MEIS one of 2-3 orders of magnitude. Although this model was built for a specific experimental conditions (300 eV Cs^+ bombardment) for As implants in silicon, it can be extended for application to different compositions once the defining parameters are determined.

Using the accurate SIMS measurements the evolution of arsenic shallow distribution was investigated with reference to the metastable electrical activation and the successive deactivation under moderate thermal treatment (550-700°C).

Two different approaches of thermal activation of arsenic in shallow junction were studied. The first one is the low temperature (550°C) solid-phase epitaxial re-growth of beam line implanted distributions. Measurements made by SIMS and MEIS captured different stages of SPER showing significant redistribution of dopant following the a/c interface. In fact, the observed redistribution is connected to the layer-by-layer recrystallization mechanism when the dopant atoms segregate at the interface and swept toward the surface. A model for As redistribution giving a good agreement with experimental results for different As concentrations was proposed. The dopant involved in the redistribution eventually becomes inactive and is segregated at the SiO_2 interface. The dopant left below the a/c interface is placed into substitutional position giving a high level of electrical activation. No significant in-depth diffusion was noticed. However, a quick deactivation of dopant occurs if the thermal treatment continues for longer time (at the same low temperature) indicating a high instability of junctions prepared by SPER.

A range of deactivation studies was performed using USJ activated by SPER and msec sub-melt LA, with more attention given to the latter. The stability during thermal treatments at 550° and 700°C was

monitored using buried delta layers doped with boron to act as 'interstitial detectors'. It was observed that even low temperature annealing is accompanied with a high flux of interstitials coming from the doped region. The TED of boron layer is caused by interstitials coming from two sources: arsenic deactivation due to clustering with point defects and lattice defect dissolution. The contribution of the latter was monitored using samples implanted with Ge which should provide lattice damage similar to As implantation. The different LA conditions (with thermal budget corresponding to the different temperature at the surface) produced similar As distributions with essentially no diffusion. However, the behavior of dopant distributions was very different during successive thermal treatment at 700°C. The reduction of boron TED for the 1300°C annealed As implanted samples is dramatic when compared to what was observed for the not laser annealed series, suggesting that at this temperature laser annealing can successfully remove most of the defects and restore all lattice damage. However, if the samples are activated at low temperature LA (1100°C) the B TED appeared be much higher than for the 1300°C LA. Furthermore, at this temperature TED in Ge implanted material appeared higher that in As one indicating that presence of dopant could affect the flux of interstitial. The discussion of experimental evidences suggested that in case of excess self-interstitials, arsenic atoms can be involved in the formation of clusters involving interstitials (As_nI_m) beside the usually expected vacancy-based clusters (As_nV_m).

Plasma ion immersion implantation together with the LA was considered as the third approach of arsenic ultra-shallow junction formation. Samples created by AsH_3^+ plasma were investigated with respect to arsenic distribution, silicon oxide thickness and arsenic local order using SIMS, INAA, and EXAFS analysis. SIMS measurement revealed the formation of thick oxide layers, rich in As and with a thickness depending on the laser annealing conditions. Additionally, a significant increase in total arsenic fluence was detected after laser annealing (up to 15x compared to the not annealed sample, according to INAA). Deposition of a protective cap *in situ* after plasma implantation prevented the formation of the thick oxide layer suggesting that the formation of this layer is the result of exposing sample surface to the atmosphere. The thickness of the oxide layer in not capped samples progressively increased during almost a year after implantation saturating at a value of 7.3 nm. Moreover, the spontaneous formation of arsenolite crystals (As_2O_3) was observed on the surface of not capped samples within a week of exposing sample surface to the air. The crystals easily sublimates at 200°C not contributing to the total amount of dopant in the samples. It is speculated that during the plasma implantation an ultra-thin (~2ML) As-rich layer was deposited on the surface of the samples. Subsequently if this layer is exposed to atmosphere, it reacts forming As_2O_3 micro-crystals and 'triggering' an enhanced oxidation of the surface. Finally, LA can drive part of the arsenic from this layer into the substrate thereby increasing the total amount of retained arsenic, otherwise lost in crystal formation.

Therefore, this research showed that integration of advanced doping schemes for As USJ in Si are possible once the main mechanisms behind As TED, clustering and in general dose loss are solved. In

particular, among the investigated annealing approaches, sub-melt LA resulted very promising in terms of x_j shallowness and stability as long as the LA temperature is relatively high. Otherwise, the interstitials left by a low temperature LA can interact with As atoms forming clusters and triggering TED. Plasma immersion ion implantation can be preferred to BL since it ensures very high dopant concentration and x_j ~10 nm, but the high reactivity of the irradiated surface is an issue. This can be avoided as long as an ultra-thin (~1 nm) cap layer is deposited in situ after P3i. Alternatively, annealing has to be carried right after implantation and possibly without atmosphere exposure in order to drive-in dopant without any loss in As_2O_3 micro-crystals and SiO_2 growth.

References

[1] L. A. W. R. Z. Shon-Roy, *Advanced Semiconductor Fabrication Handbook*. Scottsdale: Integrated Circuit Engingeering, 1998.

[2] "ITRS 2012," 2012. [Online]. Available: http://www.itrs.net/.

[3] Intel, "Moore's Law 40th Anniversary." [Online]. Available: http://www.intel.com/pressroom/kits/events/moores_law_40th/. [Accessed: 20-Feb-2013].

[4] M. Bohr and K. Mistry, "Intel's Revolutionary 22 nm Transistor Technology." 2011.

[5] J. F. Ziegler, J. P. Biersack, and U. Littmark, *The stopping and range of ions in solids*. New York: Pergamon, 1985, p. 321.

[6] K. Cho, W. R. Allen, T. G. Finstad, W. K. Chu, J. Liu, and J. J. Wortman, "Channeling effect for low energy ion implantation in Si," *Nuclear Instruments and Methods in Physics Research Section B: Beam Interactions with Materials and Atoms*, vol. 7–8, pp. 265–272, Mar. 1985.

[7] a. E. Michel, R. H. Kastl, S. R. Mader, B. J. Masters, and J. a. Gardner, "Channeling in low energy boron ion implantation," *Applied Physics Letters*, vol. 44, no. 4, p. 404, 1984.

[8] E. J. H. Collart, "Characterization of low-energy (100 eV–10 keV) boron ion implantation," *Journal of Vacuum Science & Technology B: Microelectronics and Nanometer Structures*, vol. 16, no. 1, p. 280, Jan. 1998.

[9] E. C. Jones, "Anomalous behavior of shallow BF3 plasma immersion ion implantation," *Journal of Vacuum Science & Technology B: Microelectronics and Nanometer Structures*, vol. 12, no. 2, p. 956, Mar. 1994.

[10] J. M. Ha, J. W. Park, W. S. Kim, S. P. Kikm, W. S. Song, H. S. Kim, H. J. Song, K. Fujihara, H. K. Kang, M. Y. Lee, S. Felch, U. Jeong, M. Goeckner, K. H. Shim, H. J. Kim, H. T. Cho, Y. K. Kim, D. H. Ko, and G. C. Lee, "High performance pMOSFET with BF/sub 3/ plasma doped gate/source/drain and S/D extension," in *International Electron Devices Meeting 1998. Technical Digest (Cat. No.98CH36217)*, 1998, pp. 639–642.

[11] S. Qin, A. McTeer, J. Hu, J. Liu, D. Panda, and J. Trivedi, "Plasma doping on 68nm CMOS device source/drain formations," in *Extended Abstracts - 2008 8th International Workshop on Junction Technology (IWJT '08)*, 2008, pp. 8–13.

[12] "SRIM," 2013. [Online]. Available: http://www.srim.org/. [Accessed: 20-Feb-2013].

[13] J. F. Ziegler, Ed., *Ion Implantation: Science and Technology*. Chester: Ion Implantation Technology Co., 2006.

[14] G. OLSON and J. ROTH, "Kinetics of solid phase crystallization in amorphous silicon," *Materials Science Reports*, vol. 3, no. 1, pp. 1–77, 1988.

[15] L. Csepregi, E. F. Kennedy, J. W. Mayer, and T. W. Sigmon, "Substrate-orientation dependence of the epitaxial regrowth rate from Si-implanted amorphous Si," *Journal of Applied Physics*, vol. 49, no. 7, p. 3906, 1978.

[16] H. Müller, W. K. Chu, J. Gyulai, J. W. Mayer, T. W. Sigmon, and T. R. Cass, “Crystal orientation dependence of residual disorder in As−implanted Si,” *Applied Physics Letters*, vol. 26, no. 6, p. 292, 1975.

[17] J. S. Williams and R. G. Elliman, “Limits to solid solubility in ion implanted silicon,” *Nuclear Instruments and Methods*, vol. 182–183, pp. 389–395, Apr. 1981.

[18] J. S. Williams and R. G. Elliman, “Near-surface regrowth rate effects in high-dose ion-implanted (100) silicon,” *Applied Physics Letters*, vol. 37, no. 9, p. 829, 1980.

[19] J. S. Williams, “Substitutional solid solubility limits during solid phase epitaxy of ion implanted (100) silicon,” *Applied Physics Letters*, vol. 40, no. 3, p. 266, 1982.

[20] E. F. Kennedy, L. Csepregi, J. W. Mayer, and T. W. Sigmon, “Influence of 16O, 12C, 14N, and noble gases on the crystallization of amorphous Si layers,” *Journal of Applied Physics*, vol. 48, no. 10, p. 4241, 1977.

[21] A. Claverie, B. Colombeau, B. de Mauduit, C. Bonafos, X. Hebras, G. Ben Assayag, and F. Cristiano, “Extended defects in shallow implants,” *Applied Physics A: Materials Science & Processing*, vol. 76, no. 7, pp. 1025–1033, May 2003.

[22] P. M. Rousseau, P. B. Griffin, and J. D. Plummer, “Electrical deactivation of arsenic as a source of point defects,” *Applied Physics Letters*, vol. 65, no. 5, p. 578, 1994.

[23] N. Kong, S. K. Banerjee, T. a. Kirichenko, S. G. H. Anderson, and M. C. Foisy, “Enhanced and retarded diffusion of arsenic in silicon by point defect engineering,” *Applied Physics Letters*, vol. 90, no. 6, p. 062107, 2007.

[24] A. Agarwal, H.-J. Gossmann, D. . Eaglesham, L. Pelaz, D. . Jacobson, J. . Poate, and T. . Haynes, “Critical issues in ion implantation of silicon below 5 keV: Defects and diffusion,” *Materials Science and Engineering: A*, vol. 253, no. 1–2, pp. 269–274, Sep. 1998.

[25] L. Laanab, C. Bergaud, M. M. Faye, J. Faure, A. Martinez, and A. Claverie, “A Model to Explain the Variations of ‘End-of-Range’ Defect Densities with Ion Implantation Parameters,” *MRS Proceedings*, vol. 279, p. 381, Feb. 2011.

[26] J. W. Corbett, J. P. Karins, and T. Y. Tan, “Ion-induced defects in semiconductors,” *Nuclear Instruments and Methods*, vol. 182–183, pp. 457–476, Apr. 1981.

[27] N. Cowern, G. Mannino, P. Stolk, F. Roozeboom, H. Huizing, J. van Berkum, F. Cristiano, A. Claverie, and M. Jaraíz, “Energetics of Self-Interstitial Clusters in Si,” *Physical Review Letters*, vol. 82, no. 22, pp. 4460–4463, May 1999.

[28] K. S. Jones, S. Prussin, and E. R. Weber, “A systematic analysis of defects in ion-implanted silicon,” *Applied Physics A*, vol. 45, no. 1, pp. 1–34, Jan. 1988.

[29] A. Claverie, L. Giles, M. Omri, B. de Mauduit, G. Ben Assayag, and D. Mathiot, “Nucleation, growth and dissolution of extended defects in implanted Si: impact on dopant diffusion,” *Nuclear Instruments and Methods in Physics Research Section B: Beam Interactions with Materials and Atoms*, vol. 147, no. 1–4, pp. 1–12, Jan. 1999.

[30] C. Bonafos, D. Mathiot, and A. Claverie, “Ostwald ripening of end-of-range defects in silicon,” *Journal of Applied Physics*, vol. 83, no. 6, p. 3008, 1998.

[31] N. Cowern, G. van de Walle, P. Zalm, and D. Oostra, “Reactions of point defects and dopant atoms in silicon,” *Physical Review Letters*, vol. 69, no. 1, pp. 116–119, Jul. 1992.

[32] P. M. Fahey, P. B. Griffin, and J. D. Plummer, “Point defects and dopant diffusion in silicon,” *Reviews of Modern Physics*, vol. 61, no. 2, pp. 289–384, Apr. 1989.

[33] F. Cristiano, E. M. Bazizi, P. F. Fazzini, S. Paul, W. Lerch, S. Boninelli, R. Duffy, A. Pakfar, H. Bourdon, and F. Milesi, “Defect evolution and C+/F+ co-implantation in millisecond Flash annealed ultra-shallow junctions,” in *Extended Abstracts - 2008 8th International Workshop on Junction Technology (IWJT ’08)*, 2008, vol. 1, pp. 114–119.

[34] J. a. Sharp, a. J. Smith, R. P. Webb, K. J. Kirkby, N. E. B. Cowern, D. Giubertoni, S. Gennaro, M. Bersani, M. a. Foad, P. F. Fazzini, and F. Cristiano, “Surface proximity and boron concentration effects on end-of-range defect formation during nonmelt laser annealing,” *Applied Physics Letters*, vol. 92, no. 8, p. 082109, 2008.

[35] R. Brindos, P. Keys, K. S. Jones, and M. E. Law, “Effect of arsenic doping on {311} defect dissolution in silicon,” *Applied Physics Letters*, vol. 75, no. 2, p. 229, 1999.

[36] H. Bracht, “Diffusion Mechanisms and Intrinsic Point-Defect Properties in Silicon,” *MRS Bulletin*, vol. 25, no. 06, pp. 22–27, Jan. 2011.

[37] E. Irene, *Electronic materials science*. Wiley-Interscience, 2005.

[38] W. Lerch, M. Glück, N. A. Stolwijk, H. Walk, M. Schäfer, S. D. Marcus, D. F. Downey, J. W. Chow, and H. Marquardt, “Simulation of Rapid Thermal Annealed Boron Ultra-Shallow Junctions in Inert and Oxidizing Ambient,” *MRS Proceedings*, vol. 525, p. 237, Feb. 1998.

[39] a. E. Michel, W. Rausch, P. a. Ronsheim, and R. H. Kastl, “Rapid annealing and the anomalous diffusion of ion implanted boron into silicon,” *Applied Physics Letters*, vol. 50, no. 7, p. 416, 1987.

[40] D. J. Eaglesham, P. a. Stolk, H.-J. Gossmann, and J. M. Poate, “Implantation and transient B diffusion in Si: The source of the interstitials,” *Applied Physics Letters*, vol. 65, no. 18, p. 2305, 1994.

[41] L. H. Zhang, K. S. Jones, P. H. Chi, and D. S. Simons, “Transient enhanced diffusion without {311} defects in low energy B+-implanted silicon,” *Applied Physics Letters*, vol. 67, no. 14, p. 2025, 1995.

[42] C. Bonafos, M. Omri, B. de Mauduit, G. BenAssayag, A. Claverie, D. Alquier, A. Martinez, and D. Mathiot, “Transient enhanced diffusion of boron in presence of end-of-range defects,” *Journal of Applied Physics*, vol. 82, no. 6, p. 2855, 1997.

[43] L. S. Darken, “Diffusion, mobility and their interrelation through free energy in binary metallic systems,” *TRANSACTIONS OF THE METALLURGICAL SOCIETY OF AIME*, vol. 175, pp. 184–201, 1948.

[44] H. Tsuji, M. Furuhashi, M. Tachi, and K. Taniguchi, “Anomalous Uphill Diffusion and Dose Loss of Ultra-Low-Energy Implanted Boron in Silicon during Early Stage of Annealing,” *Japanese Journal of Applied Physics*, vol. 43, no. 3, pp. 873–876, Mar. 2004.

[45] A. Shima, T. Jinbo, N. Natsuaki, J. Ushio, J.-H. Oh, K. Ono, and M. Oshima, “A model for the segregation and pileup of boron at the SiO[sub 2]/Si interface during the formation of ultrashallow p[sup +] junctions,” *Journal of Applied Physics*, vol. 89, no. 6, p. 3458, 2001.

[46] R. Duffy, V. C. Venezia, A. Heringa, T. W. T. Hüsken, M. J. P. Hopstaken, N. E. B. Cowern, P. B. Griffin, and C. C. Wang, "Boron uphill diffusion during ultrashallow junction formation," *Applied Physics Letters*, vol. 82, no. 21, p. 3647, 2003.

[47] P. B. Griffin and C. H. Diaz, "Interface induced uphill diffusion of boron: an effective approach for ultrashallow junction," *IEEE Electron Device Letters*, vol. 22, no. 2, pp. 65–67, Feb. 2001.

[48] D. E. Ward and Y.-S. Oh, "A calibrated model for trapping of implanted dopants at material interface during thermal annealing," in *International Electron Devices Meeting 1998. Technical Digest (Cat. No.98CH36217)*, 1998, pp. 509–512.

[49] H. Sato, "Diffusion coronas around quartz xenocrysts in andesite and basalt from Tertiary volcanic region in northeastern Shikoku, Japan," *Contributions to Mineralogy and Petrology*, vol. 50, no. 1, pp. 49–64, 1975.

[50] Y. Zhang, "A modified effective binary diffusion model," *Journal of Geophysical Research*, vol. 98, no. B7, p. 11901, 1993.

[51] M. Ferri, S. Solmi, A. Parisini, M. Bersani, D. Giubertoni, and M. Barozzi, "Arsenic uphill diffusion during shallow junction formation," *Journal of Applied Physics*, vol. 99, no. 11, p. 113508, 2006.

[52] N. Kong, T. A. Kirichenko, Y. Kim, M. C. Foisy, and S. K. Banerjee, "Physically based kinetic Monte Carlo modeling of arsenic-interstitial interaction and arsenic uphill diffusion during ultrashallow junction formation," *Journal of Applied Physics*, vol. 104, p. 013514, 2008.

[53] N. Kong, T. a. Kirichenko, G. S. Hwang, and S. K. Banerjee, "Arsenic defect complexes at SiO_{2}/Si interfaces: A density functional theory study," *Physical Review B*, vol. 80, p. 205328, Nov. 2009.

[54] V. C. Venezia, R. Duffy, L. Pelaz, M. Aboy, A. Heringa, P. B. Griffin, C. C. Wang, M. J. P. Hopstaken, Y. Tamminga, T. Dao, B. Pawlak, and F. Roozeboom, "Dopant redistribution effects in preamorphized silicon during low temperature annealing," in *IEEE International Electron Devices Meeting 2003*, pp. 20.3.1–20.3.4.

[55] K. Suzuki, Y. Kataoka, S. Nagayama, C. W. Magee, T. H. Buyuklimanli, and T. Nagayama, "Analytical Model for Redistribution Profile of Ion-Implanted Impurities During Solid-Phase Epitaxy," *IEEE Transactions on Electron Devices*, vol. 54, no. 2, pp. 262–271, Feb. 2007.

[56] S. Solmi, M. Ferri, M. Bersani, D. Giubertoni, and V. Soncini, "Transient enhanced diffusion of arsenic in silicon," *Journal of Applied Physics*, vol. 94, no. 8, p. 4950, 2003.

[57] R. Ghoshtagore, "Intrinsic Diffusion of Boron and Phosphorus in Silicon Free from Surface Effects," *Physical Review B*, vol. 3, no. 12, pp. 4428–4428, Jun. 1971.

[58] S.-Y. Ma and S.-Q. Wang, "Ab initio calculation of intrinsic diffusion coefficients for boron in silicon at finite temperatures," *The European Physical Journal B*, vol. 72, no. 4, pp. 567–573, Nov. 2009.

[59] D. Nobili, S. Solmi, A. Parisini, M. Derdour, A. Armigliato, and L. Moro, "Precipitation, aggregation, and diffusion in heavily arsenic-doped silicon," *Physical Review B*, vol. 49, no. 4, pp. 2477–2483, Jan. 1994.

[60] S. Solmi and D. Nobili, "High concentration diffusivity and clustering of arsenic and phosphorus in silicon," *Journal of Applied Physics*, vol. 83, no. 5, p. 2484, 1998.

[61] A. Lietoila, J. F. Gibbons, and T. W. Sigmon, “The solid solubility and thermal behavior of metastable concentrations of As in Si,” *Applied Physics Letters*, vol. 36, no. 9, p. 765, 1980.

[62] a. Lietoila, “Metastable As-concentrations in Si achieved by ion implantation and rapid thermal annealing,” *Journal of Applied Physics*, vol. 52, no. 1, p. 230, 1981.

[63] K. Pandey, A. Erbil, G. Cargill, R. Boehme, and D. Vanderbilt, “Annealing of Heavily Arsenic-Doped Silicon: Electrical Deactivation and a New Defect Complex,” *Physical Review Letters*, vol. 61, no. 11, pp. 1282–1285, Sep. 1988.

[64] M. Ramamoorthy and S. Pantelides, “Complex Dynamical Phenomena in Heavily Arsenic Doped Silicon,” *Physical Review Letters*, vol. 76, no. 25, pp. 4753–4756, Jun. 1996.

[65] M. a. Berding, A. Sher, M. van Schilfgaarde, P. M. Rousseau, and W. E. Spicer, “Deactivation in heavily arsenic-doped silicon,” *Applied Physics Letters*, vol. 72, no. 12, p. 1492, 1998.

[66] P. M. Rousseau, P. B. Griffin, W. T. Fang, and J. D. Plummer, “Arsenic deactivation enhanced diffusion: A time, temperature, and concentration study,” *Journal of Applied Physics*, vol. 84, no. 7, p. 3593, 1998.

[67] N. D. Young, J. B. Clegg, and E. a. Maydell-Ondrusz, “Low-temperature annealing of shallow arsenic-implanted layers,” *Journal of Applied Physics*, vol. 61, no. 6, p. 2189, 1987.

[68] B. J. Pawlak, R. Duffy, T. Janssens, W. Vandervorst, K. Maex, a. J. Smith, N. E. B. Cowern, T. Dao, and Y. Tamminga, “Influence of the anneal conditions on arsenic activation during solid-phase epitaxial regrowth,” *Applied Physics Letters*, vol. 87, no. 3, p. 031915, 2005.

[69] L. Capello, T. H. Metzger, M. Werner, J. a. van den Berg, M. Servidori, L. Ottaviano, C. Bongiorno, G. Mannino, T. Feudel, M. Herden, and V. Holý, “Influence of preamorphization on the structural properties of ultrashallow arsenic implants in silicon,” *Journal of Applied Physics*, vol. 100, no. 10, p. 103533, 2006.

[70] C. Brizard, J. R. Regnard, J. L. Allain, A. Bourret, M. Dubus, A. Armigliato, and A. Parisini, “Backscattering spectrometry and ion channeling studies of heavily implanted As+ in silicon,” *Journal of Applied Physics*, vol. 75, no. 1, p. 126, 1994.

[71] a Satta, E. Albertazzi, M. Bianconi, G. Lulli, S. Balboni, and L. Colombo, “Atomistic simulation of ion channeling in heavily doped Si:As,” *Nuclear Instruments and Methods in Physics Research Section B: Beam Interactions with Materials and Atoms*, vol. 230, no. 1–4, pp. 112–117, Apr. 2005.

[72] A. Satta, E. Albertazzi, G. Lulli, and L. Colombo, “Ab initio structures of AsmV complexes and the simulation of Rutherford backscattering channeling spectra in heavily As-doped crystalline silicon,” *Physical Review B*, vol. 72, no. 23, p. 235206, Dec. 2005.

[73] A. Erbil, W. Weber, G. Cargill, and R. Boehme, “Lattice distortions for arsenic in single-crystal silicon,” *Physical Review B*, vol. 34, no. 2, pp. 1392–1394, Jul. 1986.

[74] J. Allain, J. Regnard, A. Bourret, A. Parisini, A. Armigliato, G. Tourillon, and S. Pizzini, “Extended x-ray-absorption fine-structure study of the local atomic structure in As+ heavily implanted silicon,” *Physical Review B*, vol. 46, no. 15, pp. 9434–9445, Oct. 1992.

[75] a. Herrera-Gómez, P. M. Rousseau, J. C. Woicik, T. Kendelewicz, J. Plummer, and W. E. Spicer, "Lattice compression of Si crystals and crystallographic position of As impurities measured with x-ray standing wave spectroscopy," *Journal of Applied Physics*, vol. 85, no. 3, p. 1429, 1999.

[76] U. Myler, P. J. Simpson, D. W. Lawther, and P. M. Rousseau, "On the electrical deactivation of arsenic in silicon," *Journal of Vacuum Science & Technology B: Microelectronics and Nanometer Structures*, vol. 15, no. 3, p. 757, May 1997.

[77] K. Saarinen, J. Nissilä, H. Kauppinen, M. Hakala, M. Puska, P. Hautojärvi, and C. Corbel, "Identification of Vacancy-Impurity Complexes in Highly n-Type Si," *Physical Review Letters*, vol. 82, no. 9, pp. 1883–1886, Mar. 1999.

[78] V. Ranki, J. Nissilä, and K. Saarinen, "Formation of Vacancy-Impurity Complexes by Kinetic Processes in Highly As-Doped Si," *Physical Review Letters*, vol. 88, no. 10, pp. 11–14, Feb. 2002.

[79] R. Olesinski and G. Abbaschian, "The As-Si (Arsenic-Silicon) system," *Journal of Phase Equilibria*, vol. 6, no. 3, pp. 254–258, 1985.

[80] P. M. Rousseau, P. B. Griffin, and J. D. Plummer, "Electrical deactivation of arsenic as a source of point defects," *Applied Physics Letters*, vol. 65, no. 5, p. 578, 1994.

[81] A. Ural, P. B. Griffin, and J. D. Plummer, "Fractional contributions of microscopic diffusion mechanisms for common dopants and self-diffusion in silicon," *Journal of Applied Physics*, vol. 85, no. 9, p. 6440, 1999.

[82] O. Dokumaci, P. M. Rousseau, S. Luning, V. Krishnamoorthy, K. S. Jones, and M. E. Law, "Transmission electron microscopy analysis of heavily As-doped, laser, and thermally annealed layers in silicon," *Journal of Applied Physics*, vol. 78, no. 2, p. 828, 1995.

[83] S. a. Harrison, T. F. Edgar, and G. S. Hwang, "Interstitial-Mediated Arsenic Clustering in Ultrashallow Junction Formation," *Electrochemical and Solid-State Letters*, vol. 9, no. 12, p. G354, 2006.

[84] Y. Kim, T. Kirichenko, N. Kong, G. Henkelman, and S. Banerjee, "First-principles studies of small arsenic interstitial complexes in crystalline silicon," *Physical Review B*, vol. 79, p. 075201, Feb. 2009.

[85] S. a. Harrison, T. F. Edgar, and G. S. Hwang, "Structure, stability, and diffusion of arsenic-silicon interstitial pairs," *Applied Physics Letters*, vol. 87, no. 23, p. 231905, 2005.

[86] D. Mathiot, "Diffusion of arsenic in silicon: Validity of the percolation model," *Applied Physics Letters*, vol. 42, no. 12, p. 1043, 1983.

[87] J. Xie and S. P. Chen, "Diffusion and Clustering in Heavily Arsenic-Doped Silicon : Discrepancies and Explanation," *Physical Review Letters*, vol. 83, no. 9, pp. 1795–1798, 1999.

[88] S. a. Harrison, T. F. Edgar, and G. S. Hwang, "Interaction between interstitials and arsenic-vacancy complexes in crystalline silicon," *Applied Physics Letters*, vol. 85, no. 21, p. 4935, 2004.

[89] N. Kong, S. K. Banerjee, T. a. Kirichenko, S. G. H. Anderson, and M. C. Foisy, "Enhanced and retarded diffusion of arsenic in silicon by point defect engineering," *Applied Physics Letters*, vol. 90, no. 6, p. 062107, 2007.

[90] "Annual Workshop on SIMS," 2005. [Online]. Available: http://www.simsworkshop.org.

[91] P. C. Zalm, “Quantitative sputtering,” *Surface and Interface Analysis*, vol. 11, no. 1–2, pp. 1–24, Jan. 1988.

[92] P. Sigmund, “Theory of Sputtering. I. Sputtering Yield of Amorphous and Polycrystalline Targets,” *Physical Review*, vol. 184, no. 2, pp. 383–416, Aug. 1969.

[93] J. J. Thomson, “Rays of Positive electricity,” *PROCEEDINGS OF THE ROYAL SOCIETY*, vol. LXXXIX, p. 26, 1913.

[94] P. Williams, “Secondary Ion Mass Spectrometry,” in *Applied Atomic Collision Spectroscopy*, New York: Academic Press, 1983, pp. 327 – 377.

[95] J. C. RIVIERE, *Surface Analytical Techniques*. Clarendon Press, 1990, p. 716.

[96] A. Benninghoven, “Surface analysis by means of ion beams,” *C R C Critical Reviews in Solid State Sciences*, vol. 6, no. 3, pp. 291–316, 1976.

[97] “SIMS tutorial.” [Online]. Available: http://www.eaglabs.com. [Accessed: 20-Feb-2013].

[98] W. Vandervorst, J. L. Everaert, E. Rosseel, M. Jurczak, T. Hoffman, P. Eyben, J. Mody, G. Zschätzsch, S. Koelling, M. Gilbert, T. Poon, J. del Agua Borniquel, M. Foad, R. Duffy, B. J. Pawlak, E. G. Seebauer, S. B. Felch, A. Jain, and Y. V. Kondratenko, “Conformal Doping of FINFETs: a Fabrication and Metrology Challenge,” in *AIP Conference Proceedings*, 2008, pp. 449–456.

[99] M. G. Dowsett, G. Rowlands, P. N. Allen, and R. D. Barlow, “An Analytic Form for the SIMS Response Function Measured from Ultra-thin Impurity Layers,” vol. 21, pp. 310–315, 1994.

[100] M. G. Dowsett and D. P. Chu, “Quantification of secondary-ion-mass spectroscopy depth profiles using maximum entropy deconvolution with a sample independent response function,” *Journal of Vacuum Science & Technology B*, no. 16, pp. 377–381, 1997.

[101] W. L. Chan and E. Chason, “Making waves: Kinetic processes controlling surface evolution during low energy ion sputtering,” *Journal of Applied Physics*, vol. 101, no. 12, p. 121301, 2007.

[102] R. M. Bradley and J. M. E. Harper, “Theory of ripple topography induced by ion bombardment,” *Journal of Vacuum Science & Technology A: Vacuum, Surfaces, and Films*, vol. 6, no. 4, p. 2390, Jul. 1988.

[103] Z. X. Jiang and P. F. a. Alkemade, “The complex formation of ripples during depth profiling of Si with low energy, grazing oxygen beams,” *Applied Physics Letters*, vol. 73, no. 3, p. 315, 1998.

[104] A. Zalar, “Significance of sample rotation in auger electronspectroscopy sputter depth profiling of thin films,” *Thin Solid Films*, vol. 193–194, pp. 258–269, Jan. 1990.

[105] M. Bersani, D. Giubertoni, E. Iacob, M. Barozzi, S. Pederzoli, L. Vanzetti, and M. Anderle, “Boron ultra low energy SIMS depth profiling improved by rotating stage,” *Applied Surface Science*, vol. 252, no. 19, pp. 7315–7317, Jul. 2006.

[106] D. Giubertoni, E. Iacob, P. Hoenicke, B. Beckhoff, G. Pepponi, S. Gennaro, and M. Bersani, “Ultralow energy boron implants in silicon characterization by nonoxidizing secondary ion mass spectrometry analysis and soft x-ray grazing incidence x-ray fluorescence techniques,” *Journal of Vacuum Science & Technology B: Microelectronics and Nanometer Structures*, vol. 28, no. 1, p. C1C84, 2010.

[107] G. Pepponi, D. Giubertoni, M. Bersani, F. Meirer, D. Ingerle, G. Steinhauser, C. Streli, P. Hoenicke, and B. Beckhoff, “Grazing incidence x-ray fluorescence and secondary ion mass spectrometry combined approach for the characterization of ultrashallow arsenic distribution in silicon,” *Journal of Vacuum Science & Technology B: Microelectronics and Nanometer Structures*, vol. 28, no. 1, p. C1C59, 2010.

[108] P. F. A. Alkemade, “Ultrahigh depth resolution secondary ion mass spectrometry with sub-keV grazing O[sub 2][sup +] beams,” *Journal of Vacuum Science & Technology B: Microelectronics and Nanometer Structures*, vol. 16, no. 1, p. 373, Jan. 1998.

[109] Y. Kataoka and T. Itani, “Ultrashallow depth profiling using SIMS and ion scattering spectroscopy,” *Surface and Interface AnalysisInterface*, vol. 39, no. September, pp. 826–831, 2007.

[110] J. a. Van den Berg, D. G. Armour, S. Zhang, S. Whelan, H. Ohno, T.-S. Wang, A. G. Cullis, E. H. J. Collart, R. D. Goldberg, P. Bailey, and T. C. Q. Noakes, “Characterization by medium energy ion scattering of damage and dopant profiles produced by ultrashallow B and As implants into Si at different temperatures,” *Journal of Vacuum Science & Technology B: Microelectronics and Nanometer Structures*, vol. 20, no. 3, p. 974, 2002.

[111] W.-K. Chu, J. W. Mayer, and M. A. Nicolet, *Backscattering Spectrometry*. New York: Academic Press, 1980, p. 399.

[112] W. K. Chu, J. W. Mayer, and M. Nicolet, *Backscattering Spectrometry*. New York: Academic Press, 1978, p. 399.

[113] “SRIM.” [Online]. Available: http://www.srim.org/. [Accessed: 11-Mar-2013].

[114] M. Werner, “Damage formation and annealing studies of low energy ion implants in silicon using medium energy ion scattering,” The University of Salford, 2006.

[115] J. F. van der Veen, “Ion beam crystallography of surfaces and interfaces,” *Surface Science Reports*, vol. 5, no. 5–6, pp. 199–287, Dec. 1985.

[116] R. M. Tromp, *Practical Surface Analysis: Ion and neutral spectroscopy*, 2nd ed. Wiley, 1992, p. 738.

[117] D. K. Schroder, *Semiconductor Material and Device Characterization*. Hoboken, NJ, USA: John Wiley & Sons, Inc., 2005.

[118] P. Avino, G. Capannesi, and A. Rosada, “Instrumental neutron activation analysis, a powerful instrument in determining environmental pollution: theory and applications,” *Prevention Today*, vol. 3, no. 2, pp. 13–36, 2007.

[119] M. Newville, *Fundamentals of XAFS*. 2004.

[120] L. J. Van Der Pauw, “A method of measuring the resistivity and Hall coefficient on lamellae of arbitrary shape,” *Philips Technical Review*, vol. 20, no. 8. Philips Technical Review, pp. 220–224, 1958.

[121] L. J. van der Pauw, “A Method of Measuring Specific Resistivity and Hall Effect of Discs of Arbitrary Shapes,” *Philips Research Reports*, vol. 13, pp. 1–9, 1958.

[122] W. Vandervorst, D. G. Seiler, A. C. Diebold, R. McDonald, C. M. Garner, D. Herr, R. P. Khosla, and E. M. Secula, “USJ metrology : from 0D to 3D analysis.,” in *AIP Conference Proceedings*, 2007, vol. 931, no. 1, pp. 233–245.

[123] D. Giubertoni, M. Bersani, M. Barozzi, S. Pederzoli, E. Iacob, J. a. van den Berg, and M. Werner, “Comparison between the SIMS and MEIS techniques for the characterization of ultra shallow arsenic implants,” *Applied Surface Science*, vol. 252, no. 19, pp. 7214–7217, Jul. 2006.

[124] M. Barozzi, “Arsenic shallow depth profiling: accurate quantification in SiO2/Si stack,” *Applied Surface Science*, vol. 231–232, pp. 632–635, Jun. 2004.

[125] A. Merkulov, P. Peres, S. Choi, F. Horreard, H.-U. Ehrke, N. Loibl, and M. Schuhmacher, “Advanced secondary ion mass spectroscopy quantification in the first few nanometer of B, P, and As ultrashallow implants,” *Journal of Vacuum Science & Technology B: Microelectronics and Nanometer Structures*, vol. 28, no. 1, p. C1C48, 2010.

[126] M. Tomita, T. Hasegawa, S. Hashimoto, S. Hayashi, Y. Homma, S. Kakehashi, Y. Kazama, K. Koezuka, H. Kuroki, K. Kusama, Z. Li, S. Miwa, S. Miyaki, Y. Okamoto, K. Okuno, S. Saito, S. Sasaki, H. Shichi, H. Shinohara, F. Toujou, Y. Ueki, and Y. Yamamoto, “SIMS round-robin study of depth profiling of arsenic implants in silicon,” *Applied Surface Science*, vol. 203–204, pp. 465–469, Jan. 2003.

[127] N. Baboux, J. . Dupuy, G. Prudon, P. Holliger, F. Laugier, A. . Papon, and J. . Hartmann, “Ultra-low energy SIMS analysis of boron deltas in silicon,” *Journal of Crystal Growth*, vol. 245, no. 1–2, pp. 1–8, Nov. 2002.

[128] M. Anderle, M. Barozzi, M. Bersani, D. Giubertoni, and P. Lazzeri, “Ultra Shallow Depth Profiling by Secondary Ion Mass Spectrometry Techniques,” in *Frontiers of Characterization and Metrology for ULSI*, 2003, pp. 695–704.

[129] J. a. Van den Berg, D. G. Armour, S. Zhang, S. Whelan, H. Ohno, T.-S. Wang, a. G. Cullis, E. H. J. Collart, R. D. Goldberg, P. Bailey, and T. C. Q. Noakes, “Characterization by medium energy ion scattering of damage and dopant profiles produced by ultrashallow B and As implants into Si at different temperatures,” *Journal of Vacuum Science & Technology B: Microelectronics and Nanometer Structures*, vol. 20, no. 3, p. 974, 2002.

[130] M. Werner, J. Van den Berg, D. Armour, W. Vandervorst, E. Collart, R. Goldberg, P. Bailey, and T. Noakes, “Damage accumulation and dopant migration during shallow As and Sb implantation into Si,” *Nuclear Instruments and Methods in Physics Research Section B: Beam Interactions with Materials and Atoms*, vol. 216, pp. 67–74, Feb. 2004.

[131] K. Wittmaack, “Oxygen-concentration dependence of secondary ion yield enhancement,” *Surface Science*, vol. 112, no. 1–2, pp. 168–180, Dec. 1981.

[132] P. Williams, *Applied Atomic Collision Physics*. New York: Academic Press, 1983, pp. 327–377.

[133] OriginLabs, “OriginPro.” [Online]. Available: http://www.originlab.com/.

[134] L. Pelaz, L. a. Marqués, and J. Barbolla, “Ion-beam-induced amorphization and recrystallization in silicon,” *Journal of Applied Physics*, vol. 96, no. 11, p. 5947, 2004.

[135] N. G. Rudawski, K. S. Jones, S. Morarka, M. E. Law, and R. G. Elliman, “Stressed multidirectional solid-phase epitaxial growth of Si,” *Journal of Applied Physics*, vol. 105, no. 8, p. 081101, 2009.

[136] R. Duffy, T. Dao, Y. Tamminga, K. van der Tak, F. Roozeboom, and E. Augendre, “Groups III and V impurity solubilities in silicon due to laser, flash, and solid-phase-epitaxial-regrowth anneals,” *Applied Physics Letters*, vol. 89, no. 7, p. 071915, 2006.

[137] S. Whelan, J. a. Van den Berg, S. Zhang, D. G. Armour, and R. D. Goldberg, “The dependence of arsenic transient enhanced diffusion on the silicon substrate temperature during ultralow energy implantation,” *Applied Physics Letters*, vol. 76, no. 5, p. 571, 2000.

[138] G. Pepponi, D. Giubertoni, S. Gennaro, M. Bersani, M. Anderle, R. Grisenti, M. Werner, and J. A. Van Den Berg, “Local Arsenic Structure in Shallow Implants in Si following SPER : an EXAFS and MEIS study,” in *Ion Implantation Technology*, 2006, pp. 117–120.

[139] J. Narayan and O. W. Holland, “Formation of metastable supersaturated solid solutions in ion implanted silicon during solid phase crystallization,” *Applied Physics Letters*, vol. 41, no. 3, p. 239, 1982.

[140] D. Giubertoni, G. Pepponi, M. A. Sahiner, S. P. Kelty, S. Gennaro, M. Bersani, M. Kah, K. J. Kirkby, R. Doherty, M. a. Foad, F. Meirer, C. Streli, J. C. Woicik, and P. Pianetta, “Deactivation of submelt laser annealed arsenic ultrashallow junctions in silicon during subsequent thermal treatment,” *Journal of Vacuum Science & Technology B: Microelectronics and Nanometer Structures*, vol. 28, no. 1, p. C1B1, 2010.

[141] R. Kasnavi, Y. Sun, R. Mo, P. Pianetta, P. B. Griffin, and J. D. Plummer, “Characterization of arsenic dose loss at the Si/SiO[sub 2] interface,” *Journal of Applied Physics*, vol. 87, no. 5, p. 2255, 2000.

[142] S. Whelan, V. Privitera, G. Mannino, M. Italia, C. Bongiorno, A. La Magna, and E. Napolitani, “Electrical activation of ultralow energy As implants in Si,” *Journal of Applied Physics*, vol. 90, no. 8, p. 3873, 2001.

[143] J. A. Van Den Berg, D. G. Armour, M. Werner, and S. Whelan, “High depth resolution characterization of the damage and annealing behaviour of ultra shallow As implants in Si,” in *Ion Implantation Technology 2002*, 2002, vol. 32061, no. C, pp. 2–5.

[144] L. Capello, T. Metzger, M. Werner, J. Vandenberg, M. Servidori, M. Herden, and T. Feudel, “Solid-phase epitaxial regrowth of a shallow amorphised Si layer studied by X-ray and medium energy ion scattering,” *Materials Science and Engineering: B*, vol. 124–125, pp. 200–204, Dec. 2005.

[145] D. Giubertoni, G. Pepponi, S. Gennaro, M. Bersani, M. A. Sahiner, S. P. Kelty, R. Doherty, M. a. Foad, M. Kah, K. J. Kirkby, J. C. Woicik, and P. Pianetta, “Correlation of local structure and electrical activation in arsenic ultrashallow junctions in silicon,” *Journal of Applied Physics*, vol. 104, no. 10, p. 103716, 2008.

[146] K. Suzuki, Y. Kataoka, S. Nagayama, C. W. Magee, T. H. Buyuklimanli, and T. Nagayama, “Analytical Model for Redistribution Profile of Ion-Implanted Impurities During Solid-Phase Epitaxy,” *IEEE Transactions on Electron Devices*, vol. 54, no. 2, pp. 262–271, Feb. 2007.

[147] L. Csepregi, E. F. Kennedy, T. J. Gallagher, J. W. Mayer, and T. W. Sigmon, “Reordering of amorphous layers of Si implanted with 31P, 75As, and 11B ions,” *Journal of Applied Physics*, vol. 48, no. 10, p. 4234, 1977.

[148] J. S. Williams and R. G. Elliman, “Near-surface regrowth rate effects in high-dose ion-implanted (100) silicon,” *Applied Physics Letters*, vol. 37, no. 9, p. 829, 1980.

[149] Y.-J. Jeon, M. F. Becker, and R. M. Walser, “CONCENTRATION DEPENDENCE OF ARSENIC ON SOLID PHASE EPITAXIAL,” in *Materials Research Society Symposium Proceedings*, 1989, vol. 157, no. 100, pp. 745–750.

[150] G. L. Olson, J. A. Roth, L. D. Hess, and J. Narayan, “KINETIC COMPETITION DURING SOLID PHASE CRYSTALLIZATION IN ION-IMPLANTED SILICON,” in *Materials Research Society Symposium Proceedings*, 1984, vol. 23, pp. 375–382.

[151] E. Demenev, D. Giubertoni, S. Gennaro, M. Bersani, E. Hourdakis, a. G. Nassiopoulou, M. a. Reading, and J. a. van den Berg, “Arsenic redistribution after solid phase epitaxial regrowth of shallow pre-amorphized silicon layers,” in *Ion Implantation Technology 2012*, 2012, vol. 272, pp. 272–275.

[152] R. G. Elliman, J. M. Gibson, D. C. Jacobson, J. M. Poate, and J. S. Williams, “Diffusion and precipitation in amorphous Si,” *Applied Physics Letters*, vol. 46, no. 5, p. 478, 1985.

[153] M. Ferri, S. Solmi, A. Parisini, M. Bersani, D. Giubertoni, and M. Barozzi, “Arsenic uphill diffusion during shallow junction formation,” *Journal of Applied Physics*, vol. 99, no. 11, p. 113508, 2006.

[154] G. Masetti, M. Severi, and S. Solmi, “Modeling of carrier mobility against carrier concentration in arsenic-, phosphorus-, and boron-doped silicon,” *IEEE Transactions on Electron Devices*, vol. 30, no. 7, pp. 764–769, Jul. 1983.

[155] N. Bennett, N. E. B. Cowern, and B. J. Sealy, “Model for electron mobility as a function of carrier concentration and strain in heavily doped strained silicon,” *Applied Physics Letters*, vol. 94, no. 25, p. 252109, 2009.

[156] N. S. Bennett, N. E. B. Cowern, and B. J. Sealy, “Model for electron mobility as a function of carrier concentration and strain in heavily doped strained silicon,” *Applied Physics Letters*, vol. 94, no. 25, p. 252109, 2009.

[157] A. Martinez-Limia, P. Pichler, C. Steen, S. Paul, and W. Lerch, “Modeling and Simulation of Advanced Annealing Processes,” *Materials Science Forum*, vol. 573–574, pp. 279–293, 2008.

[158] S. Qin, Y. J. Hu, A. McTeer, S. Prussin, and J. Reyes, “Study of Carrier Mobility of Low-Energy, High-Dose Ion Implantations Using Continuous Anodic Oxidation Technique/Differential Hall Effect (CAOT/DHE) Measurements,” in *2010 IEEE Workshop on Microelectronics and Electron Devices*, 2010, pp. 1–4.

[159] P. M. Rousseau, P. B. Griffin, W. T. Fang, and J. D. Plummer, “Arsenic deactivation enhanced diffusion: A time, temperature, and concentration study,” *Journal of Applied Physics*, vol. 84, no. 7, p. 3593, 1998.

[160] I. Suni, G. Göltz, M. G. Grimaldi, M. Nicolet, and S. S. Lau, “Compensating impurity effect on epitaxial regrowth rate of amorphized Si,” *Applied Physics Letters*, vol. 40, no. 3, p. 269, 1982.

[161] Y.-J. Jeon, M. F. Becker, and R. M. Walser, “Concentration Dependence of Arsenic on Solid Phase Epitaxial Regrowth of Amorphous Silicon,” *MRS Proceedings*, vol. 157, p. 745, Feb. 2011.

[162] B. C. Johnson, “Kinetics of arsenic-enhanced solid phase epitaxy in silicon,” *Journal of Applied Physics*, vol. 95, no. 8, p. 4427, 2004.

[163] C. Zechner, D. Matveev, and a Erlebach, “Phase-field model for the dopant redistribution during solid phase epitaxial regrowth of amorphized silicon,” *Materials Science and Engineering B*, vol. 114–115, pp. 162–165, Dec. 2004.

[164] J. Zhang, Y. Ashizawa, and H. Oka, “Modeling and Simulation of Fluorine Related Diffusion in Silicon,” in *2006 International Workshop on Junction Technology*, 2006, pp. 50–53.

[165] E. Demenev, D. Giubertoni, S. Gennaro, M. Bersani, E. Hourdakis, A. G. Nassiopoulou, M. A. Reading, and J. A. van den Berg, “Arsenic redistribution after solid phase epitaxial regrowth of shallow pre-amorphized silicon layers,” in *AIP Conference Proceedings*, 2012, pp. 272–275.

[166] L. Pei, “DOPANT SEGREGATION AT SILICON-OXIDE INTERFACES,” North Carolina State University, 2006.

[167] J. Dabrowski, H.-J. Müssig, V. Zavodinsky, R. Baierle, and M. Caldas, “Mechanism of dopant segregation to SiO2/Si(001) interfaces,” *Physical Review B*, vol. 65, no. 24, pp. 1–11, May 2002.

[168] M. Derdour, “High-Temperature Equilibrium Carrier Density of Arsenic-Doped Silicon,” *Journal of The Electrochemical Society*, vol. 138, no. 3, p. 857, 1991.

[169] A. Parisini, A. Bourret, A. Armigliato, M. Servidori, S. Solmi, R. Fabbri, J. R. Regnard, and J. L. Allain, “Electrical activity and structural evolution correlations in laser and thermally annealed As-implanted Si specimens,” *Journal of Applied Physics*, vol. 67, no. 5, p. 2320, 1990.

[170] D. Giubertoni, G. Pepponi, M. Bersani, S. Gennaro, F. D’Acapito, R. Doherty, and M. a. Foad, “An EXAFS investigation of arsenic shallow implant activation in silicon after laser sub-melt annealing,” *Nuclear Instruments and Methods in Physics Research Section B: Beam Interactions with Materials and Atoms*, vol. 253, no. 1–2, pp. 9–12, Dec. 2006.

[171] P. Pichler, *Intrinsic Point Defects, Impurities, and Their Diffusion in Silicon*. Vienna: Springer Vienna, 2004.

[172] Y. Kataoka, K. Yamazaki, M. Shigeno, Y. Tada, and K. Wittmaack, “Surface roughening of silicon under ultra-low-energy cesium bombardment,” *Applied Surface Science*, vol. 203–204, pp. 43–47, Jan. 2003.

[173] A. Zalar, “Significance of sample rotation in auger electronspectroscopy sputter depth profiling of thin films,” *Thin Solid Films*, vol. 193–194, pp. 258–269, Jan. 1990.

[174] D. Giubertoni, M. Barozzi, M. Anderle, and M. Bersani, “Optimization of secondary ion mass spectrometry ultra-shallow boron profiles using an oblique incidence O[sub 2][sup +] beam,” *Journal of Vacuum Science & Technology B: Microelectronics and Nanometer Structures*, vol. 22, no. 1, p. 336, 2004.

[175] P. Kringhoj and R. G. Elliman, “Diffusion of ion implanted Sn in Si, Si1−xGex, and Ge,” *Applied Physics Letters*, vol. 65, no. 3, p. 324, 1994.

[176] N. Kong, T. A. Kirichenko, Y. Kim, M. C. Foisy, and S. K. Banerjee, “Physically based kinetic Monte Carlo modeling of arsenic-interstitial interaction and arsenic uphill diffusion during ultrashallow junction formation,” *Journal of Applied Physics*, vol. 104, p. 013514, 2008.

[177] P. M. Rousseau, S. W. Crowder, P. B. Griffin, and J. D. Plummer, “Arsenic deactivation enhanced diffusion and the reverse short-channel effect,” *IEEE Electron Device Letters*, vol. 18, no. 2, pp. 42–44, 1997.

[178] S. W. Jones, *Diffusion in Silicon*. 2008.

[179] S. Qin, A. McTeer, J. Hu, J. Liu, D. Panda, and J. Trivedi, “Plasma doping on 68nm CMOS device source/drain formations,” in *Extended Abstracts - 2008 8th International Workshop on Junction Technology (IWJT ’08)*, 2008, pp. 8–13.

[180] S. Qin, K. Zhuang, Y. J. Hu, A. McTeer, and S. Lu, “Direct Measurements of Self-Sputtering, Swelling, and Deposition Effects of N-Type Low-Energy Ion Implantations,” *IEEE Transactions on Plasma Science*, vol. 37, no. 10, pp. 2082–2089, Oct. 2009.

[181] S. . Felch, Z. Fang, B.-W. Koo, R. . Liebert, S. . Walther, and D. Hacker, “Plasma doping for the fabrication of ultra-shallow junctions,” *Surface and Coatings Technology*, vol. 156, no. 1–3, pp. 229–236, Jul. 2002.

[182] B. Sahli, K. Vollenweider, and W. Fichtner, “Ab initio calculations for point defect clusters with P, As, and Sb in Si,” *Physical Review B*, vol. 80, no. 7, p. 075208, Aug. 2009.

[183] F. Meirer, E. Demenev, D. Giubertoni, S. Gennaro, L. Vanzetti, G. Pepponi, M. Bersani, M. a. Sahiner, G. Steinhauser, M. a. Foad, J. C. Woicik, A. Mehta, and P. Pianetta, “Formation of arsenic rich silicon oxide under plasma immersion ion implantation and laser annealing,” in *Ion Implantation Technology 2012*, 2012, vol. 183, pp. 183–188.

[184] S. S. Choi, M. Z. Numan, W. K. Chu, and E. a. Irene, “Anomalous oxidation rate of silicon implanted with very high doses of arsenic,” *Applied Physics Letters*, vol. 51, no. 13, p. 1001, 1987.

[185] F. Benzi, I. Davoli, M. Rovezzi, and F. D’Acapito, “A new procedure for the quantitative analysis of extended x-ray absorption fine structure data in total reflection geometry.,” *The Review of scientific instruments*, vol. 79, no. 10, p. 103902, Oct. 2008.

[186] J. Kawai, S. Hayakawa, Y. Kitajima, and Y. Gohshi, “X–ray absorption fine structure (XAFS) of Si wafer measured using total reflection X–rays,” *Spectrochimica Acta Part B: Atomic Spectroscopy*, vol. 54, no. 1, pp. 215–222, Jan. 1999.

[187] P. Ballirano and A. Maras, “Refinement of the crystal structure of arsenolite , AS203,” *Zeitschrift fur Kristallographie*, vol. 217, pp. 177–178, 2002.

[188] N. A. Gokcen, “The As (Arsenic) system,” *Bulletin of Alloy Phase Diagrams*, vol. 10, no. 1, pp. 11–22, Feb. 1989.

[189] Y. Takagaki, E. Wiebicke, M. Ramsteiner, L. Däweritz, and K. H. Ploog, “Spontaneous growth of arsenic oxide micro-crystals on chemically etched MnAs surfaces,” *Applied Physics A: Materials Science & Processing*, vol. 76, no. 5, pp. 837–840, Mar. 2003.

[190] C. M. Finnie and P. W. Bohn, “Near-field photoluminescence of microcrystalline arsenic oxides produced in anodically processed gallium arsenide,” *Applied Physics Letters*, vol. 74, no. 8, p. 1096, 1999.

[191] M. Rojas-López, M. a. Vidal, H. Navarro-Contreras, J. M. Gracia-Jiménez, E. Gómez, and R. Silva-González, “Dependence on the atmosphere of preparation of the luminescence of spark processed porous GaAs,” *Journal of Applied Physics*, vol. 87, no. 3, p. 1270, 2000.